PHYSICS OF NONRADIATIVE ENERGY TRANSFER IN THE COMPLEX MEDIA OF 0D, 2D AND 3D MATERIALS

A DISSERTATION SUBMITTED TO

THE GRADUATE SCHOOL OF ENGINEERING AND SCIENCE

OF BILKENT UNIVERSITY

IN PARTIAL FULFILLMENT OF THE REQUIREMENTS FOR

THE DEGREE OF

DOCTOR OF PHILOSOPHY

IN

PHYSICS

By

Aydan Yeltik

July 2016

PHYSICS OF NONRADIATIVE ENERGY TRANSFER IN THE COMPLEX MEDIA OF 0D, 2D AND 3D MATERIALS
By Aydan Yeltik
July 2016

We certify that we have read this dissertation and that in our opinion it is fully adequate, in scope and in quality, as a dissertation for the degree of Doctor of Philosophy.

Hilmi Volkan Demir(Advisor)

Bilal Tanatar

Dönüş Tuncel

Bekir Sıtkı Kandemir

Adil Denizli

Approved for the Graduate School of Engineering and Science:

Levent Onural
Director of the Graduate School

ABSTRACT

PHYSICS OF NONRADIATIVE ENERGY TRANSFER IN THE COMPLEX MEDIA OF 0D, 2D AND 3D MATERIALS

Aydan Yeltik
Ph.D. in Physics
Advisor: Hilmi Volkan Demir
July 2016

Quantum-confined colloidal nanostructures with strong excitonic properties have emerged as promising light harvesting components in photonics and optoelectronics over the past 20 years. With their favorable photophysical characteristics, three-dimensional-confined colloidal quantum dots and 2D-confined colloidal quantum wells have garnered great attention in the fields ranging from biology and chemistry to physics and engineering. It is technologically significant to utilize the key characteristics of these brightly luminescent nanomaterials through hybridizing and/or interfacing with various technological materials including 3D bulk silicon, graphene based 2D structures such as graphene oxide and reduced graphene oxide, and 2D layered transition metal dichalcogenides such as molybdenum disulphide. Compelling partnership of these appealing materials can be achieved through the nonradiative energy transfer (NRET), which is a phenomenon involving both the exciton and charge transfer mechanisms. Along with the hybrids of low dimensional particles with the conventional bulk materials, the closely interacting structures of these colloidal and layered nanomaterials have widespread interest at both the fundamental science and application levels. From these physical and technological points of view, in this thesis, we addressed important scientific problems and proposed innovative solutions including both the experimental and theoretical approaches in interfacing complex media of 0D, 2D and 3D materials and showing strong NRET interactions. Our key achievements include high excitonic enhancement in silicon and graphene based materials with the integration of nanoparticles, comprehensive photophysical investigation of the newly emerging nanomaterials and successful tailoring of the colloidal nanostructures to the next-generation optoelectronic applications.

Keywords: Nonradiative energy transfer, colloidal quantum dots, colloidal quantum wells, layered quantum wells, semiconductors, excitonics, charge transfer, light harvesting.

ÖZET

0, 2 VE 3 BOYUTLU MALZEMELERİN OLUŞTURDUĞU KARMAŞIK YAPILARDA IŞINIMSIZ ENERJİ TRANSFERİNİN FİZİĞİ

Aydan Yeltik
Fizik, Doktora
Tez Danışmanı: Hilmi Volkan Demir
Temmuz 2016

Son yıllarda, güçlü eksitonik özelliklere sahip kuvantum sınırlı koloidal nanoyapılar fotonik ve optoelektronik alanlarında yaygın bir kullanıma ulaşmıştır. 3 boyutta sınırlı koloidal kuvantum noktaları ve 2 boyutta sınırlı koloidal kuvantum kuyuları üstün fotofiziksel özellikleri ile biyoloji ve kimyadan fizik ve mühendisliğe kadar birçok alanda büyük ilgi uyandırmıştır. Bu ışık saçan nanomalzemeler ile 3 boyutlu silikon, 2 boyutlu grafen ve 2 boyutlu dikalkogenitler gibi teknolojik açıdan önemli malzemelerin melez ve/veya arabirim yapıları özellikle önem arz etmektedir. Bu yapılarda eksitonik ve eksitonik olmayan transfer mekanizmalarını içeren ışınımsız enerji transferi gerçekleşebilmektedir. Farklı kuvantum sınırlı malzemelere sahip bu yapılara hem temel bilim hem de teknolojik uygulama seviyesinde yaygın bir ilgi mevcuttur. Bu tezde, deneysel ve teorik yaklaşımlar kullanarak 0, 2 ve 3 boyutlu malzemelerin karmaşık yapılarının oluşturulması ve ortaya çıkan güçlü ışınımsız enerji transferi etkileşimlerinin incelenmesi konularındaki önemli bilimsel problemleri ve önerdiğimiz yenilikçi çözümleri sunmaktayız. Bu tezin içerdiği önemli başarılarımız arasında silikon ve grafen tabanlı yapılarda kuvantum sınırlı koloidal parçacıklar kullanarak eksitonik verimlilik artışı, yeni ortaya çıkan nanomalzemelerin fotofiziksel açıdan kapsamlı şekilde incelenmesi ve yeni nesil optoelektronik uygulamalarda koloidal nanoparçacıkların başarılı kullanımı bulunmaktadır.

Anahtar sözcükler: Işınımsız enerji transferi, koloidal kuvantum noktacıklar, koloidal kuvantum kuyuları, katmanlı kuvantum kuyuları , yarı iletkenler, eksiton, yük transferi, ışık hasadı.

Acknowledgement

First of all, I would like to take this opportunity to express my gratitude to my supervisor Prof. Hilmi Volkan Demir, whose support, motivation and guidance made this thesis work along with other great things possible.

I would like to thank my committee members Prof. Bilal Tanatar, Prof. Dönüş Tuncel, Prof. Bekir Sıtkı Kandemir and Prof. Adil Denizli for accepting to be in my thesis jury and for their support.

I would like to thank all the past and present members of Demir Group for their friendship and having great fun together. I would also like to thank all my other friends at Bilkent University. And, I would like to acknowledge the instructors, engineers and graduate students at UNAM.

Finally, I would like to thank my family for their love, support and encouragement without any expectation.

Contents

Chapter 1 1
Introduction 1
1.1 Structure of the thesis 2
Chapter 2 5
Background on Materials, Methods and Physical Phenomena 5
2.1 Materials 5
2.1.1 Colloidal 0D semiconductor nanocrystals: colloidal quantum dots 5
2.1.2 Colloidal quasi-2D semiconductor nanocrystals: nanoplatelets 13
2.1.3 Layered 2D nanomaterials: graphene, graphene oxide, reduced graphene oxide and MoS_2 19
2.1.4 Indirect bandgap 3D semicondutor materials: silicon 23
2.2 Methods 25
2.2.1 Steady-state and time-resolved fluorescence spectroscopy 25
2.2.2 Measuring the optical absorption properties of nanoemitters 30
2.2.3 Fabrication and characterization of hybrid structures 31
2.2.4 Growth of layered 2D MoS_2 nanomaterials 32
2.3 Physical phenomena 34
2.3.1 Excitonic nonradiative energy transfer mechanism 34
2.3.2 Nonexcitonic nonradiative energy transfer mechanism 43
Chapter 3 47

Excitonic Nonradiative Energy Transfer by Using Colloidal 0D Semiconductor Nanocrystals 47

3.1 Phonon-assisted excitonic nonradiative energy transfer into silicon by using quantum dot nanoemitters 50

3.1.1 Motivation 50

3.1.2 Experiment and theory 52

3.1.3 Results and discussion 75

3.1.4 Summary 86

3.2 Enhancement of excitonic nonradiative energy transfer into bulk silicon with the hybridization of cascaded quantum dots 87

3.2.1 Motivation 87

3.2.2 Experiment and theory 88

3.2.3 Results and discussion 99

3.2.4 Summary 105

3.3 Evidence for nonradiative energy transfer from quantum dots into graphene-based nanomaterials and a short study including MoS_2 106

3.3.1 Motivation 106

3.3.2 Experiment 108

3.3.3 Results and discussion 111

3.3.4 Summary 118

3.3.5 Additional study including MoS_2 118

Chapter 4 123

Excitonic Nonradiative Energy Transfer by Using Colloidal quasi-2D Semiconductor Nanocrystals 123

4.1 Experimental determination of the absorption cross-section and molar extinction coefficient of colloidal nanoplatelets 126

4.1.1 Motivation 126

4.1.2 Experiment 128

4.1.3 Results and discussion 131

4.1.4 Summary 145

4.2 Nonradiative energy transfer between quasi-2D colloidal doped and undoped semiconductors 146

4.2.1 Motivation 146

4.2.2 Experiment 148

4.2.3 Results and discussion 149

4.2.4 Summary 160

Chapter 5 161

Conclusions 161

5.1 Concluding remarks 161

5.2 Future outlook 164

5.3 Contributions 165

Bibliography 167

List of Figures

Figure 2.1. (a) A TEM image, (b) an illustration together with (c) the energy-band diagram of a semiconductor nanocrystal (e.g. a CQD) (a rough representation)..... 7
Figure 2.2. (a) Photograph of PL from CdSe/ZnS QDs of increasing size (left to right) illuminated under UV light. (b) Qualitative changes in the QD bandgap energies, Eg, and density of states for CdSe QD510 (2.7nm diameter), QD530 (2.9 nm), QD555 (3.5 nm), QD570 (3.8 nm), QD590 (4.3 nm), and QD610 (4.8 nm). The conduction (CB) and valence (VB) bands of bulk CdSe are shown for comparison and the energy scale is expanded as 10E for clarity. Transitions for absorption and band edge emission are also presented. (Adapted and reprinted with permission from Ref. [7]. Copyright 2011, American Chemical Society.) 9
Figure 2.3. Typical absorbance and emission spectra of CQDs. 10
Figure 2.4. Schematic representation of a zincblende 4 monolayer (ML) CdSe NPL.. 14
Figure 2.5. TEM images of (a) 4ML and (b) 5ML NPLs with both the small and large lateral sizes, and their corresponding thicknesses..... 15
Figure 2.6. UV-Vis absorbance and PL emission spectra of 4ML CdSe NPLs..... 17
Figure 2.7. Energy diagrams of an optical emitter and a nearby graphene monolayer film along with schematic representation of the sample structure. (Reprinted with permission from Ref. [124]. Copyright 2013, American Chemical Society.) 21
Figure 2.8. Band structure of bulk silicon. (Reprinted with permission from Ref. [149]. Copyright 2001, Oxford University Press.) 24
Figure 2.9. Logic for operation of the TRF system. 27

Figure 2.10. FluoTime 200 TRF system. 28
Figure 2.11. Schematic representation of a TRF system. 28
Figure 2.12. CVD growth system that we use in Demir laboratory. 33
Figure 2.13. (a) Exemplary SEM images, (b) Raman spectrum and (c) PL spectrum of MoS_2 single layer structures. 33
Figure 2.14. (a) Simplified Jablonski diagram including excitation and relaxation transitions, followed by radiative decay (k^R), nonradiative decay (k^{NR}) or FRET (k_{FRET}). After the FRET, the acceptor is in an excited state (A^*), followed by radiative or nonradiative decay to the ground state (A). (b) Different energy pathways after donor excitation ($h\nu_{ex}$) possibly leading to luminescence emission of D ($h\nu_D$) or A ($h\nu_A$). (Reprinted with permission from Ref. [159]. Copyrigt 2014, Wily-VH.) 36
Figure 2.15. The overlaping area of the area-normalized emission spectrum of Donor and the extinction coefficient spectrum of Acceptor, defining the overlap integral *J*. . 39
Figure 2.16. FRET efficiency (ηFRET) as a function of donor-acceptor separation distance (r). 40

Figure 3.1. (a) Schematic of the hybrid nanostructure of multi-monolayer CQDs and silicon separated by controlled Al_2O_3 separation thickness. Here l = 1.65 nm is the native SiO_2 film thickness, h is the distance between the top-most oxide layer and center of the first CQD layer, X ranging from 0.0 to 4.0 nm is the Al_2O_3 film thickness, and d is the distance from a CQD monolayer center of interest to the bulk silicon surface. The CQDs of the same monolayer are assumed to have the same exciton transfer contribution to bulk silicon. (b) SEM image of the CQDs furnished on the $Al_2O_3/SiO_2/Si$ structures. Inset shows optical absorption and PL spectra of the CQDs (black and green curves, respectively) and absorption spectrum of silicon (red curve). (c) Atomic force microscopy image of the 10-monolayer-equivalent CQD film on top of silicon with the height profile of the line shown inside the AFM image. 54
Figure 3.2. Experimental fluorescence decays of 10-monolayer–equivalent CQD film on silicon substrate with 0.0, 1.0, 2.0 and 4.0 nm of Al_2O_3 separation layer and on sapphire as reference sample: (a) over a time decay of 200 ns and (b) zooming in the first 50 ns. The multi-exponential fits are shown inside the decay curves with the averaged lifetimes reported at the bottom. 56

Figure 3.3. Temperature dependence of PL intensity of the CQDs coated on the $Al_2O_3/SiO_2/Si$ and sapphire substrates. 57
Figure 3.4. Fluorescence decays of the ten-monolayer-equivalent CQDs measured at three different spectral positions (peak, blue- and red-tail) at FWHM. 59
Figure 3.5. TRF decays of 10-monolayer-equivalent CQD film over silicon substrate with 0.0, 1.0, 2.0 and 4.0 nm thick Al_2O_3 separation layer and over sapphire, which were recorded at 22 K. 60
Figure 3.6. A schematic of the studied 0D → 3D hybrid structure. Here, z is the dielectric thickness of the effective oxide layer on silicon, h is the distance between the dipole and the topmost dielectric layer, l = 1.65 nm is the SiO_2 film thickness, X ranging from 0 to 4.0 nm is the Al_2O_3 film thickness and d is the distance from a QD monolayer center of interest to the bulk silicon. 63
Figure 3.7. Temperature dependence of fluorescence lifetime of the CQDs integrated on top of (a) 0.0 nm, (b) 1.0 nm, (c) 2.0 nm and (d) 4.0 nm thick Al_2O_3 layer on SiO_2/Si. Black squares are amplitude averaged experiment lifetimes. Green diamonds are the lifetimes of the CQDs on sapphire as the reference sample corrected for the refractive index difference with silicon. Red circles are the calculated lifetimes of the CQDs using the "temperature-independent" energy transfer model. Blue up-triangles are the calculated lifetimes of the CQDs using the energy transfer model which considers the temperature-dependent complex dielectric function of silicon, thus "phonon-assisted" model. Orange down-triangles are the calculated lifetimes of the CQDs using the "phonon-assisted" energy transfer model with the additional inclusion of the temperature-dependent QY of the donor CQDs; thus, it is called "full temperature-dependent" model. 76
Figure 3.8. (a) Energy diagram illustrating the exciton transfer from the donor CQD to the acceptor silicon due to the Coulomb interaction between the donor-acceptor pair. The phonon-assisted process is shown as the lateral arrows to make up for the momentum mismatch in silicon. (b) Some of the Feynman diagrams for the phonon-assisted processes important for transfer of energy from a CQD to an indirect-band semiconductor. These diagrams include phonon-emission processes in the conduction band. 79

Figure 3.9. Experimental FRET rates as a function of temperature. Orange squares correspond to the FRET without Al_2O_3. Red circles correspond to the FRET for 1.0 nm Al_2O_3 thickness. Blue up-triangles correspond to the FRET for 2.0 nm Al_2O_3 thickness. Green down-triangles correspond to the FRET for 4.0 nm Al_2O_3 thickness. The FRET rates in this graph were obtained taking the modified reference rates into account. 83
Figure 3.10. Energy transfer rates as a function of the temperature for each case: Al_2O_3 thickness of 0.0, 1.0, 2.0 and 4.0 nm. Black squares correspond to the experimental data. Red circles represent the FRET without phonon assistance, blue up-triangles include phonon assistance, orange down-triangles both consider the phonon assistance and temperature dependent QY change of the CQDs. 84
Figure 3.11. FRET efficiency as a function of the temperature in the range of..... 85
Figure 3.12. (a) Schematic for the gradient energy transfer from the cascaded GQD/RQD bilayer into bulk Si. (b) Emission and absorption spectra of CdTe GQDs and CdTe RQDs (green and red curves, respectively), and absorption spectrum of bulk Si (blue curve)..... 90
Figure 3.13. Energy diagram for the excitation transfer from a bilayer of red (green)-emitting CQDs to bulk Si. Horizontal arrows represent the interaction energy between the energy levels. Vertical arrow shows relaxation process between the excited levels. Dash vertical arrows depict the relaxation between the lowest excited state and ground state. 93
Figure 3.14. Energy diagram for the excitation transfer from a layer of green-emitting CQDs and a layer of red-emitting CQDs to bulk Si. Horizontal arrows represent the interaction energy between the energy levels. Vertical arrows show relaxation process between the excited levels. Dash vertical arrows depict the relaxation between the lowest excited state and ground state. 95
Figure 3.15. Exciton population (in %) for the cases of: (1) $QD_G \rightarrow QD_R \rightarrow Si$ (black curve); (2) $QD_R \rightarrow QD_R \rightarrow Si$ (red curve); and (3) $QD_G \rightarrow QD_G \rightarrow Si$ (green curve). 97
Figure 3.16. Excitonic quenching factor (left) and enhancement factor (right) as a function of time for the relative case 1. 98
Figure 3.17. Excitonic quenching factor (left) and enhancement factor (right) as a function of time for the relative case 2. 99

Figure 3.18. Excitonic quenching factor (left) and enhancement factor (right) as a function of time for the relative case 3. 99
Figure 3.19. TRF spectroscopy at 535 nm from the bilayer integration of GQDs on Si (dark green solid line), GQD/RQD on Si (dark orange solid line), GQDs on quartz (green solid line), GQD/RQD on quartz (orange solid line), and the laser diode response function (navy solid line). 100
Figure 3.20. TRF spectroscopy at 640 nm from bilayer integration of RQDs on Si (wine solid line), GQD/RQD on Si (magenta solid line), RQDs on quartz (red solid line), GQD/RQD on quartz (pink solid line), and the laser diode response function (navy solid line). 102
Figure 3.21. (a) Exciton population for the cases of: (1) $GQD \rightarrow RQD \rightarrow Si$ (black solid line); (2) $RQD \rightarrow RQD \rightarrow Si$ (red solid line); and (3) $GQD \rightarrow GQD \rightarrow Si$ (green solid line). (b) Excitonic quenching factor (left) and enhancement factor (right) as a function of time for Case 1 with respect to Case 2. 105
Figure 3.22. (a) Schematic representation of the hybrid CQD/HfO_2/GO structure. (b) Energy diagram for the FRET from CQD into GO based acceptor. 109
Figure 3.23. Tapping-mode AFM image of 5 nm HfO_2 layer coated on GO film on quartz together with the height profile. 110
Figure 3.24. (a) Tapping mode AFM image of the GO thin film on quartz. (b) Height profile along the red line presented in (a). Inset shows the AFM image of an isolated single GO sheet on quartz. (c) Raman spectra of GO and RGO thin film reduced at 900 °C. (d) XPS spectra of GO and RGO thin films reduced at 625 and 900 °C. (e) Normalized absorption (black line) and PL (red line) spectra of CdSe/CdS CQDs with normalized absorption of GO solution (blue line). (f) HR-TEM image of the CQDs used in the study. 112
Figure 3.25. (a) Experimental TRF decays of the CQDs on GO and RGO thin films on quartz for the HfO2 separation distances of 4.0 nm and 0.2 nm; and 20.0 nm for the CQDs without GO and RGO at the bottom (Reference). Solid black lines are multi-exponential fits to the data, and gray decay curve is the laser diode response function (IRF). (b) TRF lifetimes of the CQDs as a function of the distance from GO and RGO; and of the reference. (c) Separation distance dependence of the NRET rates of the CQDs on GO and RGO reduced at 900 °C. Inset shows the experimental decays of the

CQDs on GO, RGO reduced at 625 °C, RGO reduced at 900 °C and the theoretical decay of the CQDs on graphene (d) NRET efficiency of the CQDs on GO and RGO reduced at 900 °C as a function of the separation distance. 117
Figure 3.26. SEM images of MoS_2 layers growth via CVD. 119
Figure 3.27. PL and Raman spectra of MoS_2 layers growth via CVD..... 120
Figure 3.28. Microscope images of MoS_2 layer growth around the rough surface points. 120
Figure 3.29. Layered 2D MoS_2 structures growth on patterned silicon substrates to examine the effect of surface roughness to the flow pattern and thus the growth layers. 121
Figure 3.30. TRF energy transfer rates and efficiencies of CQD-MoS_2 hybrids depending on the environmental temperature. 122

Figure 4.1 UV-Vis absorbance spectra, PL spectra and TEM images of the (a) 4 ML and (b) 5 ML thick CdSe NPLs having various lateral sizes. 132
Figure 4.2 Peak positions of the PL FWHM, PL, hh-e transition and lh-e transition of (a) 4 ML NPLs and (b) 5 ML NPLs for varying lateral sizes. 133
Figure 4.3 UV-Vis absorbance spectra of the reaction host medium solution containing cadmium acetate, oleic acid and octadecene, reaction mixture and final mixture after the extraction process of the NPLs. 134
Figure 4.4 Absorption cross-section spectra of 4 ML CdSe NPL samples with varying lateral sizes obtained by using the (a) Se and (b) Cd concentrations from ICP-OES measurements. Lateral size dependence of the absorption cross-section (c) at the energy of hh-e transition peak and (d) at high photon energy 3.1 eV..... 137
Figure 4.5 Absorption cross-section spectra of 5 ML CdSe NPL samples with varying lateral sizes obtained by using the (a) Se and (b) Cd concentrations from ICP-OES measurements. Lateral size dependence of the absorption cross-section (c) at the energy of hh-e transition peak and (d) at high photon energy 3.1 eV..... 139
Figure 4.6 Lateral size dependence of the extinction coefficients of (a) 4 ML CdSe NPLs and (b) 5 ML CdSe NPLs obtained by using the Se concentrations from ICP-OES measurements. 140

Figure 4.7 Absorption cross-section spectra of 4 ML CdSe NPL samples with varying lateral sizes obtained by using the (a) Se and (b) Cd concentrations from ICP-MS measurements. Lateral size dependence of the absorption cross-section (c) at the energy of hh-e transition peak. 142
Figure 4.8 Absorption cross-section spectra of 5 ML CdSe NPL samples with varying lateral sizes obtained by using the (a) Se and (b) Cd concentrations from ICP-MS measurements. Lateral size dependence of the absorption cross-section (c) at the energy of hh-e transition peak. 143
Figure 4.9 Dependence of the intrinsic radiative lifetime of the hh-e transition and the oscillator strength on the lateral size of (a) 4 ML and (b) 5 ML thick CdSe NPLs using the results obtained from the Se concentrations of ICP-OES measurements. 145
Figure 4.10 TEM images of the (a) Cu-doped 3ML core NPLs and (b) undoped 4ML/5ML CdSe/CdS core/shell NPLs. (c) Schematic of our hybrid structure including the Cu-doped and undoped NPLs. (d) Photoluminescence and absorbance spectra of the Cu-doped and undoped NPLs in toluene. 149
Figure 4.11 Steady-state PL spectra of the solid films of only-donor (orange), only-acceptor (red) and donor–acceptor having D/A = 2.5x10-5 (green) cases. 150
Figure 4.12 Time-resolved PL decay curves at the donor trap emission peak wavelength, 620 nm, for various D/A concentration ratios. 151
Figure 4.13 Time-resolved PL decay curves at the acceptor second excitonic absorption peak wavelength (598 nm) for various D/A ratios. 152
Figure 4.14 Time-resolved PL decay curves at the donor band-edge emission peak wavelength (465 nm) for various D/A ratios. Note: The data in (a) were continued in (b). 153
Figure 4.15 Time-resolved PL decay curves at the acceptor trap emission peak wavelength (660 nm) for various D/A ratios. Note: The data in (a) were continued in (b). 154
Figure 4.16 NRET efficiency as a function of Donor/Acceptor (D/A) molar ratio. ... 157
Figure 4.17 NRET efficiency for a single D/A pair as a function of D/A molar ratio. 158
Figure 4.18 (a) PLE spectra of the doped donor NPLs (orange) and the undoped acceptor NPLs (red) measured at their Cu-related emission peak wavelength (620 nm)

and excitonic emission peak wavelength (660 nm), respectively. (b) Photoluminescence excitation spectra of the samples having different D/A ratio, measured at 660 nm and then normalized at the second excitonic (e-lh transition) peak wavelength (598 nm) of the acceptor. Inset figure shows the enhancement of PLE through the NRET in the hybrid donor–acceptor samples. 159

List of Tables

Table 2.1. Typical separation distance ranges and distance dependences of various transfer mechanisms.....44

Table 3.1. Lifetime ratios of the CQDs in the emission spectra (lifetimes of the red-tail and blue-tail emission as compared to lifetime at the peak-emission wavelength) when measured for far tail-emission and at FWHM. 58

Table 3.2. Experimental QY and gamma ratios; and calculated radiative rate ratio for each temperature used in the study. 66

Table 3.3. Fluorescence lifetimes for the CQDs on quartz as the reference sample (corrected for refractive index variation) and on Si. 101

Table 4.1. Corresponding values of 4 ML and 5 ML thick CdSe NPLs at the energy of hh-e peak and at the high energy value 3.1 eV. 141

Table 4.2. PL decay lifetimes (τ), NRET rates and NRET efficiencies of the donor NPLs for the samples with varying D/A ratios. 156

Chapter 1

Introduction

Sustainable and renewable energy sources are envisaged to supply a significant portion of the energy demand increasing with the recent exponentially growing population in the world. Photonics technology has offered innovative and feasible optoelectronic solutions to this ultimately important energy consumption problem. Among the proposed solar-to-electric conversion systems, silicon-based photovoltaics and luminescent solar concentrators have been key elements in the modern world. As the optoelectronics of photovoltaic solar energy conversion is being developed, new photonic materials have been introduced to make low-cost, high-performance energy conversion systems. An important class of these materials consists of solution-processed, low-temperature grown nanocrystals as an alternative to high-temperature epitaxially grown semiconductors. These colloidal semiconductors exhibit superior properties including exciting optoelectronic properties, accompanied with low-cost synthesis and easy usage on arbitrary substrates. Therefore, utilization of the colloidal nanocrystals is expected to provide optical and electrical advantages for the next-generation solar light-harvesting systems. Today the most common type of the colloidal nanocrystals is the spherical ones, while are quasi zero-dimensional (0D) structures also known as colloidal quantum dots.

CQDs are promising nanomaterials also for the efficiency enhancement in newly emerging two-dimensional (2D)-material integrated optoelectronics. Atomically thin layers of 2D materials such as graphene and transition metal dichalcogenides have been studied in the recent years to be utilized in photonics technology. Their better carrier transporting and favorably larger exciton accepting properties are ultimately important together with the exotic characteristics of colloidal nanocrystals. Therefore, it is envisioned that the respective optical and electrical strengths of these materials will allow their efficient 0D-2D material hybrids to be used in novel nanotechnological devices in the future.

Recent years have witnessed many successful applications of the colloidal nanocrystals in photosensing technology. Their extraordinary properties including excitonic/multiexcitonic large absorption cross-section along with diverse band alignment and ease of utilization in device applications may open new routes for the high-sensitivity photosensors. In addition, very recent developments in the material engineering of colloidal semiconductor nanocrystals have provided new dimensionalities for the nanomaterials. One important outcome of these developments is the synthesis of colloidal quasi-2D flat semiconductor nanocrystals, which are also known as nanoplatelets (NPLs). These newly emerging rising stars with various superior properties, when compared to CQDs, exhibit great potential for the high-performance photosensing together with photovoltaic applications. Furthermore, ion doping provides additional useful characteristics to these quasi-2D structures and their quasi-0D counterparts, specifically for photovoltaics and luminescent solar concentrators. All in all, these doped and undoped quasi-0D and quasi-2D nanomaterials have great advantages to be used for opening up new directions for the future technological advances.

1.1 Structure of the thesis

In this thesis, we studied the physics of excitonic and nonexcitonic nonradiative energy transfer (NRET) mechanisms in the highly promising hybrids of 0D, 2D and 3D

materials. The thesis is organized in five chapters. In Chapter 2, we present a scientific background on the materials, methods and physical phenomena used in this thesis. We elaborate the materials section in three subsections listed as colloidal 0D semiconductor nanocrystals: colloidal quantum dots, colloidal quasi-2D semiconductor nanocrystals: nanoplatelets, layered 2D nanomaterials: graphene, graphene oxide, reduced graphene oxide and MoS_2, indirect bandgap 3D semicondutor materials: silicon. In the methods section, we explain how we utilized steady-state and time-resolved fluorescence spectroscopy, investigated the optical absorption properties of nanoemitters, fabricated and characterized the hybrid structures; and grew the layered 2D MoS_2 nanomaterials. In the last section of this chapter, we explain the physical phenomena of excitonic/nonexcitonic nonradiative energy transfer mechanisms.

In Chapter 3, we present our studies on excitonic nonradiative energy transfer using colloidal 0D semiconductor nanocrystals. First, we elucidate phonon-assistance in the excitonic NRET from nanoemitters to an indirect bandgap 3D semiconductor. We further discuss the excitonic enhancement of NRET into bulk silicon by using the energy-gradient of cascaded nanoemitters. We strongly believe that the findings of these studies will be crucial in designing new silicon-based high-efficiency solar light-harvesting systems through the excitonic sensitization of silicon. The third section of this chapter includes the study of excitonic NRET from CQDs to graphene variants including graphene oxide and reduced graphene oxide. Furthermore, in a small section, we present the growth procedures of MoS_2 layers and preliminary NRET study on the hybrids of these 2D structures with CQDs.

In Chapter 4, we uncover the optical properties of newly emerging quasi-2D nanoplatelets. In the first section of this chapter, we present the experimental determination of the absorption cross-section and molar extinction coefficient of colloidal CdSe NPLs. In this way, we provide fundamental information for the investigation of excitonic NRET in the systems including colloidal quasi-2D semiconductor nanocrystals. In the second section, we present the study on NRET between quasi-2D colloidal doped and undoped semiconductors depending on donor/acceptor molar ratios in the solid hybrid films. It is envisioned that much further improvement is possible for the nanocrystal-based optoelectronics through the

integration of Cu-doped NPLs together with undoped NPLs to the current systems such as photovoltaics, luminescent solar concentrators, LEDs and displays.

In Chapter 5, we make the concluding remarks on this thesis, and present the future outlook and the contributions of the thesis to the literature.

Chapter 2

Background on Materials, Methods and Physical Phenomena

2.1 Materials

2.1.1 Colloidal 0D semiconductor nanocrystals: colloidal quantum dots

Colloidal luminescent 0D semiconductor nanocrystals, or colloidal quantum dots (CQDs), are one of the most interesting nanomaterials emerging more than 2 decades ago. These appealing quantum-confined structures have great potential for numerous applications ranging from photonics and optoelectronics to biotechnology and medicine [1]. Some of the advantages of high-quality CQDs can be listed as the size and conformation tunable emission having narrow and symmetric profile, high luminescent quantum yield (QY), spectrally broad absorption band, large one- and two-photon absorption cross-sections, large Stokes shift, and high resistance to photobleaching and chemical degradation [2]–[8]. LED, lasing, solar energy and

display technologies are some of the applications for CQDs to be used in the field of optoelectronics [9], [10]. Because of their unique electro-optical properties, they are also considered as favorable bioimaging and energy transferring labels [3]–[5], [11].

CQDs are 0D quantum systems having charge carriers that are confined in all three dimensions. Despite the epitaxial quantum dot, first coined by Reed et al. [12], [13], CQDs are solution-processed nanoparticles with crystalline or amorphous structure. High crystallinity of CQDs gives them high-quality optical and electronic properties. After the breakthrough exploratory works of Ekimov and Onushchenko in 1981 [14], Henglein in 1982 [15] and Efros and Efros in 1982 [16], the first colloidal form of quantum dots was reported in 1983 by Brus and coworkers at Bell Laboratories [17]. In contrast to top-down epitaxial approach, Brus et al. developed a new technique using bottom-up synthesis route [18]. After these first accounts, detailed photophysics and chemistry of CQDs has been also studied by Bawendi, Alivisatos, Guyot-Sionnest and many others [19]–[21]. Binary/ternary alloys of these 0D systems such as CdS, ZnS, CdSe, CdTe, InP, CdZnS, InGaAs, their core/shell forms such as CdSe/ZnS and CdSe/CdS, and various combinations of these structures have been synthesized generally by using wet chemistry techniques [22]–[28]. In addition to these well-established bottom-up synthesis methods, newly proposed and greener biotemplated approaches have started to be used recently among the CQD community despite their low quality products for now [29], [30].

CQDs are faceted nanoparticles owing to their crystalline nature and thus are roughly spherical in shape. They have sizes typically in the range of 1-10 nm in diameter [31]–[35] having 10^2 – 10^4 atoms in their crystalline structure (generally wurtzite or zinc-blende crystal structure). An illustration and a transmission electron microscopy (TEM) image together with energy-band diagram of a CQD are shown in Figure 2.1. Size and relative composition determine the optical properties of ternary CQDs while only size can affect these properties of binary CQDs. Size also specifies the surface-to-volume ratio of a CQD, which is an important parameter for the bioapplications of these nanostructures.

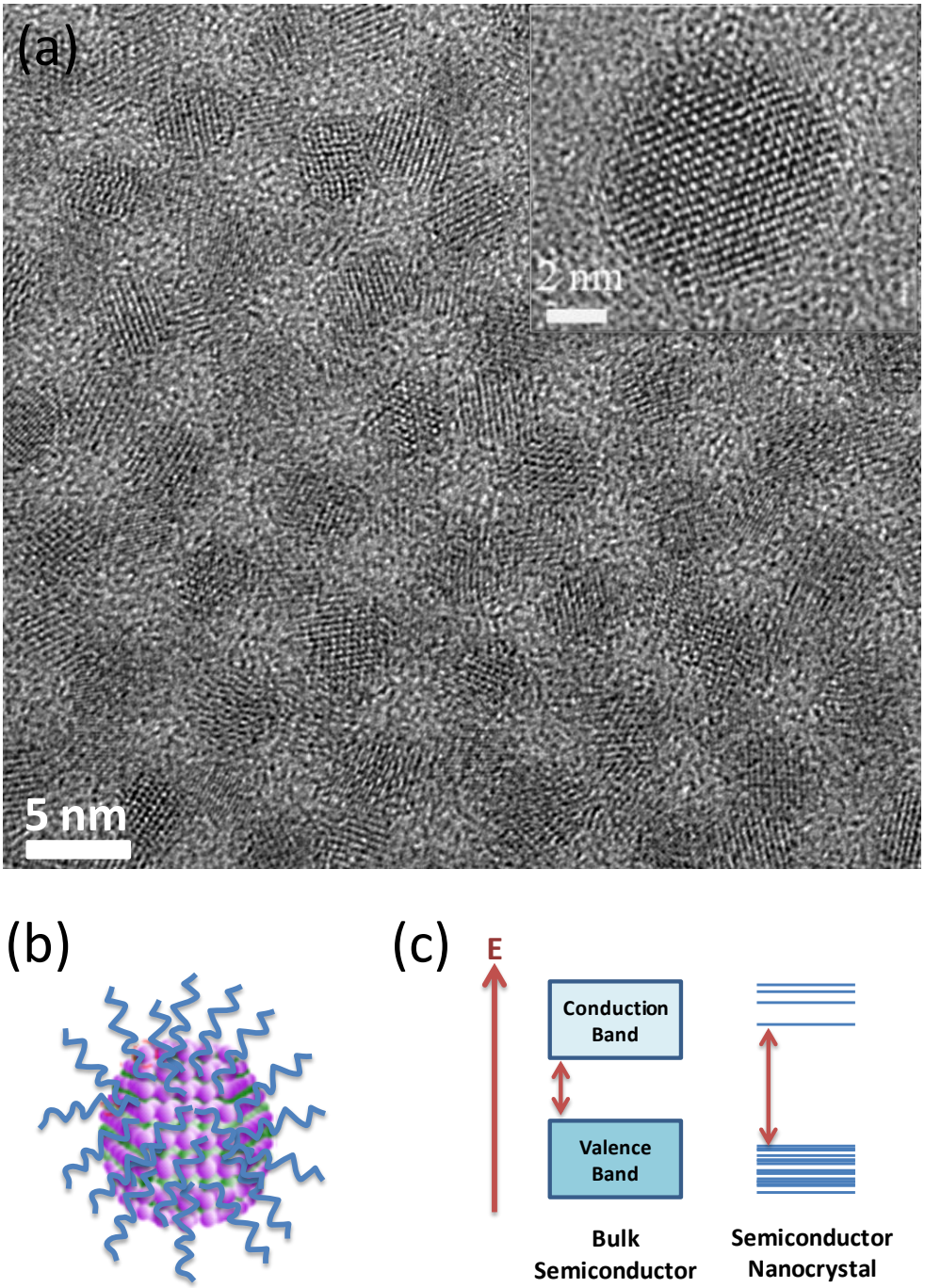

Figure 2.1. (a) A TEM image, (b) an illustration together with (c) the energy-band diagram of a semiconductor nanocrystal (e.g. a CQD) (a rough representation).

In bulk materials, energy levels atwhich electrons and holes occupy are quasi-continuum, forming the conduction band and the valence band as the lowest unoccupied and highest occupied energy levels of the system, respectively. However, CQDs have discrete energy levels of electron and hole because of the size and thus quantum confinement. Crystalline solids of CQDs are built up from their constituent atoms. When the number of atoms is high as in the bulk, linear combination of atomic orbitals constitutes the bands with a large density of states (DOS). The number of states is mediated by the number of atoms, therefore, since there is much smaller number of atoms in the CQDs, quantum confinement effects appear leading to the decrease in the number of DOS and thus the increase in the separations of energy levels. Size-tunable CQD PL, which is originated from this quantum confinement phenomenon, is shown in Figure 2.2. Typical UV-Vis absorbance and photoluminescence (PL) emission spectra of semiconductor CQDs are also represented in Figure 2.3.

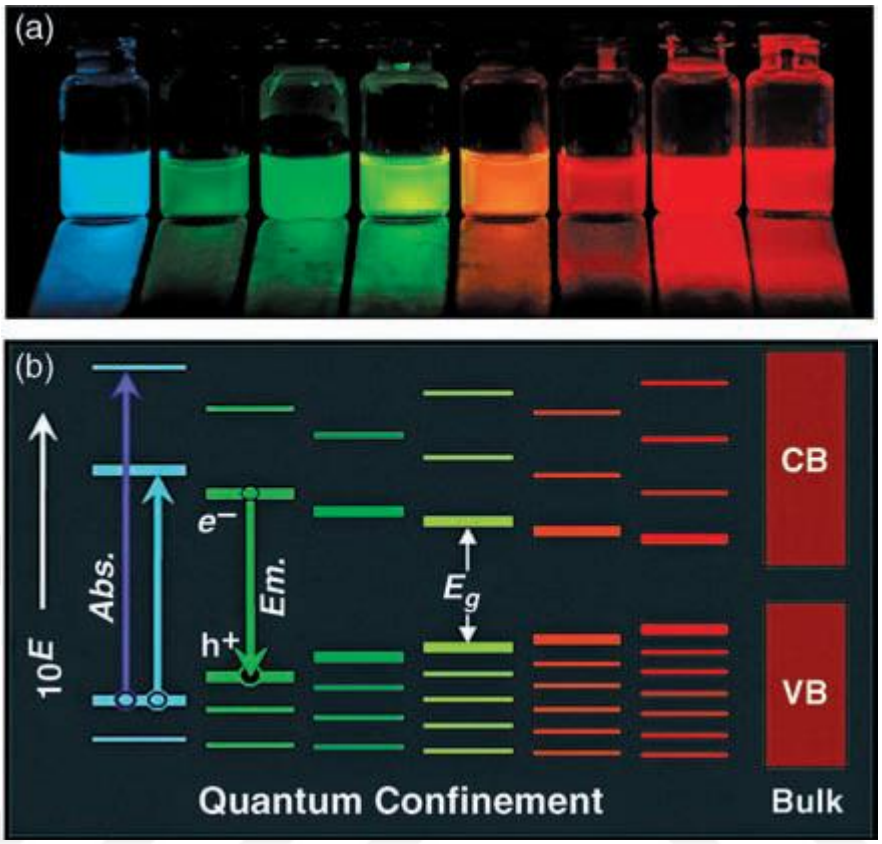

Figure 2.2. (a) Photograph of PL from CdSe/ZnS QDs of increasing size (left to right) illuminated under UV light. (b) Qualitative changes in the QD bandgap energies, Eg, and density of states for CdSe QD510 (2.7nm diameter), QD530 (2.9 nm), QD555 (3.5 nm), QD570 (3.8 nm), QD590 (4.3 nm), and QD610 (4.8 nm). The conduction (CB) and valence (VB) bands of bulk CdSe are shown for comparison and the energy scale is expanded as 10E for clarity. Transitions for absorption and band edge emission are also presented. (Adapted and reprinted with permission from Ref. [7]. Copyright 2011, American Chemical Society.)

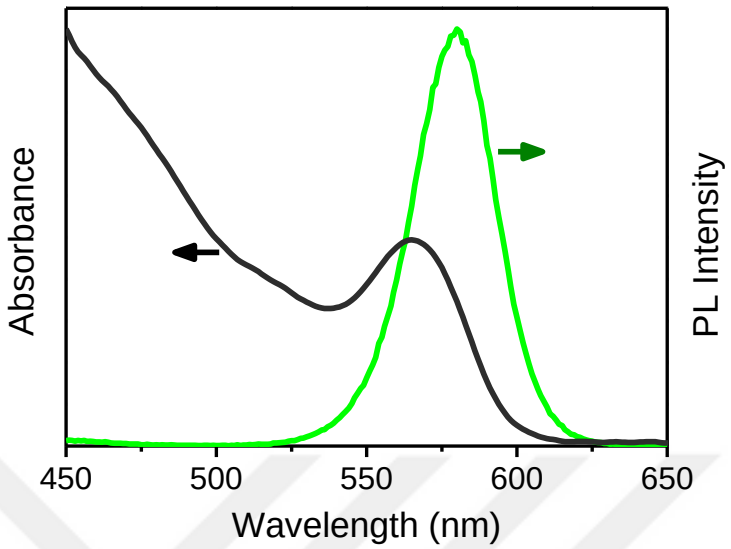

Figure 2.3. Typical absorbance and emission spectra of CQDs.

As the 3D version of particle-in-a-box character of CQDs, particle-in-a-sphere model is indicating that the allowed wave functions with the necessity of nodes at the surface of the CQD are determined by the nanocrystal dimensions [36]. From this model, the CQD bandgap energy is scaling as a^{-2}, where a is the radius of the CQD [37]. However, Brus and coworkers recognized that the energy gap is also dependent on increasing electrostatic attraction leading to the shifting of PL spectrum to lower energies and on increasing kinetic energies related to confinement of the charges leading to the shifting of spectrum to higher energies. Brus obtained a general equation for the energy gap of CQDs by utilizing particle-in-a-sphere wave functions, effective mass approximation for the kinetic energy and hydrogenic Hamiltonian [21], [38]–[41]. The resultant formula is shown in Eq. 2.1, where E_B is the bulk bandgap energy, μ is the reduced mass for electron–hole pair, ε is the semiconductor dielectric constant, and E_{Ry}^{*} is the Rydberg energy for electron–hole pair.

$$E_{CQD}(a) = \underbrace{E_B}_{1} + \underbrace{\frac{\pi^2\hbar^2}{2\mu a^2}}_{2} - \underbrace{1.786\frac{e^2}{\varepsilon a}}_{3} - \underbrace{0.248E_{Ry}^*}_{4} \tag{2.1}$$

Term 2 of Eq. (2.1) is defined as the energy of a particle-in-a-sphere and Term 3 is the energy between the electron and hole inside CQD through Coulombic interaction. Due to the large dielectric constants of semiconductors and thus significant screening, the bound electron-hole pair, also named as exciton, should have an additional tendency to keep itself near the CQD center to overcome dielectric screening and maximize Coulombic interaction. This fact is considered with the inclusion of Term 4 into the Eq. 2.1.

Quantum confinement has also a significant impact on the oscillator strength as well as that on the energy levels of the CQDs. There are two important physical phenomena directly related to the effect of quantum confinement on the probability of optical transition to an electronic state: Fermi's Golden Rule and Heisenberg's Uncertainty Principle. Fermi's Golden Rule indicates that the oscillator strength of a transition is dependent on the matrix element associated with the mixture of the initial and final states and on the extent of overlap of these states. Energy states related to the optical absorption of semiconductors are mainly the electron and hole states. Therefore, following the Fermi's Golden Rule, an increase in the overlap of electron and hole wavefunctions due to the quantum confinement leads to an enhancement in the oscillator strength. This is one reason for the sharp peaks in the absorption spectra of CQDs compared to the smoother spectra of the corresponding bulk materials [17], [38], [41], [42]. Second reason for these strong absorption peaks is Heisenberg's Uncertainty Principle. The principle rules out that, owing to the quantum confinement, the position and energy of an electron in a CQD are well defined but the momentum is uncertain. Discrete states in the quantum-confined structure can be thought as a superposition of continuum states from the bulk crystal. Energy and momentum are conserved quantities in an optical transition; therefore uncertainty in the energy

enhances the probability that a given transition will satisfy these conditions. For this reason, closely spaced transitions in the bulk are compressed into a single and intense transition in a CQD [32], [42].

Energy levels in the CQDs are also mediated by the semiconductor material as well as the size at the nanometer scale. Optical excitation of the nanoparticle creates bound electron-hole pairs in a small volume compared to the exciton Bohr radius of the material. PL shift of the CQD over the wavelength range has an upper limit determined by this preferred distance between the electron and hole in its bulk material [43], [44]. On the other hand, the lowest limit in the PL shift is determined by the capability of high-quality synthesis of the CQD and the decreasing optical absorption [45]. Typical CQDs with high optical quality have full width at half maximum (FWHM) in the range of 25 - 30 nm and stead-state PL QY as high as 95% [5], [33], [46]. Time resolved fluorescence (TRF) lifetimes of CQDs depend on various parameters such as the quality, coating and environment but, for a typical CQD, TRF lifetime generally exceeds 10 ns exhibiting multi-exponential decay components [47], [48]. Absorption profile of the CQDs shows a broader wavelength spectrum extending to the UV and having increasing amount of intensity with the decrease in wavelength.

To date, CQDs have been involved into Förster resonance energy transfer (FRET) mechanisms as both exciton donor and exciton acceptor. In the studies utilizing CQDs as exciton donor, a wide range of exciton accepting nanomaterials including colloidal quantum wells, metallic nanoparticles, polymers, fluorescent dyes and fluorescent proteins have been used [49]. CQDs are generally favorable exciton donors due to several reasons such as the easy application of CQD-FRET results to Förster theory, ability to minimize emission cross-talk of donor and acceptor particles and ability to maximize the overlap integral in the Förster theory. CQDs are also adept acceptors for efficient FRET when they are coupled with the appropriate donors [7], [50] because of their superior properties such as large extinction coefficient and spectral overlap integral. Besides these hetero-FRET systems, which involve particles with distinct chemical conformations, CQDs have also been studied for homo-FRET investigation, which is the FRET among the same kind of species. With several favorable characteristics of CQDs in the aforementioned context, the concept of QD-FRET as a

fundamental spectroscopy technique may offer new, pragmatic and exciting approaches for applications in physics, chemistry, biology and engineering.

2.1.2 Colloidal quasi-2D semiconductor nanocrystals: nanoplatelets

Colloidal luminescent quasi-2D semiconductor nanocrystals, which are commonly known as colloidal nanoplatelets (NPLs) or colloidal quantum wells, have been one of the key elements for modern nanotechnological applications since the first account of free-standing ultrathin semiconductor layers by Kotov and coworkers in 2006 [51].

Following the first attempts on the synthesis of cadmium-based colloidal NPLs by Kotov and coworkers in 2006 [51] and by Hyeon and coworkers in 2006 [52], there have been significant investigations on their growth mechanisms [53]–[56]. Synthesis routes of these free-floating NPLs can be classified in two main groups, which are top-down approaches such as exfoliation [57] and bottom-up approaches such as the method of weak/strong binding of ligands to different facets of nanoparticles [58]. To date, colloidal semiconductor NPLs have been synthesized by using disparate material combinations, some of which can be listed as follows: Indium-based colloidal NPLs (e.g. β-In_2S_3 [59]); Tin-based colloidal NPLs (e.g. SnS [60], SnSe [61], SnS_2 [60] and $SnSe_2$ [62]); Copper-based colloidal NPLs (e.g. Cu_2S [63]); Transition-metal based colloidal NPLs (e.g. TiS_2, $TiSe_2$, ZrS_2, $ZrSe_2$ and FeS_2 [64], [65]); and Cadmium-based colloidal NPLs (e.g. CdSe [54], CdS [55], CdTe [55], CdSe/CdS [56] , CdSe/CdZnS [56]). Furthermore, recent studies have showed that the heterostructures of high quality cadmium-based NPLs are possible to be synthesized despite some difficulties e.g. the problems like lattice mismatch [66], composition control of core/shell interfaces [67], [68], the type of ligands for the shell growth [69] and the change in crystal structure of the shell [70]. Core/crown, core/shell and core/crown/shell binary and ternary heterostructures of the NPLs have been recently demonstrated by several groups [56], [71]–[74]. Some of the advantages of these heterostructured NPLs over their core

counterparts can be listed as the larger absorption cross-section [73], high optical gain property [75] and elongated radiative recombination lifetime.

Among the NPLs of group II-VI semiconductors, it was observed that cadmium-based colloidal NPLs possess either wurtzite or zincblende crystal structure. Specifically, cadmium-based zincblende NPLs have ability to provide strong quantum confinement to the exciton confining in their ultrathin thickness and they have ability to grow in the lateral directions ranging from a few nanometers to a few hundred nanometers. Schematic representation of a zincblende 4 monolayer (ML) CdSe NPL is shown in Figure 2.4. A typical CdSe NPL is made up of cascaded monolayers of CdSe pair and it is terminated with Cd layer (100) on both the lateral sides [54]. Additionally, in order to show how successful the thickness and lateral size control of the NPLs is, the representative TEM images of 4ML and 5ML NPLs having both the small lateral size (with a few nanometers) and large lateral sizes (with a few ten nanometers) are given in Figure 2.5 together with the corresponding thicknesses ~1.2 nm and ~1.5 nm, respectively (1ML ≅ 0.3 nm).

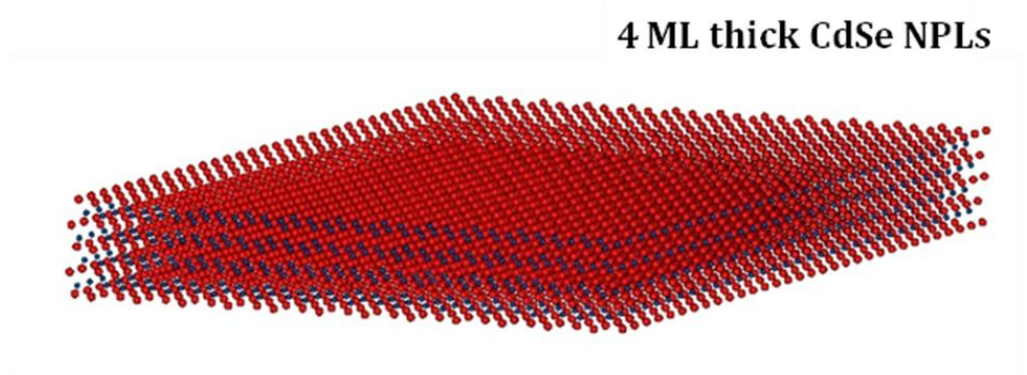

Figure 2.4. Schematic representation of a zincblende 4 monolayer (ML) CdSe NPL.

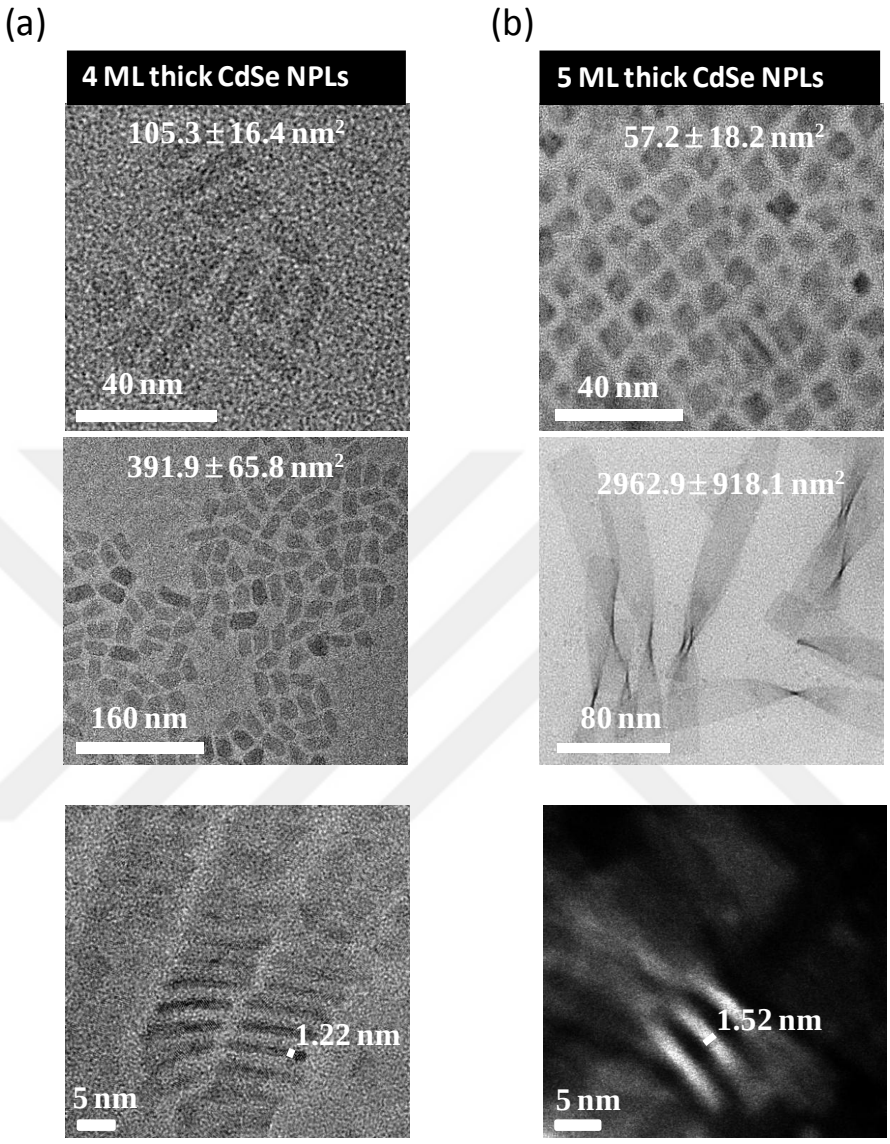

Figure 2.5. TEM images of (a) 4ML and (b) 5ML NPLs with both the small and large lateral sizes, and their corresponding thicknesses.

NPLs with cadmium-based zincblende structure have been extensively studied in terms of optical and excitonic properties [76]–[88]. It has appeared that these NPLs have several superior properties over the conventional CQDs. First of all, thickness control in three dimensions is not necessary for the NPLs; they require only one dimensional precise control in the thickness dimension where quantum confinement

happens. Therefore, cadmium-based zincblende NPLs possess spectrally narrow emission (FWHM < 10 nm) enabling very fine thickness-tunable PL in these nanostructures. An exemplary UV-Vis absorbance and PL emission spectra of 4 ML NPLs are shown in Figure 2.6. The absence of inhomogeneous broadening in these NPLs can be examined by comparing the PL FWHMs and time resolved fluorescence lifetimes for the single particle and for the ensemble of the particles. When this investigation is done, it is observed that there is not a significant difference in these two parameters of the cadmium-based zincblende NPLs. Furthermore, room temperature PL linewidth is slightly higher than 26 meV, which is the value of homogeneous broadening due to phonon coupling at room temperature. Extremely small PL linewidth of NPLs is highly desirable for color purity improvement under the context of LEDs.

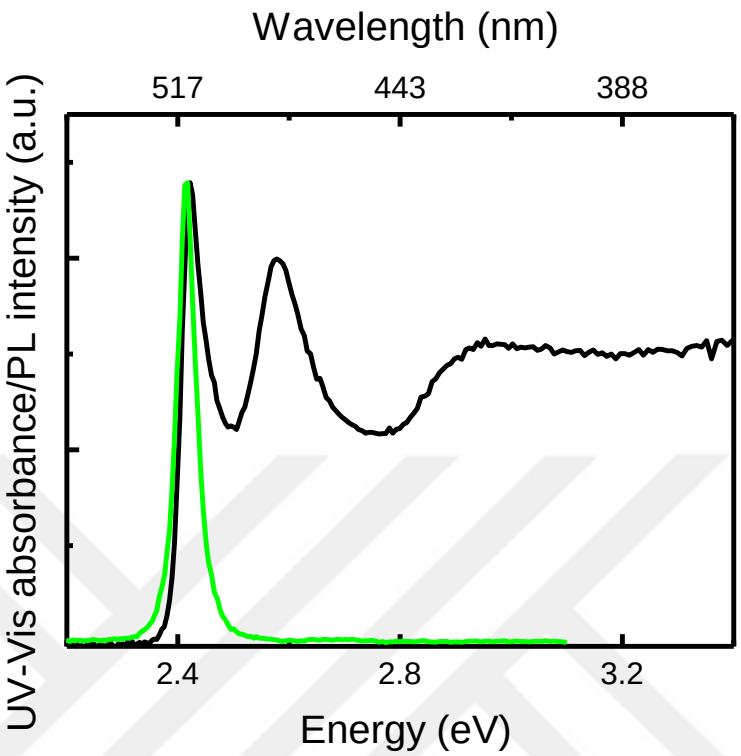

Figure 2.6. UV-Vis absorbance and PL emission spectra of 4ML CdSe NPLs.

The effect of strong quantum confinement on oscillator strength and thus the sharp absorption peaks in the nanoparticles has already been explained by using Fermi's Golden Rule and Heisenberg's Uncertainty Principle in the previous section (Section 2.1.1). As seen from the exemplary absorption spectrum of 4ML NPLs in Figure 2.6, as in the case of CQDs, NPLs have also sharp transition peaks in their absorption spectra. First peak is attributed to the transition due to the excitonic state of electron/heavy-hole pair; second peak corresponds to the electron/light-hole transition; and third peak is the transition forming the excitonic state between the electron and split off – hole [89].

Second advantage of these NPLs is that they have larger exciton binding energy than that of CQDs due to the combination of their 2D character, large in-plane charge effective mass and relatively smaller dielectric constant. Extremely large oscillator

strength and thus extremely fast radiative recombination lifetime in cadmium-based NPLs are important outcomes of their property of large exciton binding energy. While, at room temperature, the radiative recombination lifetime of these colloidal fluorescent emitters is a few nanosecond [79], it is around 10 ps at cryogenic temperatures [86], which is a strong implication of giant oscillator strength transitions in these NPLs. Large exciton binding energy and thus giant oscillator strength in the NPLs are important factors for enhanced per-volume linear absorption cross-section observed in these materials. The linear absorption cross-section along with the nonlinear absorption cross-section values of the NPLs have been recently obtained such that they are at least an order of magnitude higher than the corresponding values of CQDs [83], [84]. That much high absorption cross-section values of the NPLs allow them to be utilized for light-harvesting applications such as photovoltaics and photodetectors [90]. Additionally, they are potential exciton sinks due to their large extinction coefficient and thus the increase in the Förster radius aforementioned in the Förster theory [91].

Suppressed Auger recombination and thus long Auger lifetime is another advantage of the NPLs along with high close packing intensity and many other properties that were listed above for them to be utilized in low-threshold amplified spontaneous emission and lasing applications [79], [92]. Recently, these new nanostructures have also been used for the investigation of exciton kinetics in NPL based systems by using-FRET mechanism. Due to their superior excitonic characteristics both in absorption and emission features, high FRET efficiencies were obtained by using core, heterostructured and doped NPLs. All the advantages of cadmium-based NPLs are indicating that they are strong candidates to be used in next-generation light-harvesting and light sensing optoelectronic applications along with possible bio- and chemi-applications.

2.1.3 Layered 2D nanomaterials: graphene, graphene oxide, reduced graphene oxide and MoS_2

In the recent years, major scientific and technological challenges emerging in the fields of life science and nanoengineering have forced the scientific community to develop new materials. Carbon-based nanomaterials such as active carbon, carbon nanofibers, carbon nanotubes, graphene and graphene oxide have appeared as some of the key elements of the significant applications such as sensing, energy storage, energy conversion and transistor technologies along with the usage in catalysis and polymer composites [93]–[96]. Graphene, which is the monatomic layer of carbon, has particularly found some applications in optoelectronics [97] and biology [98], [99]. In addition, it has been offered as a new platform for the exploration of light-matter interactions at the nanoscale [100], [101]. Therefore, besides several experimental studies, many theoretical work has been conducted on the near-field interactions between an exciton donor and graphene [102]–[104]. On the other hand, graphene oxide (GO) along with its oxygen-reduced product, reduced graphene oxide (RGO), which are the variants of graphene, have been widely recognized owing to their exotic properties for several photonic, optoelectronic and biological applications.

Graphene is a single-atom thick, 2D hexagonal lattice of sp^2-hybridized carbon atoms [105]. It was first produced through micromechanical cleavage [106]. Then, despite several advantages of this method in terms of purity, mobility and optoelectronic properties, for large-scale applications, the necessity of methods providing large-scale assembly of graphene appeared recently. For this reason, several approaches have been proposed and developed, and these approaches can be listed as follows: Liquid-phase exfoliation [107], chemical vapor deposition (CVD) [108], [109], physical vapor deposition (PVD), carbon segregation [110] and chemical synthesis [111].

Graphene has fascinating electrical, optical, mechanical, thermal and practical properties such as low sheet resistance, high transparency, broad absorption wavelength range, low cost, flexibility, high thermal conductivity and high chemical durability [112]–[115]. With these favorable properties, it has a great potential to be

used in photovoltaics as transparent conductor, photoactive medium, charge transport channel and catalyst; in LEDs as transparent and flexible conductive layer, in photodetectors as absorbing layer; in lasers as broadband and fast saturable absorber; and in various other photonic and optoelectronic applications [115].

Graphene films have some advantages when compared to the CQD films. The most important one is their better carrier transport properties including the high mobilities and their property of being large exciton sink [116], [117]. When their superior optical and electrical properties are combined with the exotic characteristics of CQDs and NPLs, novel nanotechnological devices may become enabled to be produced. Therefore, bringing these different systems together for their respective strengths and investigating the possible photonic and electronic interactions in their hybrids may allow opening a new scientific and technological research field. Upon the light of this perspective, in the recent years, many studies on FRET from CQDs and NPLs to graphene as well as various other luminescent materials to graphene have been reported [102], [118]–[123]. In these studies, for the detailed investigation of FRET mechanism, steady-state and time-resolved fluorescence spectroscopy techniques, which are elaborated in the Methods section, have been widely used. As an example for the FRET mechanism in graphene-based structures, a useful schema for the energy diagrams of an optical emitter and a nearby graphene monolayer film along with a representative sample structure is given in Figure 2.7, adapted from Ref. [124].

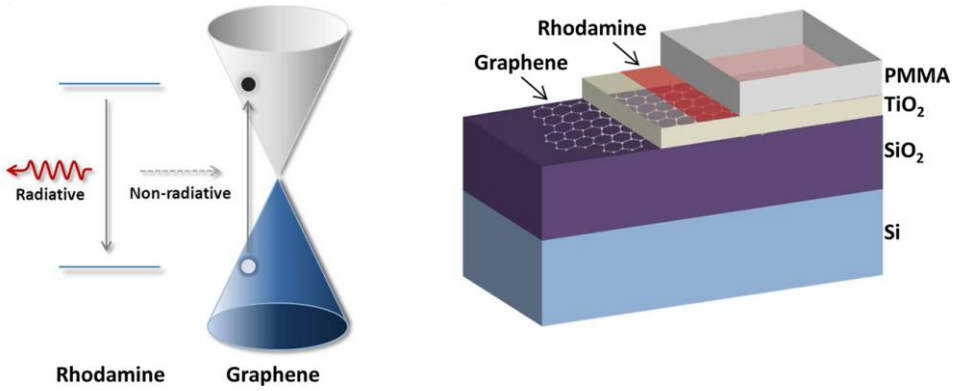

Figure 2.7. Energy diagrams of an optical emitter and a nearby graphene monolayer film along with schematic representation of the sample structure. (Reprinted with permission from Ref. [124]. Copyright 2013, American Chemical Society.)

Chemical structure of GO is very similar to graphene but having oxygen and hydrogen groups at its sp^2- and sp^3-hybridized carbon centers [125]. Production of solution-processed GO flakes was enabled after the invention of Hummers method by Hummers and Offeman in 1958 [126]. Reduced graphene oxide is another graphene-based nanomaterial, which is prepared from GO via several methods. For obtaining of RGO from GO or from graphite oxide, some of the methods that have been followed to date can be listed as thermal annealing [127], chemical reagent reduction [128] and multistep reduction [129]. When compared to pristine graphene, GO and RGO have some advantages such as greater aqueous solubility, ability to be functionalized with biomolecules, processing at lower cost, larger area coverage, and tunable energy bandgap [125], [130], [131]. Interestingly, GO can exhibit luminescence from localized electronic states rather than from band edge transitions [125]. Electrical conductivity of RGO is a direct measure of the success of reduction and, as a directly related parameter, the sheet resistance of RGO was reported as low as ~14 kΩ/sq [132], which is about two order higher than that of pristine graphene [105]. On the other hand, the highest bulk conductivity of a RGO sheet was reported to be 1314 S/cm, which is about two order lower than that of pristine graphene [133]. All these attempts for obtaining graphene-like RGO are highly remarkable and promising efforts.

In the family of graphene related materials, GO sheets are reported as fluorescence "superquenchers" having long range energy transfer characteristics, which makes them ideal candidates in FRET based applications [134]. FRET and charge transfer into GO or RGO, which have great potential to exhibit an energy quenching range comparable to graphene, are particularly important to explore and understand the feasibility and extent of being excitation energy sink [121], [123], [124], [135], [136]. Recently, several experimental studies have highlighted the importance of fluorescence quenching efficiency in the hybrids of QDs-GO [135], [137], [138], QDs-RGO [135] and dye-RGO [121] for the new developments in various application fields ranging from biology to optoelectronics.

In addition to graphene and its variants, transition metal dichalcogenide (TMD) crystals such as MoS_2 and WS_2 are also constituting another important group of two-dimensional candidates to be used in the next-generation photonics and optoelectronics [139], [140]. Monolayer TMDs possess direct energy bandgaps ranging from near-infrared to visible spectral region, which is a significant property for them to be used in various photonic and optoelectronic devices and, thereby to fulfill the space of graphene due to its lack of an energy gap [140], [141]. Besides their direct bandgap property, TMDs share many other interesting characteristics of pristine graphene, such as excellent electronic and exceptional mechanical flexibility along with partial optical transparency. With these properties, they may have usage in electronic [142], optoelectronic [142] and nanophotonic applications [143]. These 2D nanomaterials can be obtained via mechanical exfoliation of bulk crystals built up of van der Waals bonded layers [106], CVD technique and many other techniques [142]. Van der Waals interactions between the layers of TMDs allow them to be grown with distinct semiconductors on each layer without a limitation originated from the lattice mismatch, which may lead to new heterostructures or superlattices [144].

Efficient FRET from localized chromophores such as 0D quantum dots to 2D TMDs has been reported in many studies conducted to date [145], [146]. Good FRET efficiency is directly dependent on a few factors including the spectral overlap between the donor emission and acceptor absorption, the distance between the donor and acceptor, the dielectric screening of the donor dipole by the acceptor medium and the

dimensionality [147]. Recently, two particularly important parameters have come into prominence for the efficient FRET to TMDs and graphene [118], [145]. These parameters are the extent of optical absorption and the extent of dielectric screening by the 2D exciton accepting material. Number of layers of TMD or graphene can mediate these two important factors in way that FRET rate increases with the number of layers in graphene but it decreases with the layer number of TMD, which is because of the competing effect of the amount of absorption and dielectric screening in TMDs and less effectiveness of dielectric screening in graphene [118], [145], [146]. For the next-generation optoelectronics, some concerns about the CQD films such as poor carrier transport can be overcome with the hybridization of these 0D chromophores with the newly emerging stars, TMDs, leading to higher mobilities [148].

2.1.4 Indirect bandgap 3D semicondutor materials: silicon

Silicon is the most commonly used and technologically important material in today's industry. Its energy band structure having indirect absorption plays a very significant role in silicon based electronic, optoelectronic and photonic devices (see Figure 2.8). Because of the necessity of phonons for the optical bandgap transition, it needs to be treated more elegantly than the direct transitions. The bandgap of silicon has a value of 1.1 eV and its conduction band minimum is located around the point X of the Brillouin zone. When compared to the direct transitions, band edge absorption of silicon is very small because of its indirect feature and comparatively small density of states. Therefore, if the excitation energy is enough, the absorption spectrum is dominated by direct absorption at energies where the density of states is very high. Direct transition at minimum separation between the conduction band and valence band occurs near the L point and this transition is around the photon energy of 3.5 eV (~ 354 nm), which exhibits a peak shape in the absorption spectrum of silicon. Another important direct transition is around the energy of 4.3 eV (~ 288 nm), which is near the X point of the band structure [149].

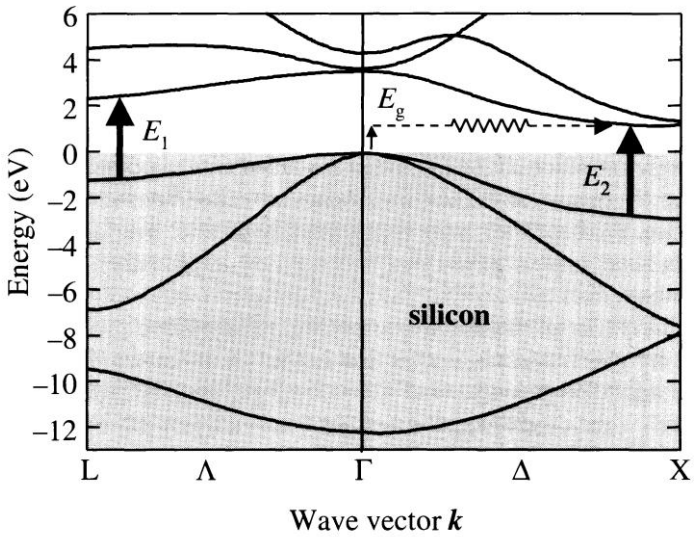

Figure 2.8. Band structure of bulk silicon. (Reprinted with permission from Ref. [149]. Copyright 2001, Oxford University Press.)

Silicon is one of the most dominantly used materials in microelectronics and optoelectronics. Silicon based microelectronic technology has great potential for chips with features at sub-micrometer ranges. It also finds wide-scale utilization in optoelectronics, especially in photovoltaic industry. However, it has intrinsic optical constraints that limit the efficiency of photovoltaic devices. One important limitation of silicon-based devices is the decrease in responsivity in the UV region [150]. There have been numerous efforts to develop effective techniques to enhance the absorption in silicon. Some of these efforts can be listed as nanostructuring to trap the light, plasmonics to localize the light and using external light-harvesters via transferring the excitation energy in the harvesting material into silicon.

CQDs were proposed as efficient sensitizers for silicon owing to their favorable optical properties (e.g., efficient and tunable emission properties). Previously, CQD sensitization of silicon has been mostly facilitated via radiative energy transfer (RET) [151], [152]. Although RET based sensitization has achieved a considerable improvement in the conversion efficiencies of silicon solar cells, RET is fundamentally limited due to the lack of effective coupling of the emitted photons with the optical

transitions in silicon. Alternatively, FRET, which is a technique relying on mostly near field dipole-dipole coupling, has been shown to be feasible for sensitizer-silicon material systems [35], [153]–[155]. Previously, by using time resolved photocurrent spectroscopy, it was shown that CQDs are good candidates to facilitate the FRET into silicon [153]. Furthermore, steady-state and time-resolved fluorescence spectroscopy techniques were also used to investigate this energy transfer mechanism in CQD-bulk silicon hybrids [35], [155], [156].

2.2 Methods

2.2.1 Steady-state and time-resolved fluorescence spectroscopy

Recent years have witnessed major progress in steady-state and time-resolved fluorescence spectroscopy instrumentation. In addition, both the techniques have become powerful tools to study FRET dynamics [157], [158].

In steady-state fluorescence spectroscopy measurements, emission spectra of the fluorescent donor and/or acceptor are obtained without temporal resolution (i.e. Intensity as a function of wavelength). Excitation is done at a fixed wavelength and scanning is performed over the wavelength spectra of the fluorophores. In the excitation part, xenon lamp with a monochromator or laser source is used. In the detection end, one of the most frequently used detector systems is photomultiplier tube (PMT), which enables to select different wavelength intervals and also it is the detection system what we use in our laboratory. Steady-state fluorescence spectroscopy allows to catch the spectral information over the wavelength range and thus to extract the FRET-related parameters along with the distances.

The analysis of steady-state fluorescence spectroscopy data requires careful treatment. For example, in order to have actual values of PL intensities from the samples, deconvolution of the spectra followed by the integration over each spectrum

is needed. On the other hand, for the well-separated spectra, peak intensity values are enough for the analysis of the spectral data. Also, the data from only-donor sample is not enough and it is important to obtain the information from both the donor and acceptor sides for the correct analysis. Detailed analysis of the PL data is necessary because the donor quenching can have become due to many reasons other than FRET but, acceptor sensitization, as the compelling evidence of FRET, together with donor quenching is a strong indication for the excitation of acceptor via donor and thereby the FRET [159].

Time-resolved fluorescence (TRF) spectroscopy method measures the fluorescence decay times at the time-domain or frequency domain. Generally, we do time-dependent measurements in our laboratory; therefore it is necessary to elaborate these measurements more carefully in this part: TRF spectroscopy is the measurement of luminescence intensity as a function of time and following a short pulse of light excitation. The decay time of the sample has to be much longer than the excitation pulse. Logic for operation of the TRF system is given in Figure 2.9.

In the TRF experiments, first, the laser is opened for a short stimulation time of ΔT and the signal counting is started simultaneously. Data acquisition is performed with time intervals of δt. The data is transferred to memory at the end of each δt. Following the time of ΔT, laser stimulation is terminated but data acquisition and storage to memory still proceed. In general, after a period of time T for completing the laser on and laser off periods, the accumulation process has to be repeated to accumulate the data over and over for high signal to noise ratio. The form of TRF signal obtained during and after the stimulation is shown in the following figure. We use the intensity decaying curves from the TRF spectroscopy to obtain the excited state excitonic lifetimes of various nanostructures.

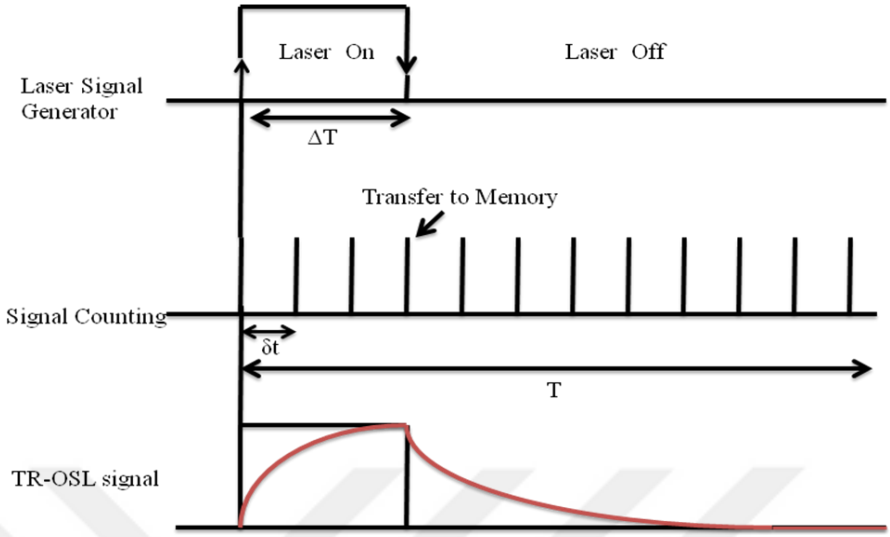

Figure 2.9. Logic for operation of the TRF system.

Typically, we use a time correlated single photon counting (TCSPC) system in the laboratory having a time resolution down to 4 ps (PicoHarp 300) integrated with a picosecond pulsed laser with an output photon energy of 3.31 eV driven by a driver module (PDL-800 series) capable of delivering laser pulses with 80 MHz repetition rate. The system utilizes a fast PMT (Hamamatsu H5783 series) to resolve lifetimes on the order of tens of picoseconds. Also, we integrate a close cycle Helium cryostat to this system in order to do temperature dependent studies. The whole system with its complementary components is shown in the Figure 2.10 and Figure 2.11.

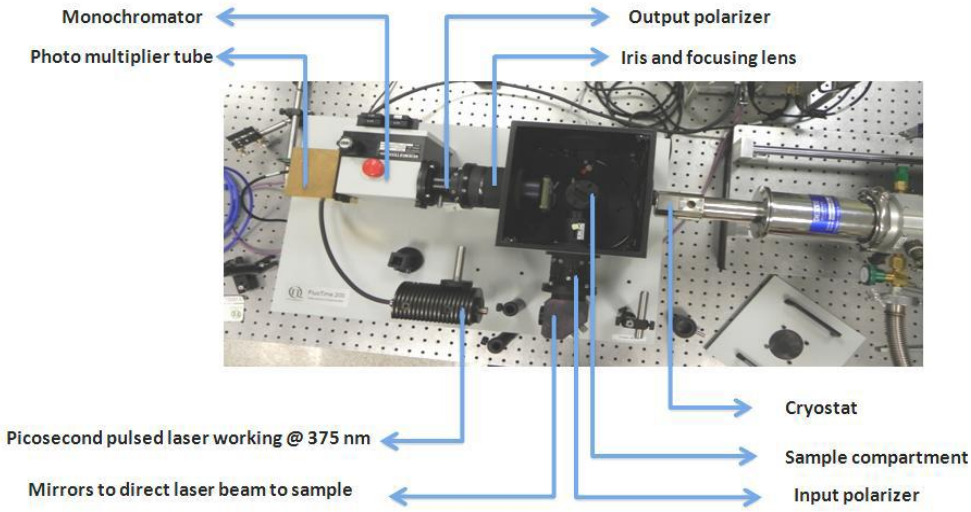

Figure 2.10. FluoTime 200 TRF system.

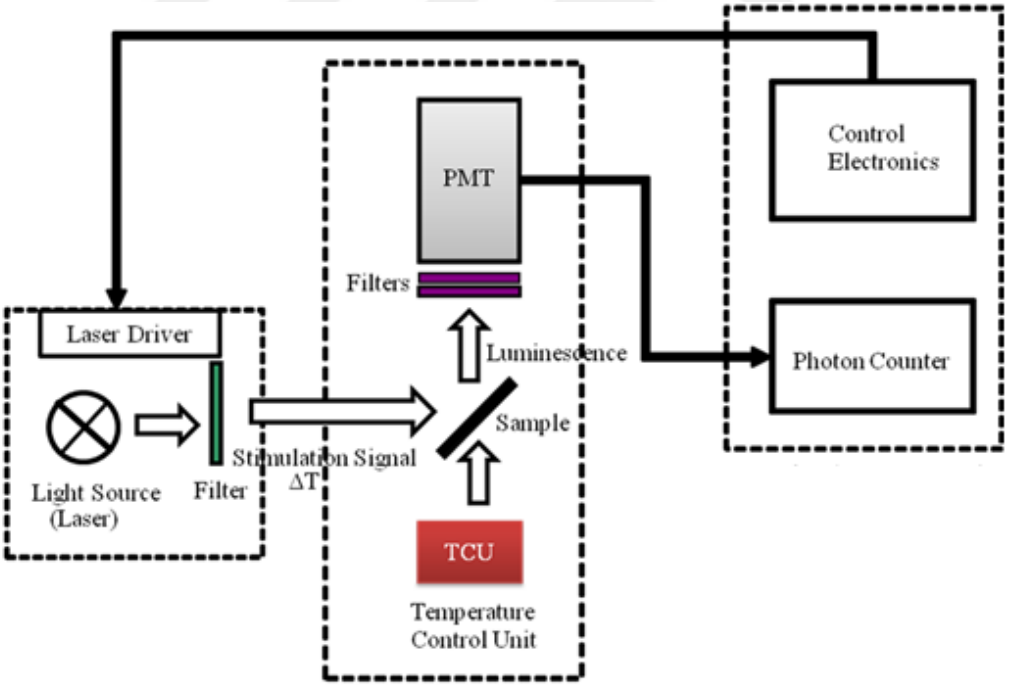

Figure 2.11. Schematic representation of a TRF system.

PL quenching of donor is mostly used to obtain the TRF decays for the investigation of FRET mechanism [160]. The mathematical description for these decays can be done as in Eq. 2.2 including multi-exponential components.

$$I = \sum_i A_i \exp\ -t / \tau_i \tag{2.2}$$

Generally, since the TRF decays have more than one decay lifetime component in the ensemble measurements, amplitude-averaging is performed using the Eq. 2.3. The reason for the amplitude-averaging instead of intensity-averaging is that the TRF signal detected at a particular time interval is proportional to the excited state population of the fluorophores, not to the integrated intensity [161], [162].

$$\langle \tau \rangle = \frac{\sum A_i \tau_i}{\sum A_i} \tag{2.3}$$

Another way of the FRET analysis is to obtain sensitized acceptor PL decays along with the donor PL decays. However, the sensitized acceptor decay curves will include information from both the donor and acceptor in the sample. Therefore, the analysis has to be done more carefully including the quenched donor excited state lifetime (τ_{DA}) together with the acceptor excited state lifetime (τ_A) [163].

2.2.2 Measuring the optical absorption properties of nanoemitters

Colloidal CQDs and NPLs possess ultimately important optical absorption properties related to their large exciton binding energies and large oscillator strengths. These properties enable them to have significantly enhanced absorption cross-section (σ) and substantially high radiative decay rates. All these significant properties make these materials highly promising candidates for optoelectronic device applications such as LEDs, lasers and solar cells [75], [164], [165].

Determination of the absorption cross-section and, the related factor, molar extinction coefficient (ε) is very important for several reasons. First, the absorption cross-section is used for a quantitative measure of the NPL fluorescence quantum yields (QYs). It also provides an easy way to estimate the number of electron-hole pairs generated within each absorption event inside the nanoparticle. Low amplified spontaneous emission thresholds are also well explained by the large absorption cross-sections of the CQDs and NPLs. Furthermore, molar extinction coefficient of the particles is of great importance for convenient and accurate measurements of the entity concentrations. Using the well-known molar extinction coefficients of the nanoparticles, different architectures of core/shell (vertically grown shell) and core/crown (laterally grown shell) NPLs can be synthesized with great control over their thicknesses and lateral sizes [84].

Absorption cross-sections and molar extinction coefficients of nanoparticles can be obtained by using a UV-Vis spectrophotometer, an inductively coupled plasma optical emission spectrometer (ICP-OES), e.g. Agilent 725 ICP-OES system, and an inductively coupled plasma mass spectrometer (ICP-MS), e.g. Thermo XSERIES II ICP-MS system. First, the purified sample of nanoparticles in a solvent is carefully dried by gentle heating inside a fume hood. The residual is dissolved in an acid solution and the digested sample is directly transferred into volumetric flasks for the ICP-OES and ICP-MS measurements. For the ICP-MS measurement, samples may need further dilution to reach the ppb ranges necessary for the measurement. The ionic molar concentrations are determined by using these methods. The dimensions of the

CdSe NPLs in the sample are measured from the TEM images. Particle concentration in the sample is calculated by using all this information. After that, the purified stock sample is dispersed in a suitable amount of desired solvent to obtain a reliable UV-Vis absorbance spectrum at room temperature. For this purpose, a UV-Vis absorption spectrophotometer, e.g. Cary 100 UV-Vis spectrophotometer, can be used. This spectrum along with the particle concentrations from ICP-OES or ICP-MS systems is used to calculate the spectral absorption cross-sections and the corresponding molar extinction coefficients of the nanoparticles [84].

2.2.3 Fabrication and characterization of hybrid structures

All the fabrication tools utilized for the hybrid structures of nanomaterials studied in this thesis can be listed as follows:

a) Atomic Layer Deposition (ALD) system

b) Spin-coating / Dip-coating system

c) Chemical Vapor Deposition (CVD) system

All the characterization tools utilized for the hybrid structures of nanomaterials studied in this thesis can be listed as follows:

a) Transmission electron microscope (TEM)

b) Atomic Force Microscope (AFM)

c) Confocal Raman Microscope

d) Ellipsometer

e) Environmental Scanning Electron Microscope (ESEM)

f) Fluorescence Spectrophotometer

g) UV-VIS Spectrophotometer

h) Inductively Coupled Plasma Optical Emission Spectroscopy (ICP-OES)

i) Inductively Coupled Plasma Mass Spectroscopy (ICP-MS)

2.2.4 Growth of layered 2D MoS_2 nanomaterials

There are various techniques to grow layered 2D MoS_2 nanostructures, e.g. exfoliation, CVD and PVD methods [166]. Among these approaches, CVD is generally consulted method for large-area, uniform and well-controlled MoS_2 single or multilayer films on a substrate.

In our laboratory, we can grow single layer, large flakes of MoS_2 as big as 50 -90 µm length at one side of their triangular shape. The CVD system that we use in the laboratory is shown in Figure 2.12. The procedure which can be given as an example to obtain these CVD grown layered nanostructures is as follows: Small amount of MoO_3 powder (≤ 1-2 mg) was located at the center of the split furnace. The temperature at the center that will reach during the growth was adjusted to ~ 670 °C and the rate of increase in temperature during the growth was adjusted to 10 °C/min. Sulphur powder with an amount of 150 mg was placed at one side of the furnace, atwhich the temperature is ~ 200 °C. Before the growth, the flow of nitrogen gas was fixed to a value of 800 sccm, which is high enough to protect the film formation from oxidation. When the center temperature reached to 350 °C, due to the melting of sulphur precursor, the furnace was positioned to 4 cm away from the powder. After that, the temperature reached to 670 °C and the furnace was kept at that position for around 18 minutes. At the end of this time, the system was cooled immediately by opening the wings of the furnace and by locating the furnace to a cooler point. The flow of nitrogen gas was gradually decreased from its initial level until the inside temperature decreases to the room temperature. As the crucial characterization methods, SEM images, Raman

spectroscopy and PL spectroscopy results of the samples from this exemplary procedure are shown in Figure 2.13.

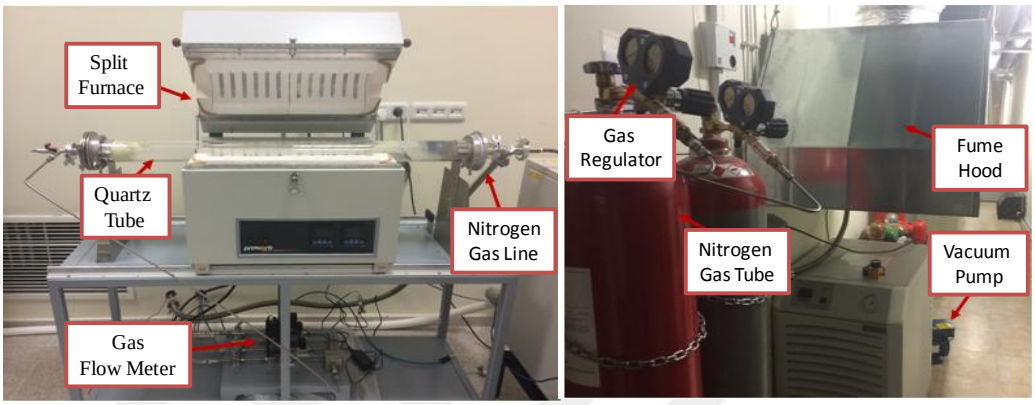

Figure 2.12. CVD growth system that we use in Demir laboratory.

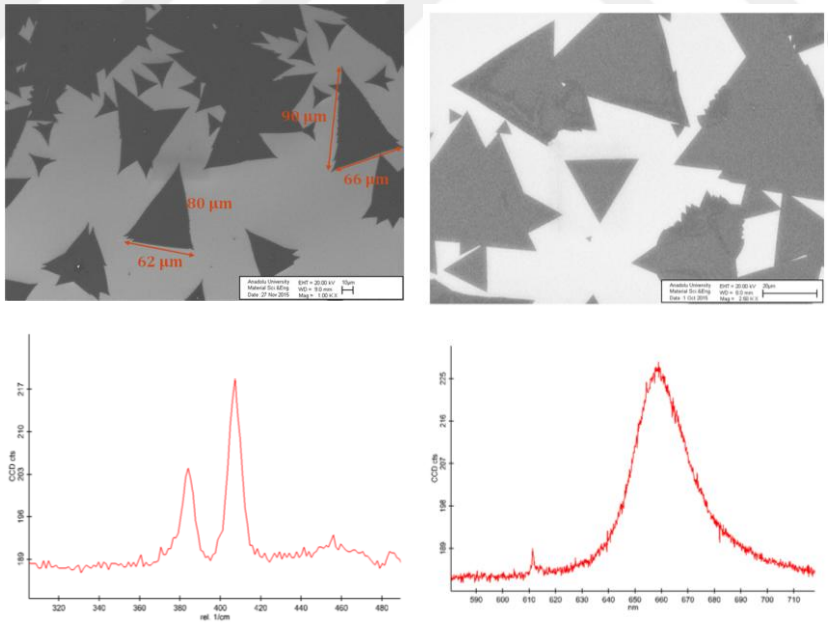

Figure 2.13. (a) Exemplary SEM images, (b) Raman spectrum and (c) PL spectrum of MoS_2 single layer structures.

In addition to the exemplary procedure that was given in this section, we developed a different procedure for the large area distribution of the MoS_2 triangular layers, which will be elaborated in the corresponding chapter of the thesis.

2.3 Physical phenomena

Excitation energy transfer from a luminescent donor (i.e., QDs) into an acceptor may occur radiatively or nonradiatively. If the distance between donor and acceptor is bigger than the wavelength of the emitted photon and there is spectral overlap between the donor emission and the acceptor absorption, radiative energy transfer (RET) becomes the dominant transfer mechanism. RET results in a decrease of the donor fluorescence intensity in the region of spectral overlap since the photons emitted by the donor are subsequently absorbed by the acceptor. In this process, some of the photons are lost without excitation of the acceptor atoms. This is not the case for nonradiative energy transfer (NRET) because there is no photon involved in the emission end of this process [158]. NRET is possible at distances much less than the excitation photon wavelength and it can be grouped in two sub-sections: Excitonic NRET and Nonexcitonic NRET. In this part of the thesis, these two phenomena will be explained in detail.

2.3.1 Excitonic nonradiative energy transfer mechanism

Excitonic nonradiative energy transfer, i.e. FRET, was first theoretically investigated, discussed, and developed in the 1940s. However, its applications have emerged recently in modern technology owing to its well-matching results with the recent discoveries and inquiries in nanoscience. It provides significant contributions to different reseach fields ranging from theoretical studies in life sciences to experimental works in applied technology [167], [168].

FRET is an energy transfer mechanism based on the approximation that the Coulombic coupling can be used for dipole-dipole interaction in the suitable donor-acceptor pair. As aforementioned, for the FRET to be observed, donor and acceptor in the pair should have small separation distances and they should have overlapping spectra of donor emission and acceptor absorption. Furthermore, a special distance, which is called Förster distance, is defined for the FRET mechanism and it includes the parameters other than the separation distance, which are the spectral overlap integral, the dipole orientation factor, quantum yield of the donor and refractive index of the medium in which the pair is located [158]. Consequently, the energy transfer efficiency is dependent on both the donor-acceptor distance and the Förster distance, and it is known as Förster radius, which is the distance at which the spontaneous decay of the excited donor and the transfer are equally probable.

In the FRET mechanism, for efficient energy transfer, donor should be luminescent and have high quantum yield. Luminescence is the general term for the emission of light following the electronic transition between different energy states. Further, fluorescence is a subterm of luminescence and it is originated from singlet-singlet optical transition [157], [158]. In the FRET distance range, radiative mechanisms, which are valid at long distances, and orbital overlap related mechanisms, which are valid at very short distances, play minor roles.

Figure 2.14 shows the FRET mechanism if there is energy resonance between donor and acceptor, and if the system satisfies all the conditions aforementioned. As seen from the figure, an electronic transition from higher to lower energy level in donor is followed by an electronic transition from lower to higher level in acceptor through the Coulombic interaction mechanism.

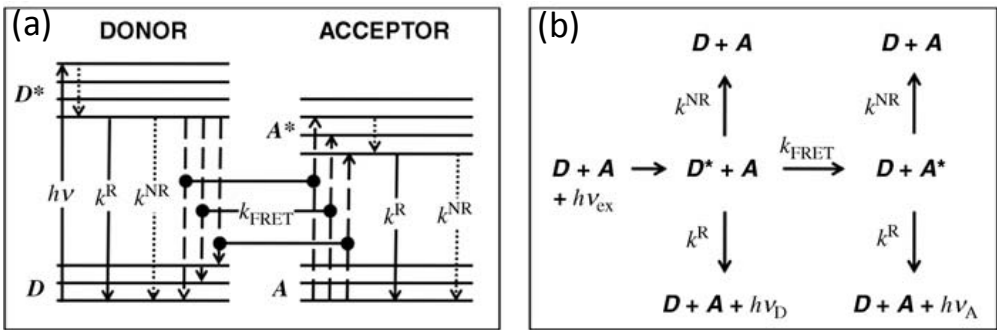

Figure 2.14. (a) Simplified Jablonski diagram including excitation and relaxation transitions, followed by radiative decay (k^{R}), nonradiative decay (k^{NR}) or FRET (k_{FRET}). After the FRET, the acceptor is in an excited state (A*), followed by radiative or nonradiative decay to the ground state (A). (b) Different energy pathways after donor excitation ($h\nu_{ex}$) possibly leading to luminescence emission of D ($h\nu_D$) or A ($h\nu_A$). (Reproduced with permission from Ref. [159]. Copyright 2014, Wiley-VCH Verlag GmbH & Co. KGaA.)

The rate of FRET can be represented by Fermi's Golden Rule as given in the following equation:

$$k_{FRET} = \frac{2\pi}{\hbar}|V|^2 \rho \tag{2.4}$$

where $\hbar$ is the reduced Planck constant, V the electronic coupling between donor and acceptor, and ρ is the density of initial and final energy states interacting to each other. ρ is related to the overlap integral J. When we consider the acceptor particle as 0D structure such as colloidal quantum dot, the coupling potential is derived as in Eq. 2.5.

$$V = \frac{\kappa \left|\overrightarrow{\mu_D}\right| \left|\overrightarrow{\mu_A}\right|}{4\pi\varepsilon_0 n^2 r^3} \tag{2.5}$$

where $\vec{\mu}_D$ and $\vec{\mu}_A$ are the transition dipole moments of donor and acceptor, respectively, κ is the orientation factor between these moments, ε_0 is the permittivity in vacuum, n is the refractive index of the medium, and r is the distance between donor and acceptor. Coupling factor for this kind of systems is dependent on the distance between donor and acceptor as r^{-3};

Substituting Eq. 2.5 into Eq. 2.4 gives an r^{-6} distance dependent FRET rate as can be seen from the following formula:

$$k_{FRET} = \frac{9 \ \ln 10 \ \kappa^2 \Phi_D}{128\pi^5 N_A n^4 \tau_D r^6} J \tag{2.6}$$

where Φ_D is the PL quantum yield of donor, N_A is Avogadro's number, and τ_D is the PL lifetime of donor in the absence of FRET.

Förster radius, R_0, is the distance atwhich the rate of two mechanisms, FRET and all other decay rates, are in equilibrium ($k_{FRET} = k_D^R + k_D^{NR} = \tau_D^{-1}$), and thereby the FRET efficiency is 50%. It is obtained by replacing k_{FRET} with τ_D^{-1} and r with R_0 as given in Eq. 2.7.

$$R_0 = \left(\frac{9 \ \ln 10 \ \ \kappa^2 \Phi_D}{128 \pi^5 N_A n^4} J \right)^{1/6} \tag{2.7}$$

The spectral overlap integral J is defined as in the following equation and depicted in Figure 2.15.

$$J = \int \bar{I}_D(\lambda) \varepsilon_A(\lambda) \lambda^4 d\lambda \tag{2.8}$$

which depends on the spectrum of the acceptor molar extinction coefficient and the spectrum of the donor emission normalized to unity ($\bar{I}_D$) as:

$$\int \bar{I}_D(\lambda) d\lambda = 1 \tag{2.9}$$

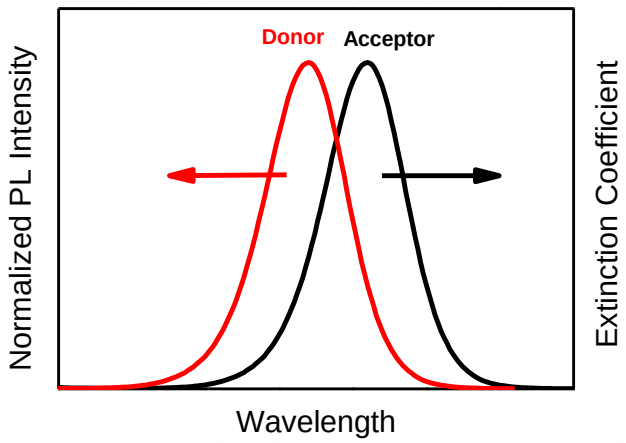

Figure 2.15. The overlaping area of the area-normalized emission spectrum of Donor and the extinction coefficient spectrum of Acceptor, defining the overlap integral *J*.

When we substitute Eq. 2.7 into Eq. 2.6, a more compact equation for the FRET rate including the donor-only PL decay lifetime, Förster radius and the distance between donor and acceptor is obtained as follows:

$$k_{FRET} = \frac{1}{\tau_D}\left[\frac{R_0}{r}\right]^6 \tag{2.10}$$

With the help of this expression, the FRET efficiency can be found by using the equation:

$$\eta_{FRET} = \frac{k_{FRET}}{k_{FRET} + \tau_D^{-1}} = \frac{1}{1 + r/R_0^{\ 6}} \tag{2.11}$$

The sensitivity of FRET efficiency to the donor-acceptor distance is shown in Figure 2.16. As seen from the figure, the sensitivity is most prominent in the region around 0.5 – 2.0 R_0.

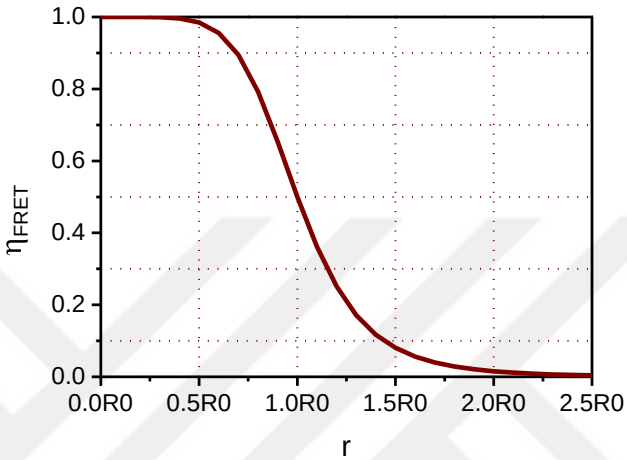

Figure 2.16. FRET efficiency (ηFRET) as a function of donor-acceptor separation distance (r).

Another important and must-seriously-considered parameter for FRET applications is the orientation factor, κ , which is defined as:

$$\kappa = \mu'_D \cdot \mu'_A - 3(\mu'_D \cdot r')(\mu'_A \cdot r') = \cos\Theta_{DA} - 3\cos\Theta_D \cdot \cos\Theta_A \qquad (2.12)$$

where μ'_D , μ'_A and r' represent their corresponding unit vectors. And, Θ_{DA}, Θ_D and Θ_A are the angles between μ'_D and μ'_A, μ'_D and the donor-acceptor connection vector, μ'_A and the donor-acceptor connection vector, respectively. After averaging over some approximations, one can obtain the values of κ^2 to be 2/3; between 1/3 and

4/3; between 0 and 4; and between 0 and 2/3, depending on the condition of the donor-acceptor system [169].

There are various experimental methods for the calculation of the FRET efficiency in a system of donor-acceptor pair. These methods can be listed as (a) donor quenching, (b) acceptor sensitization, (c) donor quenching + acceptor sensitization, (d) donor photobleaching and (e) acceptor photobleaching [159]. Among these techniques, determination of the FRET efficiency through donor quenching is the most frequently utilizied way in our laboratory, therefore it is necessary to elaborate it in detail at this part of the thesis.

The FRET efficiency through donor quenching can be accurately obtained by using the spectroscopic data (i.e. PL intensity, PL lifetime or PL quantum yield) of donor in the absence or presence of acceptor. When we write the formula of FRET efficiency as in Eq. 2.13 and use the expressions of donor and acceptor quantum yields as in Eq. 2.14, we can extract a practical formula given in Eq. 2.15 to examine the spectroscopy results in terms of the transfer efficiency. Here, D and DA correspond to only donor and donor-acceptor, respectively, and R and NR corresponds to radiative and nonradiative, respectively. PL intensity related component in Eq. 2.15 is valid if the excitation energy is absorbed only by the donor.

$$\eta_{FRET} = \frac{k_{FRET}}{k_{FRET} + \tau_D^{-1}} = \frac{k_{FRET}}{k_{FRET} + k_D^R + k_D^{NR}} = k_{FRET}\tau_{DA} \qquad (2.13)$$

$$\Phi_D = \tau_D k_D^R = \frac{k_D^R}{k_D^R + k_D^{NR}} \quad \text{and} \quad \Phi_{DA} = \tau_{DA} k_D^R = \frac{k_D^R}{k_{FRET} + k_D^R + k_D^{NR}} \qquad (2.14)$$

$$\eta_{FRET} = \frac{1}{1+ \ r / R_0 \ ^6} = \frac{R_0^6}{R_0^6 + r^6} = 1 - \frac{\Phi_{DA}}{\Phi_D} = 1 - \frac{I_{DA}}{I_D} = 1 - \frac{\tau_{DA}}{\tau_D} \qquad (2.15)$$

Additionally, if the Förster radius is known, one can easily obtain the donor-acceptor separation distance by using the following equation:

$$r = R_0 \left(\frac{\Phi_{DA}}{\Phi_D - \Phi_{DA}} \right)^{1/6} = R_0 \left(\frac{I_{DA}}{I_D - I_{DA}} \right)^{1/6} = R_0 \left(\frac{\tau_{DA}}{\tau_D - \tau_{DA}} \right)^{1/6} \qquad (2.16)$$

Calculations of the FRET efficiency become more complicated if multiple number of donors or acceptors become in the system. To overcome the difficulties in the calculations, Raicu proposed an approximation of equal distances between all donors and acceptors in the system, and assumed that all the FRET rates are equal for any donor-acceptor FRET pair in the system. Using these approximations, he derived an equation for the FRET efficiency ($\eta_{FRET}^{multiple}$) depending on the number of acceptors (n_A) and the FRET efficiency of a single donor-acceptor pair (η_{FRET}) as follows [170]:

$$\eta_{FRET}^{multiple} = \frac{n_A \eta_{FRET}}{1+ \ n_A - 1 \ \eta_{FRET}} \qquad (2.17)$$

Mattoussi, Bawendi and coworkers did the same analysis experimentally and derived the following equation along with the experimental confirmation [171]. Their expression is exactly the same with that of Raicu. Owing to the increase in the number of de-excitation pathways with the number of acceptor per donor, FRET efficiency is

observed to increase with the number of acceptors. Furthermore, one can find the FRET efficiency of a single donor-acceptor pair by using this equation (Eq. 2.18) and the data from the ensemble measurement if the number of acceptors (n_A) is known.

$$\eta_{FRET}^{multiple} = \frac{n_A k_{FRET}}{n_A k_{FRET} + \tau_D^{-1}} = \frac{n_A R_0^6}{n_A R_0^6 + r^6} \tag{2.18}$$

Dimensionality dependence of FRET rate and efficiency is another ultimately important topic in the excitonic NRET concept. It has been found out that dimensionality of the donor does not affect the transfer mechanism whereas dimensionality of the acceptor is an ultimately important factor in the FRET [147], [172]. Recent theoretical and experimental studies have shown the importance of the acceptor material dimensionality for the FRET in multidimensional systems [35], [135], [147], [154]–[156], [172]. In these studies, it was presented that the FRET rate is proportional to donor-acceptor distance at the order of 6 if the acceptor is a 0D material such as CQD; at the order of 5 if the acceptor is a 1D material such as nanowire; at the order of 4 if the acceptor is a 2D material such as quantum well; and at the order of 3 if the acceptor is a 3D material such as bulk structure.

2.3.2 Nonexcitonic nonradiative energy transfer mechanism

Nonexcitonic nonradiative energy transfer mechanism includes both the electron exchange energy transfer (Dexter-type transfer) and the charge transfer (Marcus theory). As opposed to the FRET mechanism, both the charge transfer mechanisms have exponentially decaying dependence on the distance between donor and acceptor nanoparticles. Typical distance ranges and distance dependences of different transfer mechanisms in the system of donor-acceptor pair are shown in Table 2.1 [159].

Table 2.1. Typical separation distance ranges and distance dependences of various transfer mechanisms.

Mechanism	Separation distance range	Distance dependence
Dexter Transfer	< ~ 1 nm	~ e^{-r}
Charge Transfer	< ~ 2 nm	~ e^{-r}
FRET (without electron exchange)	~ 1 - 20 nm	~ $\frac{1}{r^6}$
(metal surface as acceptor)	~ 1 - 40 nm	~ $\frac{1}{r^4}$
Plasmon Coupling	~ 5 - 300 nm	~ e^{-r}
Singlet Oxygen Transfer	~ 10 - 250 nm	~ e^{-r}

Electron exchange between a donor and an acceptor requires energetic resonance between these materials. For this reason, the transfer rate is also dependent on the overlap function as well as the distance. The theory for the exchange mechanism was developed by Dexter in 1953 [173]. The Dexter transfer rate can be written as

$$k_{DT} = KJ_{DT}e^{\left(\frac{-2r}{L}\right)} \tag{2.19}$$

where K is an orbital interaction related constant and J is the spectral overlap integral. According to this theory, due to the exponentially decaying dependence of the rate on the separation distance, Dexter transfer is effective up to the distances of around more than one or two molecular diameters. The detailed theory has been explained in various important references in the literature [158], [174].

As another nonexcitonic nonradiative energy transfer mechanism, charge transfer, or Marcus theory, was theoretically developed by Marcus in 1956 [175]–[177]. It includes some similarities with the Dexter mechanism in terms of the separation distance and the interaction if the system is consisting of two nanostructures as the donor and the acceptor: The transfer rate is again exponentially distance dependent, and orbital overlap is again a requirement for the efficient transfer of charges (electron or hole). However, unlike the Dexter exchange mechanism, charge transfer does not require two-electron transfer; instead it requires a charge (electron or hole) donor and a charge acceptor. Also, there is not a necessity of energetic resonance in this transfer mechanism. The transfer rate is given by

$$k_{CT} = \frac{2\pi}{\hbar} J_0^2 \frac{e^{-\beta(r-r_0)}}{\sqrt{4\pi\lambda(r)k_B T}} \cdot e^{\frac{-(\Delta G(r)+\lambda(r))^2}{4\lambda(r)k_B T}} \tag{2.20}$$

where J_0 is the contact value of the matrix element of the donor-acceptor coupling, β is related to the distance dependence of the electronic coupling, r_0 is the separation atwhich the donor and acceptor are in touch, ΔG is the free energy change, λ is the reorganization energy, and $\hbar$ and k_B are the reduced Planck's constant and Boltzmann constant, respectively [178]. This equation can be further simplified to be used in the practical analysis of experimental data. Several other studies on the charge transfer mechanisms in various fields have been done recently [174], [179]–[181].

Tunneling or direct transfer of electrons and holes may also occur in systems including bulk material instead of a system of nanostructures. The details of this kind of nonexcitonic NRET will be given in some of the following sections of this thesis.

Chapter 3

Excitonic Nonradiative Energy Transfer by Using Colloidal 0D Semiconductor Nanocrystals

In the first section of this chapter, we present the study on phonon-assisted excitonic nonradiative energy transfer (NRET) into an indirect bandgap semiconductor by using nanoemitters. In indirect bandgap semiconductors including silicon (Si), phonon assistance is fundamentally essential to the process of optical absorption. Silicon is a poor light absorber as compared to direct bandgap materials. Alternative techniques have been developed to enhance the absorption of light by silicon including photon down-converting sensitizers. To serve this purpose, nanoemitters including colloidal quantum dots (CQDs) are commonly used as the sensitizer. To date sensitization of monocrystalline silicon has been demonstrated heavily using radiative energy transfer (RET). Although RET has been shown to lead to considerable improvement in the spectral utilization of light by a silicon-based light-harvesting platform, RET is fundamentally restricted due to limited coupling of excitation energy in the sensitizer to silicon. Alternatively, NRET, also known as Förster resonance energy transfer

(FRET), which is strongly directional, makes it very promising for the efficient spectral sensitization of silicon. Previously, exciton transfer into silicon via FRET has been verified using time-resolved fluorescence spectroscopy and time-resolved photocurrent measurements. The nonradiative energy transfer in this case was treated as conventional Förster-type transfer as in the case of a luminescent donor and a luminescent acceptor. Therefore, indirect bandgap property of Si was not taken into account for the FRET process. Furthermore, it has been unknown whether there exists any fundamental difference in the underlying mechanism of the FRET when the acceptor is an indirect bandgap material which has phonon-mediated absorption.

In this first study presented in Chapter 3, we report the first account of phonon-assisted FRET into indirect bandgap semiconductor silicon via temperature dependent investigation of FRET. Here, we show that FRET into the silicon is intrinsically a phonon-assisted process, like its optical counterpart RET. We proposed and developed, for the first time, a phonon-assisted exciton transfer model that predicts the temperature-dependent FRET kinetics. The decreasing FRET efficiencies at cryogenic temperatures are theoretically well explained by the model considering the phonon depopulation in the indirect bandgap acceptor together with the changes in the quantum yield of the donor. We strongly believe that this understanding will be crucial in designing excitonic sensitization of silicon for high-efficiency light-harvesting systems.

In the second section of this chapter, we present the study on excitonic enhancement of NRET into bulk silicon by using the energy-gradient of cascaded colloidal quantum dots. Optical sensitization of silicon as a technologically important non-luminescent material is of great importance for silicon based light-harvesting and light-sensing systems. For the improvement in the performance of optical utilization of silicon, optical sensitization via external sensitizers such as CQDs has been previously proposed. However, in these hybrid structures, the efficiency of energy conversion from the CQDs into silicon is ultimately important for optoelectronic device performances.

In this second study presented in Chapter 3, we report the first account of excitonic enhancement in silicon through cascaded NRET-mechanism using the energy-gradient CQDs. Here, excitonic enhancement of NRET in crystalline silicon was observed by using an energy-gradient structure of cascaded green-emitting (G) and red-emitting (R) CQDs layer-by-layer grafted on silicon as compared to their mono-dispersed structure. For the theoretical analysis, a model based on the excited state population-depopulation dynamics of the CQDs was developed to explain the observed enhancement. The observed and calculated significant enhancement in exciton population of silicon offers an advantageous route for sensitization of silicon *via* excitonic NRET, which was previously limited to the reports of only mono-dispersed and/or single monolayer structures. With the new findings of this work, the cascaded architecture proves to further outperform the mono-dispersed cases for the exciton transfer to silicon.

In the final section of this chapter, we present the study on excitonic NRET from CQDs to graphene variants including graphene oxide (GO) and reduced graphene oxide (RGO). Besides widely used epitaxial graphene, solution-processed graphene variants, GO and RGO, have great potential as efficient exciton sinks to be used in optoelectronic applications. These graphene based structures offer unique capabilities including ease of processing at low cost, large-area coverage and tunable energy gap, which cannot be satisfied by the epitaxial graphene. In this sense, sensitization of GO and RGO films with CQDs and understanding the NRET processes in these hybrids are ultimately critical.

In this third study presented in Chapter 3, we address the issue of NRET from CdSe/CdS CQDs into few layer graphene derived films in terms of donor - acceptor separation distance by using TRF spectroscopy. We revealed the presence of two different mechanisms dominating the energy transfer in these graphene based hybrids. It was observed that excitonic NRET is predominant at long separation distances (> 5nm) while both excitonic and non-excitonic NRET are present at shorter distances. In general, the efficiency of NRET is strongly dependent on the distance between donor and acceptor but the systematic investigation of NRET mechanism from CQDs into graphene based materials was not reported previously. Furthermore, in order to uncover the physical and chemical effects on the film quality, we examined the

preparation process of hybrid films by using several characterization techniques including Raman spectroscopy, atomic force microscopy (AFM) and X-ray photoemission spectroscopy (XPS). Overall, the work presented in this section serves as a new source for the explanation of NRET mechanism between CQDs and graphene based films regarding the separation distances between the donor CQDs and the acceptor GO or RGO. The approach we developed in this study could be used for the cases where a well-controlled gradient in the film quality is required to accomplish a set of functions.

3.1 Phonon-assisted excitonic nonradiative energy transfer into silicon by using quantum dot nanoemitters

This section is based on the publication "Phonon-Assisted Exciton Transfer into Silicon Using Nanoemitters: The Role of Phonons and Temperature Effects in Forster Resonance Energy Transfer," **A. Yeltik**, B. Guzelturk, P. L. Hernandez-Martinez, A. O. Govorov and H. V. Demir, ACS Nano 7, 10492-10501 (2013). Adapted (or "Reproduced") with permission from American Chemical Society. Copyright 2013 American Chemical Society.

3.1.1 Motivation

The phonon-assisted absorption of light in indirect bandgap semiconductors such as silicon is a fundamentally important optical phenomenon and it is essential for photovoltaic solar conversion in silicon-based solar cells. Optical transitions *via* phonon assistance in silicon, which is the dominant material in photovoltaics [182], have been widely studied to date. The necessity of phonons for indirect interband transitions, however, imposes a significant constraint on the performance of the silicon-based solar cells. To increase the probability of photon-phonon interaction and,

in the end, to enhance optical absorption of silicon, there have been numerous efforts including light trapping [183]–[185], light field localization [186], [187], and external light sensitization *via* transferring photon energy into silicon [151], [152], [188], [189]. Recently, as good external sensitizer nanomaterials, colloidal quantum dots have been proposed owing to their favorably large absorption cross-section and easily tunable optical properties. CQD sensitization on monocrystalline silicon was previously demonstrated by using radiative energy transfer (RET) between CQDs and silicon [151], [152]. Although the sensitization of silicon through RET has been shown to lead to considerable improvement in the absorption properties of silicon-based devices, it is fundamentally restricted due to limited coupling of photons emitted by CQDs into silicon [152]. Alternatively, excitonic nonradiative energy transfer, or also known as Förster resonance energy transfer, is a promising method for the spectral sensitization of the silicon *via* CQDs [154], [156], [190]–[194]. FRET relies on near field dipole-dipole interaction between an exciton donor and an exciton acceptor, which are in close proximity [190]. The advantage of these FRET-enabled sensitization systems is the ability to directly couple the excitation energy in the strongly absorbing CQDs into silicon while avoiding otherwise necessary exciton recombination in the sensitizer itself.

Previously, exciton transfer into silicon *via* FRET has been verified by using time-resolved fluorescence (TRF) spectroscopy and time-resolved photocurrent measurements [156], [190], [194]. However, this transfer mechanism was treated as the conventional FRET between a luminescent donor and a luminescent acceptor, although Si is an indirect bandgap material and phonons are significantly involved in the optical transitions within silicon. To date, it has been hidden whether there is any fundamental difference in the underlying mechanism of the FRET into an indirect bandgap nonluminescent material possessing phonon-mediated absorption.

In this work, we studied the phonon-assisted FRET as a function of the temperature to elucidate the underpinning physics behind the dynamics of this exciton transfer process by using the donor nanoemitters integrated on the acceptor monocrystalline bulk silicon. Herein, we show that Förster-type NRET from nanoemitters into silicon is a phonon-assisted process similar to its optical counterpart RET. We proposed and

developed the first account of a phonon-assisted exciton transfer model that predicts the temperature-dependent dynamics of FRET in these CQD-Si hybrid structures. Although FRET is an emission-less process, optical properties of the acceptor strongly modifies the dynamics of FRET. It was observed that the FRET efficiencies decrease at cryogenic temperatures, which is well explained by the model including the phonon depopulation mechanism in the indirect bandgap acceptor together with the changes in the quantum yield of the donor.

3.1.2 Experiment and theory

In this study, we designed and fabricated hybrid nanostructures of multi-monolayer-equivalent film of core/shell CdSe/ZnS CQDs on single-crystal silicon. Here, the bulk monocrystalline p-type silicon (100) substrate was utilized as the acceptor and the core/shell CdSe/ZnS CQDs as the donor. The CQDs were obtained from Evident Technologies and used without further purification (20 mg/mL in toluene). The peak emission wavelength of the CQDs is 580 nm with a full-width at half-maximum (FWHM) of 35 nm. The average radius of the CQDs was obtained to be around 2.22 nm from the ensemble high-resolution transmission electron microscopy (HR-TEM) images. The CQDs are covered with hexadecylamine (HDA) ligands having a length of around 2 nm. The CQDs were spin-coated over the $Al_2O_3/SiO_2/Si$ structures, resulting in the formation of approximately 10-monolayer-equivalent CQD film, verified by an optical ellipsometer (V-Vase J.A.Woolam). The CQD film was shown to be uniformly distributed by using scanning electron microscopy (SEM) and atomic force microscopy (PSIA).

The average radius of the CQDs was obtained by FEI Tecnai G2 F30 ensemble high resolution - transmission electron microscopy (HR-TEM). Film thicknesses of the native oxide and the CQD layer on silicon substrates were recorded by V-VASE ellipsometer. We deposited Al_2O_3 thin films on SiO_2/Si substrates using $Al_2(CH_3)_6$ and H_2O precursor gases at 200 ^oC with Savannah 100 atomic layer deposition (ALD) system. The CQDs were spin-coated over our $Al_2O_3/SiO_2/Si$ structures at 2000 rpm for 150 s. To confirm the uniformity of surface coverage for the CQDs, images of the

samples including CQDs were taken by Quanta 200 FEG Environmental scanning electron microscopy (SEM) with high resolution. To assess the FRET dynamics in the CQD-Si hybrid structures, fluorescence decays of the CQDs were recorded by TRF spectrometer with a closed cycle He cryostat. QYs of the CQD samples (in-film and in-solution) were measured by Horiba Jobin Yvon steady-state photoluminescence (PL) spectrometer equipped with a QY measurement setup.

Figure 3.1a depicts the general structure of the working samples used in this study. As seen from the SEM image in Figure 3.1b, the top CQD layer is highly packed without any aggregate formation indicating the high film quality. The surface coverage fraction of the CQDs reaches ~65% as obtained by analysis of the SEM image in Figure 3.1b. Furthermore, AFM images prove that the surface uniformity is quite high with only one CQD (with ligand) thick voids on the sample (see Figure 3.1c and height profile). Overall, root-mean-square (rms) roughness is found to be ~2 nm, which is much smaller than the size of the CQDs. Therefore, the CQD-film deposited upon silicon is high quality; thus, the sample can be considered as 10-monolayer-equivalent although it is not prepared by layer-by-layer deposition. From the ensemble TEM images, the center-to-center distance between two adjacent CQDs was estimated to be 6.48 nm including the interpenetrating ligands. QYs of the 10-monolayer-equivalent CQD film on sapphire and the diluted CQD solution were measured as 25% and 29%, respectively, by using an integrating sphere. The employed single-crystal silicon is 0.5 mm thick and possesses approximately 1.65 nm thick native oxide on the top, as verified by the optical ellipsometry measurements. To incorporate a controlled separation between the CQDs and silicon, we deposited Al_2O_3 film on pre-cleaned silicon substrates having the native oxide by using ALD technique, which is one of the most suitable methods to deposit atomically thin layers conformably and controllably. The film thicknesses of Al_2O_3 layer were carefully set to 1.0, 2.0 and 4.0 nm and verified using ellipsometry measurements. In addition, the same amount of CQD-coated sapphire (Al_2O_3) substrate was utilized as a reference sample where no FRET exists. The inset in Figure 3.1b shows optical absorption and photoluminescence (PL) spectra of the CQDs when pumped at 350 nm.

While performing the TRF spectroscopy, the peak emission wavelength of the CQDs was monitored *via* time-correlated single photon counting technique. Measurements were performed for different Al_2O_3 spacer thicknesses at varying temperatures between 22 and 290 K using a closed-cycle He cryostat. Optical absorption spectrum of silicon is also depicted (in log scale) in the inset of Figure 3.1b to illustrate the spectral overlap between the silicon absorption and the CQD emission spectra.

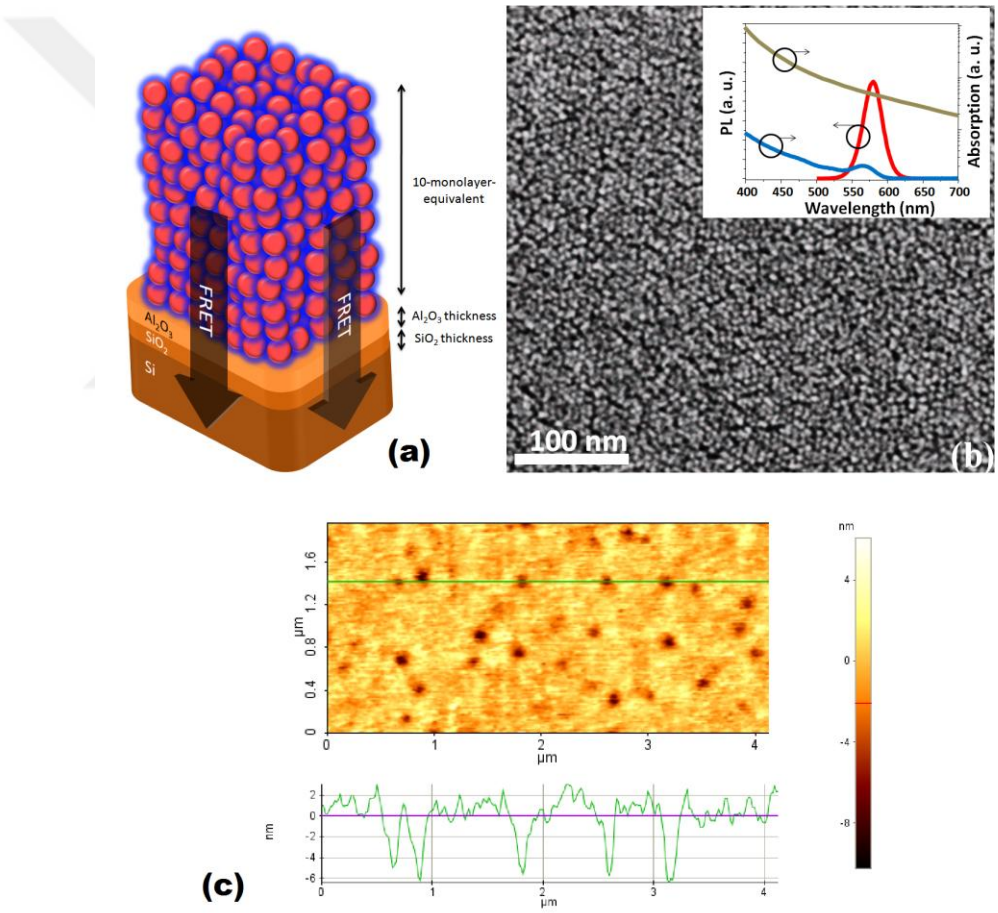

Figure 3.1. (a) Schematic of the hybrid nanostructure of multi-monolayer CQDs and silicon separated by controlled Al_2O_3 separation thickness. Here l = 1.65 nm is the native SiO_2 film thickness, h is the distance between the top-most oxide layer and center of the first CQD layer, X ranging from 0.0 to 4.0 nm is the Al_2O_3 film thickness,

and d is the distance from a CQD monolayer center of interest to the bulk silicon surface. The CQDs of the same monolayer are assumed to have the same exciton transfer contribution to bulk silicon. (b) SEM image of the CQDs furnished on the $Al_2O_3/SiO_2/Si$ structures. Inset shows optical absorption and PL spectra of the CQDs (black and green curves, respectively) and absorption spectrum of silicon (red curve). (c) Atomic force microscopy image of the 10-monolayer-equivalent CQD film on top of silicon with the height profile of the line shown inside the AFM image.

Figure 3.2 depicts the exemplary room temperature fluorescence decay curves of the 10-monolayer-equivalent film of CQDs deposited on the $Al_2O_3/SiO_2/Si$ layered samples for varying Al_2O_3 spacer thicknesses and on the sapphire. The corresponding fluorescence lifetimes were also recorded as shown in Figure 3.2. The decay curves are fitted with multi-exponential lifetimes producing reduced χ^2 close to 1 and the exciton lifetimes are calculated *via* amplitude-averaging, since there is only one type of fluorophore (i.e., the CQDs) in the system. Owing to the increased dipole-dipole coupling at short donor-acceptor separations, as the separation thickness is reduced from 4.0 to 0 nm, the lifetimes of the CQDs decreased, indicating that FRET becomes stronger at shorter separation distances (see Figure 3.2). Moreover, we checked the inter-dot FRET which could be dominant mechanism for the thick CQD-films. In our case, inter-dot FRET is found to be weak, since fluorescence lifetimes of the blue- and red-tail emission does not differ much (up to 2.5-fold) as compared to the lifetime at the peak emission wavelength. This is related to the fact that self spectral overlap is not strong to realize dominant inter-dot FRET taking into account the dot-to-dot separation due to shell and ligand length. However, as we observed from our trials with either small sized core or thin shell CQDs, where inter-dot FRET tends to become dominant, analysis of the FRET into silicon is not straightforward.

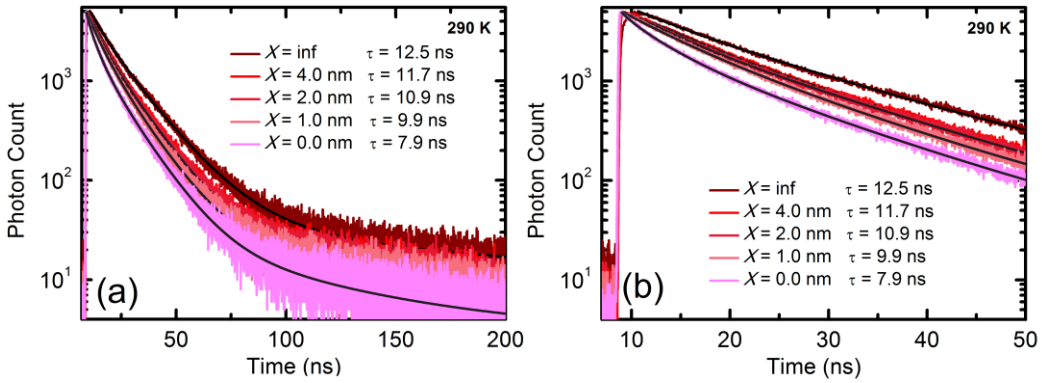

Figure 3.2. Experimental fluorescence decays of 10-monolayer–equivalent CQD film on silicon substrate with 0.0, 1.0, 2.0 and 4.0 nm of Al_2O_3 separation layer and on sapphire as reference sample: (a) over a time decay of 200 ns and (b) zooming in the first 50 ns. The multi-exponential fits are shown inside the decay curves with the averaged lifetimes reported at the bottom.

For the temperature-dependent QY measurements of the CQDs, we recorded PL intensities for each temperature by using the TRF system. We measured the counts at the wavelength range of 520-610 nm with 10 nm steps and summed them up to obtain the total photon counts at each temperature. We set the accumulation time to 20 s at each wavelength as this gives approximately the real time of the TRF lifetime measurements we presented in this study. As given in Figure 3.3, as the temperature decreases, the QY increases gradually making a peak at around 177 K, corresponding to the toluene freezing temperature and then it decreases slowly at lower temperatures. Solvent phase transition of the colloidal CQDs at low temperatures may affect the temperature dependence behavior of the CQDs PL intensity. In addition, photo-oxidation and photo-bleaching may occur as a result of the long duration of illumination in the TRF measurements [195], [196].

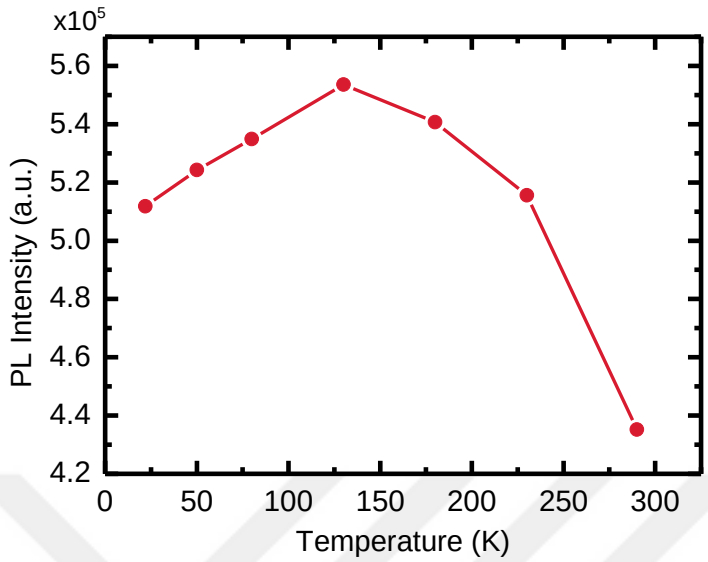

Figure 3.3. Temperature dependence of PL intensity of the CQDs coated on the $Al_2O_3/SiO_2/Si$ and sapphire substrates.

In this work, we used the CQD samples having small size distribution, i.e. less than around 10%. To investigate the effects of inter-dot FRET on the rates, we performed additional TRF measurements by using either 10-monolayer-equivalent CQD film on top of silicon or highly diluted CQDs in solution. For highly diluted CQD solution, inter-FRET is negligible since the effective dot-to-dot separation (> 50 nm) is much greater than the Förster radius (~ 6 nm), yet there is difference in the lifetime of the blue- and red-tail emission of the CQDs (see Table 3.1 for highly diluted CQD solution cases). This difference is not due to inter-CQD FRET, but it is due to intrinsic difference in the lifetimes of the CQDs that are inhomogeneously broadened. In the 10-monolayer-equivalent solid-state films of the CQDs, there is an additional difference in the lifetime of the blue- and red-tail emission of the CQDs as compared to the lifetime at the peak emission wavelength. Inter-dot FRET is the responsible channel for this extra difference. However, it is so weak that one may neglect its effects. The lifetime difference is only 2.5-fold when compared to the lifetimes of the red- to blue-tail emission considering the intrinsic lifetime difference as measured from the diluted solutions. Here, for the case of far tail emissions ± 40 nm is chosen as compared to the peak emission wavelength. When the measurements are conducted at wavelengths of

FWHM, the results indicate even smaller lifetime difference of 1.25-fold as shown in Figure 3.4.

Table 3.1. Lifetime ratios of the CQDs in the emission spectra (lifetimes of the red-tail and blue-tail emission as compared to lifetime at the peak-emission wavelength) when measured for far tail-emission and at FWHM.

At far tails	$\tau_{Red\text{-}tail} / \tau_{Peak}$	$\tau_{Blue\text{-}tail} / \tau_{Peak}$
Highly diluted CQD solution	1.2	0.714
Ten-monolayer-equivalent CQD film on silicon	1.9	0.455
At FWHM	$\tau_{Red\text{-}tail} / \tau_{Peak}$	$\tau_{Blue\text{-}tail} / \tau_{Peak}$
Highly diluted CQD solution	1.4	0.833
Ten-monolayer-equivalent CQD film on silicon	1.4	0.666

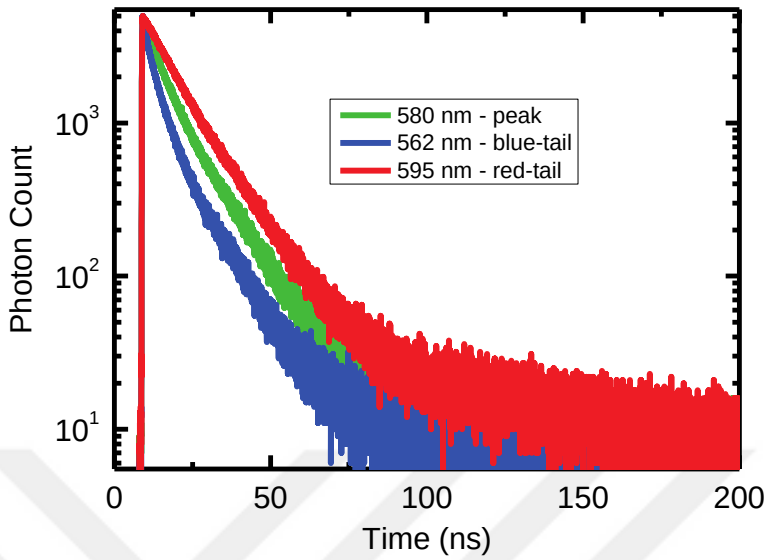

Figure 3.4. Fluorescence decays of the ten-monolayer-equivalent CQDs measured at three different spectral positions (peak, blue- and red-tail) at FWHM.

In the literature, there are several studies related to inter-dot FRET. For example, Crooker et al. utilize a similar CQD construct and observe lifetime differences up to an order of magnitude [197]. However, their film thicknesses (up to 1 µm) are totally different than ours (70 nm). In the case of thick CQD films, self-absorption effects and cyclic pumping of the smaller bandgap CQDs become important. Furthermore, since they use TOPO ligands which are ~1 nm in size, dot-to-dot separation is shorter as compared to our study in which we use HDA ligands (~2 nm in size). All these parameters may cause the differences in lifetimes at various wavelengths. On the other hand, inter-dot FRET may become dominant with large self spectral overlap and small dot-to-dot distance in between. As recently shown by B. N. Pal et al. shell thickness of the CQDs strongly affects and thicker shell CQDs suppress the inter-dot FRET in dense CQD films [198]. Therefore, depending on the material system (core-shell size) and extinction coefficient of the material (self spectral overlap) inter-dot FRET may not be significant.

Analysis of the TRF decay curves were done by using multi-exponential decay fitting to the experimental data. Interestingly, below 50 K, a fast lifetime component in

the TRF of the CQDs was observed (Figure 3.5). Since this component has a small steady-state contribution, which is below 2.5% for all the samples and temperatures, we ignored that component while fitting the curves. At cryogenic temperatures, this type of behavior for the CQDs was first observed by Labeau et al. using single CdSe/ZnS CQDs [199]. Single CQD lifetimes having more than one component including a very fast component were attributed to the relaxation rate from the combined behavior of bright and dark excited states of the CQDs. In our study, we observed the similar behavior for the CdSe/ZnS CQDs in the ensemble. However, for practical purposes, as this fast component has a weak effect, it is ignored in our analysis.

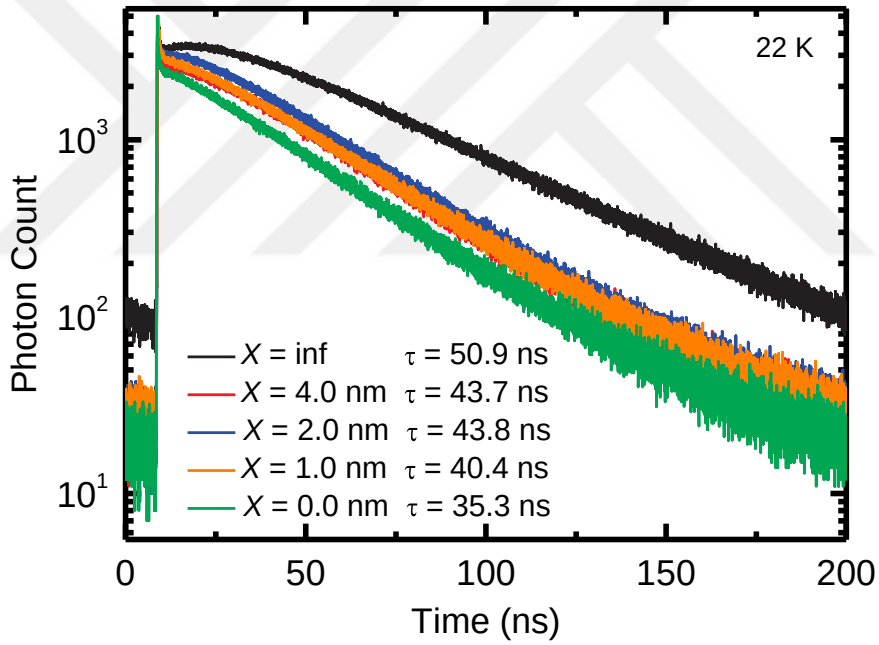

Figure 3.5. TRF decays of 10-monolayer-equivalent CQD film over silicon substrate with 0.0, 1.0, 2.0 and 4.0 nm thick Al_2O_3 separation layer and over sapphire, which were recorded at 22 K.

Fluorescence lifetimes of the CQDs on sapphire have to be corrected due to refractive index difference between sapphire and silicon to correctly account for the

reference lifetimes. Detailed calculation of the correction factor due to the difference in refractive index of substrate material for our CQD-sapphire hybrid system is estimated by using the assumptions and conditions given in ref. [200] and averaged over random dipole orientations [201]. The dipole decay rate, located at distance z above a layered dielectric system, is modified from γ_0 to γ, where γ_0 is the dipole decay rate in vacuum. The ratio between these two rates is given by

$$\frac{\gamma}{\gamma_0} = 1 + I \quad 0, \infty \tag{3.1}$$

$$I \quad a,b \quad = \frac{1}{2}\mathrm{Re}\left(\int_a^b \frac{sds}{\sqrt{1-s^2}} \left[\quad 2s^2 - 1 \quad r^{\ p} \quad s \quad + r^{\ s} \quad s \quad \right] \exp\left[2ik_0 \quad \sqrt{1-s^2} \quad h \right] \right) \tag{3.2}$$

where $r^{\ s} \quad s$ and $r^{\ p} \quad s$ are the reflection coefficients for s- and p-polarized waves (Ref. [202]), respectively, defined as

$$r^{\ s} \quad s \quad = \frac{r_{1,2}^{\ s} \quad s \quad + r_{2,3}^{\ s} \quad s \quad \exp\left[2i \quad \sqrt{k_2^2 - s^2 k_1^2} \quad z \right]}{1 + r_{1,2}^{\ s} \quad s \quad r_{2,3}^{\ s} \quad s \quad \exp\left[2i \quad \sqrt{k_2^2 - s^2 k_1^2} \quad z \right]} \tag{3.3}$$

$$r^{\ p} \quad s \quad = \frac{r_{1,2}^{\ p} \quad s \quad + r_{2,3}^{\ p} \quad s \quad \exp\left[2i \quad \sqrt{k_2^2 - s^2 k_1^2} \quad z \right]}{1 + r_{1,2}^{\ p} \quad s \quad r_{2,3}^{\ p} \quad s \quad \exp\left[2i \quad \sqrt{k_2^2 - s^2 k_1^2} \quad z \right]} \tag{3.4}$$

with

$$r_{1,2}^{\ s} \quad s \quad = \frac{k_1\sqrt{1-s^2} - \sqrt{k_2^2 - s^2 k_1^2}}{k_1\sqrt{1-s^2} + \sqrt{k_2^2 - s^2 k_1^2}} \tag{3.5}$$

$$r_{2,3}^{\ s}\ \ s\ =\frac{\sqrt{k_2^2-s^2k_1^2}-\sqrt{k_3^2-s^2k_1^2}}{\sqrt{k_2^2-s^2k_1^2}+\sqrt{k_3^2-s^2k_1^2}} \tag{3.6}$$

$$r_{1,2}^{\ p}\ \ s\ =\frac{\varepsilon_2 k_1\sqrt{1-s^2}-\varepsilon_1\sqrt{k_2^2-s^2k_1^2}}{\varepsilon_2 k_1\sqrt{1-s^2}+\varepsilon_1\sqrt{k_2^2-s^2k_1^2}} \tag{3.7}$$

$$r_{2,3}^{\ p}\ \ s\ =\frac{\varepsilon_3\sqrt{k_2^2-s^2k_1^2}-\varepsilon_2\sqrt{k_3^2-s^2k_1^2}}{\varepsilon_3\sqrt{k_2^2-s^2k_1^2}+\varepsilon_2\sqrt{k_3^2-s^2k_1^2}} \tag{3.8}$$

where $s=\frac{\sqrt{k_{ix}{}^2+k_{iy}{}^2}}{k_i}=k_i\sin(\theta)/k_i$ (3.9)

Here, ε_i and k_i $i=1,2,3$ are the dielectric constant and wave vector of the medium 1, 2 and 3 as depicted in Figure 3.6.

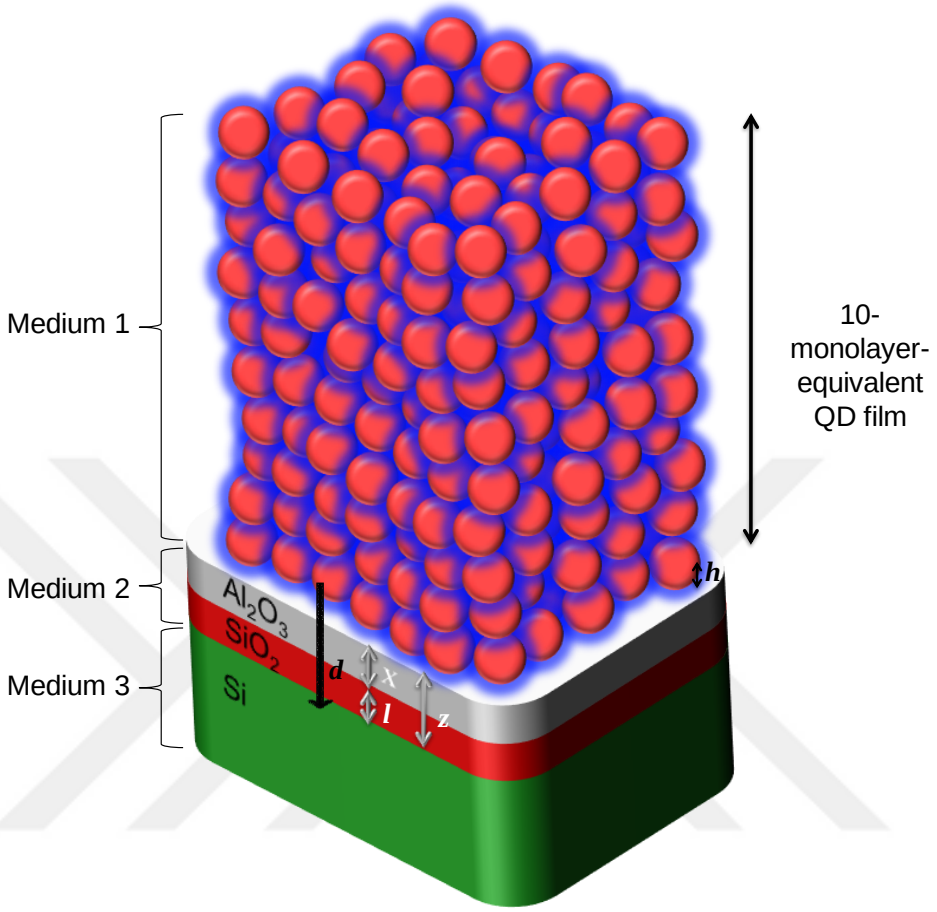

Figure 3.6. A schematic of the studied 0D → 3D hybrid structure. Here, z is the dielectric thickness of the effective oxide layer on silicon, h is the distance between the dipole and the topmost dielectric layer, l = 1.65 nm is the SiO_2 film thickness, X ranging from 0 to 4.0 nm is the Al_2O_3 film thickness and d is the distance from a QD monolayer center of interest to the bulk silicon.

In a QD, the exciton recombination rate is

$$\gamma^{QD} = \gamma_r^{QD} + \gamma_{nr}^{QD} \tag{3.10}$$

The average recombination rate for 10-monolayer-equivalent QD film (ignoring QD-QD FRET) can be written as

$$\left\langle \gamma^{QD} \right\rangle = \frac{1}{N}\sum_{i=1}^{N} \gamma_i^{QD} \tag{3.11}$$

However, the QD recombination rate changes when a QD is placed in close proximity to a dielectric layer because of the inhomogeneity of the dielectric constants. This alters the radiative recombination rates, while nonradiative part remains unchanged $\gamma_{nr}^{QD} = \gamma_{0,nr}^{QD}$. This change in radiative part is expressed for QDs on Si and Al_2O_3 as follows

$$\gamma_{Al_2O_3,r}^{QD} = \alpha^{Al_2O_3} \gamma_{0,r}^{QD} \tag{3.12}$$

$$\gamma_{Si,r}^{QD} = \alpha^{Si} \gamma_{0,r}^{QD} \tag{3.13}$$

where

$$\alpha^{Al_2O_3} = \frac{1}{N}\left(\sum_{i=1}^{N} \alpha_i^{Al_2O_3} \right) \tag{3.14}$$

$$\alpha^{Si} = \frac{1}{N}\left(\sum_{i=1}^{N} \alpha_i^{Si} \right) \tag{3.15}$$

$\gamma_{0,r}^{QD}$ $\gamma_{Al_2O_3,r}^{QD}$ $\gamma_{Si,r}^{QD}$ are the radiative recombination rates in vacuum, on Al_2O_3 and Si, respectively. Here, α_i is the factor, which relates the modification of radiative lifetimes with respect to vacuum, calculated for the i-th QD monolayer using Eq. 3.1 and averaged for all QD monolayers on Al_2O_3 and Si denoted as $\alpha^{Al_2O_3}$ and α^{Si}, respectively. We took the integral in Eq. 3.2 from 0 to 4 in order to correct the radiative part including the effects of the QDs' intrinsic radiative recombination and RET from the QDs into silicon.

To account for the effect of refractive index difference between Al_2O_3 and Si on the radiative lifetime of QDs, we calculate a correction factor α using the expression

$$\alpha = \frac{\gamma_{Si,r}^{QD}}{\gamma_{Al_2O_3,r}^{QD}} = \frac{\alpha^{Si}}{\alpha^{Al_2O_3}} \tag{3.16}$$

On Al_2O_3 radiative and nonradiative recombination rates are written in terms of quantum yields (Y_{QD}) as $\gamma_{Al_2O_3,r}^{QD} = Y_{QD}\gamma_{Al_2O_3}^{QD}$ and $\gamma_{Al_2O_3,nr}^{QD} = 1 - Y_{QD}\ \gamma_{Al_2O_3}^{QD}$ and α is employed to correct the reference radiative lifetime

$$\left\langle \gamma_{Al_2O_3}^{QD^*} \right\rangle = \left[\alpha Y_{QD} + 1 - Y_{QD} \right] \gamma_{Al_2O_3}^{QD} \tag{3.17}$$

Theoretical parameters that we used for the calculation of correction factors for the radiative transfer rates can be listed in four groups as follows:

a) Dielectric constants and dipole moments for the CQDs

ε_{SiO_2} = 2.37, $\varepsilon_{Al_2O_3}$ = 3.10, ε_{Ligand} = 1.5, ε_{av} = (ε_{SiO_2} + $\varepsilon_{Al_2O_3}$ + ε_{Ligand})/3 = 2.32, $\varepsilon_{CdSeBulk}$ = 6.2, $\varepsilon_{ZnSBulk}$ = 8.3, ε_{QD} = ($\varepsilon_{CdSeBulk}$ + $\varepsilon_{ZnSBulk}$)/2 = 7.25, ε_{eff_QD} = (2ε_{Ligand} + ε_{QD})/3, and d_{exc} = 0.4 nm.

The separation distance from center of the first CQD layer to the bulk Si was calculated as follows: $d = l + X + L_l + r$, where X goes from 0 to 4 nm as shown above. Therefore, *d = 5.91 nm, 6.91 nm, 7.91 nm*, and *9.91 nm*.

The separation distance from center of the second CQD layer to the bulk Si was calculated as follows: $d = l + X + L_l + r + D$, where X goes from 0 to 4 nm as shown above. Therefore, *d = 12.39 nm, 13.39 nm, 14.39 nm*, and *16.39 nm*.

The separation distance from center of the third CQD layer to the bulk Si was calculated as follows: $d = l + X + L_l + r + 2D$, where X goes from 0 to 4 nm as shown above. Therefore, *d = 18.87 nm, 19.87 nm, 20.87 nm,* and *22.87 nm*.

The separation distance from center of the fourth CQD layer to the bulk Si was calculated as follows: $d = l + X + L_l + r + 3D$, where X goes from 0 to 4 nm as shown above. Therefore, *d = 25.35 nm, 26.35 nm, 27.35 nm,* and *29.35 nm*.

The separation distance from center of the fifth CQD layer to the bulk Si was calculated as follows: $d = l + X + L_l + r + 4D$, where X goes from 0 to 4 nm as shown above. Therefore, *d = 31.83 nm, 32.83 nm, 33.83 nm,* and *35.83 nm*.

After the fifth layer the FRET was neglected due to the large separation distance between the CQD layer and bulk Si.

b) Factors for temperature-dependent quantum yield

Table 3.2 shows the experimental QY and gamma ratios with calculated radiative rate ratio compared to room temperature values as obtained by using Eq. 3.27.

Table 3.2. Experimental QY and gamma ratios; and calculated radiative rate ratio for each temperature used in the study.

Temperature (K)	QY ratio	Gamma ratio	Radiative rate ratio
290	1.000	1.000	1.000
230	1.185	0.940	1.114
180	1.242	0.870	1.081
130	1.272	0.780	0.992
80	1.229	0.610	0.750
50	1.205	0.480	0.578
22	1.176	0.270	0.318

d) Temperature-dependent dielectric function of silicon

In the model, we used the following parameters for the temperature-dependent Si dielectric function (Ref. [203]):

$\hbar\Omega_{ph,i=1,2} / k_B$ = 212 K, 670 K; $E_{g,j=1,2}(T)$ = 1.16 eV - $\beta T^2/(T+\gamma)$, 2.25 eV - $\beta T^2/(T+\gamma)$; $\beta = 7\text{x}10^{-4}$ eV / K, γ = 1108 K; $A_{j=1,2}$ = 253 cm^{-1} eV^{-2}, 3312 cm^{-1} eV^{-2}; $C_{i=1,2}$ = 5.5, 4.2 cm^{-1} eV^{-2}.

In this work, in order to estimate the exciton transfer from the CQD to bulk silicon, the well-known Fermi's Golden rule was used. After using the fluctuation dissipation theorem [204] and algebraic manipulation, the resulting FRET rate can be derived in a form convenient for numeric calculations [205], [206]. The transfer probability of an exciton from a donor to an acceptor is obtained by the Fermi's Golden rule

$$\gamma_{NRET} = \frac{2}{\hbar}\left\{\sum_f \left|\langle f_{exc};0_{exc}|\hat{V}_{\text{int}}|i_{exc};0_{exc}\rangle\right|^2 \delta\ \ \hbar\omega_{exc} - \hbar\omega_f\ \right\} \qquad (3.18)$$

where $|i_{exc};0_{exc}\rangle$ represents the initial state having an exciton in the donor nanostructure and zero exciton in the acceptor nanostructure; $|f_{exc};0_{exc}\rangle$ represents the final state having an exciton in the acceptor nanostructure and zero exciton in the donor nanostructure; $\hat{V}_{\text{int}}$ represents the operator of excitonic Coulombic interaction; and $\hbar\omega_{exc}$ represents the energy of exciton. With the approximation that there is not a coherent coupling between the excitons, i.e., the initial and final states can be rewritten as $|i_{exc};0_{exc}\rangle = |i_{exc}\rangle|0_{exc}\rangle$ and $|f_{exc};0_{exc}\rangle = |f_{exc}\rangle|0_{exc}\rangle$, and by using the fluctuation dissipation theorem (FDT) [204] together with the CQD formalisms developed in Refs. [205], [206], the Fermi's Golden rule can be simplified as follows.

$$\gamma_{NRET} = \frac{2}{\hbar}\text{Im}\left[\int dV\left(\frac{\varepsilon_A\ \ \omega}{4\pi}\right)\mathbf{E}_{in}\ \ \mathbf{r}\ \cdot\mathbf{E}^*_{in}\ \ \mathbf{r}\ \right] \qquad (3.19)$$

where $\mathbf{E}_{in}\ \mathbf{r}$ is the effective electric field owing to an exciton inside the donor. The electric field was calculated with the following equation.

$$\mathbf{E}\ \mathbf{r} = -\nabla\Phi\ \mathbf{r} \tag{3.20}$$

The electric potential, $\Phi\ \mathbf{r}$, which is necessary to compute γ_{NRET} (Eq. 3.18) was calculated as the total potential created by the electric potential of an exciton inside the donor.

$$\Phi_{\alpha}\ \mathbf{r} = \left(\frac{ed_{exc}}{\varepsilon_{eff_D}}\right)\frac{\mathbf{r}-\mathbf{r}_0\ \cdot\hat{\boldsymbol{\alpha}}}{\left|\mathbf{r}-\mathbf{r}_0\right|^3} \tag{3.21}$$

where ed_{exc} is the exciton dipole moment, and ε_{eff_D} is the donor effective dielectric constant, which depends on the geometry of donor and the dipole direction of exciton ($\alpha = x, y, z$).

The average FRET rate was calculated by using the following expression.

$$\gamma_{NRET} = \frac{\gamma_{x,NRET} + \gamma_{y,NRET} + \gamma_{z,NRET}}{3} \tag{3.22}$$

where $\gamma_{\alpha,NRET}$ represents the transfer rate for the α-exciton ($\alpha = x, y, z$). For a spherical CQD structure, the corresponding transfer rates are calculated as follows:

$$\gamma_{\alpha,NRET}\ d, \omega_{exc} = \frac{2}{\hbar} b_{\alpha}\left(\frac{ed_{exc}}{\varepsilon_{eff}}\right)^2 \frac{1}{d^3}\left|\frac{2\varepsilon_0}{\varepsilon_{si}\ \omega_{exc} + \varepsilon_0}\right|^2 \mathrm{Im}\left[\varepsilon_{si}\ \omega_{exc}\right] \tag{3.23}$$

where ε_0 is the medium dielectric constant, $\varepsilon_{eff} = \frac{2\varepsilon_0+\varepsilon_{QD}}{3}$ is the effective dielectric constant, ε_{QD} is the CQD dielectric constant, $\varepsilon_{Si}\ \omega$ is the silicon dielectric function (taking from Ref. [207]), and $b_\alpha = \frac{1}{8}, \frac{1}{16}, \frac{1}{16}$ for an exciton *x*, *y*, and *z*, respectively. Thus, the total FRET rate is

$$\gamma_{NRET}\ d, \omega_{exc} = \frac{2}{\hbar}\left(\frac{1}{12}\right)\left(\frac{ed_{exc}}{\varepsilon_{eff}}\right)^2 \frac{1}{d^3}\left|\frac{2\varepsilon_0}{\varepsilon_{si}\ \omega_{exc} + \varepsilon_0}\right|^2 \mathrm{Im}\left[\varepsilon_{si}\ \omega_{exc}\right] \quad (3.24)$$

Eq. 3.24 describes the energy transfer from a CQD to a bulk semiconductor material. In this study, the FRET rates are investigated using a hybrid structure consisting of 10-monolayer-equivalent CQD film on bulk silicon as proposed here. For simplicity, the excitation energy transfer from a monolayer of the CQDs to bulk silicon is considered as the energy transfer from a single CQD in the same layer to the silicon, and it is attributed to the average energy transfer. To find the lifetimes of the CQDs, the FRET rate of the CQDs, $\langle \gamma_{NP} \rangle = 1/\tau_{NP}$, was formulated as

$$\langle \gamma_{NP}\ d, \omega, T \rangle = \gamma_0\ d, \omega, T + \frac{1}{N}\sum_{i=1}^{N} \gamma_{i,NRET}\ d_i, \omega \quad (3.25)$$

where $\gamma_0\ d, \omega, T = \frac{1}{\tau_0\ d, \omega, T}$ is the CQD exciton recombination rate in the absence of silicon; τ_0 is the CQD exciton lifetime in the absence of silicon; $\gamma_{i,NRET}\ d_i, \omega$ energy transfer for a CQD in the *i-th* layer; and *N* is the total number of CQD layers. Since silicon is an indirect bandgap semiconductor, we included its temperature-dependent parameters into the model, which provides us with a phonon-assisted FRET model as shown in Eq. 3.26.

$$\gamma_{NRET}\ d, \omega_{exc}, T = \frac{2}{\hbar}\left(\frac{1}{12}\right)\left(\frac{ed_{exc}}{\varepsilon_{eff}}\right)^2 \frac{1}{d^3}\left|\frac{2\varepsilon_0}{\varepsilon_{si}\ \omega_{exc}, T + \varepsilon_0}\right|^2 \mathrm{Im}\left[\varepsilon_{si}\ \omega_{exc}, T\right] \quad (3.26)$$

Eq. 3.26 gives the energy transfer rate for two point-like dipoles, i.e., a perfect donor and acceptor pair. To include the energy transfer losses for the CQDs due to imperfections, traps, etc. (i.e., nonradiative channels not included in our derivation) as a function of the temperature, we introduced the factor $\frac{Y_{QD}\ T\ \gamma_0^D\ T}{Y_{QD}\gamma_0^D\ T_{Room}}$ from the QY definition. Thus, Eq. 3.26 was modified as

$$\gamma_{NRET}\ d,\omega_{exc},T\ = \left(\frac{Y_{QD}\ T\ \gamma_0^D\ T}{Y_{QD}\ T_{Room}\ \gamma_0^D\ T_{Room}}\right)\frac{2}{\hbar}\left(\frac{1}{12}\right)\left(\frac{ed_{exc}}{\varepsilon_{eff}}\right)^2\frac{1}{d^3}\left|\frac{2\varepsilon_0}{\varepsilon_{si}\ \omega_{exc},T\ +\varepsilon_0}\right|^2 \mathrm{Im}\left[\varepsilon_{si}\ \omega_{exc},T\ \right] \quad (3.27)$$

Eq. 3.27 models the energy transfer rate as a function of the temperature and exciton energy.

The model (“phonon-assisted” one) is extended to include temperature-dependent silicon dielectric function which is directly related to the phonon-assisted optical properties of silicon. Furthermore, temperature-dependent QYs of the donor CQDs are considered in the modified model (“full temperature-dependent” one). This allowed us to correctly account for the radiative decay part of the CQDs as a function of the temperature which is important to calculate the dipole-dipole coupling. With these modifications, the phonon-assisted FRET model fitted better to the TRF lifetimes, as it is shown in the study.

To understand the origins of the temperature dependence in transfer, we are now ready to elaborate three forms of the equation for the FRET rate:

$$\gamma_{NRET,Palik}\left(d,\omega_{exc}\right)=F(d)\cdot\mathrm{Im}\left[\varepsilon_{Si,Palik}\left(\omega_{exc}\right)\right], \tag{3.28a}$$

$$\gamma_{NRET,T-dependence}\left(d,\omega_{exc},T\right)=F(d,T)\cdot\mathrm{Im}\left[\varepsilon_{Si}\left(\omega_{exc},T\right)\right], \tag{3.28b}$$

$$\gamma_{NRET,full}\left(d,\omega_{exc},T\right)=\left(\frac{Y_{QD}(T)\gamma_0^D(T)}{Y_{QD}(T_{Room})\gamma_0^D(T_{Room})}\right)\cdot F(d,T)\cdot\mathrm{Im}[\varepsilon_{Si}(\omega_{exc},T)], \tag{3.28c}$$

$$F(d,T)=\frac{2}{\hbar}\left(\frac{1}{12}\right)\left(\frac{ed_{exc}}{\varepsilon_{eff}}\right)^2\frac{1}{d^3}\left|\frac{2\varepsilon_0}{\varepsilon_{Si}(T)+\varepsilon_0}\right|^2, \tag{3.28d}$$

where ed_{exc} and ω_{exc} are the exciton dipole moment and angular frequency, respectively; d is the CQD-silicon separation distance, $\varepsilon_{eff}=(2\varepsilon_0+\varepsilon_{QD})/3$ is the effective dielectric constant, ε_{QD} is the CQD dielectric constant, ε_0 is the medium dielectric constant, and $\varepsilon_{Si}\left(\omega,T\right)$ is the silicon dielectric function [207]. In Eq. 3.28, we assumed $\mathrm{Re}[\varepsilon_{Si}(\omega,T)]=\varepsilon_{Si}>>\mathrm{Im}[\varepsilon_{Si}(\omega,T)]$ that is a very good approximation for the considered exciton energy ($\lambda_{exc}\sim 580nm, \hbar\omega_{exc}\sim 2.1eV$). The function $F(d)$ in Eq. 3.28 involves the optical dipole moment of CQD, which is taken as d_{exc} = 0.4 nm. It is estimated from the CQD exciton lifetime of the reference sample. This exciton dipole moment was estimated from the exciton lifetime and the QY of CQDs in the reference sample. Here, we assume that the CQDs on the quasi-monolayer have the same exciton transfer contribution to bulk silicon, such that the average exciton transfer can be described by the energy transfer of a single CQD in a given monolayer to bulk silicon. In this derived analytical model, it is worth noting that the distance dependence of the FRET rate is proportional to d^{-3}, which is because the acceptor is bulk. This distance dependence is quite different than FRET in the dye-dye [190] and CQD-CQD [208], [209] systems where a FRET rate for a donor-acceptor pair is ~ d^{-6}. Here one fixed set of material parameters are employed for all samples and no fetch factor is employed.

Including the FRET process, the lifetimes of the CQDs on the $Al_2O_3/SiO_2/Si$ substrates can be calculated in the following way:

$$\gamma\ d,\omega\ = \left\langle \gamma^{*}_{0,ref}\ d,\omega\ \right\rangle + \frac{1}{N}\sum_{i=1}^{N}\gamma_{i,NRET}\ d_i,\omega \qquad (3.29)$$

Here, $\gamma\ d,\omega$ is the decay rate of the CQDs on $Al_2O_3/SiO_2/Si$ layer, $\left\langle \gamma^{*}_{0,ref}\ d,\omega\ \right\rangle$ is the decay rate of CQDs corrected for the refractive index difference as obtained from the reference sample, (see Eq. 3.17), N is the total number of monolayers, and $\gamma_{i,NRET}\ d_i,\omega$ is the FRET rate for each corresponding layer. The contribution coming from each different CQD-layer was taken into account by considering the respective separation of the given monolayer to the bulk silicon. Practically, it is assumed that after the fifth CQD-layer, there is no considerable FRET into silicon, thus the entire FRET is caused by the first 5 CQD-layers and it is averaged over the total decay of the 10 CQD-layers (see Eq. 3.29). Inter-dot FRET is ruled out here, since the same CQD film (10 monolayer-equivalent CQDs) on sapphire is utilized as the reference sample.

Now, we briefly show the derivation for the microscopic mechanisms of phonon-assisted FRET which are hidden in the key function $\mathrm{Im}\left[\varepsilon_{Si}\ \omega_{exc},T\ \right]$ in Eq. 3.28. Below, we see that the theory based on the experimental dielectric constants taken from Refs. [203], [207] provides us with an overall good description of the temperature and distance trends for the FRET rates. The imaginary part of the dielectric constant and the related absorption in silicon at the peak CQD emission wavelength is due to the phonon-assistant processes [210] shown in Figure 3.8. To illustrate the process of phonon-assistant FRET to an indirect semiconductor, we now consider transfer of a CQD exciton energy to a small volume, ΔV, at the position R_0 within the Si half-space. An exciton in a CQD can be viewed as an oscillating dipole creating a time-varying electric field E_{exc}. The rate of energy dissipation due to the field of an oscillating dipole in the volume ΔV is:

$$\Delta Q = \Delta V \left| E_{exc} \right|^2 \frac{\omega_{exc}}{2\pi} \mathrm{Im}\ \varepsilon_{Si}(\omega_{exc}, T) \tag{3.30}$$

The absorption rate can also be calculated by the Feynman diagrams (two of them are shown in Figure 3.8b) in combination with the Fermi's golden rule:

$$\begin{aligned} &\Delta Q = \Delta Q_+ + \Delta Q_- \\ &\Delta Q_\pm = \hbar\omega_{exc} \frac{2\pi}{\hbar} \left(\sum_{f=\ p,p'} \left| \sum_i \frac{\langle f | \hat{V}_{e-phonon} | i \rangle \langle i | \hat{V}_{exc} | 0 \rangle}{E_0 + \hbar\omega_{exc} - E_i} \right|^2 \delta(\hbar\omega_{exc} + \varepsilon_{p,v} - \varepsilon_{p',c'} \pm \hbar\Omega_{q_{ph}}) \right) \end{aligned} \tag{3.31}$$

In this equation, $\hat{V}_{exc}$ is the amplitude of the time-oscillating potential of the exciton and $\hat{V}_{e-phonon}$ is the electron-phonon interaction in Si. E_0 and E_i are the energies of the initial and intermediate states, respectively, and whereas $\varepsilon_{p,v(c)}$ denote the energies of single electrons in the valence and conduction bands. The indices p and p' describe the momenta of single electrons in the initial and final states. The functions ΔQ_- and ΔQ_+ give the absorption processes with emission and absorption of phonons, respectively. Correspondingly, the final states in Eq. 3.31 can be of two types:

$$\left| p', c; n_{q_{ph}} - 1 \right\rangle \text{ and } \left| p', c; n_{q_{ph}} + 1 \right\rangle \tag{3.32}$$

These final states appear a result of phonon-absorption and phonon-emission inter-band processes. Here, the state $\left| n_{q_{ph}} \right\rangle$ denotes an initial phonon state with an occupation number $n_{q_{ph}}$, where q_{ph} is a phonon momentum. The Eq. 3.31 has very characteristic temperature- and exciton energy-dependencies. The phonon-emission term in $\hat{V}_{e-phonon}$ will produce the standard factor $\sqrt{n_{q_{ph}} + 1}$ inside the sum and after taking square it will become $n_{q_{ph}} + 1$. In the same way, the phonon-annihilation term in

$\hat{V}_{e-phonon}$ will give the factor $n_{q_{ph}}$. The occupation numbers are, of course, given, by the Bose-Einstein function,

$$n_{q_{ph}} = n_B(\omega_{ph}) = \frac{1}{e^{\frac{\hbar\omega_{ph}}{k_B T}} - 1} \tag{3.33}$$

The effective density of states for the indirect inter-band phonon-assisted transitions is well known and, near the bandgap, has the form: $\hbar\omega - E_{gap}{}^{2}$, where E_{gap} is an indirect bandgap of a semiconductor. These considerations allow us to write the dissipation and the imaginary part of the dielectric constant in the following way adopted from Ref. [203]:

$$\begin{aligned}\mathrm{Im}\ \varepsilon_{Si}(\omega_{exc},T) &= \frac{n_{Si}^{0}C_0}{\omega_{exc}}\alpha(\omega_{exc},T) = \left(\frac{n_{Si}^{0}C_0}{\omega_{exc}}\right)\times \\ \times \sum_{\substack{i=1,2\ \text{(phonons)}\\ j=1,2\ \text{(band-gaps in Si)}}} & A_j C_i \cdot n_B(\Omega_{ph,i},T)\cdot\left[\hbar\omega - E_{g,j}(T) + \hbar\Omega_{ph,i}\right]^2 + A_j C_i \cdot \left[n_B(\Omega_{ph,i},T)+1\right]\cdot\left[\hbar\omega - E_{g,j}(T) - \hbar\Omega_{ph,i}\right]^2\end{aligned} \tag{3.34}$$

Eq. 3.34 involves two types of optical phonons and two indirect bandgaps typical for the silicon crystal and provides a rather realistic approximation for silicon. Importantly, two sources of temperature-dependence can be identified from Eq. 3.34: The phonon populations ($n_B(\Omega_{ph,i},T)$) and the temperature-dependent bandgaps. Both sources are important for Si. The above consideration has shown the microscopic origin of the FRET process in the hybrid CQD-Si system, in which phonon-assisted processes are crucial for energy transfer. This is in striking contrast to the systems with direct bandgap crystals, such as CdSe and CdTe systems [211].

3.1.3 Results and discussion

In this study, we employed five different samples: 10-monolayer-equivalent CQDs on top of either sapphire (reference), 0.0, 1.0, 2.0 or 4.0 nm Al_2O_3 separated SiO_2/Si substrates. Temperature-dependent amplitude-averaged fluorescence lifetimes of the CQDs grafted on these five different substrates are presented in Figure 3.7a – Figure 3.7d for the cases of 0.0, 1.0, 2.0 and 4.0 nm thick Al_2O_3 separations, respectively. Green diamonds are the experimental reference lifetimes (CQDs on sapphire – no FRET), which are corrected for the refractive index difference between sapphire and silicon causing radiative energy transfer as the reason of this correction will be explained in the next part. Black squares are the experimental lifetimes of the CQDs when placed on a respective Al_2O_3 separation thickness. As a general trend, the lifetimes of the CQDs are observed to increase with the decreasing temperature, which is in agreement with previous reports [199].

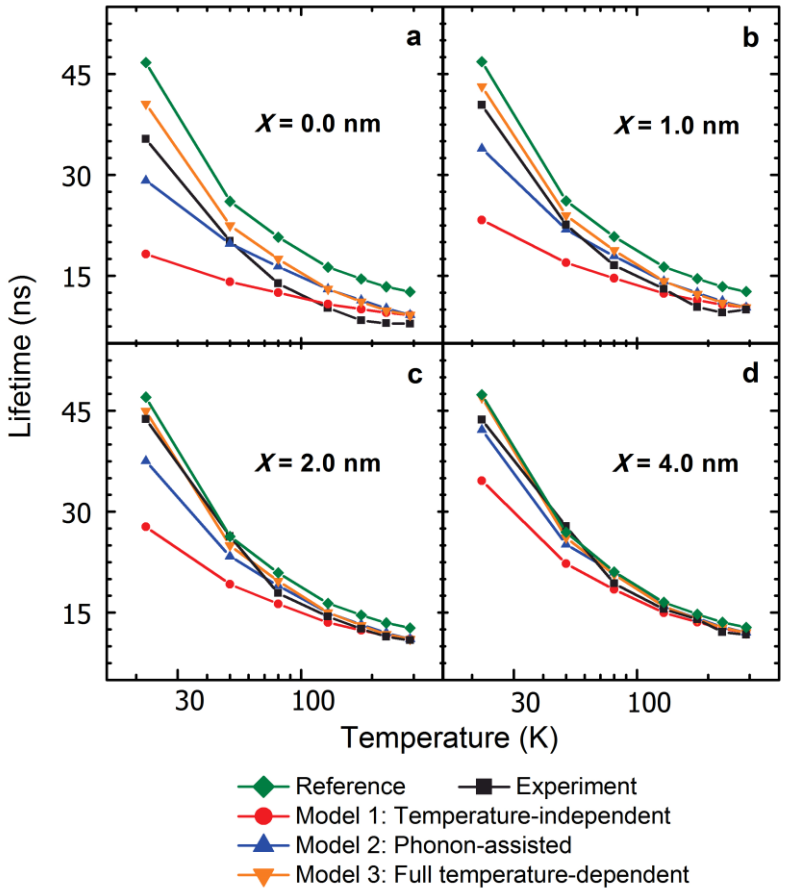

Figure 3.7. Temperature dependence of fluorescence lifetime of the CQDs integrated on top of (a) 0.0 nm, (b) 1.0 nm, (c) 2.0 nm and (d) 4.0 nm thick Al_2O_3 layer on SiO_2/Si. Black squares are amplitude averaged experiment lifetimes. Green diamonds are the lifetimes of the CQDs on sapphire as the reference sample corrected for the refractive index difference with silicon. Red circles are the calculated lifetimes of the CQDs using the "temperature-independent" energy transfer model. Blue up-triangles are the calculated lifetimes of the CQDs using the energy transfer model which considers the temperature-dependent complex dielectric function of silicon, thus "phonon-assisted" model. Orange down-triangles are the calculated lifetimes of the CQDs using the "phonon-assisted" energy transfer model with the additional inclusion of the temperature-dependent QY of the donor CQDs; thus, it is called "full temperature-dependent" model.

As aforementioned, fluorescence lifetimes of the CQDs on sapphire (reference sample, green diamonds in Figure 3.7 have to be corrected due to refractive index difference between sapphire and silicon to correctly account for the reference lifetimes. This effect is summarized in terms of rate equations below

$$\gamma_{Al_2O_3} = \gamma_r + \gamma_{nr} + \gamma_{Al_2O_3,RET} \tag{3.35}$$

$$\gamma_{Si} = \gamma_r + \gamma_{nr} + \gamma_{Si,RET} + \gamma_{FRET} \tag{3.36}$$

γ_r and γ_{nr} are the radiative and nonradiative decay rates of the CQDs in vacuum. $\gamma_{Al2O3,RET}$ and $\gamma_{Si,RET}$ are the radiative energy transfer terms arising due to the difference of the refractive index of the substrate than vacuum, which alters the radiative decay rate of the CQDs. RET terms are different for the case of sapphire and silicon due to difference of the refractive indices, therefore we calculate a correction factor for the reference sample to account for the difference in refractive indices. For this correction, the model developed by Chance, Prock and Silbey (CPS), as introduced in Ref. [202], is adapted while taking radiative decay of a randomly oriented dipole into account in the presence of reflected electric fields due to the inhomogeneous environment. The changes of CQD lifetimes from on sapphire to on hypothetical-silicon, having no absorption component in the dielectric function, were calculated [154], [200]. The radiative lifetime of a CQD placed on hypothetical-silicon is decreased by ~ 2.1 times as compared to the one placed on sapphire. In our case, since 10-monolayer-equivalent CQD film has been employed as the sample, and QY of the CQD film was not unity (it is measured as 25%), the correction factor boils down to a smaller value of ~1.1. After the correction, RET terms in Eq. 3.35 and Eq. 3.36 become equal so that the extra change of the decay rate on silicon could be attributed to the term γ_{FRET}, which is the nonradiative energy transfer of the excitons in the CQDs to silicon *via* near-field dipole-dipole coupling.

After the refractive index correction of the experimental results, to develop a deeper understanding of the FRET between the CQDs and silicon, we proposed a physical model for the energy transfer in the studied hybrid CQD-Si nanostructure. Figure 3.8

illustrates the dipole-dipole Coulomb interaction between the donor CQD and the acceptor silicon. An absorbed photon in a CQD photogenerates a bound electron-hole pair (exciton), which rapidly relaxes to the first excited state through higher order processes. These excitons can subsequently either recombine through a radiative or nonradiative means inside the CQD, or be transferred to silicon *via* Coulomb interaction between dipoles in the donor-acceptor pair provided that the separation distance between the donor and the acceptor is on the order of a few nanometers. Although this type of energy transfer has been well known and studied as Förster resonance energy transfer, it has not been fully understood when an indirect bandgap acceptor is involved. Previously, Stavola et al. discussed the effects of donor-acceptor distance to FRET, while having an indirect bandgap acceptor [191]. There, they have defined proximity effects, which were calculated to be dominant for the donor-acceptor separations on the order of a few lattice constants of the acceptor crystal. Here, the smallest donor-acceptor separation is 5.9 nm (distance from the center of the closest CQD layer to the surface of silicon for the case of no alumina separation), which is much larger than the silicon's lattice constant (~0.54 nm). Therefore, the transitional interactions can be assumed to occur mainly in the optical near-field region around $k \approx 0$ [192], [212]. To date, such phonon-mediated FRET dynamics have not been studied in terms of physical models for this kind of unique donor-acceptor material systems.

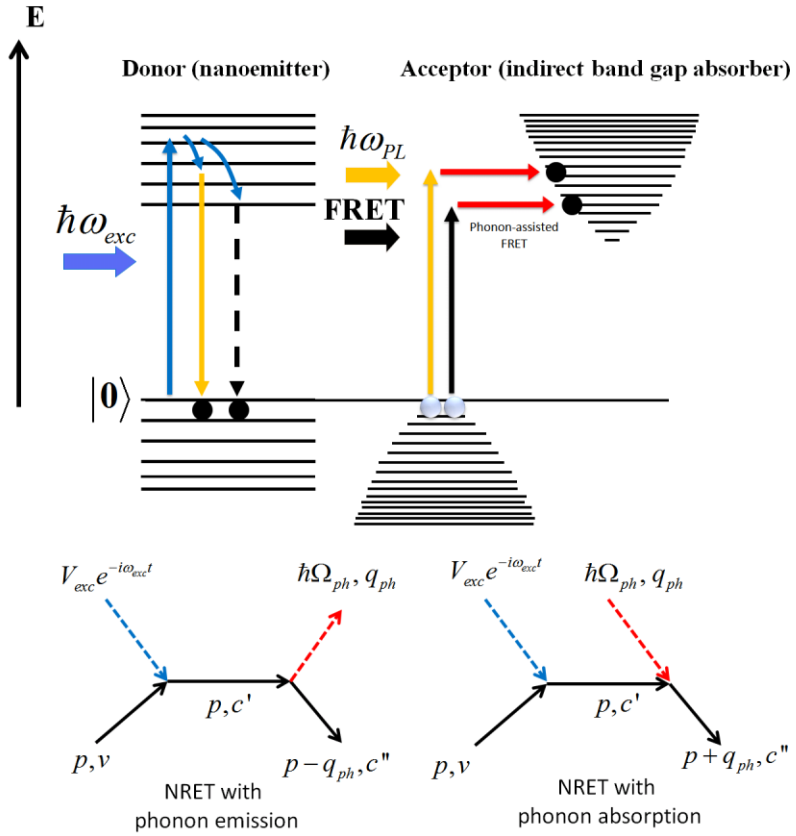

Figure 3.8. (a) Energy diagram illustrating the exciton transfer from the donor CQD to the acceptor silicon due to the Coulomb interaction between the donor-acceptor pair. The phonon-assisted process is shown as the lateral arrows to make up for the momentum mismatch in silicon. (b) Some of the Feynman diagrams for the phonon-assisted processes important for transfer of energy from a CQD to an indirect-band semiconductor. These diagrams include phonon-emission processes in the conduction band.

Here, using Eq.s 3.28, 3.29, and 3.34 the experimental data is contrasted at various temperatures with three different theoretical approaches: “Temperature-independent”, “Phonon-assisted” and “Full temperature-dependent”.

1. *Palik’s dielectric function at* $T = T_{room}$ *- “Model 1 - Temperature independent”:*

   Using the temperature-independent function $\gamma_{NRET,Palik}\ \omega_{exc}$ and Eq. 3.28a, we obtain the rates that have clearly a weaker T-dependence compared to the

experimental data (Figure 3.7). The temperature dependence in this case comes from the intrinsic CQD lifetime $\tau_0 \quad T$.

2. *Temperature-dependent dielectrics function from Ref. [203]. – "Model 2 - Phonon-assisted FRET":* To improve our model and include temperature dependence into the FRET rate, we now include the temperature-dependent processes in Si and use Eq. 3.28b with the dielectric function from Ref. [203]. For different temperatures, almost a temperature independent refractive index is taken as 4 at the wavelengths of interest according to Bucher et al.[203]. Results are given again in Figure 3.7. The insertion of the phonon-assisted absorption of silicon improved the theoretical prediction considerably as shown in Figure 3.7 by blue up-triangles. The low temperature agreement is much better compared to bare energy transfer model, which do not involve any temperature dependent process. This means that phonon-assisted properties of silicon as being the acceptor in our energy harvesting system directly affect the energy transfer rates. Generally, it is not common in the context of FRET being a phonon-assisted process, since most of the time the excitation energy is resonantly transferred to the state in the acceptor without absorption or emission of any phonons. However, it is well accepted that the radiative transitions in indirect bandgap materials involve phonons for the transitions to take place. In the energy transfer process from CQDs to bulk silicon, similar to optical transitions, this suggests that phonons are required to assist the energy transfer. As a result, this type of energy transfer cannot be called merely Förster-type, since its resonance condition can be relaxed due to involvement of the phonons. Furthermore, the effects of different types of phonons on this energy transfer are different. Especially, acoustic phonons are considered responsible for the optical transitions at low temperatures due to their lower activation energies. At cryogenic temperatures, however, there are fewer optical phonons as compared to the acoustic ones, since the optical phonons have much higher activation energy. In addition, considering the optical absorption for silicon, which includes phonon absorption and emission effects

in addition to direct transitions with no phonon assistance, the phonon emission is observed to be a more dominating process at low temperatures.

3. *Temperature dependent QY of the donor CQDs - "Model 3 - Full temperature-dependent approach":* Despite of the reasonable agreement between the results of the phonon-included model and the experimental data, there remains some discrepancy especially at the cryogenic temperatures below 100 K. We attribute it to the CQD's temperature-dependent optical properties, i.e., QY. We measured and calculated the relative change of the temperature-dependent QY for the CQDs and observed that, as the sample temperature is gradually decreased, the QY increases until 150 K, peaking at this temperature, and then decreases towards lower temperatures (Figure 3.19) [213]. Our energy transfer model intrinsically includes theoretical radiative decay rate of the donor CQDs at room temperature. By further including the QY changes as function of temperature in the model, we therefore modify the radiative decay rate of the CQDs as a function of temperature in accordance with the experimentally measured total decay rates and the QYs. Using these temperature-dependent QYs and the ratio between the transfer rates of the CQDs on the reference sample, we obtain the final modified model, which includes both temperature dependent effects of the CQDs and silicon as given in Eq. 3.28c. The final model results in improved match between the theory and experiment especially at the lowest temperature cases as shown in Figure 3.7. The "full temperature-dependent approach" reproduces qualitatively all experimentally observed trends for the FRET rate as a function of separation distance and temperature with a slight improvement over the "phonon-assisted" model, compared to the improvement of the "phonon-assisted" model introduced over the "temperature independent" analytical one. All in all, the energy transfer model including the phonon-assisted processes in the absorption of silicon with the help of temperature dependent optical properties in the CQDs proved its effectiveness to assess temperature-dependent fluorescence lifetimes of the donor CQDs better and showed reasonable agreement with the experimental measurements.

Experimental FRET rates are summarized in Figure 3.9. These rates were calculated as

$$\gamma_{NRET,tot}(T) = \gamma_{QD,Si} - \gamma_{QD,0} \tag{3.37}$$

where $\gamma_{QD,Si}$ is the decay rate for CQDs on Si and $\gamma_{QD,0}$ is the intrinsic decay rate of the excitons corrected due to the modified radiation probability on silicon. Theoretically, the FRET rates are obtained from

$$\gamma_{NRET,tot}(T) = \frac{1}{N}\sum_{i=1}^{N}\gamma_{i,NRET} \quad d_i, \omega \; = f_d(X_{\mathrm{Al_2O_3}}) \cdot F_T(T, \omega_{exc}) \tag{3.38}$$

We can see from the above equation that the FRET rate can be conveniently expressed as a product of two functions, $f_d(X_{\mathrm{Al_2O_3}})$ and $F_T(T, \omega_{exc})$, where $X_{\mathrm{Al_2O_3}}$ is the thickness of the separation layer. Figure 3.9 shows the initial experimental rates, whereas Figure 3.10 displays the comparison between the experimental and theoretical data. In Figure 3.10, we see clearly the trend; the FRET rates are much higher for small Al_2O_3 separations. This is expected, since the Coulomb-induced energy-transfer process rapidly decays with increasing the distance. Important results on the temperature dependence of FRET are shown in Figure 3.10. We see overall good agreement between the “full temperature-dependent” model and the experiment. After including both temperature dependent dielectric function of acceptor silicon and QY of the donor CQDs, the theoretical model reasonably reproduces the experimental data. We note that the effect of temperature dependent dielectric function of silicon comes from two physical factors: the thermal phonon population and the temperature-variation of the bandgap.

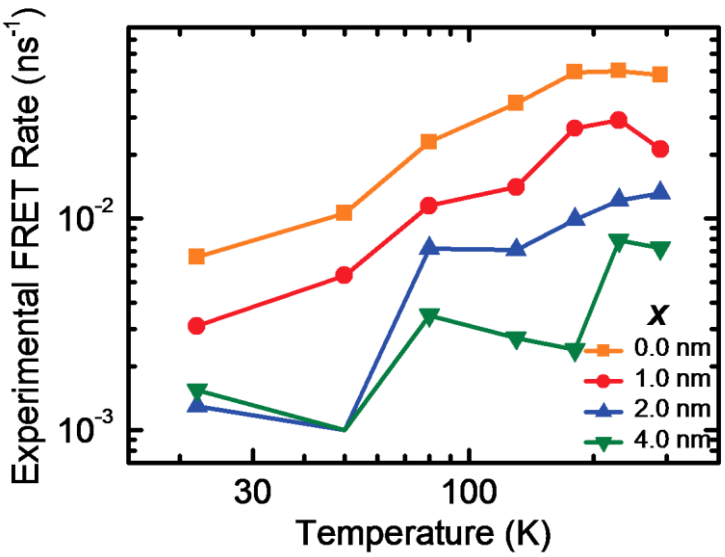

Figure 3.9. Experimental FRET rates as a function of temperature. Orange squares correspond to the FRET without Al_2O_3. Red circles correspond to the FRET for 1.0 nm Al_2O_3 thickness. Blue up-triangles correspond to the FRET for 2.0 nm Al_2O_3 thickness. Green down-triangles correspond to the FRET for 4.0 nm Al_2O_3 thickness. The FRET rates in this graph were obtained taking the modified reference rates into account.

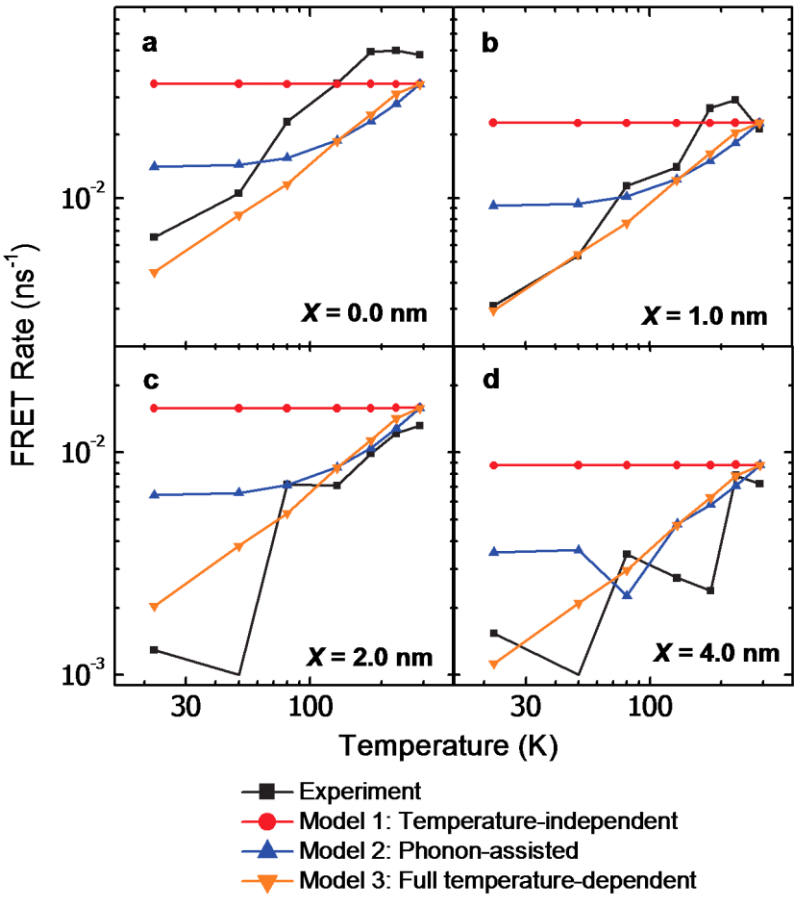

Figure 3.10. Energy transfer rates as a function of the temperature for each case: Al_2O_3 thickness of 0.0, 1.0, 2.0 and 4.0 nm. Black squares correspond to the experimental data. Red circles represent the FRET without phonon assistance, blue up-triangles include phonon assistance, orange down-triangles both consider the phonon assistance and temperature dependent QY change of the CQDs.

As an additional study, we examined the phonon assistance to NRET from CQDs into silicon with increasing temperature, by performing TRF measurements at temperatures higher than the room temperature. To this end, we prepared and employed a new sample without using alumina spacer. For the experimental characterization, we worked in the range of the elevated temperatures possible in our time-resolved setup. Here we observed that NRET process becomes more efficient going from 290 to 370 K as presented as a function of temperature in Figure 3.11. The

observed increase in this temperature range is attributed to enhancement of the phonon-assisted inter-band transitions in silicon owing to occupation of the phonon modes in silicon even if the PL QY of the CQDs is expected to be comparatively reduced due to the thermal droop. Therefore, the net observed result is that the phonon-assisted enhancement in inter-band transitions in silicon is strong enough and enhances NRET with increasing temperature in spite of various adverse effects there might be in the studied temperature range. This finding indicates the technological importance of the phonon assistance in the optical sensitization in silicon devices and may open up new possibilities for enhanced silicon photonics including photovoltaics and photodetectors.

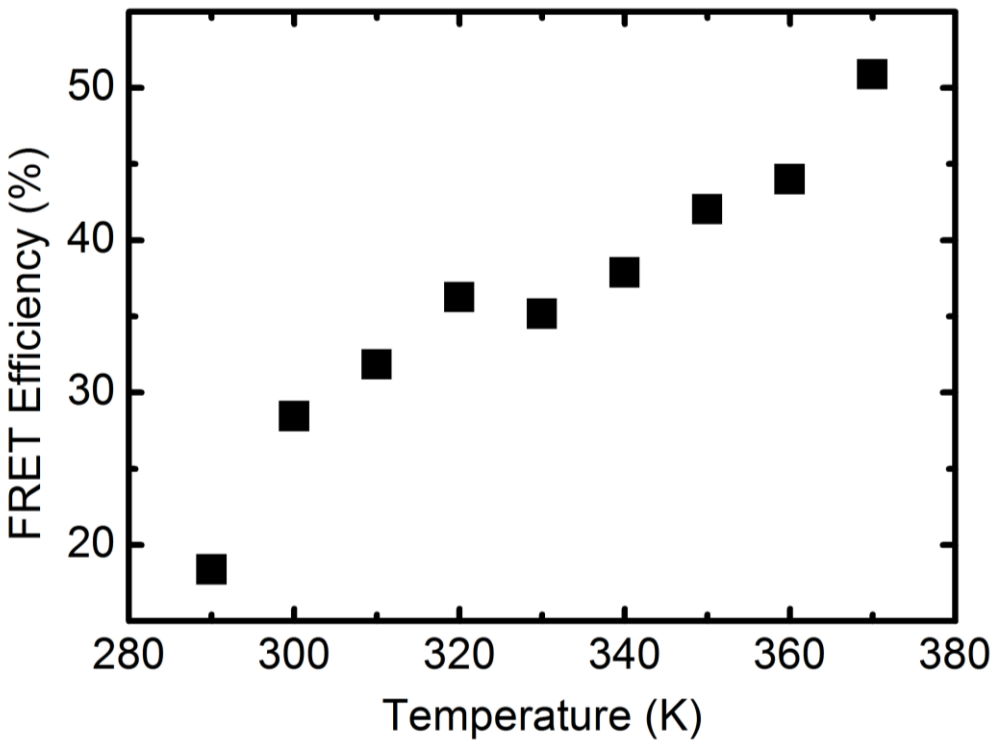

Figure 3.11. FRET efficiency as a function of the temperature in the range of 290 – 370 K.

3.1.4 Summary

In summary, we presented and analyzed the temperature-dependent fluorescence lifetimes and energy transfer efficiencies in hybrid CQD-silicon nanostructures to reveal dynamics of the FRET based on the phonon assistance for the absorption process. To study systematically the underlying physics behind FRET, we utilized the CQD-silicon nanostructure platforms with varying separation thicknesses between the donor CQDs and the acceptor silicon. Our experimental data showed that FRET from the CQDs into silicon substrates becomes weaker at low temperatures, which is attributed to the phonon involved interband transitions in silicon. To explain these experimental measurements, we first developed a temperature independent analytical model using dipole-dipole interaction, leading to $\propto d^{-3}$ distance dependence and then suggested a modified physical model introducing temperature effects based on phonon-assisted absorption into this analytical model as a semiemprical approach. The model proves to be successful in analyzing and explaining temperature dependence, leading to reasonably well matching results with the experimental data. In addition, full temperature dependent model, which also takes temperature dependent QY changes of the donor CQDs into account, is presented to improve the match between the theory and the experiments. Therefore, these findings indicate the assistance of phonons in FRET for the case of indirect bandgap acceptor such as silicon as the phonon assists for the case of optical absorption.

3.2 Enhancement of excitonic nonradiative energy transfer into bulk silicon with the hybridization of cascaded quantum dots

This section is based on the publication "Excitonic Enhancement of Nonradiative Energy Transfer to Bulk Silicon with the Hybridization of Cascaded Quantum Dots," **A. Yeltik**, B. Guzelturk, P. L. Hernandez-Martinez, S. Akhavan and H. V. Demir, Appl. Phys. Lett. 103, 261103 (2013). Adapted (or "Reproduced") with permission from American Chemical Society. Copyright 2013 AIP Publishing.

3.2.1 Motivation

Previously, a monolayer of single type of CQDs was employed to realize nonradiative sensitization of Si [156]. In the previous section, we show that this type of NRET is phonon-assisted process unlike conventional NRET systems of both fluorescent donor and acceptor [155]. Since Si is an indirect bandgap material, phonon-assistance is required to realize nonradiative transfer of the excitation energy in the near-field. However, these types of CQD-sensitized Si systems were always limited to a single type of CQD donor. Alternatively, it has been reported that excitonic energy transfer among the CQDs can be boosted using multilayer of CQD structures with different sizes, which enables the energy gradient useful for exciton funneling [214]–[216]. Using this exciton funneling, photoluminescence enhancement was achieved via inter-CQD NRET in an energy-gradient structure [215]. Such multi-layered CQD solids were also used as an efficient platform for enhanced exciton transfer from an epitaxial quantum well to the gradient-CQD bilayer [34]. Lee et al. demonstrated a cascaded-NRET scheme to boost the absorption of CdTe nanowires *via* green and yellow CdTe CQDs [211]. A remarkable NRET from the outer-layer CdTe CQDs into CdTe nanowires using chemical linkers was observed in their structures, resulting in a 4-fold luminescence enhancement of the nanowires. All these results indicate the great

potential of these energy-channeling composite systems for the enhancement of exciton population in a luminescent acceptor.

Here, we proposed and demonstrated enhanced sensitization of silicon by using energy gradient layers of cascaded CQDs without any need to chemical linkers between CQDs. To this end, we used the energy-gradient structure composed of a hybrid bilayered construct of green- and red-emitting CdTe CQDs (GQDs and RQDs, respectively) on bulk Si. Dynamics of NRET from the CQDs into Si ($NRET_{CQD \rightarrow Si}$) for such a cascaded structure with two types of CQDs were investigated and compared to those for the structures with mono-dispersed CQDs. Here, we found substantially enhanced $NRET_{CQD \rightarrow Si}$ using Si with the energy-gradient structure as compared to the mono-dispersed CQD structures, which suggests the increased exciton population of the CQDs closer to Si in the energy-gradient structure. Energy-gradient structure enables the migration of a favorably greater number of excitons from GQDs into RQDs to transfer into Si, which leads to the improved sensitization in addition to enhanced overall NRET efficiency. Resultant significant enhancement of exciton population in Si offers an advantageous route for sensitization of Si *via* NRET, which was previously limited to mono-dispersed and single monolayer cases.

3.2.2 Experiment and theory

In this study, CdTe GQDs and RQDs were synthesized with the respective radii of 1.29 and 1.86 nm, according to the procedure reported by Rogach et al. [217]. We prepared hybrid nanostructures by using layer-by-layer (LBL) deposition technique. The LBL deposition procedure relies on alternatingly adsorbing of oppositely charged species, i.e, positively and negatively charged polyelectrolyte pairs. Negatively charged CdTe CQDs were deposited on silicon substrates by using a fully computerized dip-coater system. We used poly(diallyldimethylammonium chloride) (positive polyelectrolyte) and poly(sodium 4-styrenesulfonate) (negative polyelectrolyte) for the positive-negative-positive alternating polymer layer to achieve uniform CQD monolayers. The concentrations of these polyelectrolytes were 2 mg/mL in 0.1 M NaCl solution, which helps the polymer chain relax on the surface. LBL coating was performed using a

cyclic procedure: (1) dipping of silicon wafer into a PDDA solution for 4 min, (2) rinsing it with water for 1 min, (3) dipping it into a PSS solution for 4 min, (4) rinsing it with water for 1 min, (5) dipping it into a PDDA solution for 4 min, (6) rinsing it with water for 1 min, (7) dipping it into the red-emitting CQDs solution for 20 min, (8) rinsing it with water for 1 min, (9) following the same steps again from 1 to 6, (10) dipping it into a green-emitting CQDs solution for 20 min or, a red-emitting CQDs solution for 20 min (control sample), and (11) rinsing it with water for 1 min.

Following the LbL-deposition, samples were kept for 3.5 h in a glovebox for the complete drying and place in a dark environment to prevent photodegradation. Figure 3.12a illustrates the generic architecture of the samples consisting of cascaded GQD and RQD bilayer separated by consecutive adsorption of poly(diallyldimethylammonium chloride) (PDDA) and poly(sodium 4-styrenesulfonate) (PSS) polyelectrolytes. Here, the PDDA-PSS-PDDA stack has a thickness of ~2.2 nm and suppresses charge transport. Si substrate possesses approximately 1.7 nm thick native oxide on the top, as verified by ellipsometry measurement. In addition, Figure 3.12b depicts the emission and absorption spectra of GQDs and RQDs along with the absorption spectrum of bulk Si to illustrate the strong spectral overlap between the CQDs and Si, which is required to realize NRET.

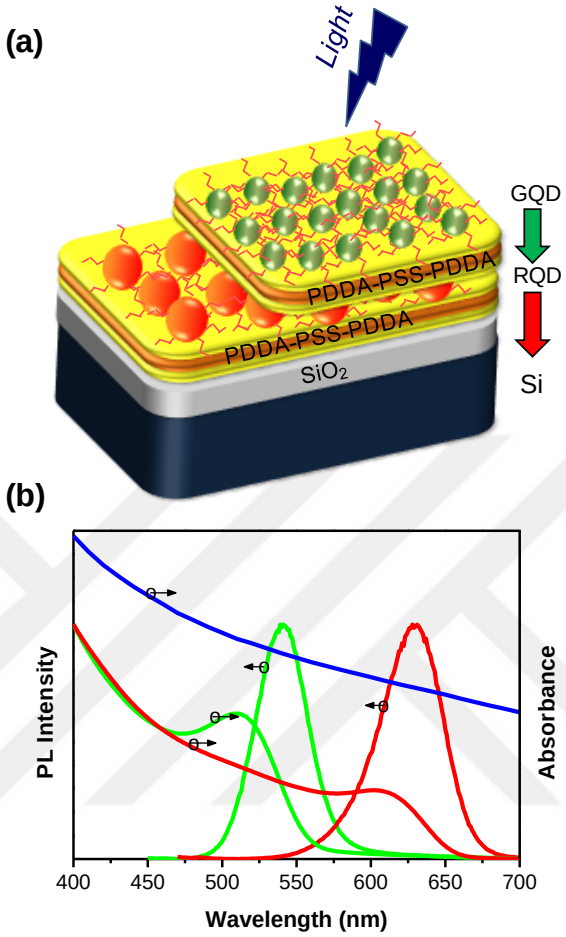

Figure 3.12. (a) Schematic for the gradient energy transfer from the cascaded GQD/RQD bilayer into bulk Si. (b) Emission and absorption spectra of CdTe GQDs and CdTe RQDs (green and red curves, respectively), and absorption spectrum of bulk Si (blue curve).

To assess the NRET among CQDs ($NRET_{GQD \rightarrow RQD}$) and $NRET_{CQD \rightarrow Si}$, fluorescence decays of the CQDs were recorded at room temperature by time resolved fluorescence (TRF) spectroscopy (PicoQuant FluoTime 200) with a pulsed laser at 375 nm as the excitation source. We prepared six different samples for a systematic study: (1) RQD/RQD/quartz, (2) GQD/GQD/quartz, (3) GQD/RQD/quartz, (4) RQD/RQD/Si, (5) GQD/GQD/Si, and (6) GQD/RQD/Si. For these structures, we investigated the emission dynamics of GQDs and RQDs recorded at their solid-state film peak emission

wavelengths of 535 and 640 nm, respectively. Due to the finite temporal response of the pulsed laser system, the decays were deconvoluted with the instrument response function. TRF decays were analyzed by 1/e fitting and lifetimes were obtained via amplitude-averaging of multi-exponentials (χ^2 ~ 1). Samples (1), (2) and (3) are the references. However, quantum mechanically, a dipole nearby a different refractive index medium alters its radiative recombination dynamics. Therefore, the lifetimes are corrected in the case of quartz references considering the theory by Novotny and Hecht [200]. In the lifetime analysis, $NRET_{CQD \rightarrow Si}$ rates were calculated using the expression $\gamma_{NRET_{QD->Si}} = \gamma_{hybrid_{QD,Si}} - \gamma_{ref\,(corrected)_{QD,Quartz}}$, where $\gamma_{hybrid_{QD,Si}}$ = $1/\tau_{\mathrm{hybrid}CQD,Si}$ is the excited state relaxation rate of either GQDs or RQDs in the hybrid structure and $\gamma_{ref\,(corrected)}$ = $1/\tau_{\mathrm{ref(corrected)}CQD,Quartz}$ is the recombination rate of the CQDs in the quartz reference sample, where there is no NRET into the bulk-substrate. Efficiency of $NRET_{CQD \rightarrow Si}$ was found using the relation $\eta = \dfrac{\gamma_{NRET_{QD->Si}}}{(\gamma_{NRET_{QD->Si}} + \gamma_{ref\,(corrected)_{QD,Quartz}})}$.

The excitonic energy transfer in the CQD-Si nanostructure was also modeled considering the properties of individual CdTe CQDs and the bulk Si. The relevant parameters included for this model are the exciton recombination rate, $\gamma_\alpha = 1/\tau_\alpha$; the sublevel relaxation rate, Γ_α; and the interaction rate, U_{ij}. Here, τ_α is the intrinsic exciton lifetime and α denotes the type of CQDs, which are green-emitting quantum dot, (CQD_G); red-emitting quantum dot, (CQD_R); and bulk Si. We start with our theoretical analysis and numerical results for the excitation transfer in the case of a bilayered of red(green)-emitting CQDs (Case 1: $QD_{R\,G} \rightarrow QD_{R\,G} \rightarrow Si$) and then continue with the case of a cascaded bilayered of green-emitting CQDs and red-emitting CQDs (Case 2: $QD_G \rightarrow QD_R \rightarrow Si$).

Case A: $QD_{R\ G} \rightarrow QD_{R\ G} \rightarrow Si$

In this section, we consider the excitation energy transfer between a bilayer of red (green)-emitting CQDs and bulk Si. We start with ρ^{AB} as the density matrix corresponding to the energy level E_1 (Figure 3.13.), then the master equation is given by

$$\frac{\partial \rho^{AB}}{\partial t} = -\frac{i}{\hbar}\left[V_{AB}, \rho^{AB}\right] - N_{\Gamma}^{AB}\rho^{AB} + \rho^{AB}N_{\Gamma}^{AB} \tag{3.39}$$

where N_{Γ}^{AB} is a diagonal matrix whose diagonal elements are γ_{α} and Γ_{α}. V_{AB} is the interaction between levels with energy $E_1 = \hbar U_{QD_1 \rightarrow QD_2}$. The master equation, corresponding to the density matrix ρ^{BC} with energy E_1, can be written as

$$\frac{\partial \rho^{BC}}{\partial t} = -\frac{i}{\hbar}\left[V_{BC}, \rho^{BC}\right] - N_{\Gamma}^{BC}\rho^{BC} + \rho^{BC}N_{\Gamma}^{BC} + P_{AB}\left[\rho^{AB}\right] \tag{3.40}$$

where $P_{AB}\left[\rho^{AB}\right]$ represents the excitons coming from CQD_1 to CQD_2; $V_{BC} = \hbar U_{QD_2 \rightarrow Si}$ and N_{Γ}^{BC} are defined similar to Eq. 3.39. Finally, the master equation for bulk Si with energy E_2 is given by

$$\frac{\partial \rho^{C}}{\partial t} = - N_{\Gamma}^{C}\rho^{C} + \rho^{C}N_{\Gamma}^{C} + P_{BC}\left[\rho^{BC}\right] \tag{3.41}$$

where $P_{BC}\left[\rho^{BC}\right]$ represents the relaxation from the energy level E_1 to E_2; and N_{Γ}^{C} is a diagonal matrix with matrix elements γ_{α}. The corresponding matrices for Eq.s 3.39, 3.40, and 3.41 are extracted with the help of Figure 3.13. and they are shown below.

$$\rho^{AB} = \begin{pmatrix} \rho_{11}^{AB} & \rho_{12}^{AB} \\ \rho_{21}^{AB} & \rho_{22}^{AB} \end{pmatrix} \qquad \rho^{BC} = \begin{pmatrix} \rho_{11}^{BC} & \rho_{12}^{BC} \\ \rho_{21}^{BC} & \rho_{22}^{BC} \end{pmatrix} \qquad \rho^{C} = \begin{pmatrix} \rho_{11}^{C} & 0 \\ 0 & 0 \end{pmatrix}$$

$$V_{AB} = \hbar \begin{pmatrix} 0 & U_{QD_1 \to QD_2} \\ U_{QD_1 \to QD_2} & 0 \end{pmatrix} \qquad V_{23} = \hbar \begin{pmatrix} 0 & U_{QD_2 \to Si} \\ U_{QD_2 \to Si} & 0 \end{pmatrix} \tag{3.42}$$

$$N_{\Gamma}^{AB} = \frac{1}{2} \begin{pmatrix} \gamma_{QD1} & 0 \\ 0 & \gamma_{QD2} \end{pmatrix} \qquad N_{\Gamma}^{BC} = \frac{1}{2} \begin{pmatrix} \gamma_{QD2} & 0 \\ 0 & \Gamma_{Si} \end{pmatrix} \qquad N_{\Gamma}^{C} = \frac{1}{2} \begin{pmatrix} \gamma_{Si} & 0 \\ 0 & 0 \end{pmatrix}$$

$$P_{AB}\left[\rho^{AB}\right] = \begin{pmatrix} \gamma_{QD2}\rho_{22}^{AB} & 0 \\ 0 & 0 \end{pmatrix} \qquad P_{BC}\left[\rho^{BC}\right] = \begin{pmatrix} \Gamma_{Si}\rho_{22}^{BC} & 0 \\ 0 & 0 \end{pmatrix}$$

where ρ_{11}^{AB} represents the exciton population of the first excited state in the first CQD layer, ρ_{22}^{AB} is the exciton population of the first excited state of the second CQD layer; ρ_{11}^{BC} represents the exciton population of the first excited state in the second CQD layer; ρ_{22}^{BC} is the exciton population of the second excited state of bulk Si; and ρ_{11}^{C} is the exciton population in the first excited state of bulk Si.

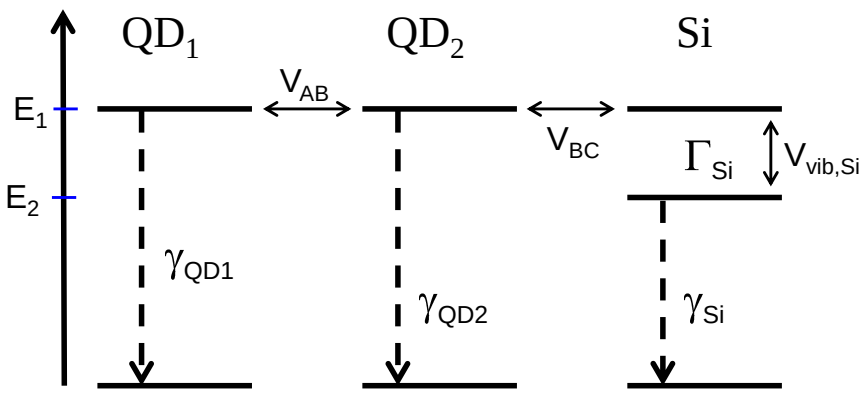

Figure 3.13. Energy diagram for the excitation transfer from a bilayer of red (green)-emitting CQDs to bulk Si. Horizontal arrows represent the interaction energy between the energy levels. Vertical arrow shows relaxation process between the excited levels. Dash vertical arrows depict the relaxation between the lowest excited state and ground state.

Case B: $QD_G \rightarrow QD_R \rightarrow Si$

Here, we consider the excitation transfer from a layer of green-emitting CQDs and a second layer of red-emitting CQDs to bulk Si. Similar to the previous case, ρ^{AB} is the density matrix corresponding to the energy level E_1 (Figure 3.14). Thus, the master equation is given by

$$\frac{\partial \rho^{AB}}{\partial t} = -\frac{i}{\hbar}\left[V_{AB}, \rho^{AB}\right] - N_{\Gamma}^{AB}\rho^{AB} + \rho^{AB}N_{\Gamma}^{AB} \tag{3.43}$$

where N_{Γ}^{AB} is a diagonal matrix with diagonal elements of γ_{α} and Γ_{α}. V_{AB} is the interaction between levels with energy $E_1 = \hbar U_{QD_1 \rightarrow QD_2}$. The master equation, corresponding to the density matrix ρ^{BC} with energy E_2, can be written as

$$\frac{\partial \rho^{BC}}{\partial t} = -\frac{i}{\hbar}\left[V_{BC}, \rho^{BC}\right] - N_{\Gamma}^{BC}\rho^{BC} + \rho^{BC}N_{\Gamma}^{BC} + P_{AB}\left[\rho^{AB}\right] \tag{3.44}$$

where $P_{AB}\left[\rho^{AB}\right]$ represents the relaxation form the energy level E_1 to E_2; $V_{BC} = \hbar U_{QD_2 \rightarrow Si}$ and N_{Γ}^{BC} are defined similar to Eq. 3.43. Finally, the master equation for the density matrix ρ^{C} with energy E_3 is written as

$$\frac{\partial \rho^{C}}{\partial t} = - N_{\Gamma}^{C}\rho^{C} + \rho^{C}N_{\Gamma}^{C} + P_{BC}\left[\rho^{BC}\right] \tag{3.45}$$

where $P_{BC}\left[\rho^{BC}\right]$ represents the relaxation from the energy level E_2 to E_3; and N_{Γ}^{C} is a diagonal matrix with matrix elements γ_{α}. The corresponding matrices for Eq.s 3.43, 3.44, and 3.45 are extracted with the help of Figure 3.14 and they are shown below.

$$\rho^{AB} = \begin{pmatrix} \rho_{11}^{AB} & \rho_{12}^{AB} \\ \rho_{21}^{AB} & \rho_{22}^{AB} \end{pmatrix} \qquad \rho^{BC} = \begin{pmatrix} \rho_{11}^{BC} & \rho_{12}^{BC} \\ \rho_{21}^{BC} & \rho_{22}^{BC} \end{pmatrix} \qquad \rho^{C} = \begin{pmatrix} \rho_{11}^{C} & 0 \\ 0 & 0 \end{pmatrix}$$

$$V_{AB} = \hbar \begin{pmatrix} 0 & U_{QD_1 \to QD_2} \\ U_{QD_1 \to QD_2} & 0 \end{pmatrix} \qquad V_{23} = \hbar \begin{pmatrix} 0 & U_{QD_2 \to Si} \\ U_{QD_2 \to Si} & 0 \end{pmatrix} \tag{3.46}$$

$$N_{\Gamma}^{AB} = \frac{1}{2} \begin{pmatrix} \gamma_{QD1} & 0 \\ 0 & \Gamma_{QD2} \end{pmatrix} \qquad N_{\Gamma}^{BC} = \frac{1}{2} \begin{pmatrix} \gamma_{QD2} & 0 \\ 0 & \Gamma_{Si} \end{pmatrix} \qquad N_{\Gamma}^{C} = \frac{1}{2} \begin{pmatrix} \gamma_{Si} & 0 \\ 0 & 0 \end{pmatrix}$$

$$P_{AB}\left[\rho^{AB}\right] = \begin{pmatrix} \Gamma_{QD2}\rho_{22}^{AB} & 0 \\ 0 & 0 \end{pmatrix} \qquad P_{BC}\left[\rho^{BC}\right] = \begin{pmatrix} \Gamma_{Si}\rho_{22}^{BC} & 0 \\ 0 & 0 \end{pmatrix}$$

ρ_{11}^{AB} represents the exciton population of the first excited state in the first CQD layer, ρ_{22}^{AB} is the exciton population of the second excited state of the second CQD layer; ρ_{11}^{BC} represents the exciton population of the first excited state in the second CQD layer; ρ_{22}^{BC} is the exciton population of the second excited state of bulk Si; and ρ_{11}^{C} is the exciton population in the first excited state of bulk Si.

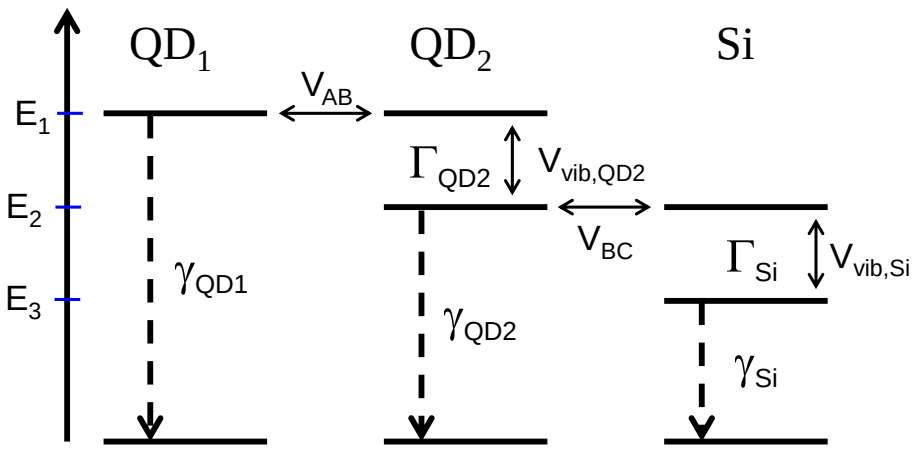

Figure 3.14. Energy diagram for the excitation transfer from a layer of green-emitting CQDs and a layer of red-emitting CQDs to bulk Si. Horizontal arrows represent the interaction energy between the energy levels. Vertical arrows show relaxation process between the excited levels. Dash vertical arrows depict the relaxation between the lowest excited state and ground state.

Here, we computed the exciton population for the complexes (Case A and B) described in the previous section. The experimental lifetimes for the samples on top of quartz and on top of silicon are shown in Table 3.3. The parameter use to calculate the exciton population are: $\gamma_G = \frac{1}{0.444\ ns}$, $\gamma_R = \frac{1}{1.763\ ns}$, and $\gamma_{Si} = \frac{1}{1\ ms}$. The interaction rate between CQDs was taken from ref [218] and [34] as $U_{QD_1 \to QD_2} = \frac{1}{100\ ns}$. The CQD and Si relaxation rates were assumed to be $\Gamma_{QD} = \frac{1}{20\ ps}$ and $\Gamma_{Si} = \frac{1}{2\ ps}$, which are reasonable values found in the literature [219], [220]. And, finally, the CdTe CQD to Si interaction rate was taken as $U_{QD_2 \to Si} = \frac{1}{437\ ns}$. This values was estimated by the difference between rate of CQD_R-CQD_R on Silicon and CQD_R-CQD_R on quartz $U_{QD_2 \to Si} \approx \frac{1}{0.35\ ns} - \frac{1}{1.763\ ns}$.

The exciton population for the following cases: (1) $QD_G \to QD_R \to Si$; (2) $QD_R \to QD_R \to Si$; and (3) $QD_G \to QD_G \to Si$ are shown in Figure 3.15. As we can see, the best case for exciton transfer is given by Case (1) where the exciton is cascaded from the green to the red CQD and finally to Si. The worst case corresponds to Case (3) where the exciton is transfer from the green CQD in the first layer to the green CQD in the second layer and finally to Si.

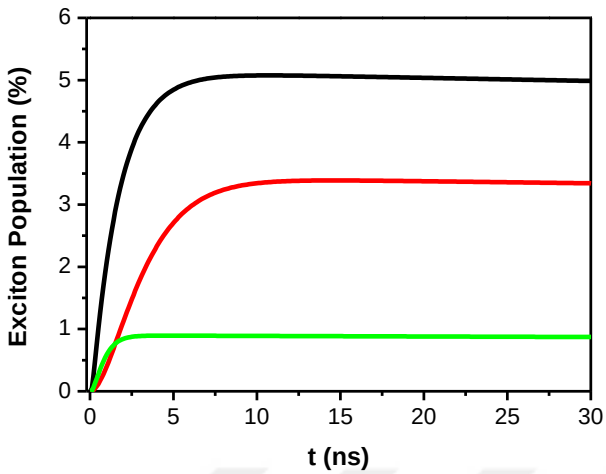

Figure 3.15. Exciton population (in %) for the cases of: (1) $QD_G \rightarrow QD_R \rightarrow Si$ (black curve); (2) $QD_R \rightarrow QD_R \rightarrow Si$ (red curve); and (3) $QD_G \rightarrow QD_G \rightarrow Si$ (green curve).

To compare relative exciton population for all cases we define an enhancement (E) and quenching (Q) factor as

$$E = \frac{\left| \rho_{XY}^{Si}\ t - \rho_{XX}^{Si}\ t \right|}{\rho_{XX}^{Si}\ t} \tag{3.47}$$

$$Q = \frac{\left| \rho_{XY}^{Si}\ t - \rho_{XX}^{Si}\ t \right|}{\rho_{XY}^{Si}\ t} \tag{3.48}$$

where $\rho_{XY}^{Si}\ t$ is the exciton population in Si as a function of time. XY and XX stand for the relative case: (1) $QD_G \rightarrow QD_R \rightarrow Si$ vs. $QD_R \rightarrow QD_R \rightarrow Si$; (2) $QD_G \rightarrow QD_R \rightarrow Si$ vs. $QD_G \rightarrow QD_G \rightarrow Si$; and (3) $QD_R \rightarrow QD_R \rightarrow Si$ vs. $QD_G \rightarrow QD_G \rightarrow Si$. Figure 3.16, Figure 3.17 and Figure 3.18 show the enhancement and quenching factors of excitonic population in Si for the relative Case (1), (2), and (3), respectively. From these figures, it is observed that the exciton population

decreases by 70%, 15%, and 25%, respectively. From Figure 3.16, we can infer that the number of exciton between these cases is comparable, however the number of exciton on $QD_G \rightarrow QD_R \rightarrow Si$ is larger than $QD_R \rightarrow QD_R \rightarrow Si$. For the Case (2) (Figure 3.17), it is seen that the number of exciton on $QD_G \rightarrow QD_G \rightarrow Si$ is much smaller than $QD_G \rightarrow QD_R \rightarrow Si$ leading to a small quenching factor. Finally, the Case (3) (Figure 3.18) shows that relative exciton population when there is no energy difference between CQDs, that is the CQD layers have the same CQD (either red or green emitters only). Here, the number of exciton on $QD_R \rightarrow QD_R \rightarrow Si$ is larger than $QD_G \rightarrow QD_G \rightarrow Si$ though the quenching factor is not as small as Case (2). By comparing these 3 figures, we can conclude that the configuration with the larger number of exciton is given by $QD_G \rightarrow QD_R \rightarrow Si$, following by $QD_R \rightarrow QD_R \rightarrow Si$, and finally $QD_G \rightarrow QD_G \rightarrow Si$.

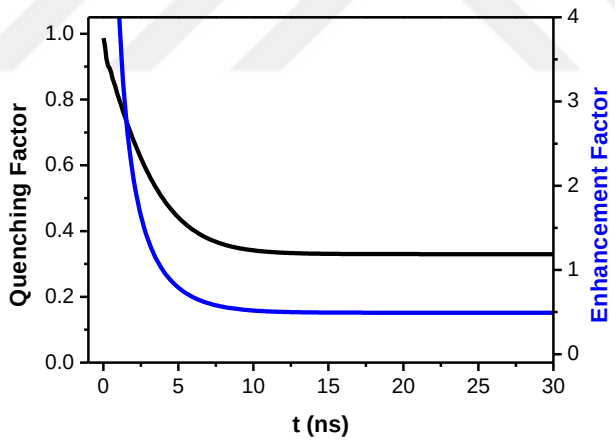

Figure 3.16. Excitonic quenching factor (left) and enhancement factor (right) as a function of time for the relative case 1.

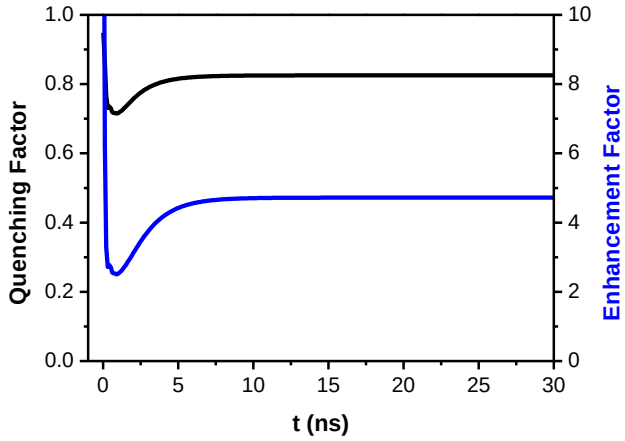

Figure 3.17. Excitonic quenching factor (left) and enhancement factor (right) as a function of time for the relative case 2.

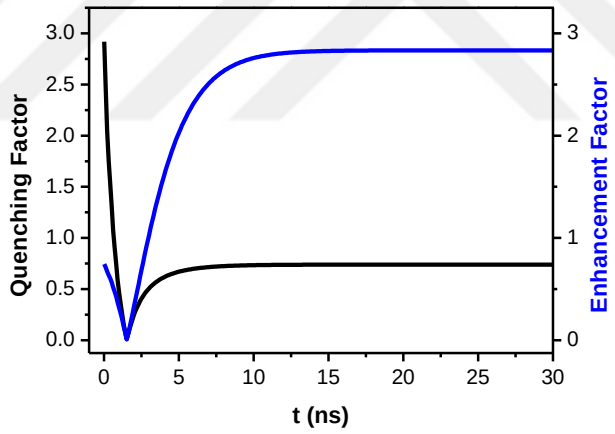

Figure 3.18. Excitonic quenching factor (left) and enhancement factor (right) as a function of time for the relative case 3.

3.2.3 Results and discussion

In this study, exciton transfer dynamics of GQDs bilayer (GQD/GQD/Si) and cascaded bilayer on Si (GQD/RQD/Si), and their control groups on quartz (GQD/GQD/quartz and GQD/RQD/quartz) were investigated. As depicted in Figure 3.19, we observed

faster decays for the GQD/GQD/Si and GQD/RQD/Si samples as compared to their respective control groups, which is an indication of NRET from the CQDs into Si. Moreover, $NRET_{GQD \rightarrow Si}$ efficiency of 20% for the exciton migration from the GQDs into Si was calculated by using the lifetimes measured for the GQD/GQD/Si and GQD/GQD/quartz structures at 535 nm. All the TRF lifetimes are presented in Table 3.3. A considerable amount of exciton migration exists from GQD into RQD (with an NRET efficiency of 24%) calculated by using the rates for the GQD/RQD/quartz and GQD/GQD/quartz structures. Furthermore, exciton population inside the GQDs decays faster for the GQD/RQD/Si sample as compared to that for the GQD/GQD/Si sample and this indicates an enhanced NRET as a result of the funneling effect in the cascaded structure.

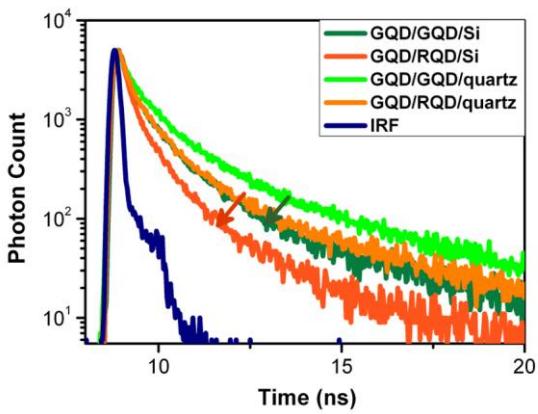

Figure 3.19. TRF spectroscopy at 535 nm from the bilayer integration of GQDs on Si (dark green solid line), GQD/RQD on Si (dark orange solid line), GQDs on quartz (green solid line), GQD/RQD on quartz (orange solid line), and the laser diode response function (navy solid line).

Table 3.3. Fluorescence lifetimes for the CQDs on quartz as the reference sample (corrected for refractive index variation) and on Si.

GQD/GQD/quartz at 535 nm	RQD/RQD/quartz at 640 nm	GQD/RQD/quartz at 535 nm	GQD/RQD/quartz at 640 nm
0.444 ns	1.763 ns	0.338 ns	2.262 ns
GQD/GQD/Si at 535 nm	RQD/RQD/Si at 640 nm	GQD/RQD/Si at 535 nm	GQD/RQD/Si at 640 nm
0.363 ns	0.350 ns	0.263 ns	0.707 ns

In order to verify the gradient exciton feeding from the cascaded bilayered of differently sized CQDs into Si, we further investigated the exciton transfer dynamics of the donor CQDs at the RQD emission wavelength in detail. TRF decay curves of RQD/RQD/Si, GQD/RQD/Si and their respective control groups on quartz substrates are presented in Figure 3.20. We obtained $NRET_{RQD \rightarrow Si}$ efficiency of 80% for the exciton migration from the RQDs into Si by using the lifetimes for the RQD/RQD/Si and RQD/RQD/quartz structures measured at 640 nm (Table 3.4). In the context of gradient energy feeding, we observed an increased RQD lifetime for the cascaded GQD/RQD/Si structure as compared to that for the RQD/RQD/Si sample. This is owing to the strong exciton migration into RQDs via $NRET_{GQD \rightarrow RQD}$, which is formed using the gradient energy feeding system resulting in higher exciton population in Si.

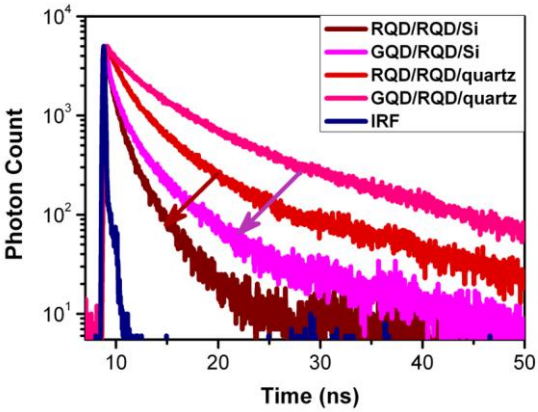

Figure 3.20. TRF spectroscopy at 640 nm from bilayer integration of RQDs on Si (wine solid line), GQD/RQD on Si (magenta solid line), RQDs on quartz (red solid line), GQD/RQD on quartz (pink solid line), and the laser diode response function (navy solid line).

To examine the experimentally observed NRET behaviors, relative exciton populations in Si were calculated by using the efficiencies extracted from the TRF rates. The GQD lifetime is shortened down to 0.263 ns in the GQD/RQD/Si structure, while it is measured to be 0.444 ns in the GQD/GQD/quartz structure as the reference sample (Table 3.4). By using these data, we estimated an exciton transfer rate of $\gamma_{NRET_{GQD->RQD}}$ = 1.550 ns^{-1} and the $NRET_{GQD \rightarrow RQD}$ efficiency is calculated to be around 41%. Based on this result and $NRET_{RQD \rightarrow Si}$ efficiency (80%), we found the exciton populations for the GQD/RQD/Si structure (Case 1) and RQD/RQD/Si structure (Case 2). Comparing the population levels with each other, the enhancement factor[221] for the exciton transfer into Si ((# of excitons for Case 1 - # of excitons for Case 2) / # of excitons for Case 2) was found to be ~40%. Moreover, the enhancement factor is ~450% when the exciton population for the GQD/RQD/Si structure is compared with the exciton population for the GQD/GQD/Si structure. This relatively huge factor probably stems from the efficient use of the trapped excitons in surface states of the GQDs, which have more trap states at the surface resulting from the synthesis process [214]. Both of these results (~40% and ~450%) remain approximately the same when

we calculate the population for the GQD/RQD/Si structure using $NRET_{GQD \rightarrow RQD}$ efficiency of 24% and $NRET_{RQD \rightarrow Si}$ efficiency of 80%.

To further investigate the importance of energy gradient for $NRET_{CQD \rightarrow Si}$, we also analyzed the decay curves from the GQD/GQD/Si sample, which has a slower GQD exciton population decay than its cascaded structure (Figure 3.19). In this configuration, the TRF lifetime is measured to be 0.363 ns (Table 3.4). Weaker exciton transfer with a lower rate of $\gamma_{NRET_{GQD->Si}}$ = 0.503 ns^{-1} is calculated using the GQD/GQD/quartz structure as the reference, and a smaller $NRET_{GQD \rightarrow Si}$ efficiency (18%) is observed as compared to the energy gradient structure ($NRET_{GQD \rightarrow RQD}$ = 41%). In the case of employing the cascaded structure, it is therefore possible to boost this exciton funneling owing to the better utilization of the excitons in the CQD layer via directed exciton transfer.

Furthermore, a theoretical study was performed to investigate the exciton populations in Si as a result of the $NRET_{CQD \rightarrow Si}$ process. For this purpose, we used a model based on density matrix formulation of near-field interactions. The master equations corresponding to the density matrices are derived as

$$\frac{\partial \rho^{AB}}{\partial t} = -\frac{i}{\hbar}\left[V_{AB}, \rho^{AB}\right] - N_{\Gamma}^{AB}\rho^{AB} + \rho^{AB}N_{\Gamma}^{AB} \tag{3.49}$$

$$\frac{\partial \rho^{BC}}{\partial t} = -\frac{i}{\hbar}\left[V_{BC}, \rho^{BC}\right] - N_{\Gamma}^{BC}\rho^{BC} + \rho^{BC}N_{\Gamma}^{BC} + P_{AB}\left[\rho^{AB}\right] \tag{3.50}$$

$$\frac{\partial \rho^{C}}{\partial t} = - N_{\Gamma}^{C}\rho^{C} + \rho^{C}N_{\Gamma}^{C} + P_{BC}\left[\rho^{BC}\right] \tag{3.51}$$

where ρ^{AB}, ρ^{BC}, and ρ^{C} represent the density matrices with the energy level E_1, E_2 and E_3, respectively (Figure 3.21b inset). Herein, $V_{AB} = \hbar U_{QD_1 \rightarrow QD_2}$ is the interaction between the levels with energy E_1 of the top CQD layer (CQD_1) and the bottom CQD

layer (CQD_2); $V_{BC} = \hbar U_{QD_2 \to Si}$ is the interaction between levels with energy E_2; N_Γ^{AB}, N_Γ^{BC}, and N_Γ^{C} are the diagonal matrices whose diagonal elements are given by γ_α and Γ_α; $P_{AB}\left[\rho^{AB}\right]$ represents the relaxation from the energy level E_1 to E_2; and $P_{BC}\left[\rho^{BC}\right]$ represents the relaxation from the energy level E_2 to E_3 [221]. Excitonic relaxation rates for the GQDs and RQDs were obtained experimentally as $\gamma_{GQD} = \frac{1}{0.444\,ns}$ and $\gamma_{RQD} = \frac{1}{1.763\,ns}$, and, for Si, it was taken as $\gamma_{Si} = \frac{1}{1\,ms}$. The interaction rate between the CQDs was taken as $U_{QD_1 \to QD_2} = \frac{1}{100\,ns}$ [34], [218]. The CQD and Si relaxation rates were assumed to be $\Gamma_{QD} = \frac{1}{20\,ps}$ and $\Gamma_{Si} = \frac{1}{2\,ps}$, which are reasonable values present in the literature [219], [220]. Finally, for the interaction rate between the CQD and Si, we used $U_{QD_2 \to Si} = \frac{1}{437\,ns}$. Figure 3.21a shows the exciton population (in %) for the cases of: (1) $GQD \to RQD \to Si$; (2) $RQD \to RQD \to Si$; and (3) $GQD \to GQD \to Si$. As it is shown, the best case for exciton transfer is given by Case 1, where the exciton transfer is cascaded from the GQD into the RQD and, at the end, into Si. The worst case corresponds to Case 3, where the exciton is transferred from the GQD in the first layer into the GQD in the second layer and, finally, into Si. The relative decrease in the exciton population for Case 1 with respect to Case 2 ((# of excitons for Case 1 - # of excitons for Case 2) / # of excitons for Case 1) is given in Figure 3.21b as the quenching factor (Eq. 3.48). The enhancement factor for Case 1 with respect to Case 2 is also depicted in Figure 3.21b. As given in this figure, the enhancement factor reaches up to ~50% at the steady state condition, which is similar to the aforementioned experimental value of 40%. All in all, the theoretical model is in good agreement with the experimental results and all these findings offer a strong evidence for the formation of gradient energy transfer, which leads to higher exciton population inside Si.

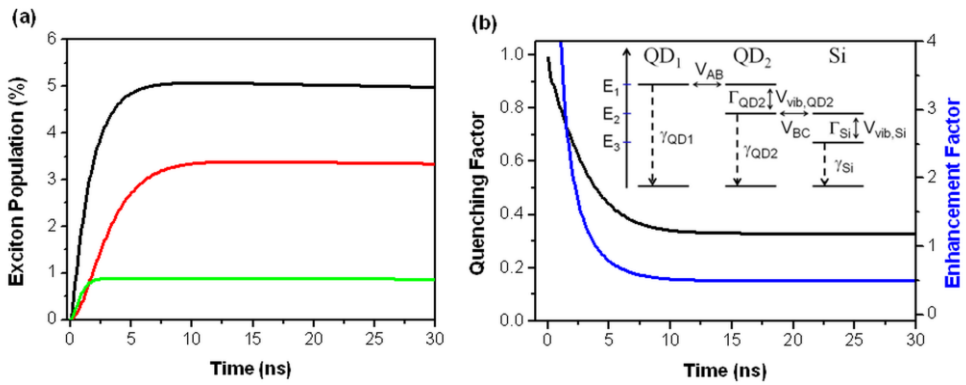

Figure 3.21. (a) Exciton population for the cases of: (1) $GQD \rightarrow RQD \rightarrow Si$ (black solid line); (2) $RQD \rightarrow RQD \rightarrow Si$ (red solid line); and (3) $GQD \rightarrow GQD \rightarrow Si$ (green solid line). (b) Excitonic quenching factor (left) and enhancement factor (right) as a function of time for Case 1 with respect to Case 2.

3.2.4 Summary

In summary, we demonstrated strong enhancement in the exciton population transferred into Si using the energy-gradient hybrid structures composed of cascaded bilayered green- and red-emitting CQDs on Si. NRET dynamics were investigated for the cascaded structure and the structures with mono-dispersed CQDs. For the cascaded architecture, exciton transfer efficiency of 41% from the GQDs into the RQDs and of 80% from the RQDs into Si was achieved at room temperature. As compared to the exciton population for the RQD/RQD/Si structure, the enhancement factor of exciton transfer into Si for the cascaded structure was found to be ~1.4 (40%), which is in good agreement with the theoretical results of ~1.5 (50%). All these findings suggest that the energy-gradient structures with hybridized CQDs on top of Si allow for high efficiency, which can be utilized in photovoltaic, photodetection and possibly other optoelectronic hybrid devices.

3.3 Evidence for nonradiative energy transfer from quantum dots into graphene-based nanomaterials and a short study including MoS_2

This section is based on the publication "Evidence for Nonradiative Energy Transfer in Graphene-Oxide-Based Hybrid Structures," **A. Yeltik**, G. Kucukayan-Dogu, B. Guzelturk, S. Fardindoost, Y. Kelestemur and H. V. Demir, J. Phys. Chem. C 117, 25298-25304 (2013). Adapted (or "Reproduced") with permission from American Chemical Society. Copyright 2013 American Chemical Society.

3.3.1 Motivation

Graphene, two-dimensional honeycomb structure of carbon atoms, has become a subject of great interest due to its unique optical and electronic properties [105]. Despite its one-atom-thick nature, optical absorbance of graphene is ~2.3 % over a broad photonic energy spectrum above 0.5 eV (significantly in visible and infrared region), which originates from its linear energy dispersion near the Fermi level and its zero band gap structure [222], [223]. As compared to other materials, graphene provides significantly large surface area (2630 m^2g^{-1}) [93] and high intrinsic room-temperature mobility (up to 250,000 $cm^2V^{-1}s^{-1}$) [224]. These properties make graphene promising for optoelectronic applications [97]. Additionally, graphene is shown to be a good exciton (electron – hole pair) sink due to highly efficient nonradiative energy transfer (NRET) from the near-by fluorescent nanostructures through dipole-dipole coupling, which is also known as Förster-type resonant energy transfer (FRET) [118], [124]. For this type of hybrid structures including a donor and an acceptor, non-excitonic NRET mechanisms are also possible at short ranges feeding higher excitation energy into the acceptor [157], [158]. Thus, utilization of graphene as an efficient excitation energy acceptor through NRET holds promise for various photonic and optoelectronic applications including new ways of light-harvesting based on graphene's hybrid structures [225], [226].

Previous reports present that graphene accepts excitons from hybridized quantum confined structures (e.g., quantum dots (CQDs)) and dye molecules [118], [124]. This exciton transfer has been experimentally and theoretically demonstrated to be dominantly FRET [118], [123], [124], [136]. In this regard, owing to their favorable optical properties such as size tunable and strong luminescence emission, and photostability, CQDs are good candidates to sensitize graphene for possible application in photodetectors and light-harvesting systems [227]. To date, although epitaxial graphene has been widely studied solution-processed graphene i.e., graphene oxide (GO) and reduced graphene oxide (RGO) can offer unique capabilities including ease of processing at low cost, large area coverage and tunable energy gap, which cannot be satisfied by the epitaxial graphene [125], [130]. Therefore, NRET into GO or RGO considering both FRET and non-excitonic NRET processes, which may exhibit an energy quenching range comparable to graphene, is particularly important to explore and it is essential to understand feasibility and extend of excitation energy sink as well as the required conditions [121], [123], [124], [136].

Recently, most of the experimental studies have highlighted the importance of fluorescence quenching efficiency in CQDs-GO[137] and dye-RGO[121] hybrids for the development of various application fields. In these studies, fluorescence quenching measurements provide limited information about the energy transfer mechanism. For the detailed analysis of excited state dynamics of the fluorophores, time-resolved fluorescence spectroscopy (TRF) is required. As a powerful technique, TRF can reveal the fluorescence lifetime modifications which can be directly attributed to the NRET since it opens up a new channel for the donor excitons to relax. TRF decay rates enable to analyze NRET channels between CQDs and GO or RGO, which occurs under a broad resonance absorption spectrum at short separations as compared to the ranges of radiative energy transfer (RET). In general, NRET efficiency is strongly dependent on separating distance between the donor and acceptor [190], [208]. However to date, the efficiency of the NRET into GO or RGO has not been known in terms of the donor-acceptor distance.

Herein, we report the distance dependence of the NRET in CQD-GO and CQD-RGO hybrid films, where a thin layer of CQD coating is achieved over uniformly full-

covered thin GO (1-2 layers) and thermally annealed thin RGO layers. Furthermore, NRET rates are found to be dependent on the degree of reduction of GO films. The NRET efficiencies are measured to be around 97% and 89% at the closest separation for the CQD-RGO and the CQD-GO hybrids, respectively. These results indicate that the strong NRET from CQDs into GO based thin layers makes these hybrid structures promising candidates to be used in light-harvesting and detecting applications.

3.3.2 Experiment

In this study, we achieved to show a strong evidence for the excitonic NRET from CQDs to few layer solution-processed graphene variants (GO and RGO). To this end, we coated the GO and RGO films on quartz substrates. Then, CQDs were coated following the HfO_2 separation layer was located between the GO (or RGO) and CQD layers on the substrate. The schematic representation of the CQD-GO based structures is shown in Figure 3.22a. In these hybrid structures, the HfO_2 thickness was carefully set to 0.2, 0.4, 0.7, 1.0, 2.0, 3.0, 4.0, 5.0, 10.0 and 20.0 nm on GO or RGO coated quartz substrates through ALD. These thicknesses are much smaller than the emission wavelength of the CQDs (580 nm in film), which is a favorable condition for the occurrence of NRET before RET becomes the dominant transfer mechanism [124]. NRET refers to the combination of the excitonic transfer, which is based on FRET in our study (Figure 3.22b) and the non-excitonic transfer coming from the contribution of charge transfer mechanisms.

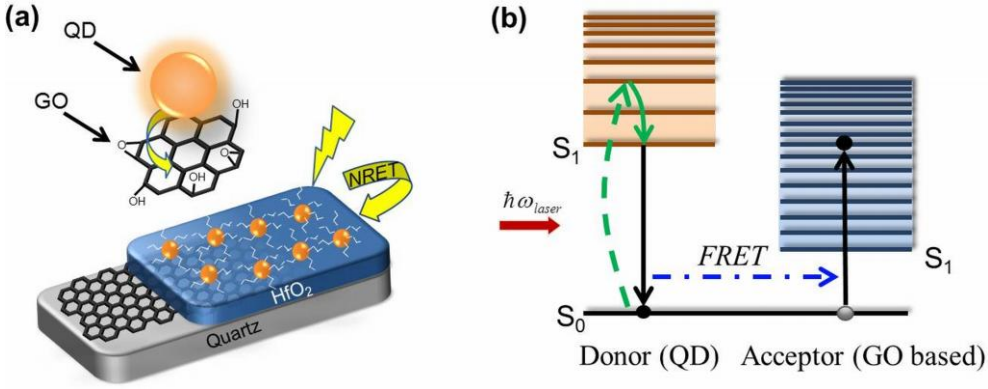

Figure 3.22. (a) Schematic representation of the hybrid CQD/HfO_2/GO structure. (b) Energy diagram for the FRET from CQD into GO based acceptor.

Preparation of GO Solution: For the preparation of well-dispersed GO solution, the GO powder (Timesnano, Chengdu Organic Chemicals Co. Ltd., China) was first suspended in deionized water at a concentration of 1.6 mg/mL and then ultrasonicated for 30 min. Subsequently, the prepared solution was centrifuged at 14500 rpm for 10 min. After the centrifugation, multiple GO layers were descended and the supernatant is recovered for re-sonication and re-centrifugation in the same manner. The resultant supernatant solution, which is stable against precipitation, was the GO solution used in this study.

Coating of GO Thin Films: 3 mm thick 1.5 cm × 1.5 cm sized quartz slides were used as the substrates for GO coating. Prior to the GO coating, quartz substrates were cleaned in piranha solution (7:3 vol. H_2SO_4:H_2O_2 mixture) for 40 min, rinsed with deionized water and dried under nitrogen flow. Then, the prepared GO solution was spin-coated over the quartz substrates at 2000 rpm for 3 min, which resulted in well-covered thin GO films.

Thermal Reduction of GO Thin Films: GO coated quartz wafers were placed in a vacuum capable quartz-tube furnace with controlled pressure. Substrates were heated up to 625 °C or 900 °C and held at these temperatures for 30 min under flowing Ar/H_2 (1:1) atmosphere. Here, the heating rate is a key parameter for the thermal reduction process to accomplish the reduction of GO without any film loss due to the presence of

oxygen containing groups. Therefore, low heating rate (5 °C/min) was preferred to eliminate any possible film loss from substrates. The prepared GO and RGO films were characterized by using Raman spectroscopy at a laser wavelength of 532 nm, X-ray photoelectron spectroscopy (XPS) and tapping mode atomic force microscopy (AFM).

Deposition of HfO_2 and CQD Layers: For the systematic investigation of the separation dependence of energy transfer from CQDs into GO and RGO, we coated a thin layer of HfO_2 on the GO and RGO films using atomic layer deposition (ALD) at a deposition temperature of 150 °C. In this study, 0.2, 0.4, 0.7, 1.0, 2.0, 3.0, 4.0, 5.0, 10.0 and 20.0 nm thick HfO_2 layers were used as the barrier layer. To determine the roughness of HfO_2 layers on GO and RGO films, we obtained the AFM image as represented in Figure 3.23.

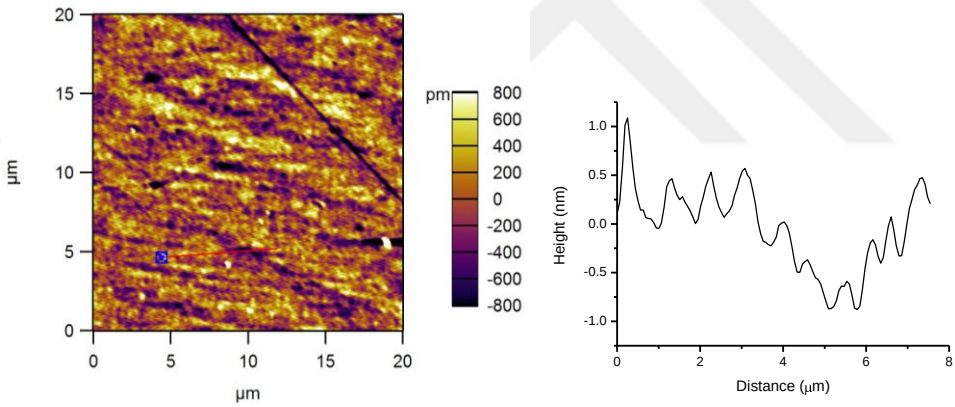

Figure 3.23. Tapping-mode AFM image of 5 nm HfO_2 layer coated on GO film on quartz together with the height profile.

We found the roughness of GO layer to be around 0.8 nm and the roughness of RGO layer to be around 0.4 nm. The roughness of GO and RGO films was found not to change with the ALD coating of thin HfO_2 layers whose film thicknesses are 0.2, 0.4 and 0.7 nm. Variation in the roughness as compared to the GO and RGO films was found to become 0.3 nm for the samples coated with thicker HfO_2 layers with the thicknesses of 1.0, 2.0, 3.0, 4.0, 5.0, 10.0 and 20.0 nm. All these AFM results indicate that roughness is low and is expected not to have a significant impact on the energy

transfer in our structures. CdSe/CdS CQDs were spin-coated on the GO and RGO samples (with/without HfO_2) at 2000 rpm for 180 s. The average radius of the CQDs was measured to be around 5.8 nm by high resolution transmission electron microscopy (HR-TEM). The thickness of HfO_2 and CQD layers were determined by ellipsometry. From the analysis of the ellipsometry data for the HfO_2 layers, we observed small mean square errors in film thickness determination less than 0.02 nm.

TRF Spectroscopy of CQDs-GO and CQDs-RGO Hybrid Structures: CQDs-GO and CQDs-RGO hybrid structures both with and without HfO_2 layer were characterized by TRF in order to investigate the energy transfer mechanism between the CQDs and GO or RGO layers. Room-temperature fluorescence decays of the CQDs were recorded in vacuum to completely eliminate the photo-oxidation of the CQDs. The laser excitation of TRF system was performed at 375 nm. The TRF detection wavelength was set to 580 nm, which is the peak emission wavelength of the CQDs on GO or RGO films.

3.3.3 Results and discussion

In this study, NRET mechanism was investigated on the hybrid structures composed of CdSe/CdS CQDs decorated on top of HfO_2 deposited GO or RGO films which serve as the donor, the separation dielectric layer and the acceptor, respectively. Figure 3.24a shows the AFM image of the 10 µm × 10 µm area of the spin-coated GO film on a quartz substrate. It is clear that GO coating on the surface is continuous having an average roughness (rms) of 1.3 nm, which is comparable to the average roughness of only quartz. From the height profile analysis as presented by the red line in Figure 3.24a, the average thickness of the GO film is found to be ~2 nm (Figure 3.24b), which is also verified via high-sensitivity optical profilometry technique (Zygo 3D Optical Profilometer, USA). Isolated GO sheets obtained through spin coating of lower density GO solution lead to a film thickness of ~1 nm (Figure 3.24b inset), and such a film thickness value is larger than a single layer pristine graphene owing to the presence of oxygen-containing groups in the GO structure [125]. Therefore, GO samples have on

the average double equivalent layers of GO sheets on the quartz substrates (AFM image given in the inset in Figure 3.24b).

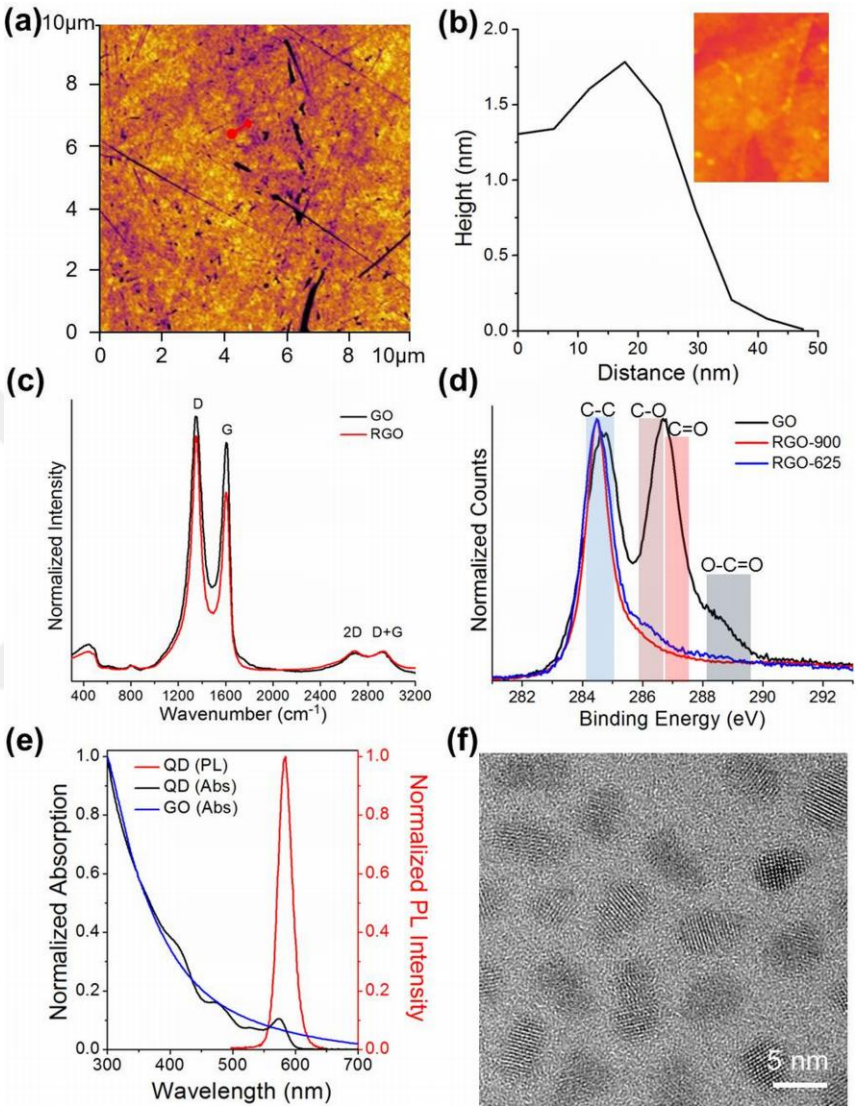

Figure 3.24. (a) Tapping mode AFM image of the GO thin film on quartz. (b) Height profile along the red line presented in (a). Inset shows the AFM image of an isolated single GO sheet on quartz. (c) Raman spectra of GO and RGO thin film reduced at 900 °C. (d) XPS spectra of GO and RGO thin films reduced at 625 and 900 °C. (e) Normalized absorption (black line) and PL (red line) spectra of CdSe/CdS CQDs with normalized absorption of GO solution (blue line). (f) HR-TEM image of the CQDs used in the study.

Thermal reduction at various temperatures is employed to obtain RGO under H_2/Ar ambient in an atmosphere-controlled furnace. To evaluate the effect of reduction process on film characteristics, GO and RGO films were analyzed by using Raman spectroscopy and XPS. Raman spectroscopy is a powerful technique for the analysis of defects and disorders in carbon-based materials [228]. For typical GO and RGO films, there are two characteristic peaks located around 1350 cm^{-1} (D band) and 1580 cm^{-1} (G band), which are assigned to the disordered carbon atoms and the vibration of sp^2 bonded carbon atoms, respectively [229], [230]. In this study, D and G bands appear at the wavenumbers of 1352 cm^{-1} and 1605 cm^{-1} for both prepared GO and RGO films, which is in good agreement with the previous studies (Figure 3.24c) [229], [230]. Although some of the recent reports show that no shift occurs in D and G peaks after reduction [231]–[233], there are few studies reporting the red shift of G band [121], [234]. In our case, we did not observe any shift for D or G peaks after the reduction process while D band was narrowed owing to the loss of oxygen groups. Furthermore, the intensity ratio I(D)/I(G) is used to characterize the quality of GO and RGO films [234], [235]. The I(D)/I(G) intensity ratio for the GO film is found to be 1.1, which is increased to 1.3 after the reduction. There is a conflict in the literature for the effect of reduction on I(G)/I(D) ratio: while some reports claim no change or a decrease for the ratio of I(G)/I(D),[234], [236], [237] others observe an increase [232], [238], [239]. The possible reason of the increase in the ratio in our study might be attributed to the presence of unrepaired defects after the removal of oxygen groups with the help of reduction at the specified temperatures [232], [239].

Furthermore, XPS analysis was conducted on the GO and RGO films to better understand the chemical structure after the reduction process for the NRET study. Figure 3.24d shows the C1s peak for GO and RGO films reduced at two different temperatures, 625 and 900 °C. Deconvolution of C1s peak for GO clearly indicates the presence of C-C bond (~284.8 eV) beside the C-O (~286.3 eV), C=O (~287.6 eV) and O-C=O (~289.0 eV) bonds, which is reasonably consistent with the previous reports for GO films [115], [240], [241]. However, for the case of RGO, the main C-C peak chemically shifts to 284.3 eV and becomes narrower than the peak at GO case. Furthermore, the C/O atomic ratio was obtained through the deconvolution of C1s

peaks for GO and RGO samples. The C/O ratio of GO film was found to be 0.9, which was increased to 2.7 and 3.1 after the reduction at 625 and 900 °C, respectively. All these C1s peak properties of the RGO samples indicate that there is a significant amount of reduction on the GO films at 900 °C by considering the C/O ratio and the decrease in the intensity of oxygenated carbon peaks.

Figure 3.24e shows the optical absorbance and fluorescence of the 5.8 nm-sized CdSe/CdS CQDs along with the absorbance of the GO solution in water. CQDs exhibit PL centered at ~590 nm. Owing to the narrow size distribution of the CQDs, higher order excitonic peaks are also visible in the UV-Vis absorbance. For NRET, a spectral overlap is required between emission of the donor and absorption of the acceptor. As shown in Figure 3.24e, there is a considerable absorption by GO in the emission range of the CQDs. Beside PL analysis of the size distribution HR-TEM analysis provides evidence for a narrow size distribution of the CQDs (Figure 3.24f).

After the preparation of GO and RGO surfaces, HfO_2 layer is deposited on the GO and RGO films by ALD technique in order to systematically investigate the effect of separation layer thickness on NRET from the donor CQDs to the acceptor GO or RGO films. First, TRF was employed to measure the fluorescence decays of the CQD emission when placed on top of GO or RGO films having varying HfO_2 thickness. Figure 3.25a depicts the exemplary room-temperature TRF decay curves with the corresponding numerical fits for the CQD-GO and CQD-RGO hybrid structures having 4.0 and 0.2 nm thick HfO_2 layer as the separation layer between the CQDs and GO or RGO thin film on quartz substrates in addition to the instrument response function (IRF) of the TRF system. The spin-coated CQDs on quartz that was pre-deposited with a 20.0 nm thick HfO_2 film is used as a reference. Here, the HfO_2 pre-deposition is used to ensure the CQDs film quality. The fluorescence lifetimes of the CQDs were fitted via multi-exponential fitting and the average lifetimes were calculated using amplitude averaging technique (reduced $\chi^2 \sim 1$). In comparison with the reference sample, there was a significant alteration of the CQDs emission decay kinetics as the separation distance between the CQDs and the GO based films was decreased. Clear reduction in lifetimes with the decreasing distance indicates faster decays at shorter separations (Figure 3.25a). In Figure 3.25b, fluorescence lifetimes of the CQDs are depicted for the

CQD-GO, CQD-RGO and CQD-quartz structures parameterized with respect to HfO_2 separation layer thickness. The reference CQD lifetime was found to be 2.61 ns, which was verified to be independent from the thickness of HfO_2 deposited on quartz substrate. The lifetimes of CQD-GO and CQD-RGO (reduced at 900 °C) structures prolong as the separation distances increase. At longer distances (> 5 nm), the CQDs attain almost the same lifetime values for both GO and RGO acceptors. However, for the shorter HfO_2 separation distances (< 5nm), lifetime of the CQDs on top of RGO is shorter than that on GO. Two different lifetime behaviors with respect to distances indicate the presence of more than one mechanisms acting simultaneously, which can be explained by the combination of FRET and non-excitonic NRET. To better understand the underpinning mechanisms, the excitation transfer rates are calculated using the expression $\gamma_{NRET} = \gamma_{DA} - \gamma_D$, where γ_{DA} ($1/\tau_{DA}$) is the rate for the donor-acceptor hybrid structure (CQDs-GO or RGO) and γ_D ($1/\tau_D$) is the rate for the structure with only donor (CQDs). Figure 3.25c presents the NRET rates as a function of the HfO_2 separation thickness. In accordance with the lifetimes shown in Figure 3.25b, at the shorter separations, the rates are modified by the combination of both FRET and non-excitonic NRET. For the longer separations, the rates are dominated by FRET since the charge transfer processes are strongly distance limited.

Previously, it was debatable whether the observed extraordinary steady-state PL quenching of the fluorescence of the emitters in the proximity of graphene based film is due to the FRET or non-excitonic NRET. The parametric study enables us to determine that both types of mechanisms are viable (Figure 3.25b and Figure 3.25c). In a recent study, it has been demonstrated that different sp^2/sp^3 ratios in the functionalized and as-synthesized carbon nanotubes alter the quenching of the fluorescent molecules possibly due to varying non-excitonic NRET rates [242]. In our case, RGO is shown to exhibit greater effect on the lifetimes of the CQDs in the non-excitonic NRET regime. This is expected since GO is decorated with epoxy and hydroxyl groups in its hexagonal basal plane and, following the reduction process, the density of oxygen containing groups is decreased. As a result, it leads to larger sp^2/sp^3 ratio in RGO as compared to that in GO, which would favor the non-excitonic NRET.

Recently, there have been a number of studies reporting the NRET rates for graphene based hybrid structures with the inverse fourth order power of the separation distance ($1/d^4$) [123], [124]. However, there is no study for the reduction dependent systematic rate analysis of GO-based hybrids although there are reports for the investigation of energy transfer into these structures [137], [243]. Using this dependency, a theoretical distance dependence NRET rate for a graphene layer is represented by a black line in the inset of Figure 3.25c. In order to investigate the effect of reduction on the energy transfer rate behavior, the normalized NRET rates of GO and RGO samples reduced at either 625 or 900 °C are also presented as an inset in Figure 3.25c. It is clear that there is an increase in the order of inverse power with the temperature of the reduction process and it approaches to that of graphene, which has fourth order dependence.

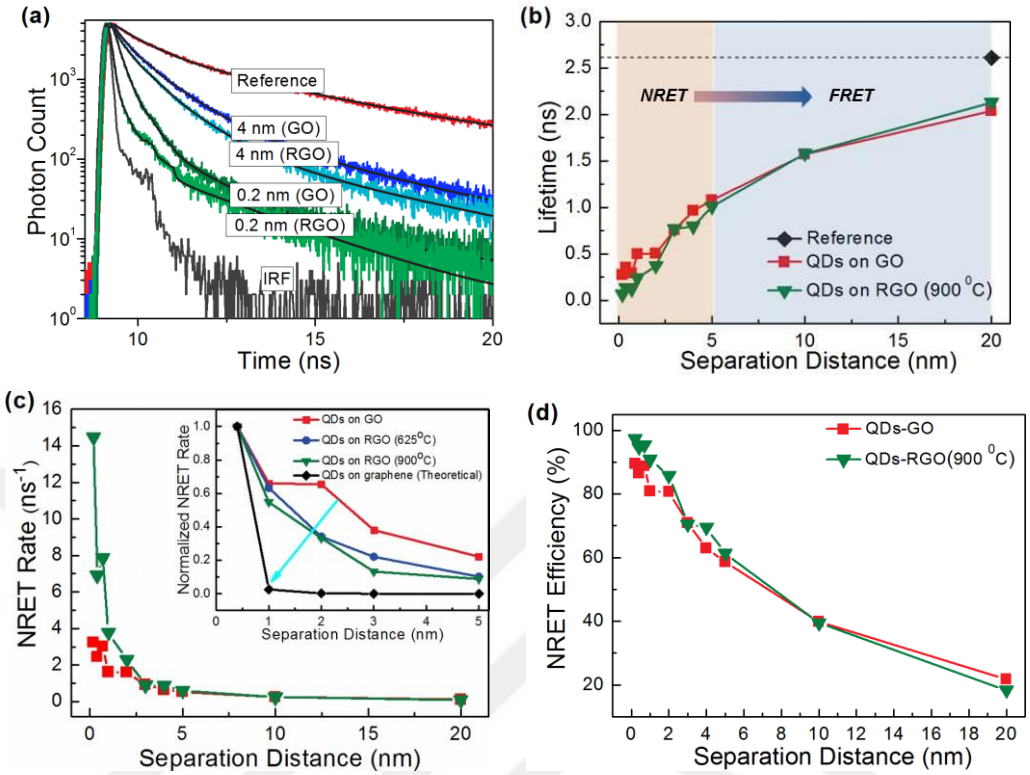

Figure 3.25. (a) Experimental TRF decays of the CQDs on GO and RGO thin films on quartz for the HfO2 separation distances of 4.0 nm and 0.2 nm; and 20.0 nm for the CQDs without GO and RGO at the bottom (Reference). Solid black lines are multi-exponential fits to the data, and gray decay curve is the laser diode response function (IRF). (b) TRF lifetimes of the CQDs as a function of the distance from GO and RGO; and of the reference. (c) Separation distance dependence of the NRET rates of the CQDs on GO and RGO reduced at 900 °C. Inset shows the experimental decays of the CQDs on GO, RGO reduced at 625 °C, RGO reduced at 900 °C and the theoretical decay of the CQDs on graphene (d) NRET efficiency of the CQDs on GO and RGO reduced at 900 °C as a function of the separation distance.

Furthermore, we calculated the NRET efficiencies using the relation $\eta = \gamma_{NRET} / (\gamma_{NRET} + \gamma_D)$. High efficiencies were obtained, yielding around 97% for the closest separation of CQDs-RGO (900 °C) structures and around 89% for the closest separation of CQDs-GO structures, as depicted in Figure 3.25d. It is also worth

noting again that efficiencies become sample independent as the separation between the donor and the acceptor increases.

3.3.4 Summary

We investigated NRET from CdSe/CdS CQDs into uniformly coated GO and RGO thin layers using TRF spectroscopy. It is shown that, as the separation distance between the CQDs and GO or RGO decreases, TRF lifetimes are shortened, which indicates faster NRET rates. For the CQDs-GO and CQDs-RGO hybrids, NRET mechanism consists of excitonic-NRET at longer separations, and both excitonic and non-excitonic NRET at shorter distances. In close proximity, NRET rate from the CQDs into RGO layer is higher than the CQDs into GO layer which mostly results from the structural defects. However, at longer separations (> 5 nm), rates are almost the same for both hybrid nanostructures. In addition, it is found that reduction process directly affects the behavior of NRET rates for these structures. Furthermore, NRET efficiencies are calculated from the experimental data to be high around 97% and 89% for the closest separation of the CQD-RGO and the CQD-GO pairs, respectively. In the light of these results, we conclude that hybrid structures including acceptor GO or RGO layers together with donor CQDs hold great promise for use in several optoelectronic applications.

3.3.5 Additional study including MoS_2

Within the framework of this study, the investigation of NRET from donor CQDs to acceptor transition metal dichalcogenites (TMDs) was achieved. In this way, NQD-TMC hybrid structures were examined in terms of the capacity for charged particle transfer and light absorption. To this end, MoS_2 mono-/bi-layers were grown by using chemical vapor deposition technique (Figure 3.26). Chemical and structural characterizations of the grown samples were carried out in detailed (Figure 3.27). On the other hand, colloidal SILAR technique was used to obtain CdSe(core)/CdS(shell)

QDs with high quantum efficiency. Using these hybrid structures, studies on the NRET from CQDs to TMDs were conducted via time resolved fluorescence spectroscopy. Herein, any variation in the efficiency of nonradiative energy transfer between QD and MoS_2 was investigated from the optical point of view. With these CQDs-MoS_2 hybrid structures studied in the project, in the near future, considerable enhancement in the performance of numerous optoelectronic devices is strongly probable. In addition, we studied the growth patterns on the gas flow pattern in the CVD growth system and, as can be seen from Figure 3.28 and Figure 3.29, instead of surface energy, we can attribute it directly to the gas flow pattern changing with the surface roughnesses.

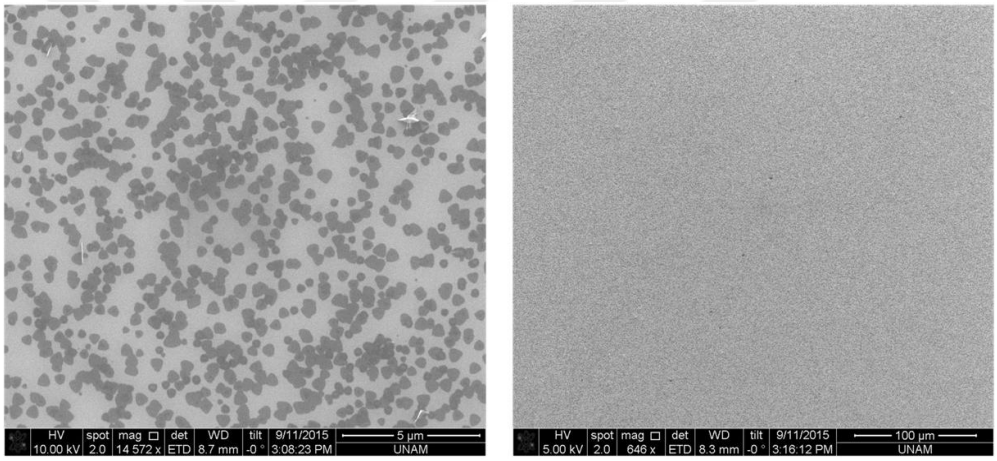

Figure 3.26. SEM images of MoS_2 layers growth via CVD.

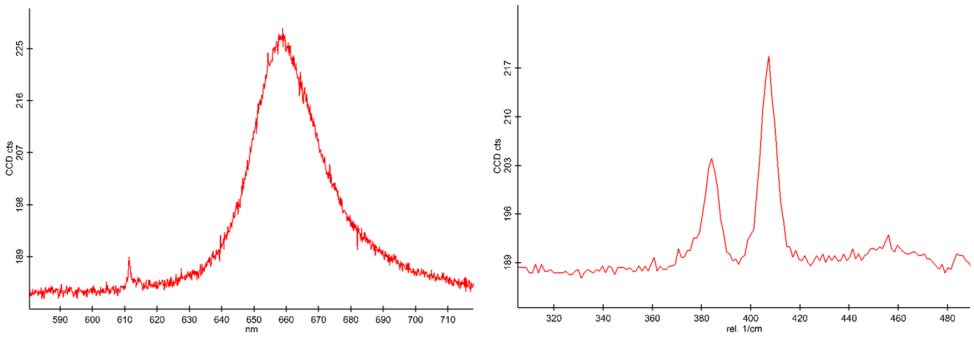

Figure 3.27. PL and Raman spectra of MoS_2 layers growth via CVD.

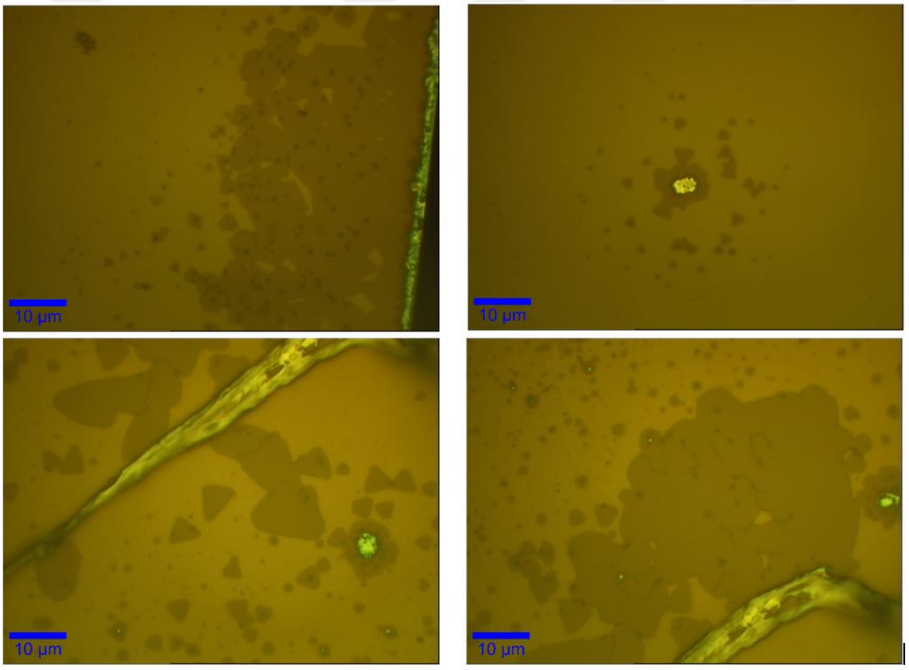

Figure 3.28. Microscope images of MoS_2 layer growth around the rough surface points.

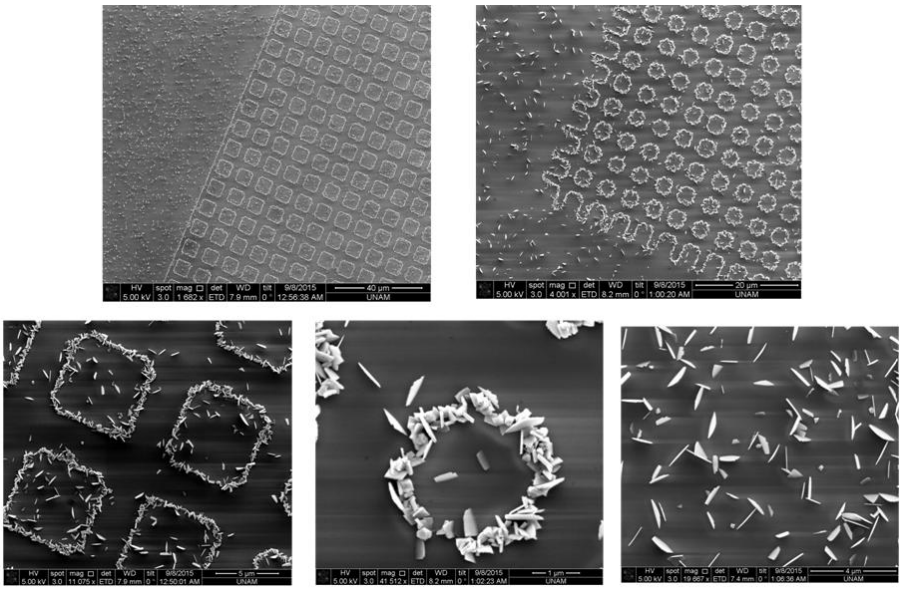

Figure 3.29. Layered 2D MoS_2 structures growth on patterned silicon substrates to examine the effect of surface roughness to the flow pattern and thus the growth layers.

$MoS_2/SiO_2/Si$ structures obtained via CVD technique were utilized for the temperature dependence study of NRET. For this purpose, TRF measurements were performed at different temperatures ranging from 290 ° K to 17 ° K. TRF spectroscopy was used in this study to understand the underlying physical mechanisms for these hybrids. An integrated cooling system was also used to do the measurements at cryogenic temperatures. We obtained the TRF energy transfer rates and efficiencies of CQD-MoS_2 hybrids depending on the environmental temperature (Figure 3.30).

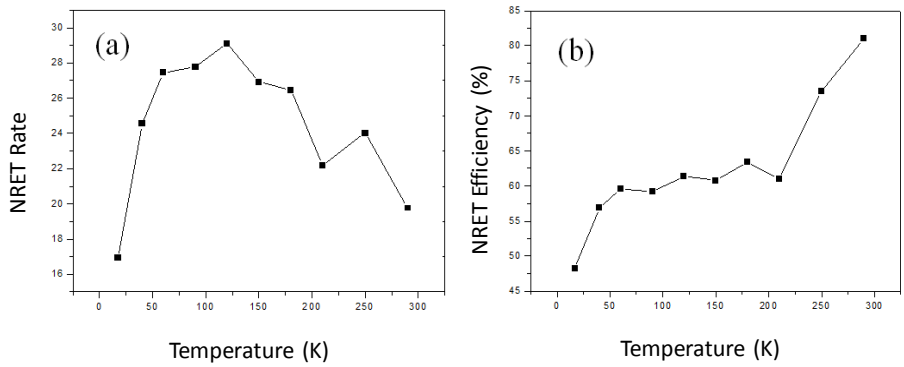

Figure 3.30. TRF energy transfer rates and efficiencies of CQD-MoS_2 hybrids depending on the environmental temperature.

We observed that the rates are following the quantum yield of the CQDs and the efficiencies are decreasing as the temperature decreases for the multi-layers of MoS_2. Since they have indirect bandgap structure, we can attribute these behaviors to the phonon assistance in multi-layer MoS_2. To further investigate the physics behind this process, we are also planning to do the same measurements by using mono-layer MoS_2 including samples which have direct bandgap structure.

Chapter 4

Excitonic Nonradiative Energy Transfer by Using Colloidal quasi-2D Semiconductor Nanocrystals

In the first section of this chapter, we present the study on the experimental determination of the absorption cross-section and molar extinction coefficient of colloidal CdSe nanoplatelets (NPLs) to provide fundamental information for the investigations of excitonic nonradiative energy transfer (NRET) in the systems including colloidal quasi-2D semiconductor nanocrystals. The NPLs as solution-processed quantum wells offer great potential for optoelectronic devices including LEDs, lasers and solar cells. To this end, determination of the absorption cross section, extinction coefficient, intrinsic radiative lifetime and oscillator strength is of great importance to understand the underlying optical properties of NPLs.

In this first study presented in Chapter 5, we report the absorption cross-sections, the extinction coefficients and the related optical parameters (intrinsic radiative lifetimes and oscillator strengths) of 4 and 5 monolayer (ML) thick colloidal CdSe NPLs by using various spectroscopy techniques. Herein, we systematically

investigated lateral area dependence of the absorption cross-sections and the corresponding molar extinction coefficients of 4 ML and 5 ML thick NPLs. For this purpose, we used ICP-OES, ICP-MS and absorption spectroscopy techniques in addition to transmission electron microscopy. We observed that the absorption cross-sections and the extinction coefficients substantially increase with the lateral area for both the 4 ML and 5 ML NPLs and there is an excellent agreement between the experimental results and the calculated values based on the small-particle light absorption model. Furthermore, we found that the intrinsic radiative lifetime of the first exciton (heavy hole – electron (hh-e)) decreases with the lateral area and ranges from 153 to 28 ps for the 4 ML NPLs and 249 to 4 ps for the 5 ML NPLs. Also, the per-platelet particle oscillator strength of the hh-e transition rises with the increasing lateral area. All of these new findings provide useful knowledge in exploiting NPLs for the next-generation optoelectronic applications and, with these appealing optical properties; we believe that NPLs hold great promise for future colloidal optoelectronics.

In the second section of this chapter, we present the study on nonradiative energy transfer between quasi-2D colloidal doped and undoped semiconductors. In this work, we approached the issue of the NRET from doped 3ML CdSe core NPLs to undoped 4ML/5ML CdSe/CdS core/shell NPLs in terms of donor/acceptor molar ratios in the hybrid solid films. Recent developments in the nanocrystal research allowed the colloidal nanocrystals to be used in various optoelectronic applications. The sophisticated understanding of these highly promising materials provided new routes for further improvement of their exciting photophysical properties. For example, the Stokes-shifted photoluminescence yielding no self-absorption has been possible through the doping of the nanocrystals with cation such as copper. Investigations on the luminescent Cu-containing bulk semiconductors are dating back to the late 19th century; however, the copper doping of luminescent semiconductor nanocrystals is a new area of material science encompassed by photonics technology. It is ultimately important to enhance the energy conversion efficiency in the light-harvesting and detection systems by using the colloidal nanocrystals. In this sense, colloidal undoped and Cu-doped nanocrystals offer great advantages through the direct nonradiative

transfer of the excitons to the electronic system. It is envisioned that much further improvement in the nanocrystal integrated devices is possible with the utilization of Cu-doped nanocrystals together with undoped nanocrystals hybridized in the optoelectronic systems. To this end, the spectroscopic, physical and electrical characteristics of both the doped and undoped materials are significantly important. Besides the 0D colloidal nanocrystal quantum dots, another class of colloidal materials having quasi-2D quantum well structure, NPLs, has also emerged recently. These newly emerging materials along with their Cu-doped companions have superior properties compared to their 0D counterparts, culminating in their promising broad technological adoption. Therefore, the hybrids of undoped and Cu-doped nanoplatelets are favorable candidates for the next-generation photonics applications including photovoltaics, luminescent solar concentrators, LEDs and display technologies.

In this second study presented in Chapter 5, we investigate the NRET on the hybrid films composed of doped and undoped NPLs. The work presented here is serving a new source for the explanation of NRET mechanism between quasi-2D colloidal doped and undoped semiconductors depending on the donor/acceptor molar ratios. To this end, we applied steady-state and time-resolved PL spectroscopy techniques on the solid films of doped/undoped NPLs having discrete molar concentration ratios. We revealed that there is a strong excitonic energy transfer from the doped donor to the undoped acceptor NPLs, which are in close proximity. Herein, we report the first account of near-unity room-temperature energy transfer efficiency, 0.99, in these all-colloidal all-quasi-2D solid films. It is envisaged that such highly efficient energy transfer in the quantum confined doped-undoped hybrids will enable high-performance novel optoelectronic devices including Cu-doped nanoplatelets as the energy conversion components.

4.1 Experimental determination of the absorption cross-section and molar extinction coefficient of colloidal nanoplatelets

This section is based on the publication "Experimental Determination of the Absorption Cross-Section and Molar Extinction Coefficient of Colloidal CdSe Nanoplatelets," **A. Yeltik**, S. Delikanli, M. Olutas, Y. Kelestemur, B. Guzelturk and H. V. Demir, J. Phys. Chem. C 119, 26768-26775 (2015). Adapted (or "Reproduced") with permission from American Chemical Society. Copyright 2015 American Chemical Society.

4.1.1 Motivation

Colloidal luminescent quasi-2D semiconductor quantum wells, which are commonly known as colloidal NPLs, have been a subject of intense study in recent years [55], [244]. By controlling the quantum confinement and composition, the electronic structure and the optical properties of these colloidal quantum wells can easily be tuned. They offer superior properties compared to the nanocrystal quantum dots (QDs) [245], including thickness control at the monolayer level and extremely narrow emission bandwidth (<11 nm). In addition to the large exciton binding energy as a consequence of the strong vertical confinement [246]–[249], NPLs feature giant oscillator strengths resulting from increased exciton center-of-mass extension [55], [250], [251]. Their huge oscillator strength enables significantly enhanced absorption cross-section (σ) and substantially increased radiative decay rates [252]. All these significant properties make the NPLs highly promising colloidal counterparts of epitaxial quantum wells, which can further be exploited for optoelectronic devices including LEDs, lasers and solar cells [75], [164], [165].

As an important measure of electromagnetic absorption by nanostructures, determining the absorption cross-section is of a primary interest for quantifying

fundamental optical properties of NPLs. For example, the knowledge of the absorption cross-section allows for a quantitative measure of the NPL fluorescence quantum yields. The absorption cross-section also provides an easy way to estimate the number of electron-hole pairs generated with each absorption event inside an NPL. Low amplified spontaneous emission threshold of the NPLs is also well explained by their large absorption cross-section [253]. Using the information of the absorption cross-section spectrum of the NPLs, one can obtain their oscillator strengths and intrinsic radiative lifetimes.

Knowing molar extinction coefficient (ε) of the NPLs is also of great importance for convenient and accurate measurements of the NPL concentrations [254]. With the well-known molar extinction coefficients, different architectures of core/shell (vertically grown shell) and core/crown (laterally grown shell) NPLs can be synthesized with great control over their thicknesses and lateral sizes.

Previous reports of individual NPL absorption cross-sections indicate that NPLs exhibit higher σ values compared to their spherical counterparts with the same size [79], [253]. In the work by She et al., σ of CdSe NPL was observed to increase after the CdS shell growth, which was discussed as one of the indications of lower amplified spontaneous emission threshold compared to the core CdSe NPLs. Fluorescent lifetimes measured for CdSe NPLs were provided by Tessier et al. and much shorter values were reported compared to the ones measured for spherical quantum dots [35], [79], [135]. In addition, Naeem et al. studied the giant oscillator strength of CdSe NPLs and concluded that decrease in the radiative lifetime is associated with the exciton coherence area, which is larger than that of spherical CdSe nanocrystals [86]. Furthermore, radiative lifetimes on the order of picoseconds for NPLs were measured and/or predicted by several groups [86], [250]. In the previous literature, a complete and systematic study on the absorption cross-section and related optical properties of CdSe NPLs has, however, not been reported to date. There is thus a strong need for the experimental determination of the absorption cross-section of the NPLs of a specific vertical thickness as a function of their lateral size. This is particularly essential as a series of reference measurements for finding molar extinction coefficients.

In this work, we experimentally determined the absorption cross-sections, extinction coefficients and related optical properties (oscillator strengths and intrinsic radiative lifetimes) of 4 and 5 monolayer (ML) thick CdSe NPLs. For this purpose, two independent experimental methods, inductively coupled plasma optical emission spectroscopy (ICP-OES) and inductively coupled plasma mass spectroscopy (ICP-MS), were used. For both of the methods, the NPL samples were purified by efficient purification procedures. Concentrations of the NPLs were first determined via ICP-OES measurements. Then, results of the first method were confirmed by the second method, ICP-MS. In the ICP-MS measurements, concentrations were diluted to reach reliable ranges. Using these concentrations, σ values were found with the help of absorption spectroscopy technique. Results indicate that the absorption cross-sections of both the 4 ML and 5 ML thick NPLs are in direct correlation with the lateral sizes. Furthermore, the experimental σ values agree well with the calculated ones based on the Ricard model [255]. The corresponding ε values were also calculated using the concentrations obtained from ICP-OES and ICP-MS and strong lateral size dependence was observed for both NPL sets. In addition to the dependence of σ and ε on the NPL lateral size, the oscillator strength at the heavy hole – electron (hh-e) transition band was observed to increase with the lateral size. This implies that the intrinsic radiative lifetime decreases with increasing lateral size of the NPLs.

4.1.2 Experiment

Experimental sample preperation and measurement procedures that are used in this study can be listed and elaborated as follows:

Chemicals: Cadmium acetate dihydrate ($Cd(OAc)_2 \cdot 2H_2O$) (> 98%), selenium (Se) (99.999% trace metals basis), technical grade 1-octadecene (ODE) and technical grade oleic acid (OA) (90%) were purchased from Sigma-Aldrich. Cadmium (Cd) myristate was prepared at our laboratory. Hexane, methanol and acetone were purchased from Merck Millipore.

Preparation of Cadmium myristate: Cadmium myristate was prepared by following the procedure given in the literature [72]. Concisely, 1.23 g of cadmium nitrate tetrahydrate was dissolved in 40 mL of methanol and 3.13 g of sodium myristate was dissolved in 250 mL of methanol. The mixture was completely dissolved for complete dissolution and then gently mixed. The solution was stirred strongly for 1 h. Following that, the solution was centrifuged and the precipitation was dissolved in methanol. This washing step with methanol was performed at least three times to remove the excess precursors. At the end, the final precipitated part was kept under vacuum for 24 h for complete drying.

Synthesis of 4ML thick CdSe NPLs: 4 ML CdSe NPLs were synthesized according to the given recipe in the literature [72]. First, 170 mg of cadmium myristate, 12 mg of Se and 15 mL of ODE were loaded into a three-neck flask. Then, the solution was degassed at room temperature for half an hour to remove excess oxygen and volatile solvents. Subsequently, the solution was heated to 240 ^{0}C for 4 ML thick NPLs under argon atmosphere. When the temperature reaches 195 ^{0}C, 80 mg of cadmium acetate dehydrate was introduced swiftly into the reaction. After the growth of CdSe NPLs at 240 ^{0}C for 10 min, 0.5 mL of OA was injected and the temperature of the solution was decreased to room temperature. In order to obtain these CdSe NPLs in different lateral sizes, the growth time was carefully changed. The resulting 4 ML thick CdSe NPLs synthesized with this recipe exhibit a peak emission at 513 nm and other side products including NPLs having different thicknesses can be removed by size-selective precipitation. Finally, the CdSe NPLs were dissolved and stored in hexane.

Synthesis of 5 ML thick core CdSe NPLs: 5 ML CdSe NPLs were synthesized following a recipe in the literature [72]. 170 mg of cadmium myristate and 14 mL of ODE were loaded into a three-neck flask and degassed for 1 h at room temperature. Then, the temperature was raised to 250 ^{0}C under argon flow and a solution of 12 mg Se dissolved in 1 mL of ODE was quickly injected. 120 mg of cadmium acetate dehydrate was added 1 min later. The solution was kept at 250 ^{0}C for 10 min and 0.5 mL of OA was injected before cooling down to room temperature. The resulting CdSe NPLs were precipitated with the addition of acetone and dispersed in hexane.

Lateral growth of 5 ML thick CdSe NPLs: 5 ML CdSe NPLs were dissolved in hexane and 15 mL of ODE were loaded into a three-neck flask. The solution was degassed at room temperature for 10 min and the temperature was raised up to 80 ^{0}C under vacuum. The solution was kept at 80 ^{0}C about 1 h for the complete removal of hexane. Then, the temperature was increased to 255 ^{0}C under argon flow. At 255 ^{0}C, anisotropic growth mixture for the lateral extension of CdSe NPLs was injected at a rate of 3 mL/h. The lateral size of the CdSe NPLs can be tuned by adjusting the injection amount. After the injection, the temperature was quickly cooled down to room temperature. The resulting 5 ML CdSe NPLs were precipitated with the addition of acetone and dispersed in hexane.

Extraction and Precipitation Procedures: Unreacted Cd precursors were removed by using methanol since the NPLs are insoluble in this solution while the Cd precursors are highly soluble. Excess amount of methanol was added into NPLs dispersed in hexane to dissolve Cd precursors in methanol. Then, the mixture was centrifuged and dissolved in hexane. This process was repeated three times for the complete removal of excess Cd precursors. The final product was redissolved in hexane for the following measurements.

ICP-OES and ICP-MS Measurements: A solution of 2 mL of purified 4 ML thick NPL sample and 3 mL of purified 5 ML thick NPL sample were carefully dried by gentle heating in a fume hood. Then the residual was dissolved in 20 mL of nitric-acid solution. The digested sample was directly transferred into a volumetric flask for the ICP-OES measurement. For the ICP-MS measurement, the samples were diluted by 100 times to reach the ppb ranges necessary for the measurement. The selenium and cadmium molar concentrations (C_{Se} and C_{Cd}) were determined using an Agilent 725 ICP-OES system and a Thermo XSERIES II ICP-MS system. The dimensions of the CdSe NPLs were measured from transmission electron microscopy (TEM) images. The concentrations of NPLs (C_{NPL}) were calculated according to the relation $C_{NPL} = C_{Se\,(Cd)} V_{unit}/(4V_{NPL})$, where V_{unit} is the volume of the CdSe unit cell and V_{NPL} is the physical volume of CdSe NPL. Herein we assumed that the NPL has the same density as its bulk material.

UV-Vis Measurements: The purified NPLs were dispersed in a suitable amount of desired solvent to obtain reliable UV-Vis absorbance spectra at room temperature (Cary 100 UV-Vis spectrophotometer). The absorbance values were used to calculate the absorption cross-sections and the corresponding molar extinction coefficients at room temperature.

4.1.3 Results and discussion

Synthesis and Characterization of Nanoplatelets: The 4 ML and 5 ML thick CdSe NPLs used for the experiments were synthesized through the recently reported approach of Tessier et al. with a slight modification [72]. Using this route, we achieved to synthesize NPLs with varying lateral sizes. Figure 4.1a and Figure 4.1b show the TEM images and the absorption and photoluminescence (PL) spectra of 4 ML and 5 ML NPL samples. TEM measurements of the NPLs revealed that they are approximately square- or rectangular-shape as seen from Figure 4.1. Their quantum yields are ~ 30-50%, which is high compared to colloidal core CdSe quantum dots. The emission peak positions and their full-width-half-maxima (FWHM) are almost independent of the platelet area for both the 4 ML and 5 ML thick NPLs as observed in Figure 4.2a and Figure 4.2b. For the 4 ML NPLs, the emission peak is obtained at ~513 nm with a FWHM of ~8 nm and it is at ~553 nm with a FWHM of ~10 nm for the 5 ML NPLs. Similarly, the first and second absorption peaks are also independent of the NPL lateral area as given in Figure 4.2a and Figure 4.2b. The first absorption peak is at ~ 513 nm for the 4 ML NPLs and at ~553 nm for the 5 ML NPLs. The second absorption peak is at ~482 for the 4 ML NPLs while it is at ~520 nm for the 5 ML ones. These first and second absorption peaks correspond to the hh-e and light hole - electron (lh-e) transitions of the NPLs, respectively [55].

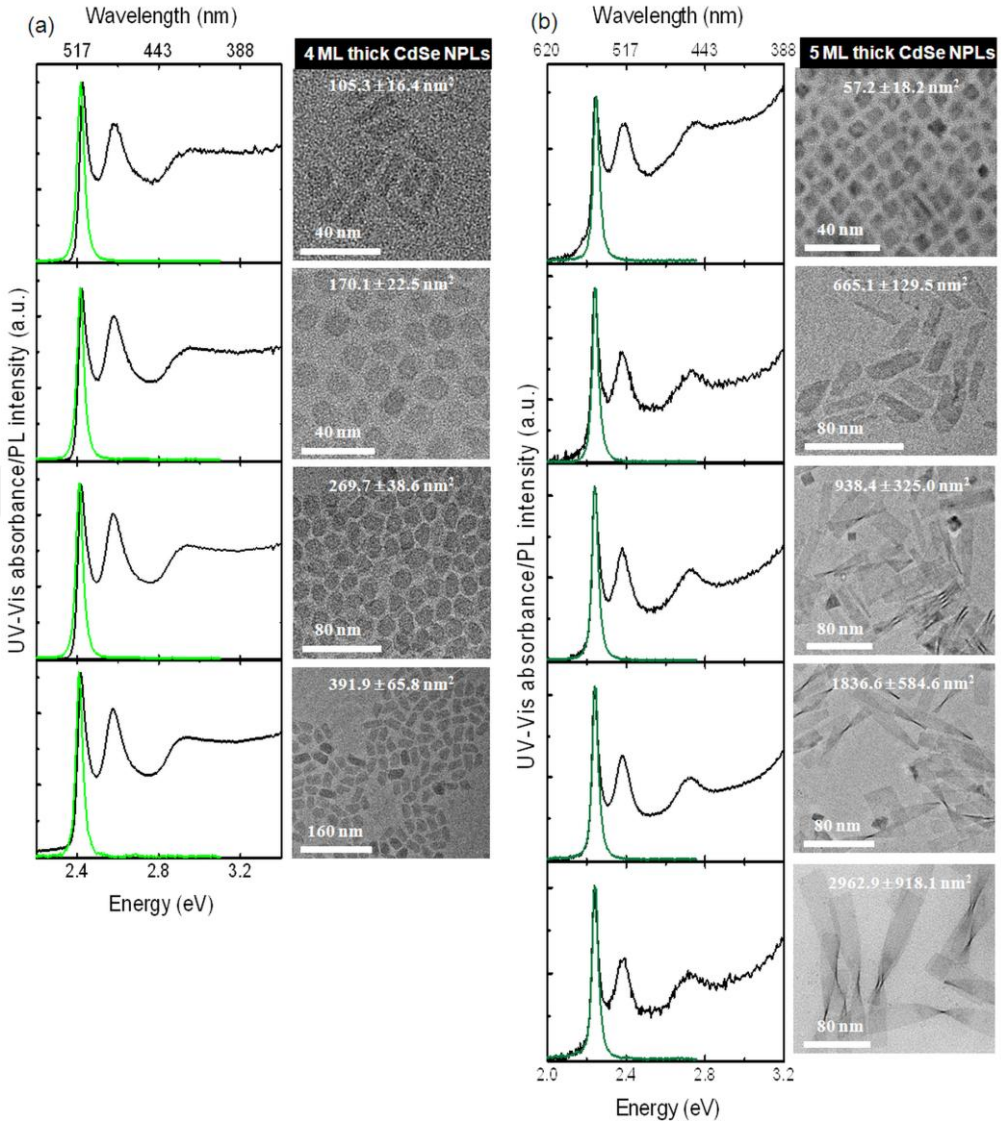

Figure 4.1 UV-Vis absorbance spectra, PL spectra and TEM images of the (a) 4 ML and (b) 5 ML thick CdSe NPLs having various lateral sizes.

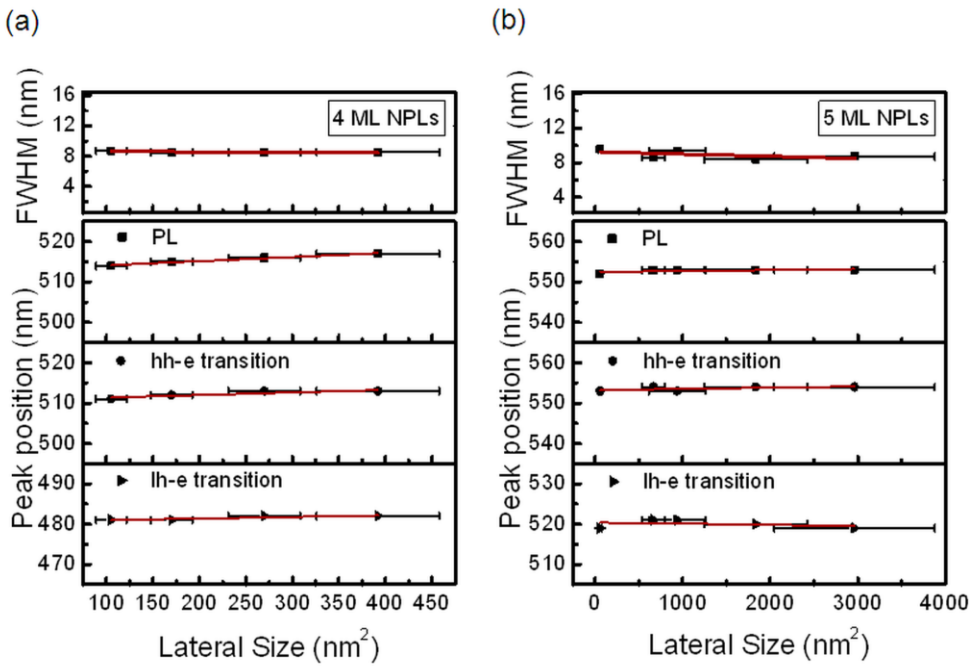

Figure 4.2 Peak positions of the PL FWHM, PL, hh-e transition and lh-e transition of (a) 4 ML NPLs and (b) 5 ML NPLs for varying lateral sizes.

In this work, it was critical to remove excess cadmium to the best possible extent. Therefore, the samples were carefully purified using the procedure described in the Extraction and Precipitation Procedures section. Conveniently, the purification was monitored by UV-Vis absorbance measurements. The absorption spectra of the host medium, the as-synthesized sample and the sample after cleaning are shown in Figure 4.3. Further discussion for the Cd/Se ratios is given in the following section.

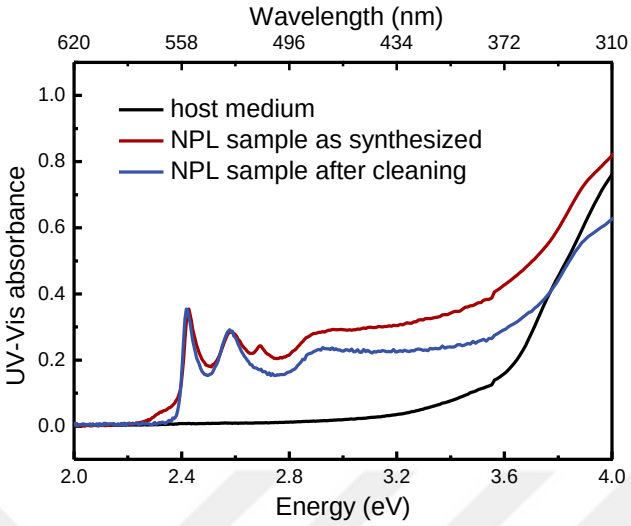

Figure 4.3 UV-Vis absorbance spectra of the reaction host medium solution containing cadmium acetate, oleic acid and octadecene, reaction mixture and final mixture after the extraction process of the NPLs.

Absorption Cross-Section and Corresponding Molar Extinction Coefficient of Nanoplatelets via Inductively Coupled Plasma Optical Emission Spectroscopy: We obtained the absorption cross-sections of each NPL sample based on the Se and Cd concentrations. First, the NPL concentration was determined by dissolving the platelets in a nitric-acid solution and by measuring the ion concentrations using ICP-OES. Then, the NPL concentrations were calculated by extracting the dimensions from TEM images and using the relation given above in the ICP-OES and ICP-MS Measurements section. The per-particle σ values for the 4 ML NPLs having various areas were determined by using the formula, $\sigma = 2303A/(C_{NPL}N_A L)$, where A is the absorbance, N_A is the Avogadro's number and L is the optical path length [253]. The results are presented as a function of the absorption energy in Figure 4.4a using the Se concentration and Figure 4.4b using the Cd concentration. As given in the figure, the absorption cross-section was observed to increase with the platelet area over the whole absorbance spectrum.

The observation of lower absorption cross-sections extracted using the Cd concentrations compared to those from the Se concentrations indicate an excess amount of Cd in the NPL samples, which is also common for colloidal quantum dots. To investigate this observation, the Cd-to-Se molar ratio (Cd/Se ratio) of the purified samples was calculated by using the results of ICP-OES measurements. The ratio was found to be 1.80±0.07 for the 4 ML NPL sample and 1.72±0.11 for the 5 ML NPL sample. For the further confirmation, the ICP-MS analysis was also performed and similar ratios were obtained as with the ICP-OES analysis (1.64±0.12 for the 4 ML NPL sample and 1.39±0.10 for the 5 ML NPL sample). These values are higher than the expected theoretical values as discussed in the study by Li et al.[256]. The reasons for these higher ratio values are mainly twofold: First, not only the basal planes but also the side facets of the NPLs terminate with Cd^{2+} ions [256]. Second, the Cd precursor was in excess during the synthesis. Also, the cleaning process with aceton/methanol may not completely remove the excess Cd. As a result, measuring the Se content should provide a more reliable approach in determining the absorption cross-section, which will thus be used for the extraction of molar extinction coefficient.

We also investigated the lateral size dependence of the absorption cross-section for the hh-e absorption band by using the results in Figure 4.4a and Figure 4.4b. The absorption cross-sections (both using the Se and Cd concentrations) were observed to depend on the platelet area as can be seen in Figure 4.4c. The single σ value previously reported in the study of She et al. is comparable to that of our 4 ML NPL with the similar size obtained from the Se concentration [253]. In addition, the experimental σ values for high photon energy at 3.1 eV are shown in Figure 4.4d. Here those obtained from the Cd concentration were observed to be lower than those from the Se concentration as expected. More importantly, the σ trend indicates only a slight nonlinearity in the dependence of the platelet area. To understand these observations, we used a theoretical model derived by Ricard et al. [255], [257], [258]:

$$\sigma(\omega) = \frac{\omega}{n_s c} V_{NPL} \left| f(\omega) \right|^2 \varepsilon_{2,NPL}(\omega) \tag{4.1}$$

where n_s is the refractive index of the nanostructure's surrounding medium, c is the speed of light and $\varepsilon_{2,NPL}(\omega)$ is the imaginary part of the dielectric constant at frequency ω, which is obtained from the literature [207], [258]. The σ values resulting from the model are also presented in Figure 4.4d. Here, the local-field correction factor $|f(\omega)|^2$ is taken in the range between $(0.78)^2$ and $(1.00)^2$, which are the corresponding values for the colloidal CdSe nanowire in hexane and the epitaxial CdSe quantum well [258]. Using the Se concentrations of ICP-OES measurements, the local–field correction factor for the 4 ML NPLs from the best numerical fit to the experimental results was found as ~$(0.86)^2$, which falls between the values for the colloidal nanowire and the epitaxial quantum well. This suggests that NPLs are different than the epitaxial counterparts and that they exhibit a distinct character between the epitaxial quantum wells and the colloidal nanowires. Here it is worth noting that, for the theoretical σ calculations, we chose the high energy value, 3.1 eV, since this model is only valid in the energy region where the confinement effects are insignificant and the NPL absorption is equivalent to that of the bulk case.

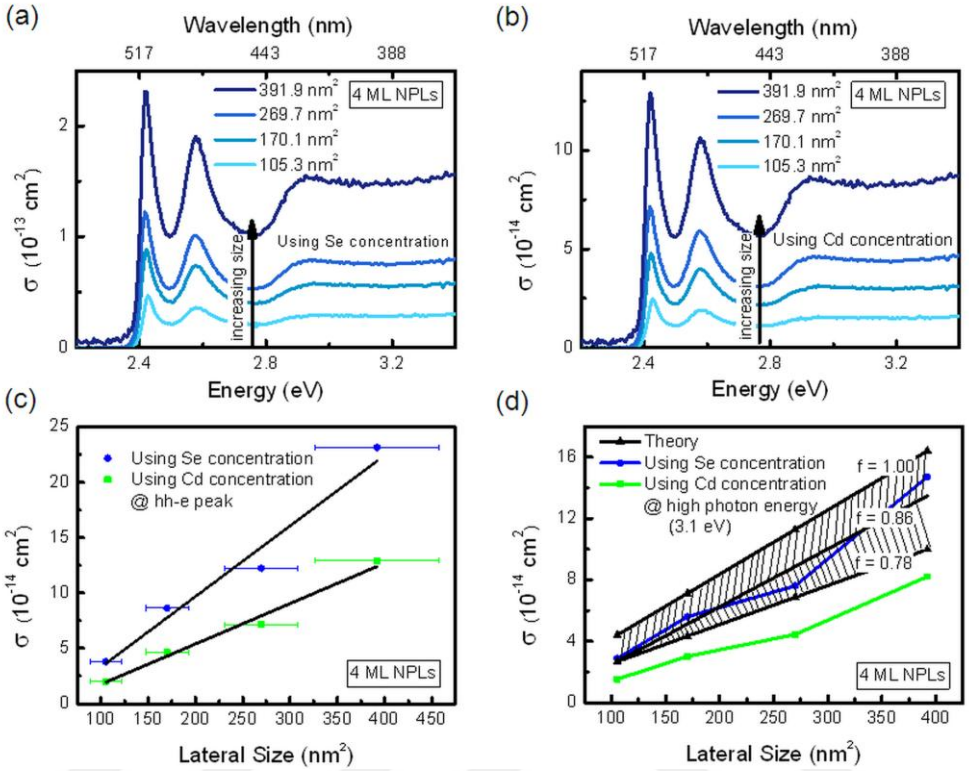

Figure 4.4 Absorption cross-section spectra of 4 ML CdSe NPL samples with varying lateral sizes obtained by using the (a) Se and (b) Cd concentrations from ICP-OES measurements. Lateral size dependence of the absorption cross-section (c) at the energy of hh-e transition peak and (d) at high photon energy 3.1 eV.

The absorption cross-sections of the 5 ML NPLs were also obtained over the absorbance spectrum similar to the 4 ML NPLs. For these measurements, the same sample preparation procedure was followed as in the ICP-OES measurements of the 4 ML NPLs. The σ results for the 5 ML are shown as a function of the absorption energy in Figure 4.5a using the Se concentration and Figure 4.5b using the Cd concentration. Similar to the 4 ML NPL case, here the resulting absorption cross-sections were also observed to increase with the platelet area over the whole absorbance spectrum. Again, the σ values obtained from the Cd concentrations are smaller than those from the Se concentrations due to the excess of Cd in the samples.

For the 5 ML NPLs, the absorption cross-sections for the hh-e absorption band were also obtained by using the results in Figure 4.5a and Figure 4.5b and it was observed that there is a strong lateral size dependence of σ (Figure 4.5c). Tessier et al. reported a similar level of absorption cross-section for a single NPL size, which is comparable to the ones presented here [259]. Herein, the σ trend of the main transition band obtained using the Cd ion concentration exhibits a different slope compared to that obtained using the Se ion concentration. This is probably due to the effect of the excess Cd in the sample, increasing with the lateral area. Moreover, the experimental absorption cross-sections at high photon energy 3.1 eV are also presented in Figure 4.5d and the values obtained from the Cd concentrations are again lower than those from the Se concentrations. For the theoretical σ calculations, we again used the Ricard model. The local–field correction factor for the 5 ML NPLs from the best numerical fit to the experimental data using the Se concentrations of ICP-OES measurements was found to be ~$(0.83)^2$, which is between the values of the colloidal nanowire and the epitaxial quantum well. This is a very similar result as in the case of the 4 ML NPL samples.

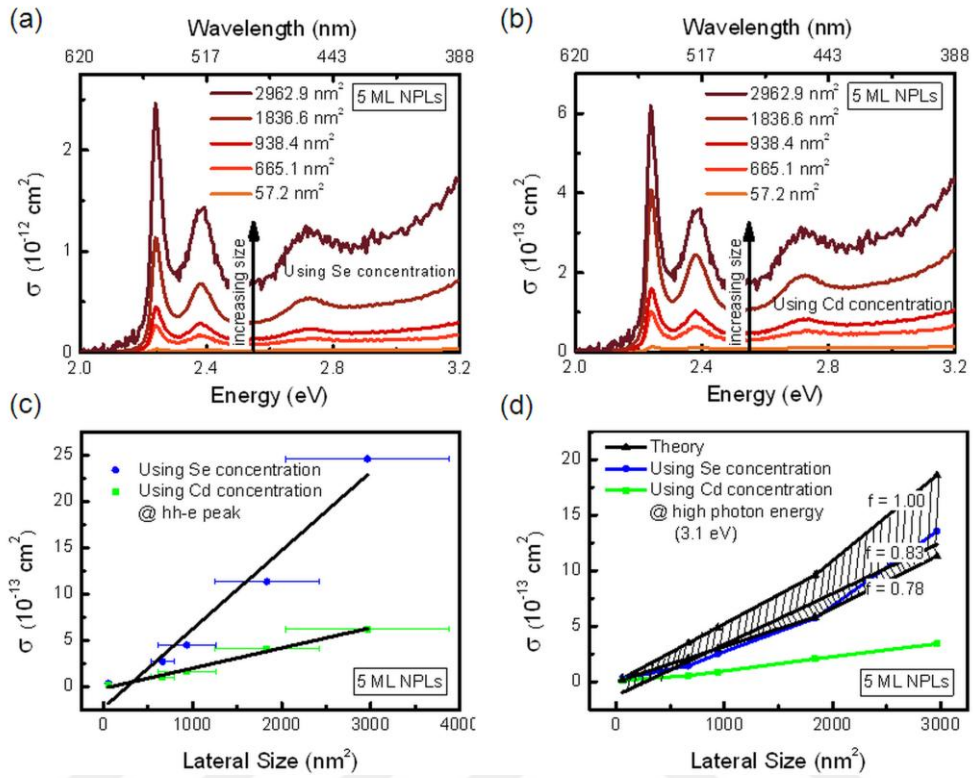

Figure 4.5 Absorption cross-section spectra of 5 ML CdSe NPL samples with varying lateral sizes obtained by using the (a) Se and (b) Cd concentrations from ICP-OES measurements. Lateral size dependence of the absorption cross-section (c) at the energy of hh-e transition peak and (d) at high photon energy 3.1 eV.

The corresponding extinction coefficients of 4 ML and 5 ML CdSe NPLs were extracted from the absorption cross-sections obtained via the ICP-OES measurements of the Se concentrations. The molar extinction coefficients at the transition energy of the hh-e transition peak are given in Figure 4.6a for the 4 ML NPLs and in Figure 4.6b for the 5 ML NPLs. As can be seen from the figures, there is a significant dependence of the extinction coefficient on the lateral area. Using the numerical fitting analysis, we obtained general relations between the molar extinction coefficient and the NPL lateral area given in Eq. 4.2 for the 4 ML NPLs and Eq. 4.3 for the 5 ML NPLs.

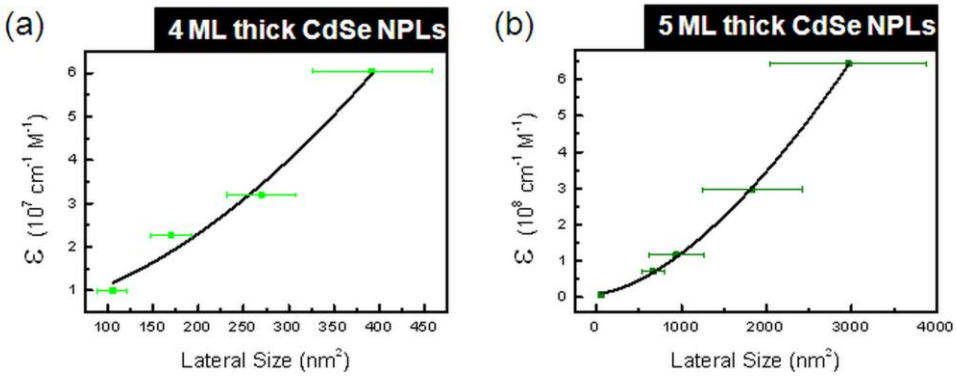

Figure 4.6 Lateral size dependence of the extinction coefficients of (a) 4 ML CdSe NPLs and (b) 5 ML CdSe NPLs obtained by using the Se concentrations from ICP-OES measurements.

$$\text{4 ML CdSe NPLs: } \varepsilon = 6130012 + 1861(LS)^{1.72} \tag{4.2}$$

$$\text{5 ML CdSe NPLs: } \varepsilon = 10377045 + 1757(LS)^{1.60} \tag{4.3}$$

where LS is the lateral size of the NPL and must be taken here in nm^2, which will give ε in the units of cm^{-1} M^{-1}. These empiric formulations will allow for finding concentration (molarity) from the absorption measurement of the 4 ML and 5 ML NPL samples with known lateral size.

In addition, the molar extinction coefficient values at the energy of hh-e transition peak and at the high energy value 3.1 eV are listed in Table 4.1. These extinction coefficients are desirably substantially very high, which makes NPLs promising for optoelectronic applications.

Table 4.1 Corresponding values of 4 ML and 5 ML thick CdSe NPLs at the energy of hh-e peak and at the high energy value 3.1 eV.

Lateral Size (nm^2)	ε for 4 ML thick NPL (cm^{-1} M^{-1})		Lateral Size (nm^2)	ε for 5 ML thick NPL (cm^{-1} M^{-1})	
	hh-e peak 2.42 eV	high energy 3.1 eV		hh-e peak 2.24 eV	high energy 3.1 eV
105.3 ± 16.4	$9.92x10^6$	$7.54x10^6$	57.2 ± 18.2	$7.94x10^6$	$7.79x10^6$
170.1 ± 22.5	$2.26x10^7$	$1.46x10^7$	665.1 ± 129.5	$7.05x10^7$	$3.76x10^7$
269.7 ± 38.6	$3.19x10^7$	$1.99x10^7$	938.4 ± 325.0	$1.17x10^8$	$6.49x10^7$
391.9 ± 65.8	$6.05x10^7$	$3.85x10^7$	1836.6 ± 584.6	$2.96x10^8$	$1.49x10^8$
			2962.9 ± 918.1	$6.43x10^8$	$3.54x10^8$

Inductively Coupled Plasma Mass Spectroscopy for further confirmation: To verify the results from the ICP-OES measurements, we used another spectroscopy technique, ICP-MS. Based on the Se and Cd concentrations obtained from ICP-MS, the absorption cross-sections over the large absorption spectra were obtained for the same NPLs. For this purpose, the NPL samples were diluted to reliable measurement ranges for ICP-MS. The results for the 4 ML NPLs using the ICP-MS technique are depicted in Figure 4.7a based on the Se concentration and Figure 4.7b based on the Cd concentration. As seen from the figure, the absorption cross-section increases with the platelet area for the whole absorption range. The σ results extracted using both the Se and Cd ICP-MS concentrations of 4 ML NPLs are consistent with those from the ICP-

OES measurements in terms of the trend. However, due to the dilution process, the measurable range of sizes has been limited with ICP-MS. Also in the case of ICP-MS similar to ICP-OES, the absorption cross-sections from the Cd concentrations are lower than those from the Se concentrations due to the excess Cd in the samples. Furthermore, the absorption cross-sections at the transition energy of hh-e peak exhibit a monotonous trend over the platelet area (Figure 4.7c) and this is strongly correlated with the trend observed in the ICP-OES measurements.

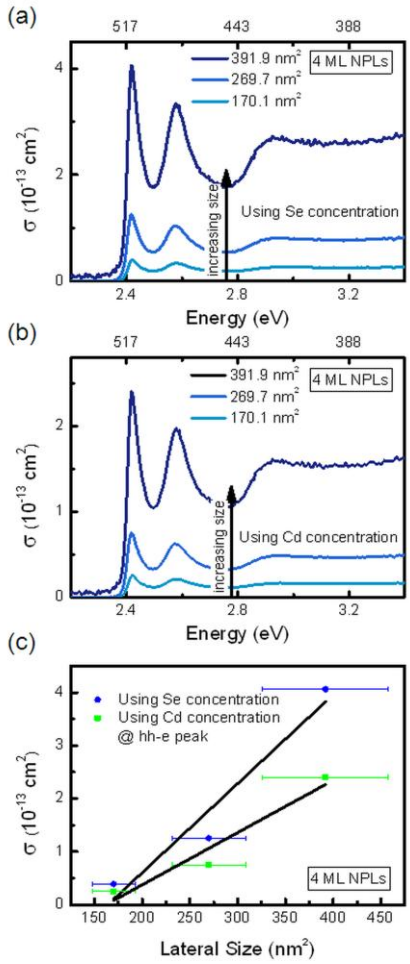

Figure 4.7 Absorption cross-section spectra of 4 ML CdSe NPL samples with varying lateral sizes obtained by using the (a) Se and (b) Cd concentrations from ICP-MS measurements. Lateral size dependence of the absorption cross-section (c) at the energy of hh-e transition peak.

The absorption cross sections of the 5 ML NPLs obtained via the ICP-OES technique were also confirmed by using the ICP-MS technique. The resulting absorption cross section spectra are shown in Figure 4.8a using the Se concentration and Figure 4.8b using the Cd concentration. It was observed that the σ values increase with the platelet area as in the case of the ICP-OES measurements and the values from the Cd concentrations are smaller than those from the Se concentrations as expected. Moreover, as can be seen in Figure 4.8c, the σ values at the hh-e transition peak present a monotonically increasing trend over the lateral size, which is in good agreement with the trend observed for the ICP-OES results of the same samples.

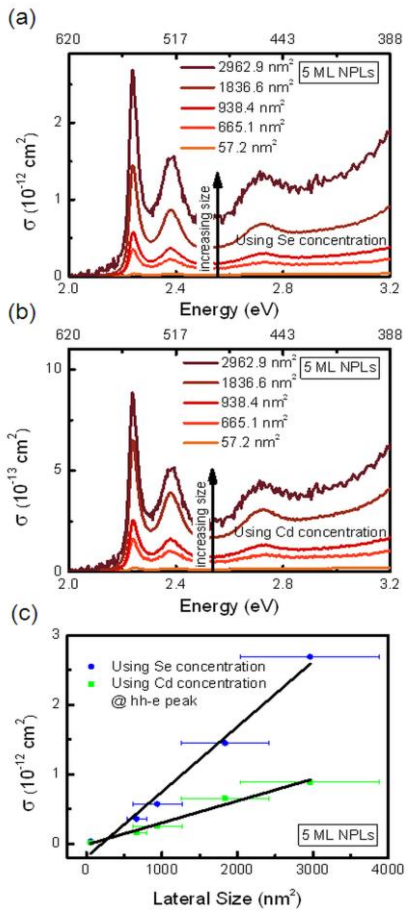

Figure 4.8 Absorption cross-section spectra of 5 ML CdSe NPL samples with varying lateral sizes obtained by using the (a) Se and (b) Cd concentrations from ICP-MS measurements. Lateral size dependence of the absorption cross-section (c) at the energy of hh-e transition peak.

Oscillator Strength and Intrinsic Radiative Lifetime of Nanoplatelets: The intrinsic radiative rate γ and the oscillator strength f of the hh-e exciton can be calculated by integrating σ over the transition band [260]–[262].

$$\gamma = \frac{8\pi}{\lambda^2}\int_{\nu_1}^{\nu_2}\sigma(\nu)d\nu \tag{4.4}$$

$$f = \frac{4m\varepsilon_0 c}{e^2}\int_{\nu_1}^{\nu_2}\sigma(\nu)d\nu \tag{4.5}$$

where ν_1 and ν_2 are the start and end frequencies of the hh-e absorption band (in Hz), λ is the wavelength of the hh-e transition peak (in cm), m is the mass of an electron, ε_0 is the permittivity of free space, c is the speed of light, and e is the charge of an electron. The integral was performed by fitting a Gaussian function to the hh-e band and then integrating over the fitted band shape. The radiative lifetime is the reciprocal of γ

$$\tau = \frac{1}{\gamma} \tag{4.6}$$

The room-temperature intrinsic radiative lifetimes were calculated by using Eq. 4.4 and Eq. 4.6. As given in Figure 4.9a and Figure 4.9b, for both the 4 ML and 5 ML NPLs, the radiative lifetimes are found on the order of picoseconds and the values are decreasing with the NPL lateral area. These room-temperature radiative lifetimes, which are on the order of picoseconds, and the lateral size dependence of the NPL intrinsic radiative lifetime are in good agreement with the reports in the literature [86], [250].

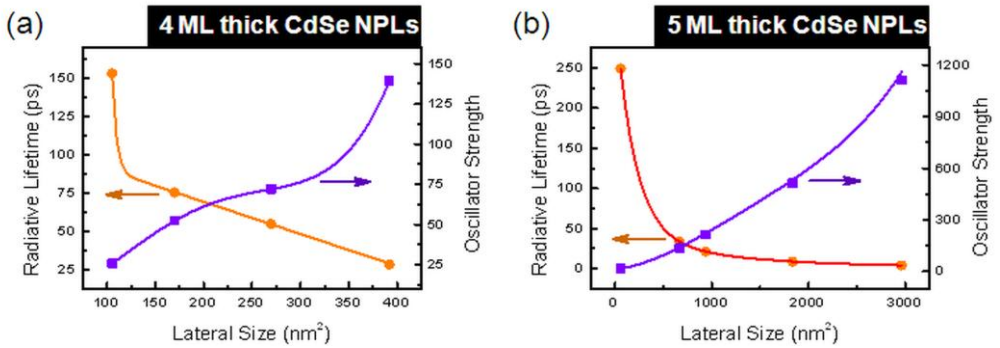

Figure 4.9 Dependence of the intrinsic radiative lifetime of the hh-e transition and the oscillator strength on the lateral size of (a) 4 ML and (b) 5 ML thick CdSe NPLs using the results obtained from the Se concentrations of ICP-OES measurements.

In addition, the oscillator strength of the hh-e transition band was calculated for all the NPLs used in the study by using Eq. 4.5. As can be seen from Figure 4.9a and Figure 4.9b, the oscillator strength increases with the NPL area. According to the oscillator strength sum rule [263], this indicates that a large number of electrons are involved in the hh-e transition. Such high oscillator strength values explain the short lifetimes on the order of picoseconds and the giant oscillator strength effect in the 2D systems and energy transfer [55], [250], [251], [264].

Experimental Errors: The experimental errors in this study should mainly come from the size distribution of the NPLs and the determination of the NPL size using TEM technique [254]. In addition, twists and breaks for the big NPLs can give some additional error to the exact determination of the size via TEM [265], [266]. Moreover, extraction and precipitation procedures cannot completely remove the unconverted Cd atoms from the Cd precursors.

4.1.4 Summary

In summary, we have systematically demonstrated that the absorption cross-sections and the extinction coefficients of the 4 ML and 5 ML NPLs strongly depend on the lateral size. The per-NPL absorption cross-section and molar extinction coefficient at

the hh-e energy band, and the per-NPL absorption cross-section in the high photon energy regime were observed to increase substantially with the platelet area. We obtained empiric formulae relating the molar extinction coefficients to the lateral size for specific thickness (4 ML and 5 ML) of the NPLs, which will be very useful for calculating molarity from absorption data for the NPL samples of known lateral size. We also showed that the intrinsic radiative lifetimes of the first-exciton transition at the hh-e band decrease with the increasing lateral area. Correspondingly, the first-exciton oscillator strengths increase with the lateral size for both the 4 ML and 5 ML NPLs. We believe that the findings presented in this study will help to exploit NPLs for next-generation optoelectronic applications.

4.2 Nonradiative energy transfer between quasi-2D colloidal doped and undoped semiconductors

This section is based in part on the publication "Nonradiative Energy Transfer between Quasi-2D Colloidal Doped and Undoped Semiconductors," A. Yeltik, M. Olutas, M. Sharma, K. Gungor and H. V. Demir, in submission.

4.2.1 Motivation

Colloidal luminescent quasi-2D NPLs have been one of the potential key elements of modern nanotechnological applications for less than a decade. Among the group II-VI semiconductors, the NPLs having cadmium-based zincblende structure have been widely studied in terms of optical and excitonic properties [76]–[88]. They have superior properties such as spectrally narrow emission (FWHM < 10 nm) due to their 1D precise thickness control, large absorption cross section thanks to their large exciton binding energy and thus the giant oscillator strength, and high close packing intensity along with suppressed Auger recombination property. All the ultimately significant characteristics of these quantum well nanostructures allow them to become

favorable candidates in several optoelectronic applications including LEDs, solar cells, low-threshold amplified spontaneous emission and lasing [79], [85], [92], [253], [267].

In the recent years, doped quantum dots (QDs) have emerged as entirely new form of phosphor materials exhibiting innovative features in the fields of nanophotonics, nanooptoelectronics and biology [268]–[276]. Other than the 0D phosphors, copper doped quasi-2D NPLs have great potential especially in luminescent solar concentrators, possessing a broad and high Stock-shifted sub-band-gap copper-related photoluminescence (PL), and thus almost unaffected energy conversion efficiency due to the absence of self absorption. Furthermore, copper-related emission is much broader than the band edge emission due to the strong electron-phonon coupling at these dopant states [277], which is an important feature for the efficient NRET from doped to undoped NPLs. Additionally, Cu-doped cadmium-based NPLs are providing a particularly important platform for the investigation of exciton kinetics in colloidal quasi-2D doped/undoped hybrids by using the NRET phenomenon.

NRET is an energy transfer mechanism through dipole-dipole Coulombic interaction in the material system of suitable donor-acceptor pair. Efficiency of the NRET is essentially dependent on various factors including the extent of being in close proximity of donor and acceptor, the extent of overlapping spectra of donor emission and acceptor absorption, quantum yield (QY) of the donor, the dipole orientation factor and the refractive index of the medium in which the pair is located [159], [278]. Hybrid nanostructures including Cu-doped and undoped NPLs have great potential to satisfy all these requirements for the highly efficient NRET. All the features of Cu-doped cadmium-based NPLs together with their undoped counterparts indicate that they are strong candidates to be used as hybrids in next-generation light-harvesting and light sensing optoelectronic applications along with possible bio- and chemi-applications.

Previously, the PL energy transfer between doped and undoped QDs was investigated by Pradhan and coworkers, reporting the transfer efficiency of 0.39 [279]. However, any study has not been done yet for the doped-undoped NPL structures, which offers superior characteristics compared to the QD hybrids. In this study, we investigate the NRET between colloidal Cu-doped CdSe and undoped CdSe/CdS

NPLs. We demonstrate the nonradiative quenching of PL from Cu-related trap state by increasing the number of undoped nanoplatelets in close proximity. We report the first and record energy transfer efficiency of 0.99 for the 2D doped/undoped hybrid structures at room temperature. All these findings indicate that our colloidal quasi-2D hybrid nanosystems may exhibit new opportunities for the efficiency enhancement of different photonic and optoelectronic devices.

4.2.2 Experiment

The transmission electron microscopy (TEM) images of the Cu-doped 3ML CdSe core NPLs and undoped 4ML/5ML CdSe/CdS core/shell NPLs are shown in Figure 4.10a and Figure 4.10b, respectively. Undoped and Cu-doped NPLs were synthesized via the hot-injection technique [280], [281]. A schematic of our experimental system including the doped and undoped NPLs is depicted in Figure 4.10c. Ensemble of the Cu-doped NPLs in toluene has Cu-state-related PL at around 620 nm along with the band-edge emission at around 465 nm as seen from Figure 4.10d. Their absorbance spectrum is starting at the point little blue-shifted from the band-edge PL peak of the 3ML CdSe NPLs as expected (Figure 4.10d). The samples including undoped CdSe/CdS NPLs in toluene have PL peak at around 660 nm, which is significantly red-shifted with respect to the PL peak of the doped samples. The PL spectra of the doped and undoped samples do not significantly overlap at the wavelength of peak intensity of donor Cu-doped NPLs (620 nm). The small amount of overlap was further investigated by doing the experiments also at the second absorption peak of the undoped NPLs (598 nm). As shown in Figure 4.10d, absorbance spectrum of the acceptor undoped NPLs exhibits significant overlap with the emission of donor Cu-doped NPLs, which is a favorable condition along with the absence of cross-talk in the PL spectra to achieve efficient NRET in these systems.

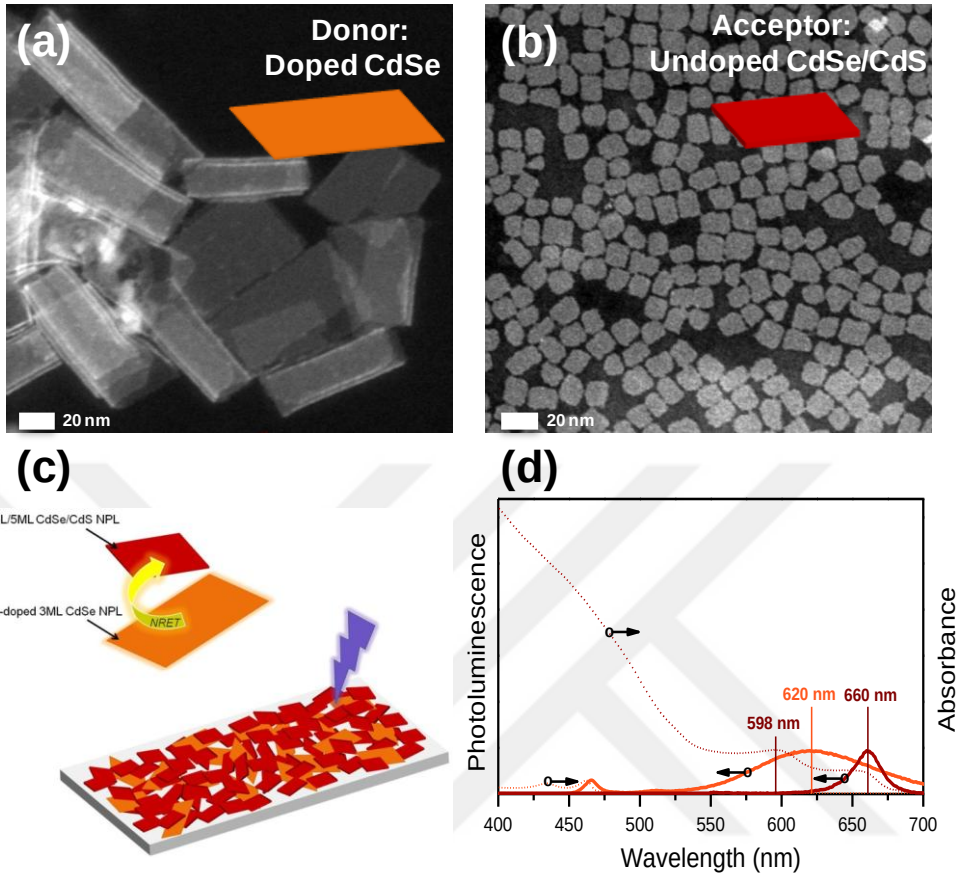

Figure 4.10 TEM images of the (a) Cu-doped 3ML core NPLs and (b) undoped 4ML/5ML CdSe/CdS core/shell NPLs. (c) Schematic of our hybrid structure including the Cu-doped and undoped NPLs. (d) Photoluminescence and absorbance spectra of the Cu-doped and undoped NPLs in toluene.

4.2.3 Results and discussion

Systematic study of the NRET in the hybrid films of the doped and undoped NPLs was performed first by doing the steady-state PL measurements with the excitation pumping at 350 nm. The PL spectra of only-donor NPLs, only-acceptor NPLs and the hybrid of these NPLs with the molar D/A ratio of 2.5×10^{-5} were obtained as presented in Figure 4.11. Donor PL from the band-edge and Cu-related states is strongly quenched to almost zero level in the hybrid film, resulting in significant enhancement

in the acceptor PL from the acceptor band-edge state. Since the NPLs are in close proximity in the samples, the transfer is expected to be dominated by the NRET mechanism and negligibly affected by radiative energy transfer mechanism including photon emission-absorption processes. The PL intensities of the only-donor and hybrid samples suggest the energy transfer efficiency as ~ 0.93. This is a significantly high value for this kind of colloidal nanoparticle hybrid systems. However, much higher values could be obtained if the donor had higher quantum efficiency exhibiting higher PL emission in both the only-donor and hybrid samples simultaneously. In order to further analyze this potential of the samples and to reveal directly the NRET efficiencies and rates, we systematically studied the time-resolved PL kinetics in the samples with varying D/A ratio along with the only-donor and only-acceptor cases.

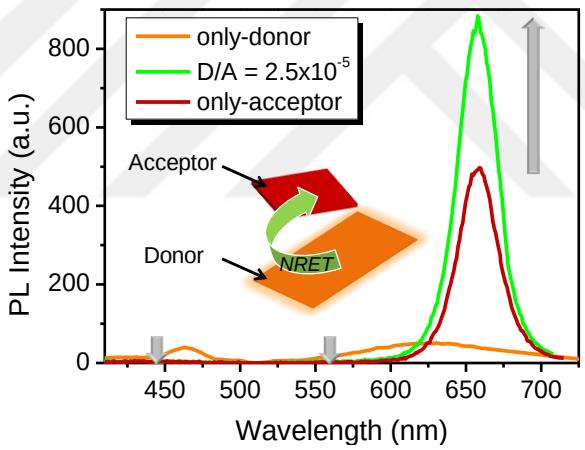

Figure 4.11 Steady-state PL spectra of the solid films of only-donor (orange), only-acceptor (red) and donor–acceptor having D/A = 2.5x10-5 (green) cases.

We performed the time-resolved PL measurements by using a time-correlated single photon counting system having a time resolution down to 4 ps and a picosecond pulsed laser with an output photon energy of 3.307 eV (375 nm). The PL decay curves were obtained at room temperature and at low power intensity for various donor/acceptor (D/A) molar ratios. The curves were measured at the Cu-state-related PL peak of the donor NPLs (620 nm) and at the second excitonic absorption peak of the acceptor NPLs (598 nm).

Figure 4.12 shows the time-resolved PL decay curves of the samples having discrete D/A molar ratios at the peak PL wavelength of the donor, which is around 620 nm. As depicted in Figure 4.12a, PL decay of the donor NPLs becomes faster as the acceptor concentration in the hybrid film increases. It is also seen from the first few nanoseconds of the curves presented in Figure 4.12b along with the instrument response function curve that this behavior is obviously not in the limits of our experimental system. This feature of the curves is a strong evidence of opening a new nonradiative channel for the excited state energy relaxation in the donor NPLs due to the acceptor NPLs around in close proximity.

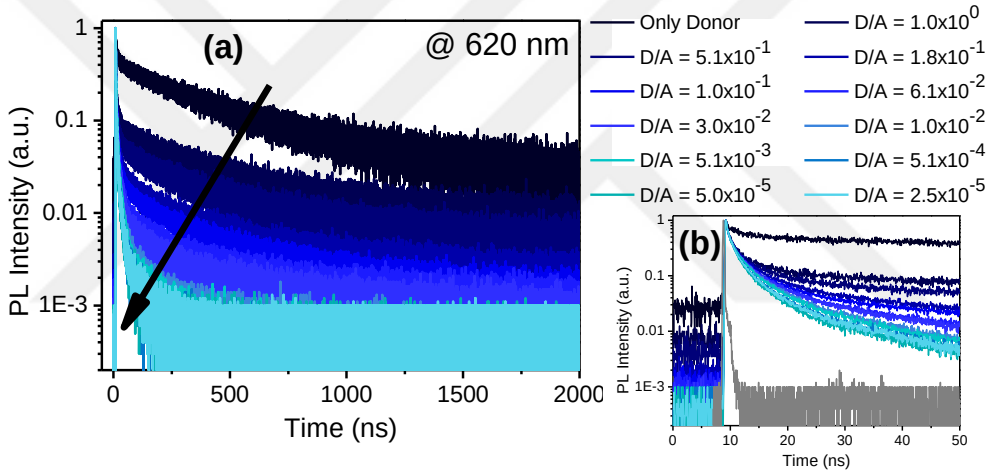

Figure 4.12 Time-resolved PL decay curves at the donor trap emission peak wavelength, 620 nm, for various D/A concentration ratios.

In order to further examine the findings from the PL decay curves at the donor Cu-related peak emission wavelength (620 nm), we performed the time-resolved PL spectroscopy with the same samples having discrete D/A ratios but at a different emission wavelength, which is the wavelength of the acceptor second absorption peak (598 nm). Besides no cross-talk of the donor and acceptor emissions, another reason for choosing this wavelength is to analyze the possible effect of the very small overlapping in the donor emission with the acceptor emission at 620 nm. As shown in Figure 4.13a, faster decays were observed at 598 nm with the decreasing D/A molar

ratio, which is an agreed result previously obtained at 620 nm (see Figure 4.12). The curves are also far from the limits of the time-resolved PL instrumentation as shown in Figure 4.13b, which supports the reliability of the results.

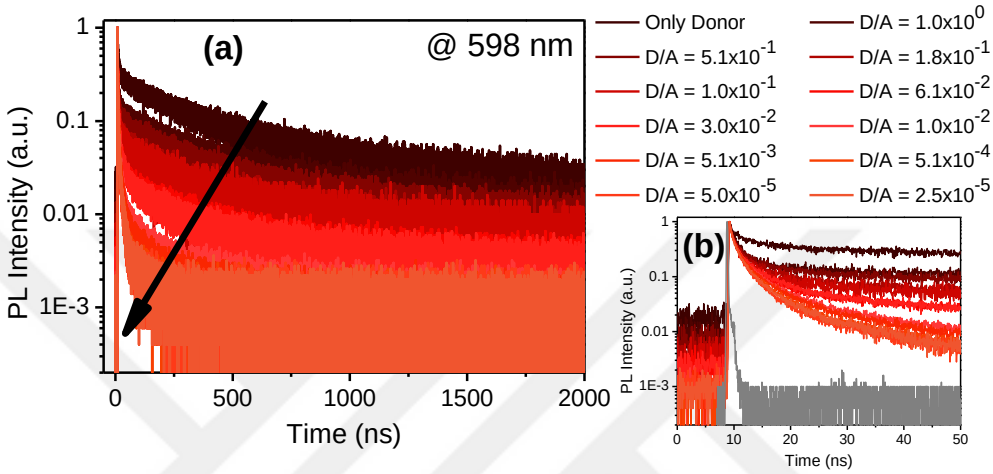

Figure 4.13 Time-resolved PL decay curves at the acceptor second excitonic absorption peak wavelength (598 nm) for various D/A ratios.

The decay curves at the band-edge peak emission wavelength of the donor NPLs (465 nm) were also measured. As shown in Figure 4.14, we did not observe any obvious behavior in the time-resolved PL curves at the donor band-edge PL peak wavelength, 465 nm, for the various D/A ratios used in the study. The small variations are negligible when compared to those in the curves at the donor trap-related peak emission wavelengths, 620 nm and 598 nm (Figure 4.12 and Figure 4.13). Up to the saturation value of the D/A ratio, ~ 6.1 x 10^{-2}, the shortening in the curves is negligibly small as given in Figure 4.14a. After that point, as the D/A ratio further decreases, the decays behave in the opposite way, elongating in again small extents (Figure 4.14b). This elongation can be due to the variation in the dielectric medium resulting from the already saturated number of acceptor NPLs. These results indicate that the NRET is considerably originated from the Cu-trap-related states. Furthermore, the band-edge emission of the acceptor at 660 nm was also recorded for the various D/A cases; however, due to the cross-talk of the donor and acceptor PL, not quantitative but the

qualitative analysis of the decays at this wavelength is presented here. Figure 4.15 shows the time-resolved PL decays for various D/A ratios and measured at 660 nm, which is the acceptor trap emission peak wavelength. As seen from the figure, as the concentration of the acceptor NPLs increases in the donor-acceptor hybrid film, the curves resemble much more to the curve of the only-acceptor case as expected.

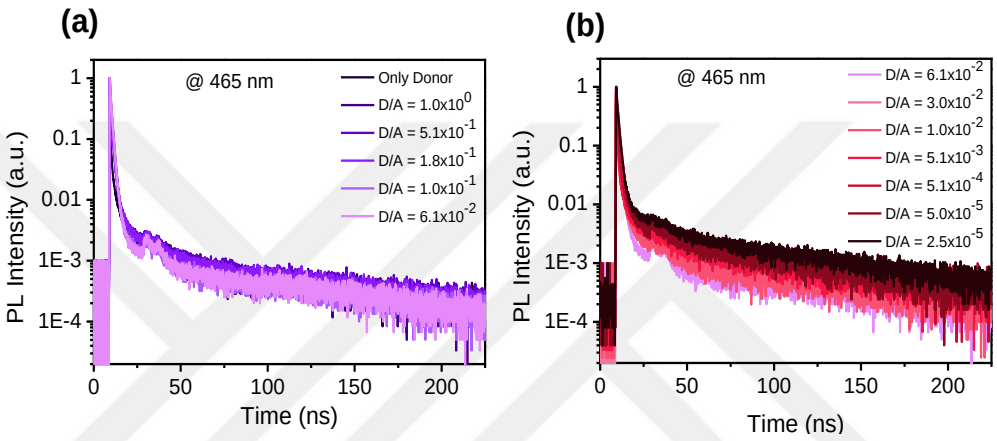

Figure 4.14 Time-resolved PL decay curves at the donor band-edge emission peak wavelength (465 nm) for various D/A ratios. Note: The data in (a) were continued in (b).

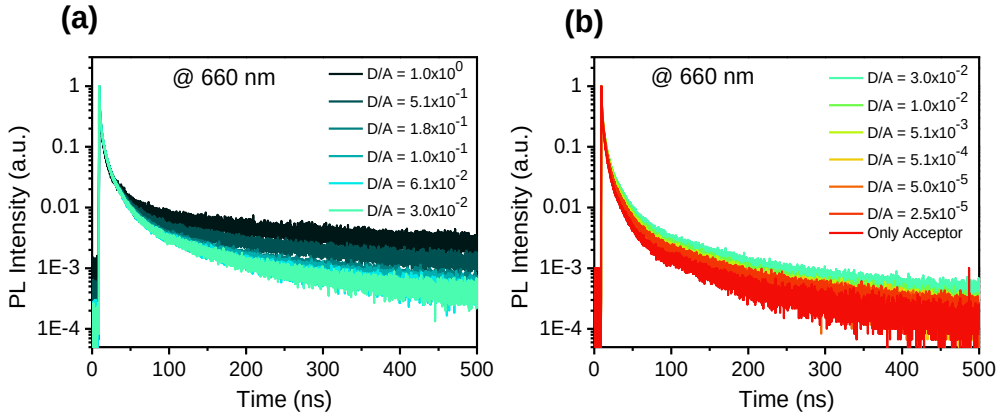

Figure 4.15 Time-resolved PL decay curves at the acceptor trap emission peak wavelength (660 nm) for various D/A ratios. Note: The data in (a) were continued in (b).

The time-resolved PL decay curves obtained at the wavelengths of 620 nm and 598 nm were analyzed through the fitting with a multi-exponential decay function having four exponential components. Four different components in the fitting function can be attributed to four completely independent or partially dependent decay channels in the NPL and it is an intrinsic property of the colloidal nanomaterials as it was previously observed in the literature [282], [283]. PL intensities of the only-donor solid film exhibits amplitude-averaged lifetimes (τ_{av}) as 191.9 ns at 620 nm and as 127.4 ns at 598 nm. These average decay lifetimes decrease to 2.2 ns at 620 nm and 2.1 ns at 598 nm in the best sample case with D/A = 5.0×10^{-5}. Furthermore, they saturate at around these values of the best sample case. Major modifications in the PL lifetimes of the donor as a function of the increasing acceptor-to-donor ratio are strong indications of the NRET from the donor Cu-doped core NPLs to the acceptor undoped core/shell NPLs. Further analysis of the donor PL lifetimes provides the NRET rates and efficiencies as presented in Table 4.2. The analysis of the NRET rates was done by using the Eq. 4.7. As seen from the table, the NRET rates at both the wavelengths, 620 nm and 598 nm, increase with the number of acceptor per donor, reaching to the maximum value of around 0.46 (Table 4.2).

$$\gamma_{NRET} = \frac{1}{\tau_{DA}} - \frac{1}{\tau_D} \tag{4.7}$$

where τ_{DA} and τ_D are the amplitude-averaged PL lifetimes of the donor NPLs in the presence and absence of acceptor NPLs, respectively. As also given in Table 4.2, record NRET efficiencies were obtained by using the following relation

$$\eta_{NRET} = \frac{\gamma_{NRET}}{\gamma_{NRET} + \tau_D^{-1}} = 1 - \frac{\tau_{DA}}{\tau_D} \tag{4.8}$$

Table 4.2 PL decay lifetimes (τ), NRET rates and NRET efficiencies of the donor NPLs for the samples with varying D/A ratios.

D/A ratio	τ_{av_donor} (ns) @ 620 nm	τ_{av_donor} (ns) @ 598 nm	γ_{NRET} (ns-1) @ 620 nm	γ_{NRET} (ns-1) @ 598 nm	η_{NRET} @ 620 nm	η_{NRET} @ 598 nm
$2.5x10^{-5}$	2.4	2.3	0.419	0.427	0.99	0.98
$5.0x10^{-5}$	2.2	2.1	0.456	0.468	0.99	0.98
$5.1x10^{-4}$	2.5	2.5	0.401	0.394	0.99	0.98
$5.1x10^{-3}$	2.9	3.7	0.341	0.262	0.99	0.97
$1.0x10^{-2}$	3.1	4.1	0.319	0.239	0.98	0.97
$3.0x10^{-2}$	4.5	9.4	0.219	0.099	0.98	0.93
$6.1x10^{-2}$	5.1	10.1	0.191	0.091	0.97	0.92
$1.0x10^{-1}$	9	15.7	0.106	0.056	0.95	0.88
$1.8x10^{-1}$	10	22.5	0.095	0.037	0.95	0.82
$5.1x10^{-1}$	21	37.7	0.042	0.019	0.89	0.7
$1.1x10^{0}$	34.2	44.9	0.024	0.014	0.82	0.65
Only Donor	191.9	127.4	_	_	_	_

Figure 4.16 depicts the NRET efficiencies as a function of the varying ratio of D/A molar concentration. Progressive increase saturating at high efficiency levels with the decreasing D/A ratio is observed due to the large absorption cross-section of the acceptor NPLs. As seen from the figure, the saturations occur at around 0.99 (for the emission wavelength of 620 nm) and at around 0.98 (for the emission wavelength of 598 nm). These are, to the best of our knowledge, the first and highest reported NRET efficiencies in the doped-undoped hybrids of colloidal quasi-2D quantum well structures. Previously, the NRET efficiency was reported for the undoped QD-QD donor-acceptor pairs up to 0.80 [284], [285]; for the undoped QD-NPL pairs up to 0.90 [49]; and for the undoped NPL-NPL pairs up to 0.60 [85] and 0.90 [267] at room temperature. Another important point is the saturation molar ratio value of the efficiencies, which is starting at ~ 0.1 and reaching to the saturation value at ~ 0.02. From the surface calculations, we also obtained the saturation value at ~ 0.02, which is in good agreement with the experimental results in Figure 4.16.

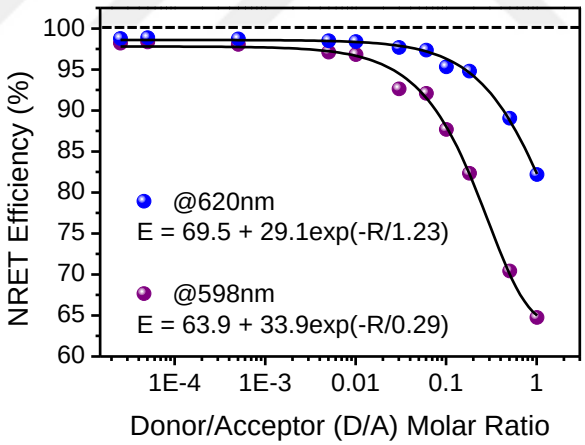

Figure 4.16 NRET efficiency as a function of Donor/Acceptor (D/A) molar ratio.

Further analysis was performed on the NRET efficiencies including single donor and multiple numbers of acceptor to obtain the efficiency for a single donor-acceptor (D-A) pair in the ensemble of NPLs. To this end, we used a well-known model developed by Raicu [170], [171]. As presented in Figure 4.17, efficiency per D-A pair

was calculated as almost the same up to a saturation value of D/A molar ratio and then it rapidly decreases to very small values of around zero. The decreasing behavior in the pair efficiencies is due to the approximation of constant dependence of the NRET to the distance between donor and acceptor in a pair. This drawback of the model is favorable for us to observe the D/A ratio of a single pair at the efficiency saturation point, which is significant to explain the behavior in the NRET efficiencies from the ensemble measurements (Figure 4.16). The saturation values from the ensemble measurements and the single-pair calculations (~ 0.1) are consistent with each other. This method provided useful and important evaluation of the NRET efficiencies from our ensemble measurements.

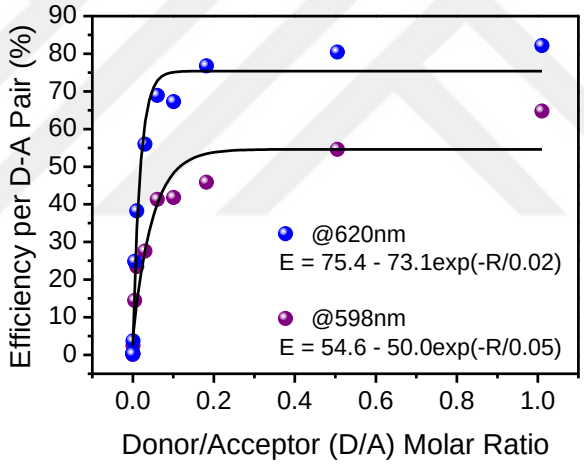

Figure 4.17 NRET efficiency for a single D/A pair as a function of D/A molar ratio.

For further steady-state PL investigation of the NRET, photoluminescence excitation (PLE) spectroscopy was carried out in the hybrid solid films along with the only-donor and only-acceptor samples. The PLE spectra of the bare donor and acceptor films, which were measured at their peak PL wavelengths, are shown in Figure 4.18a. As seen from the figure, the excitation spectra exhibit similar features as the absorption spectra of the NPLs (see Figure 4.10d). After this confirmation of the PLE spectra, we measured the excitation spectra of the hybrid films having discrete D/A molar ratios: $1.0\text{x}10^{0}$, $1.0\text{x}10^{-1}$, $1.0\text{x}10^{-2}$ and $5.1\text{x}10^{-4}$. Figure 4.18b depicts the excitation spectra of

the hybrid NPL films, which are measured at the acceptor peak emission wavelength, 660 nm. These PLE spectra are normalized at the second excitonic absorption peak (~ 598 nm) of the acceptor NPLs since the donor NPLs do not possess absorption at this spectral region (see Figure 4.10d). These normalized excitation spectra of the NPLs show gradual enhancement in the PL intensity at shorter wavelengths with increasing number of donor NPLs per an acceptor NPL. This result is in good agreement with the phenomenon of exciton funneling from the donor to the acceptor. The PLE spectra were further examined for the enhancements in the hybrid samples by dividing the normalized excitation spectra of the hybrids with those of the only-acceptor sample. The relative variations in the acceptor emission through the NRET are represented for the corresponding molar ratios in the inset of Figure 4.18b. With the increasing number of donor doped NPLs relative to the acceptor undoped NPLs; the PLE spectrum resembles the absorption features of the donor NPLs.

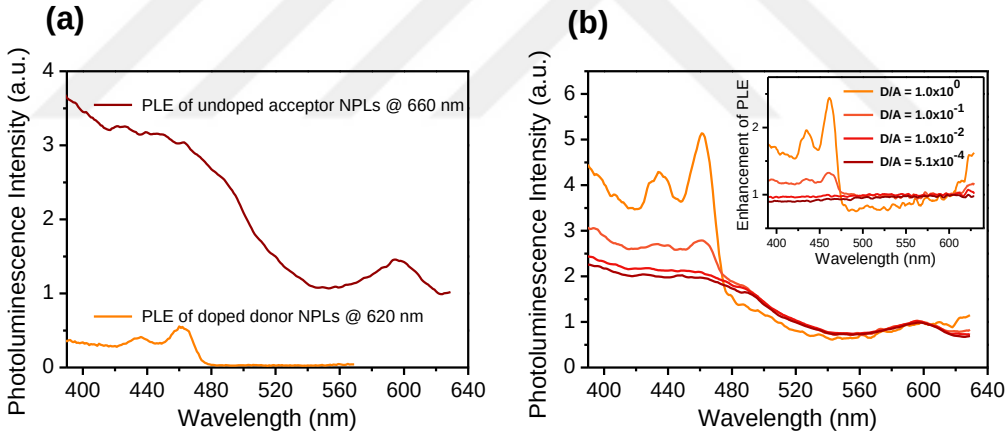

Figure 4.18 (a) PLE spectra of the doped donor NPLs (orange) and the undoped acceptor NPLs (red) measured at their Cu-related emission peak wavelength (620 nm) and excitonic emission peak wavelength (660 nm), respectively. (b) Photoluminescence excitation spectra of the samples having different D/A ratio, measured at 660 nm and then normalized at the second excitonic (e-lh transition) peak wavelength (598 nm) of the acceptor. Inset figure shows the enhancement of PLE through the NRET in the hybrid donor–acceptor samples.

4.2.4 Summary

In summary, we studied the efficiency of excitonic energy transfer between colloidal Cu-doped core CdSe and undoped core/shell CdSe/CdS nanoplatelets. We showed the PL quenching of the donor Cu-doped NPLs and the systematic modifications in the time-resolved PL kinetics when the acceptor undoped NPLs are located in close proximity. To this end, we used steady-state and time-resolved PL spectroscopy techniques. The first and record energy transfer efficiency in our all-colloidal and all-2D system was reported as 0.99 at room temperature. All these investigations and results provide fundamentally important knowledge for the NRET dynamics of 2D colloidal hybrid material systems. We also believe that such strongly efficient NRET in these quantum confined structures will enable high-performance photonics and optoelectronics including Cu-doped nanoplatelets.

Chapter 5

Conclusions

5.1 Concluding remarks

In this thesis, we have demonstrated the phonon assistance in the NRET from the CdSe/ZnS CQDs to bulk silicon as an indirect bandgap semiconductor both experimentally and theoretically. The temperature-dependent fluorescence lifetimes and energy transfer efficiencies were obtained in the hybrid CQD-silicon nanostructures to reveal the dynamics of NRET. For the systematic study of the underlying physics behind NRET, the CQD-silicon nanostructure platforms with varying separation thicknesses between the donor CQDs and the acceptor silicon were utilized. Our experimental data have showed that NRET from the CQDs into silicon substrates becomes weaker at low temperatures. This important result was attributed to the phonon involved interband transitions in silicon. Following this experimental finding, a temperature independent analytical model was developed by using dipole-dipole interactions. From this model, we obtained d-3 distance dependence and then suggested a modified physical model introducing temperature effects based on phonon-assisted absorption into this analytical model. The model that we suggested proved to be successful in analyzing and explaining temperature dependence, leading to reasonably well matching results with the experimental data. Additionally, full

temperature-dependent model was also presented to improve the consistency between the theoretical and the experimental results. Therefore, these findings strongly indicate the assistance of phonons in the NRET for the structures including indirect bandgap acceptor.

We have also demonstrated strong enhancement in the exciton population transferred into Si by using the energy-gradient hybrid structures composed of cascaded bilayered green- and red-emitting CQDs on Si. NRET dynamics were investigated for the cascaded structure and the structures with mono-dispersed CQDs. For the cascaded architecture, exciton transfer efficiency of 41% from the green-emitting CQDs into the red-emitting CQDs and of 80% subsequently from the red-emitting CQDs into Si was achieved at room temperature. As compared to the exciton population for the red-CQD/red-CQD/Si structure, the enhancement factor of exciton transfer into Si for the cascaded structure was found to be ~1.4, which is in agreement with the theoretical results of ~1.5.

We have also uncovered the significance of NRET from CdSe/CdS CQDs into uniformly coated GO and RGO thin layers by using TRF spectroscopy. As the separation distance between the CQDs and GO or RGO decreases, TRF lifetimes were observed to be shortening. This behavior in the lifetimes indicates faster NRET rates. For both the CQDs-GO and CQDs-RGO hybrids, the NRET mechanism consists of excitonic-NRET (exciton transfer) at longer separations, and both excitonic NRET (exciton transfer) and non-excitonic NRET (charge transfer) at shorter distances. In close proximity, NRET rate from the CQDs into RGO layer is higher than the CQDs into GO layer, which results from the structural defects. However, rates are almost the same for both the hybrid nanostructures at longer separations (> 5 nm). Furthermore, NRET efficiencies were calculated from the experimental data to be high around 97% and 89% for the closest separation of the CQD-RGO and the CQD-GO pairs, respectively. As an additional study, we could also grow 2D MoS_2 mono-/bi-layers on SiO_2/Si substrates and performed a preliminary temperature-dependent TRF study.

We have also demonstrated the strong dependence of absorption cross-sections and the extinction coefficients of the 4 ML and 5 ML NPLs on the lateral size. The

absorption cross-section per NPL and the molar extinction coefficient at the hh-e energy band, and the absorption cross-section per-NPL in the high photon energy regime were observed to increase substantially with the platelet area. We obtained empiric formulae relating the molar extinction coefficients to the lateral size for specific thickness (4 ML and 5 ML) of the NPLs, which will be very useful for calculating molarity from absorption data for the NPL samples of known lateral size. We also showed that the intrinsic radiative lifetimes of the first-exciton transition at the hh-e band decrease with the increasing lateral area. Correspondingly, the first-exciton oscillator strengths increase with the lateral size for both the 4 ML and 5 ML NPLs. We believe that the findings presented in this study will help to exploit NPLs for next-generation optoelectronic applications.

Finally, we have studied on the efficiency of excitonic energy transfer between colloidal Cu-doped core CdSe and undoped core/shell CdSe/CdS nanoplatelets. We showed the PL quenching of the donor Cu-doped NPLs and the systematic modifications in the time-resolved PL kinetics when the acceptor undoped NPLs are located in close proximity. For this purpose, we used steady-state and time-resolved PL spectroscopy techniques. Here, a record high energy transfer efficiency among our all-colloidal and all-2D system was obtained at 99% at room temperature in this thesis.

Overall, the findings of this thesis will be crucial in designing excitonic sensitization of technologically important materials such as silicon, graphene and MoS_2. All the great advantages of CQDs and NPLs will enable promising applications as we have showed in this thesis for the next-generation light-sensing technologies. We strongly believe that all of the results that have been presented in this thesis will provide useful knowledge in exploiting CQDs and NPLs for the next-generation photonics applications including photovoltaics, luminescent solar concentrators, LEDs and display technologies.

5.2 Future outlook

In this thesis, we addressed important problems in the context of the NRET studies for the complex structures of various 0D, 2D and 3D materials. Within the scope of the thesis, significantly high excitonic enhancements in 3D silicon, 2D layered GO and RGO, and quasi-2D NPLs have been reported by using quasi-0D and quasi-2D nanoparticles as the exciton donors. Furthermore, we provided useful platforms for the NRET studies in these structures to be used by the scientific community. All the promising results that we obtained in these studies are mainly based on the detailed analyses including optical measurements and theoretical investigations. For the real-life applications, besides the optical and theoretical studies, electrical measurements are also ultimately important especially for the light harvesting and the excitonic enhancement in silicon and graphene based optoelectronic devices as well as the systems including quasi-0D and quasi-2D colloidal nanoparticles.

In the recent years, metal dichalcogenides have been widely studied as a new class of 2D materials. These materials, unlike graphene, have an energy bandgap, which is a significant property for the electronic and optoelectronic applications. We have an ongoing study on light-harvesting in the structures including colloidal nanoparticles as the exciton donor and metal dichalcogenides as the exciton sink. High surface coverage and uniform growth are ultimately important characteristics for the real applications of these materials. To be used for this purpose, new growth procedures and methods will be crucial in the near future. Also, new patterned substrates utilized for the growth of these nanostructures are expected to be exciting for the examinations on the underlying mechanism of the growth pattern. Furthermore, the hybridization of different metallic compounds is used to produce new metal dichalcogenides, which can be used as exciton acceptors in the context of NRET studies.

Self-assembly of colloidal nanocrystals has also been a recent, newly emerging topic because of its great potential for the various light-harvesting applications. It can be especially significant for the uniform coating on patterned structures, which is expected to be necessary for the NRET into materials on patterned substrates. Also, the investigations on the directed NRET depending on the dipole orientation in the quasi-

2D nanoplatelets will be crucial for both the theoretical and experimental studies on the exciton transfer.

In addition, ion doping gives new optical and electrical properties to the nanoparticles and utilization of these properties is expected to be necessary for the next-generation light harvesting applications such as luminescent solar concentrators integrated to solar cells. For better performance in these systems, self-absorption in the dopant states should be minimized. Therefore, as the new nanomaterials having reduced self-absorption, they can be considered for better light utilization in future photovoltaic systems.

5.3 Contributions

This thesis work contributed to the following journal papers.

1. A. Yeltik, B. Guzelturk, P. L. H. Martinez, A. O. Govorov, and H. V. Demir, Phonon-assisted exciton transfer into silicon using nanoemitters: the role of phonons and temperature effects in Forster resonance energy transfer, ACS Nano 7 (12), 10492 (2013).

2. A. Yeltik, G. K. Dogu, B. Guzelturk, S. Fardindoost, Y. Kelestemur, and H. V. Demir,Evidence for nonradiative energy transfer in graphene-oxide-based hybrid structures, The Journal of Physical Chemistry C 117 (48), 25298 (2013).

3. A. Yeltik, B. Guzelturk, P. L. H. Martinez, S. Akhavan, and H. V. Demir, Excitonic enhancement of nonradiative energy transfer to bulk silicon with the hybridization of cascaded quantum dots, Applied Physics Letters 103 (26), 261103 (2013).

4. A. Yeltik, S. Delikanli, M. Olutas, Y. Kelestemur, B. Guzelturk and H. V. Demir, Experimental Determination of the Absorption Cross-Section and Molar Extinction Coefficient of Colloidal CdSe Nanoplatelets, The Journal of Physical Chemistry C 119 (47), 26768 (2015).

5. A. Yeltik, M. Olutas, M. Sharma, K. Gungor and H. V. Demir, Nonradiative Energy Transfer between Quasi-2D Colloidal Doped and Undoped Semiconductors, in submission.

6. B. Guzelturk, Y. Kelestemur, K. Gungor, **A. Yeltik**, M. Z. Akgul, Y. Wang, R. Chen, C. Dang, H. Sun and H. V. Demir, Stable and Low-Threshold Optical Gain in CdSe/CdS Quantum Dots: An All-Colloidal Frequency Up-Converted Laser, Advanced Materials 27 (17), 2741 (2015).

7. B. Guzelturk, Y. Kelestemur, K. Gungor, **A. Yeltik**, M. Z. Akgul, Y. Wang, R. Chen, C. Dang, H. Sun and H. V. Demir, Upconversion Lasers: Stable and Low-Threshold Optical Gain in CdSe/CdS Quantum Dots: An All-Colloidal Frequency Up-Converted Laser, Advanced Materials 27 (17), 2678 (2015).

8. M. Olutas, B. Guzelturk, Y. Kelestemur, **A. Yeltik**, S. Delikanli and H. V. Demir, Lateral Size-Dependent Spontaneous and Stimulated Emission Properties in Colloidal CdSe Nanoplatelets, ACS Nano 9 (5), 5041 (2015).

9. H. Zare, M. Marandi, S. Fardindoost, V. K. Sharma, **A. Yeltik**, O. Akhavan, H. V. Demir and N. Taghavinia, High-efficiency CdTe/CdS core/shell nanocrystals in water enabled by photo-induced colloidal hetero-epitaxy of CdS shelling at room temperature, Nano Research 8 (7), 2317 (2015).

10. S. Akhavan, **A. Yeltik** and H. V. Demir, Photosensitivity Enhancement with TiO2 in Semitransparent Light-Sensitive Skins of Nanocrystal Monolayers, ACS Applied Materials & Interfaces 6 (12), 9023 (2014).

11. S. Akhavan, A. F. Cihan, **A. Yeltik**, B. Bozok, V. Lesnyak, N. Gaponik, A. Eychmüller and H. V. Demir, Multiexciton generation assisted highly photosensitive CdHgTe nanocrystal skins, Nano Energy 26, 324 (2016).

Bibliography

[1] K. Sanderson, "Quantum dots go large," *Nature*, vol. 459, pp. 760–761, 2009.

[2] T. Pons, I. L. Medintz, X. Wang, D. S. English, and H. Mattoussi, "Solution-Phase Single Quantum Dot Fluorescence Resonance Energy Transfer," *J. Am. Chem. Soc.*, vol. 128, no. 47, pp. 15324–15331, Nov. 2006.

[3] U. Resch-Genger, M. Grabolle, S. Cavaliere-Jaricot, R. Nitschke, and T. Nann, "Quantum dots versus organic dyes as fluorescent labels," *Nat Meth*, vol. 5, no. 9, pp. 763–775, Sep. 2008.

[4] W. R. Algar, A. J. Tavares, and U. J. Krull, "Beyond labels: A review of the application of quantum dots as integrated components of assays, bioprobes, and biosensors utilizing optical transduction," *Anal. Chim. Acta*, vol. 673, no. 1, pp. 1–25, 2010.

[5] I. L. Medintz, H. T. Uyeda, E. R. Goldman, and H. Mattoussi, "Quantum dot bioconjugates for imaging, labelling and sensing," *Nat Mater*, vol. 4, no. 6, pp. 435–446, Jun. 2005.

[6] I. L. Medintz and H. Mattoussi, "Quantum dot-based resonance energy transfer and its growing application in biology," *Phys. Chem. Chem. Phys.*, vol. 11, no. 1, pp. 17–45, 2009.

[7] W. R. Algar, K. Susumu, J. B. Delehanty, and I. L. Medintz, "Semiconductor Quantum Dots in Bioanalysis: Crossing the Valley of Death," *Anal. Chem.*, vol. 83, no. 23, pp. 8826–8837, Dec. 2011.

[8] F. A. Esteve-Turrillas and A. Abad-Fuentes, "Applications of quantum dots as probes in immunosensing of small-sized analytes," *Biosens. Bioelectron.*, vol. 41, pp. 12–29, 2013.

[9] V. L. Colvin, M. C. Schlamp, and A. P. Alivisatos, "Light-emitting diodes made from cadmium selenide nanocrystals and a semiconducting polymer," *Nature*, vol. 370, no. 6488, pp. 354–357, Aug. 1994.

[10] A. Nurmikko, "What future for quantum dot-based light emitters?," *Nat Nano*, vol. 10, no. 12, pp. 1001–1004, Dec. 2015.

[11] M. Bruchez, M. Moronne, P. Gin, S. Weiss, and A. P. Alivisatos, “Semiconductor Nanocrystals as Fluorescent Biological Labels,” *Science (80-.).*, vol. 281, no. 5385, pp. 2013–2016, Sep. 1998.

[12] M. A. Reed, J. N. Randall, R. J. Aggarwal, R. J. Matyi, T. M. Moore, and A. E. Wetsel, “Observation of discrete electronic states in a zero-dimensional semiconductor nanostructure,” *Phys. Rev. Lett.*, vol. 60, no. 6, pp. 535–537, Feb. 1988.

[13] M. A. Reed, R. T. Bate, K. Bradshaw, W. M. Duncan, W. R. Frensley, J. W. Lee, and H. D. Shih, “Spatial quantization in GaAs–AlGaAs multiple quantum dots,” *J. Vac. Sci. Technol. B*, vol. 4, no. 1, pp. 358–360, 1986.

[14] A. I. Ekimov and A. A. Onushchenko, “Quantum size effect in three-dimensional microscopic semiconductor crystals,” *Jetp Lett.*, vol. 34, pp. 345–349, 1981.

[15] A. Henglein, “Photo-Degradation and Fluorescence of Colloidal-Cadmium Sulfide in Aqueous Solution,” *Berichte der Bunsengesellschaft für Phys. Chemie*, vol. 86, no. 4, pp. 301–305, Apr. 1982.

[16] A. L. EFROS and A. L. EFROS, “Interband absorption of light in a semiconductor sphere,” *Sov. Phys. Semicond. - USSR*, vol. 16, no. 7, pp. 772–775, 1982.

[17] R. Rossetti, S. Nakahara, and L. E. Brus, “Quantum size effects in the redox potentials, resonance Raman spectra, and electronic spectra of CdS crystallites in aqueous solution,” *J. Chem. Phys.*, vol. 79, no. 2, p. 1086, 1983.

[18] M. L. Steigerwald, A. P. Alivisatos, J. M. Gibson, T. D. Harris, R. Kortan, A. J. Muller, A. M. Thayer, T. M. Duncan, D. C. Douglass, and L. E. Brus, “Surface derivatization and isolation of semiconductor cluster molecules,” *J. Am. Chem. Soc.*, vol. 110, no. 10, pp. 3046–3050, May 1988.

[19] A. P. Alivisatos, A. L. Harris, N. J. Levinos, M. L. Steigerwald, and L. E. Brus, “Electronic states of semiconductor clusters: Homogeneous and inhomogeneous broadening of the optical spectrum,” *J. Chem. Phys.*, vol. 89, no. 7, p. 4001, 1988.

[20] M. G. Bawendi, W. L. Wilson, L. Rothberg, P. J. Carroll, T. M. Jedju, M. L. Steigerwald, and L. E. Brus, “Electronic structure and photoexcited-carrier

dynamics in nanometer-size CdSe clusters," *Phys. Rev. Lett.*, vol. 65, no. 13, pp. 1623–1626, Sep. 1990.

[21] M. G. Bawendi, M. L. Steigerwald, and L. E. Brus, "The Quantum Mechanics of Larger Semiconductor Clusters ('Quantum Dots')," *Annu. Rev. Phys. Chem.*, vol. 41, no. 1, pp. 477–496, 1990.

[22] B. O. Dabbousi, J. Rodriguez-Viejo, F. V. Mikulec, J. R. Heine, H. Mattoussi, R. Ober, K. F. Jensen, and M. G. Bawendi, "(CdSe)ZnS Core−Shell Quantum Dots: Synthesis and Characterization of a Size Series of Highly Luminescent Nanocrystallites," *J. Phys. Chem. B*, vol. 101, no. 46, pp. 9463–9475, Nov. 1997.

[23] M. A. Hines and and Philippe Guyot-Sionnest, "Synthesis and Characterization of Strongly Luminescing ZnS-Capped CdSe Nanocrystals," *J. Phys. Chem.*, vol. 100, no. 2, pp. 468–471, 1996.

[24] C. B. Murray, D. J. Noms, and M. G. Bawendi, "Synthesis and Characterization of Nearly Monodisperse CdE (E = S, Se, Te) Semiconductor Nanocrystallites," *J. Am. Chem. Soc.*, vol. 115, no. 4, pp. 8706–15, 1993.

[25] A. Eychmüller, A. Mews, and H. Weller, "A quantum dot quantum well: CdS/HgS/CdS," *Chem. Phys. Lett.*, vol. 208, no. 1–2, pp. 59–62, Jun. 1993.

[26] I. Moreels, Y. Justo, B. De Geyter, K. Haustraete, J. C. Martins, and Z. Hens, "Size-Tunable, Bright, and Stable PbS Quantum Dots: A Surface Chemistry Study," *ACS Nano*, vol. 5, no. 3, pp. 2004–2012, 2011.

[27] L. Zhang, L. Yin, C. Wang, N. lun, Y. Qi, and D. Xiang, "Origin of Visible Photoluminescence of ZnO Quantum Dots: Defect-Dependent and Size-Dependent," *J. Phys. Chem. C*, vol. 114, no. 21, pp. 9651–9658, 2010.

[28] O. Obonyo, E. Fisher, M. Edwards, and D. Douroumis, "Quantum dots synthesis and biological applications as imaging and drug delivery systems," *Crit. Rev. Biotechnol.*, vol. 30, no. 4, pp. 283–301, 2010.

[29] W. Zhou, D. T. Schwartz, and F. Baneyx, "Single-Pot Biofabrication of Zinc Sulfide Immuno-Quantum Dots," *J. Am. Chem. Soc.*, vol. 132, no. 13, pp. 4731–4738, 2010.

[30] M. Rai and C. Posten, *Green Biosynthesis of Nanoparticles: Mechanisms and Applications*. CAB International, 2013.

[31] G. D. Scholes and G. Rumbles, “Excitons in nanoscale systems,” *Nat Mater*, vol. 5, no. 9, pp. 683–696, Sep. 2006.

[32] A. P. Alivisatos, “Semiconductor Clusters, Nanocrystals, and Quantum Dots,” *Science (80-.).*, vol. 271, no. 5251, pp. 933–937, 1996.

[33] A. M. Smith, X. Gao, and S. Nie, “Quantum Dot Nanocrystals for In Vivo Molecular and Cellular Imaging,” *Photochem. Photobiol.*, vol. 80, no. 3, pp. 377–385, 2004.

[34] - , E. Mutlugun, D. Ugur Karatay, and H. Volkan Demir, “Excitonic enhancement of nonradiative energy transfer from a quantum well in the optical near field of energy gradient quantum dots,” *Appl. Phys. Lett.*, vol. 100, no. 24, p. 241109, 2012.

[35] A. Yeltik, B. Guzelturk, P. Ludwig Hernandez-Martinez, S. Akhavan, and H. V. Demir, “Excitonic enhancement of nonradiative energy transfer to bulk silicon with the hybridization of cascaded quantum dots,” *Appl. Phys. Lett.*, vol. 103, no. 26, p. 261103 1–4, Dec. 2013.

[36] M L Steigerwald and and L E Brus, “Synthesis, Stabilization, and Electronic Structure of Quantum Semiconductor Nanoclusters,” *Annu. Rev. Mater. Sci.*, vol. 19, no. 1, pp. 471–495, 1989.

[37] J. A. McGuire, J. Joo, J. M. Pietryga, R. D. Schaller, and V. I. Klimov, “New Aspects of Carrier Multiplication in Semiconductor Nanocrystals,” *Acc. Chem. Res.*, vol. 41, no. 12, pp. 1810–1819, 2008.

[38] Y. Wang and N. Herron, “Nanometer-sized semiconductor clusters: materials synthesis, quantum size effects, and photophysical properties,” *J. Phys. Chem.*, vol. 95, no. 2, pp. 525–532, 1991.

[39] C. J. Murphy and J. L. Coffer, “Quantum Dots: A Primer,” *Appl. Spectrosc.*, vol. 56, no. 1, p. 16A–27A, Jan. 2002.

[40] L. E. Brus, “Electron–electron and electron-hole interactions in small semiconductor crystallites: The size dependence of the lowest excited electronic state,” *J. Chem. Phys.*, vol. 80, no. 9, pp. 4403–4409, 1984.

[41] L. E. Brus, “On the development of bulk optical properties in small semiconductor crystallites,” *J. Lumin.*, vol. 31, pp. 381–384, 1984.

[42] A. P. Alivisatos, “Perspectives on the Physical Chemistry of Semiconductor

Nanocrystals," *J. Phys. Chem.*, vol. 100, no. 31, pp. 13226–13239, 1996.

[43] W. C. W. Chan, D. J. Maxwell, X. Gao, R. E. Bailey, M. Han, and S. Nie, "Luminescent quantum dots for multiplexed biological detection and imaging," *Curr. Opin. Biotechnol.*, vol. 13, no. 1, pp. 40–46, 2002.

[44] X. Michalet, F. F. Pinaud, L. A. Bentolila, J. M. Tsay, S. Doose, J. J. Li, G. Sundaresan, A. M. Wu, S. S. Gambhir, and S. Weiss, "Quantum Dots for Live Cells, in Vivo Imaging, and Diagnostics," *Science (80-.).*, vol. 307, no. 5709, pp. 538–544, 2005.

[45] J. S. Steckel, J. P. Zimmer, S. Coe-Sullivan, N. E. Stott, V. Bulović, and M. G. Bawendi, "Blue Luminescence from (CdS)ZnS Core–Shell Nanocrystals," *Angew. Chemie Int. Ed.*, vol. 43, no. 16, pp. 2154–2158, 2004.

[46] Peter Reiss, Joël Bleuse, and and Adam Pron, "Highly Luminescent CdSe/ZnSe Core/Shell Nanocrystals of Low Size Dispersion," *Nano Lett.*, vol. 2, no. 7, pp. 781–784, 2002.

[47] A. Javier, D. Magana, T. Jennings, and G. F. Strouse, "Nanosecond exciton recombination dynamics in colloidal CdSe quantum dots under ambient conditions," *Appl. Phys. Lett.*, vol. 83, no. 7, pp. 1423–1425, 2003.

[48] M. Grabolle, P. Kapusta, T. Nann, X. Shu, J. Ziegler, and U. Resch-Genger, "Fluorescence Lifetime Multiplexing with Nanocrystals and Organic Labels," *Anal. Chem.*, vol. 81, no. 18, pp. 7807–7813, 2009.

[49] M. Olutas, B. Guzelturk, Y. Kelestemur, K. Gungor, and H. V. Demir, "Highly Efficient Nonradiative Energy Transfer from Colloidal Semiconductor Quantum Dots to Wells for Sensitive Noncontact Temperature Probing," *Adv. Funct. Mater.*, vol. 26, no. 17, pp. 2891–2899, 2016.

[50] N. Hildebrandt and D. Geißler, "Semiconductor Quantum Dots as FRET Acceptors for Multiplexed Diagnostics and Molecular Ruler Application," in *Nano-Biotechnology for Biomedical and Diagnostic Research*, E. Zahavy, A. Ordentlich, S. Yitzhaki, and A. Shafferman, Eds. Dordrecht: Springer Netherlands, 2012, pp. 75–86.

[51] Z. Tang, Z. Zhang, Y. Wang, S. C. Glotzer, and N. A. Kotov, "Self-Assembly of CdTe Nanocrystals into Free-Floating Sheets," *Science (80-.).*, vol. 314, no. 5797, pp. 274–278, 2006.

[52] Jin Joo, Jae Sung Son, Soon Gu Kwon, Jung Ho Yu, and and Taeghwan Hyeon, "Low-Temperature Solution-Phase Synthesis of Quantum Well Structured CdSe Nanoribbons," *J. Am. Chem. Soc.*, vol. 128, no. 17, pp. 5632–5633, 2006.

[53] J. S. Son, X.-D. Wen, J. Joo, J. Chae, S. Baek, K. Park, J. H. Kim, K. An, J. H. Yu, S. G. Kwon, S.-H. Choi, Z. Wang, Y.-W. Kim, Y. Kuk, R. Hoffmann, and T. Hyeon, "Large-Scale Soft Colloidal Template Synthesis of 1.4 nm Thick CdSe Nanosheets," *Angew. Chemie*, vol. 121, no. 37, pp. 6993–6996, Sep. 2009.

[54] S. Ithurria and B. Dubertret, "Quasi 2D colloidal CdSe platelets with thicknesses controlled at the atomic level," *J. Am. Chem. Soc.*, vol. 130, no. 49, pp. 16504–16505, 2008.

[55] S. Ithurria, M. D. Tessier, B. Mahler, R. P. S. M. Lobo, B. Dubertret, and A. L. Efros, "Colloidal nanoplatelets with two-dimensional electronic structure.," *Nat. Mater.*, vol. 10, no. 12, pp. 936–941, Dec. 2011.

[56] B. Mahler, B. Nadal, C. Bouet, G. Patriarche, and B. Dubertret, "Core/shell colloidal semiconductor nanoplatelets," *J. Am. Chem. Soc.*, vol. 134, no. 45, pp. 18591–8, Nov. 2012.

[57] J. N. Coleman, M. Lotya, A. O'Neill, S. D. Bergin, P. J. King, U. Khan, K. Young, A. Gaucher, S. De, R. J. Smith, I. V Shvets, S. K. Arora, G. Stanton, H.-Y. Kim, K. Lee, G. T. Kim, G. S. Duesberg, T. Hallam, J. J. Boland, J. J. Wang, J. F. Donegan, J. C. Grunlan, G. Moriarty, A. Shmeliov, R. J. Nicholls, J. M. Perkins, E. M. Grieveson, K. Theuwissen, D. W. McComb, P. D. Nellist, and V. Nicolosi, "Two-Dimensional Nanosheets Produced by Liquid Exfoliation of Layered Materials," *Science (80-.).*, vol. 331, no. 6017, pp. 568–571, 2011.

[58] Y. Yin and A. P. Alivisatos, "Colloidal nanocrystal synthesis and the organic-inorganic interface," *Nature*, vol. 437, no. 7059, pp. 664–670, Sep. 2005.

[59] K. H. Park, K. Jang, and S. U. Son, "Synthesis, Optical Properties, and Self-Assembly of Ultrathin Hexagonal In2S3 Nanoplates," *Angew. Chemie Int. Ed.*, vol. 45, no. 28, pp. 4608–4612, 2006.

[60] Y. Zhang, J. Lu, S. Shen, H. Xu, and Q. Wang, "Ultralarge single crystal SnS rectangular nanosheets," *Chem. Commun.*, vol. 47, no. 18, pp. 5226–5228,

2011.

[61] I. I. Dimitri D. Vaughn, S.-I. In, and R. E. Schaak, “A Precursor-Limited Nanoparticle Coalescence Pathway for Tuning the Thickness of Laterally-Uniform Colloidal Nanosheets: The Case of SnSe,” *ACS Nano*, vol. 5, no. 11, pp. 8852–8860, 2011.

[62] J. Choi, J. Jin, I. G. Jung, J. M. Kim, H. J. Kim, and S. U. Son, “SnSe2 nanoplate-graphene composites as anode materials for lithium ion batteries,” *Chem. Commun.*, vol. 47, no. 18, pp. 5241–5243, 2011.

[63] A. Ghezelbash and and Brian A. Korgel, “Nickel Sulfide and Copper Sulfide Nanocrystal Synthesis and Polymorphism,” *Langmuir*, vol. 21, no. 21, pp. 9451–9456, 2005.

[64] S. Jeong, D. Yoo, J. Jang, M. Kim, and J. Cheon, “Well-Defined Colloidal 2-D Layered Transition-Metal Chalcogenide Nanocrystals via Generalized Synthetic Protocols,” *J. Am. Chem. Soc.*, vol. 134, no. 44, pp. 18233–18236, 2012.

[65] A. Kirkeminde, B. A. Ruzicka, R. Wang, S. Puna, H. Zhao, and S. Ren, “Synthesis and Optoelectronic Properties of Two-Dimensional FeS2 Nanoplates,” *ACS Appl. Mater. Interfaces*, vol. 4, no. 3, pp. 1174–1177, 2012.

[66] Z. Yu, L. Guo, H. Du, T. Krauss, and and J. Silcox, “Shell Distribution on Colloidal CdSe/ZnS Quantum Dots,” *Nano Lett.*, vol. 5, no. 4, pp. 565–570, 2005.

[67] D. H. Son, S. M. Hughes, Y. Yin, and A. Paul Alivisatos, “Cation Exchange Reactions in Ionic Nanocrystals,” *Science (80-.).*, vol. 306, no. 5698, pp. 1009–1012, 2004.

[68] J. Park, H. Zheng, Y. Jun, and A. P. Alivisatos, “Hetero-Epitaxial Anion Exchange Yields Single-Crystalline Hollow Nanoparticles,” *J. Am. Chem. Soc.*, vol. 131, no. 39, pp. 13943–13945, 2009.

[69] L. Carbone, C. Nobile, M. De Giorgi, F. Della Sala, G. Morello, P. Pompa, M. Hytch, E. Snoeck, A. Fiore, I. R. Franchini, M. Nadasan, A. F. Silvestre, L. Chiodo, S. Kudera, R. Cingolani, R. Krahne, and and L. Manna, “Synthesis and Micrometer-Scale Assembly of Colloidal CdSe/CdS Nanorods Prepared by a Seeded Growth Approach,” *Nano Lett.*, vol. 7, no. 10, pp. 2942–2950, 2007.

[70] B. Mahler, N. Lequeux, and B. Dubertret, “Ligand-Controlled Polytypism of

Thick-Shell CdSe/CdS Nanocrystals," *J. Am. Chem. Soc.*, vol. 132, no. 3, pp. 953–959, 2010.

[71] S. Ithurria and D. V. Talapin, "Colloidal atomic layer deposition (c-ALD) using self-limiting reactions at nanocrystal surface coupled to phase transfer between polar and nonpolar media," *J. Am. Chem. Soc.*, vol. 134, no. 45, pp. 18585–18590, 2012.

[72] M. D. Tessier, P. Spinicelli, D. Dupont, G. Patriarche, S. Ithurria, and B. Dubertret, "Efficient Exciton Concentrators Built from Colloidal Core/Crown CdSe/CdS Semiconductor Nanoplatelets.," *Nano Lett.*, vol. 14, pp. 207–213, 2014.

[73] A. Prudnikau, A. Chuvilin, and M. Artemyev, "CdSe–CdS Nanoheteroplatelets with Efficient Photoexcitation of Central CdSe Region through Epitaxially Grown CdS Wings," *J. Am. Chem. Soc.*, vol. 135, no. 39, pp. 14476–14479, 2013.

[74] Y. Kelestemur, B. Guzelturk, O. Erdem, M. Olutas, K. Gungor, and H. V. Demir, "Colloidal Nanoplatelets: Platelet-in-Box Colloidal Quantum Wells: CdSe/CdS@CdS Core/Crown@Shell Heteronanoplatelets," *Adv. Funct. Mater.*, vol. 26, no. 21, p. 3554, 2016.

[75] B. Guzelturk, Y. Kelestemur, M. Olutas, S. Delikanli, and H. V. Demir, "Amplified Spontaneous Emission and Lasing in Colloidal Nanoplatelets," *ACS Nano*, vol. 8, no. 7, pp. 6599–6605, 2014.

[76] B. Guzelturk, O. Erdem, M. Olutas, Y. Kelestemur, and H. V. Demir, "Stacking in Colloidal Nanoplatelets: Tuning Excitonic Properties," *ACS Nano*, vol. 8, no. 12, pp. 12524–12533, 2014.

[77] M. D. Tessier, B. Mahler, B. Nadal, H. Heuclin, S. Pedetti, and B. Dubertret, "Spectroscopy of colloidal semiconductor core/shell nanoplatelets with high quantum yield," *Nano Lett.*, vol. 13, no. 7, pp. 3321–8, Jul. 2013.

[78] L. T. Kunneman, J. M. Schins, S. Pedetti, H. Heuclin, F. C. Grozema, A. J. Houtepen, B. Dubertret, and L. D. a Siebbeles, "Nature and decay pathways of photoexcited states in CdSe and CdSe/CdS nanoplatelets," *Nano Lett.*, vol. 14, no. 12, pp. 7039–7045, Nov. 2014.

[79] M. D. Tessier, C. Javaux, I. Maksimovic, V. Loriette, and B. Dubertret,

"Spectroscopy of single CdSe nanoplatelets.," *ACS Nano*, vol. 6, pp. 6751–6758, 2012.

[80] M. D. Tessier, L. Biadala, C. Bouet, S. Ithurria, B. Abecassis, and B. Dubertret, "Phonon Line Emission Revealed by Self-Assembly of Colloidal Nanoplatelets," *ACS Nano*, vol. 7, no. 4, pp. 3332–3340, 2013.

[81] E. Baghani, S. K. O'Leary, I. Fedin, D. V Talapin, and M. Pelton, "Auger-Limited Carrier Recombination and Relaxation in CdSe Colloidal Quantum Wells," *J. Phys. Chem. Lett.*, vol. 6, no. 6, pp. 1032–1036, 2015.

[82] M. Pelton, S. Ithurria, R. D. Schaller, D. S. Dolzhnikov, and D. V Talapin, "Carrier cooling in colloidal quantum wells," *Nano Lett.*, vol. 12, no. 12, pp. 6158–63, Dec. 2012.

[83] M. Olutas, B. Guzelturk, Y. Kelestemur, A. Yeltik, S. Delikanli, and H. V. Demir, "Lateral Size-Dependent Spontaneous and Stimulated Emission Properties in Colloidal CdSe Nanoplatelets," *ACS Nano*, vol. 9, no. 5, pp. 5041–5050, 2015.

[84] A. Yeltik, S. Delikanli, M. Olutas, Y. Kelestemur, B. Guzelturk, and H. V. Demir, "Experimental Determination of the Absorption Cross-Section and Molar Extinction Coefficient of Colloidal CdSe Nanoplatelets," *J. Phys. Chem. C*, p. acs.jpcc.5b09275, 2015.

[85] B. Guzelturk, M. Olutas, S. Delikanli, Y. Kelestemur, O. Erdem, and H. V. Demir, "Nonradiative energy transfer in colloidal CdSe nanoplatelet films," *Nanoscale*, vol. 7, no. 6, pp. 2545–2551, 2015.

[86] A. Naeem, F. Masia, S. Christodoulou, I. Moreels, P. Borri, and W. Langbein, "Evidence of giant oscillator strength in the exciton dephasing of CdSe nanoplatelets measured by resonant four-wave mixing," *Arxiv*, pp. 1–8, 2014.

[87] K. Wu, Q. Li, Y. Du, Z. Chen, and T. Lian, "Ultrafast exciton quenching by energy and electron transfer in colloidal CdSe nanosheet-Pt heterostructures," *Chem. Sci.*, vol. 6, no. 2, pp. 1049–1054, 2015.

[88] A. W. Achtstein, A. V Prudnikau, M. V Ermolenko, L. I. Gurinovich, S. V Gaponenko, U. Woggon, A. V Baranov, M. Y. Leonov, I. D. Rukhlenko, A. V Fedorov, and M. V Artemyev, "Electroabsorption by 0D, 1D, and 2D Nanocrystals: A Comparative Study of CdSe Colloidal Quantum Dots,

Nanorods, and Nanoplatelets," *ACS Nano*, vol. 8, no. 8, pp. 7678–7686, 2014.

[89] D. A. . Miller, *Quantum Mechanics for Scientists and Engineers*. Cambridge University Press, 2008.

[90] E. Lhuillier, J.-F. Dayen, D. O. Thomas, A. Robin, B. Doudin, and B. Dubertret, "Nanoplatelets Bridging a Nanotrench: A New Architecture for Photodetectors with Increased Sensitivity," *Nano Lett.*, vol. 15, no. 3, pp. 1736–1742, Feb. 2015.

[91] T. Förster, "Energiewanderung und fluoreszenz," *Naturwissenschaften*, vol. 33, no. 6, pp. 166–175, 1946.

[92] J. Q. Grim, S. Christodoulou, F. Di Stasio, R. Krahne, R. Cingolani, L. Manna, and I. Moreels, "Continuous-wave biexciton lasing at room temperature using solution-processed quantum wells," *Nat. Nanotechnol.*, vol. 9, no. 11, pp. 891–895, 2014.

[93] Y. Zhu, S. Murali, W. Cai, X. Li, J. W. Suk, J. R. Potts, and R. S. Ruoff, "Graphene and graphene oxide: synthesis, properties, and applications.," *Adv. Mater.*, vol. 22, no. 35, pp. 3906–24, Sep. 2010.

[94] K. P. D. E. Jong and J. W. Geus, "Carbon Nanofibers: Catalytic Synthesis and Applications," *Catal. Rev.*, vol. 42, no. 4, pp. 481–510, 2000.

[95] B. C. Thompson and J. M. J. Fréchet, "Polymer–Fullerene Composite Solar Cells," *Angew. Chemie Int. Ed.*, vol. 47, no. 1, pp. 58–77, 2008.

[96] D. A. C. Brownson and C. E. Banks, "Graphene electrochemistry: an overview of potential applications," *Analyst*, vol. 135, no. 11, pp. 2768–2778, 2010.

[97] F. Bonaccorso, Z. Sun, T. Hasan, and a. C. Ferrari, "Graphene photonics and optoelectronics," *Nat. Photonics*, vol. 4, no. 9, pp. 611–622, Aug. 2010.

[98] F. Liu, J. Y. Choi, and T. S. Seo, "Graphene oxide arrays for detecting specific DNA hybridization by fluorescence resonance energy transfer," *Biosens. Bioelectron.*, vol. 25, no. 10, pp. 2361–2365, 2010.

[99] Y. Wang, Z. Li, J. Wang, J. Li, and Y. Lin, "Graphene and graphene oxide: biofunctionalization and applications in biotechnology.," *Trends Biotechnol.*, vol. 29, no. 5, pp. 205–12, May 2011.

[100] F. H. L. Koppens, D. E. Chang, and F. J. G. de Abajo, "Graphene Plasmonics: A Platform for Strong Light–Matter Interactions," *Nano Lett.*, vol. 11, no. 8, pp.

3370–3377, 2011.

[101] A. Y. Nikitin, F. Guinea, F. J. García-Vidal, and L. Martín-Moreno, “Edge and waveguide terahertz surface plasmon modes in graphene microribbons,” *Phys. Rev. B*, vol. 84, no. 16, p. 161407, Oct. 2011.

[102] R. S. Swathi and K. L. Sebastian, “Resonance energy transfer from a dye molecule to graphene,” *J. Chem. Phys.*, vol. 129, no. 5, p. 054703, Aug. 2008.

[103] G. Gómez-Santos and T. Stauber, “Fluorescence quenching in graphene: A fundamental ruler and evidence for transverse plasmons,” *Phys. Rev. B*, vol. 84, no. 16, p. 165438, Oct. 2011.

[104] K. A. Velizhanin and A. Efimov, “Probing plasmons in graphene by resonance energy transfer,” *Phys. Rev. B*, vol. 84, no. 8, p. 85401, Aug. 2011.

[105] K. S. Novoselov, A. K. Geim, S. V Morozov, D. Jiang, Y. Zhang, S. V Dubonos, I. V Grigorieva, and A. A. Firsov, “Electric field effect in atomically thin carbon films.,” *Science (80-.).*, vol. 306, no. 5696, pp. 666–669, Oct. 2004.

[106] K. S. Novoselov, D. Jiang, F. Schedin, T. J. Booth, V. V Khotkevich, S. V Morozov, and A. K. Geim, “Two-dimensional atomic crystals,” *Proc. Natl. Acad. Sci. U. S. A.*, vol. 102, no. 30, pp. 10451–3, Jul. 2005.

[107] Y. Hernandez, V. Nicolosi, M. Lotya, F. M. Blighe, Z. Sun, S. De, M. T., B. Holland, M. Byrne, Y. K. Gun’Ko, J. J. Boland, P. Niraj, G. Duesberg, S. Krishnamurthy, R. Goodhue, J. Hutchison, V. Scardaci, A. C. Ferrari, and J. N. Coleman, “High-yield production of graphene by liquid-phase exfoliation of graphite,” *Nat Nano*, vol. 3, no. 9, pp. 563–568, Sep. 2008.

[108] A. N. Obraztsov, E. A. Obraztsova, A. V Tyurnina, and A. A. Zolotukhin, “Chemical vapor deposition of thin graphite films of nanometer thickness,” *Carbon N. Y.*, vol. 45, no. 10, pp. 2017–2021, 2007.

[109] K. S. Kim, Y. Zhao, H. Jang, S. Y. Lee, J. M. Kim, K. S. Kim, J.-H. Ahn, P. Kim, J.-Y. Choi, and B. H. Hong, “Large-scale pattern growth of graphene films for stretchable transparent electrodes,” *Nature*, vol. 457, no. 7230, pp. 706–710, Feb. 2009.

[110] Claire Berger, Zhimin Song, Tianbo Li, Xuebin Li, Asmerom Y. Ogbazghi, Rui Feng, Zhenting Dai, Alexei N. Marchenkov, Edward H. Conrad, Phillip N. First, and and Walt A. de Heer, “Ultrathin Epitaxial Graphite: 2D Electron Gas

Properties and a Route toward Graphene-based Nanoelectronics," *J. Phys. Chem. B*, vol. 108, no. 52, pp. 19912–19916, 2004.

[111] M. Choucair, P. Thordarson, and J. A. Stride, "Gram-scale production of graphene based on solvothermal synthesis and sonication," *Nat Nano*, vol. 4, no. 1, pp. 30–33, Jan. 2009.

[112] C. Lee, X. Wei, J. W. Kysar, and J. Hone, "Measurement of the Elastic Properties and Intrinsic Strength of Monolayer Graphene," *Science (80-.).*, vol. 321, no. 5887, pp. 385–388, 2008.

[113] A. A. Balandin, S. Ghosh, W. Bao, I. Calizo, D. Teweldebrhan, F. Miao, and C. N. Lau, "Superior Thermal Conductivity of Single-Layer Graphene," *Nano Lett.*, vol. 8, no. 3, pp. 902–907, 2008.

[114] M. Orlita, C. Faugeras, P. Plochocka, P. Neugebauer, G. Martinez, D. K. Maude, A.-L. Barra, M. Sprinkle, C. Berger, W. A. de Heer, and M. Potemski, "Approaching the Dirac Point in High-Mobility Multilayer Epitaxial Graphene," *Phys. Rev. Lett.*, vol. 101, no. 26, p. 267601, Dec. 2008.

[115] S. Pei and H. Cheng, "The reduction of graphene oxide," *Carbon N. Y.*, vol. 50, no. 9, pp. 3210–3228, Aug. 2012.

[116] D. R., Y. F., MericI., LeeC., WangL., SorgenfreiS., WatanabeK., TaniguchiT., KimP., S. L., and HoneJ., "Boron nitride substrates for high-quality graphene electronics," *Nat Nano*, vol. 5, no. 10, pp. 722–726, Oct. 2010.

[117] G. Konstantatos and E. H. Sargent, "Nanostructured materials for photon detection.," *Nat. Nanotechnol.*, vol. 5, no. 6, pp. 391–400, Jun. 2010.

[118] Z. Chen, S. Berciaud, C. Nuckolls, T. F. Heinz, and L. E. Brus, "Energy transfer from individual semiconductor nanocrystals to graphene.," *ACS Nano*, vol. 4, no. 5, pp. 2964–8, May 2010.

[119] R. J. Stöhr, R. Kolesov, K. Xia, R. Reuter, J. Meijer, G. Logvenov, and J. Wrachtrup, "Super-resolution Fluorescence Quenching Microscopy of Graphene," *ACS Nano*, vol. 6, no. 10, pp. 9175–9181, 2012.

[120] E. Treossi, M. Melucci, A. Liscio, M. Gazzano, P. Samorì, and V. Palermo, "High-Contrast Visualization of Graphene Oxide on Dye-Sensitized Glass, Quartz, and Silicon by Fluorescence Quenching," *J. Am. Chem. Soc.*, vol. 131, no. 43, pp. 15576–15577, 2009.

[121] J. Kim, L. J. Cote, F. Kim, and J. Huang, “Visualizing graphene based sheets by fluorescence quenching microscopy.,” *J. Am. Chem. Soc.*, vol. 132, no. 1, pp. 260–7, Jan. 2010.

[122] F. Federspiel, G. Froehlicher, M. Nasilowski, S. Pedetti, A. Mahmood, B. Doudin, S. Park, J.-O. Lee, D. Halley, B. Dubertret, P. Gilliot, and S. Berciaud, “Distance Dependence of the Energy Transfer Rate from a Single Semiconductor Nanostructure to Graphene,” *Nano Lett.*, vol. 15, no. 2, pp. 1252–1258, 2015.

[123] R. S. Swathi and K. L. Sebastian, “Long range resonance energy transfer from a dye molecule to graphene has (distance)(-4) dependence.,” *J. Chem. Phys.*, vol. 130, no. 8, p. 086101, Feb. 2009.

[124] L. Gaudreau, K. J. Tielrooij, G. E. D. K. Prawiroatmodjo, J. Osmond, F. J. G. de Abajo, and F. H. L. Koppens, “Universal distance-scaling of nonradiative energy transfer to graphene,” *Nano Lett.*, vol. 13, no. 5, pp. 2030–5, May 2013.

[125] K. P. Loh, Q. Bao, G. Eda, and M. Chhowalla, “Graphene oxide as a chemically tunable platform for optical applications.,” *Nat. Chem.*, vol. 2, no. 12, pp. 1015–24, Dec. 2010.

[126] W. S. H. Jr. and R. E. Offeman, “Preparation of Graphitic Oxide,” *J. Am. Chem. Soc.*, vol. 80, no. 6, p. 1339, 1958.

[127] H. C. Schniepp, J.-L. Li, M. J. McAllister, H. Sai, M. Herrera-Alonso, D. H. Adamson, R. K. Prud’homme, R. Car, D. A. Saville, and and I. A. Aksay, “Functionalized Single Graphene Sheets Derived from Splitting Graphite Oxide,” *J. Phys. Chem. B*, vol. 110, no. 17, pp. 8535–8539, 2006.

[128] S. Stankovich, D. A. Dikin, R. D. Piner, K. A. Kohlhaas, A. Kleinhammes, Y. Jia, Y. Wu, S. T. Nguyen, and R. S. Ruoff, “Synthesis of graphene-based nanosheets via chemical reduction of exfoliated graphite oxide,” *Carbon N. Y.*, vol. 45, no. 7, pp. 1558–1565, 2007.

[129] G. Eda, G. Fanchini, and M. Chhowalla, “Large-area ultrathin films of reduced graphene oxide as a transparent and flexible electronic material.,” *Nat. Nanotechnol.*, vol. 3, no. 5, pp. 270–4, May 2008.

[130] S. Park and R. S. Ruoff, “Chemical methods for the production of graphenes.,” *Nat. Nanotechnol.*, vol. 4, no. 4, pp. 217–24, Apr. 2009.

[131] M. Liu, H. Zhao, X. Quan, S. Chen, and X. Fan, “Distance-independent quenching of quantum dots by nanoscale-graphene in self-assembled sandwich immunoassay,” *Chem. Commun.*, vol. 46, no. 42, pp. 7909–7911, 2010.

[132] V. López, R. S. Sundaram, C. Gómez-Navarro, D. Olea, M. Burghard, J. Gómez-Herrero, F. Zamora, and K. Kern, “Chemical Vapor Deposition Repair of Graphene Oxide: A Route to Highly-Conductive Graphene Monolayers,” *Adv. Mater.*, vol. 21, no. 46, pp. 4683–4686, 2009.

[133] Q. Su, S. Pang, V. Alijani, C. Li, X. Feng, and K. Müllen, “Composites of Graphene with Large Aromatic Molecules,” *Adv. Mater.*, vol. 21, no. 31, pp. 3191–3195, 2009.

[134] S. Kochmann, T. Hirsch, and O. S. Wolfbeis, “Graphenes in chemical sensors and biosensors,” *TrAC Trends Anal. Chem.*, vol. 39, pp. 87–113, 2012.

[135] A. Yeltik, G. Kucukayan-Dogu, B. Guzelturk, S. Fardindoost, Y. Kelestemur, and H. V. Demir, “Evidence for Nonradiative Energy Transfer in Graphene Oxide Based Hybrid Structures,” *J. Phys. Chem. C*, vol. 117, no. 48, pp. 25298–25304, 2013.

[136] R. S. Swathi and K. L. Sebastian, “Resonance energy transfer from a dye molecule to graphene.,” *J. Chem. Phys.*, vol. 129, no. 5, p. 054703, Aug. 2008.

[137] E. Morales-Narváez, B. Pérez-López, L. B. Pires, and A. Merkoçi, “Simple Förster resonance energy transfer evidence for the ultrahigh quantum dot quenching efficiency by graphene oxide compared to other carbon structures,” *Carbon N. Y.*, vol. 50, no. 8, pp. 2987–2993, Jul. 2012.

[138] Y. Liu, X. Dong, and P. Chen, “Biological and chemical sensors based on graphene materials,” *Chem. Soc. Rev.*, vol. 41, no. 6, pp. 2283–2307, 2012.

[139] A. Splendiani, L. Sun, Y. Zhang, T. Li, J. Kim, C.-Y. Chim, G. Galli, and F. Wang, “Emerging Photoluminescence in Monolayer MoS2,” *Nano Lett.*, vol. 10, no. 4, pp. 1271–1275, 2010.

[140] K. F. Mak, C. Lee, J. Hone, J. Shan, and T. F. Heinz, “Atomically Thin MoS2: A New Direct-Gap Semiconductor,” *Phys. Rev. Lett.*, vol. 105, no. 13, p. 136805, Sep. 2010.

[141] D. Xiao, G.-B. Liu, W. Feng, X. Xu, and W. Yao, “Coupled Spin and Valley Physics in Monolayers of MoS2 and Other Group-VI Dichalcogenides,” *Phys.*

Rev. Lett., vol. 108, no. 19, p. 196802, May 2012.

[142] Q. H. Wang, K. Kalantar-Zadeh, A. Kis, J. N. Coleman, and M. S. Strano, "Electronics and optoelectronics of two-dimensional transition metal dichalcogenides," *Nat Nano*, vol. 7, no. 11, pp. 699–712, Nov. 2012.

[143] F. Xia, H. Wang, D. Xiao, M. Dubey, and A. Ramasubramaniam, "Two-dimensional material nanophotonics," *Nat Phot.*, vol. 8, no. 12, pp. 899–907, Dec. 2014.

[144] A. K. Geim and I. V Grigorieva, "Van der Waals heterostructures," *Nature*, vol. 499, no. 7459, pp. 419–425, Jul. 2013.

[145] F. Prins, A. J. Goodman, and W. A. Tisdale, "Reduced Dielectric Screening and Enhanced Energy Transfer in Single- and Few-Layer MoS2," *Nano Lett.*, vol. 14, no. 11, pp. 6087–6091, 2014.

[146] A. Raja, A. Montoya−Castillo, J. Zultak, X.-X. Zhang, Z. Ye, C. Roquelet, D. A. Chenet, A. M. van der Zande, P. Huang, S. Jockusch, J. Hone, D. R. Reichman, L. E. Brus, and T. F. Heinz, "Energy Transfer from Quantum Dots to Graphene and MoS2: The Role of Absorption and Screening in Two-Dimensional Materials," *Nano Lett.*, vol. 16, no. 4, pp. 2328–2333, 2016.

[147] P. L. Hernández-Martínez, A. O. Govorov, and H. V. Demir, "Förster-Type Nonradiative Energy Transfer for Assemblies of Arrayed Nanostructures: Confinement Dimension vs Stacking Dimension," *J. Phys. Chem. C*, vol. 118, no. 9, pp. 4951–4958, 2014.

[148] D. Prasai, A. R. Klots, A. K. M. Newaz, J. S. Niezgoda, N. J. Orfield, C. A. Escobar, A. Wynn, A. Efimov, G. K. Jennings, S. J. Rosenthal, and K. I. Bolotin, "Electrical Control of near-Field Energy Transfer between Quantum Dots and Two-Dimensional Semiconductors," *Nano Lett.*, vol. 15, no. 7, pp. 4374–4380, 2015.

[149] M. Fox, *Optical Properties of Solids*. Oxford University Press, 2001.

[150] S. M. Sze, *Semiconductor devices: physics and technology*. Wiley and Sons Inc., 1985.

[151] E. Mutlugun, I. M. Soganci, and H. V. Demir, "Photovoltaic nanocrystal scintillators hybridized on Si solar cells for enhanced conversion efficiency in UV," *Opt. Express*, vol. 16, no. 6, pp. 3537–3545, Mar. 2008.

[152] B. Guzelturk, E. Mutlugun, X. Wang, K. L. Pey, and H. V. Demir, “Photovoltaic nanopillar radial junction diode architecture enhanced by integrating semiconductor quantum dot nanocrystals as light harvesters,” *Appl. Phys. Lett.*, vol. 97, no. 9, p. 093111, 2010.

[153] S. Lu, Z. Lingley, T. Asano, D. Harris, T. Barwicz, S. Guha, and A. Madhukar, “Photocurrent induced by nonradiative energy transfer from nanocrystal quantum dots to adjacent silicon nanowire conducting channels: toward a new solar cell paradigm.,” *Nano Lett.*, vol. 9, no. 12, pp. 4548–52, Dec. 2009.

[154] H. M. Nguyen, O. Seitz, W. Peng, Y. N. Gartstein, Y. J. Chabal, and A. V Malko, “Efficient Radiative and Nonradiative Energy Transfer from Proximal CdSe/ZnS Nanocrystals into Silicon Nanomembranes,” *ACS Nano*, vol. 6, no. 6, pp. 5574–5582, 2012.

[155] A. Yeltik, B. Guzelturk, P. L. Hernandez-Martinez, A. O. Govorov, and H. V. Demir, “Phonon-Assisted Exciton Transfer into Silicon Using Nanoemitters: The Role of Phonons and Temperature Effects in Förster Resonance Energy Transfer,” *ACS Nano*, vol. 7, no. 12, pp. 10492–10501, 2013.

[156] H. M. Nguyen, O. Seitz, D. Aureau, A. Sra, N. Nijem, Y. N. Gartstein, Y. J. Chabal, and A. V. Malko, “Spectroscopic evidence for nonradiative energy transfer between colloidal CdSe/ZnS nanocrystals and functionalized silicon substrates,” *Appl. Phys. Lett.*, vol. 98, no. 16, p. 161904, 2011.

[157] J. R. Lakowicz, *Principles of Fluorescence Spectroscopy*. Springer, 2006.

[158] B. Valeur, *Molecular Fluorescence: Principles and Applications*. WILEY-VCH, 2002.

[159] I. Medintz and N. Hildebrandt, *FRET – Förster Resonance Energy Transfer*. Wiley-VCH Verlag GmbH & Co. KGaA, 2014.

[160] A. K. Kenworthy, “Photobleaching FRET microscopy,” in *Molecular Imaging: FRET Microscopy and Spectroscopy*, A. Periasamy and R. N. Day, Eds. New York: Oxford University Press, 2005, pp. 146 – 164.

[161] P. G. Wu and L. Brand, “Resonance Energy Transfer: Methods and Applications,” *Anal. Biochem.*, vol. 218, no. 1, pp. 1–13, 1994.

[162] A. Sillen and Y. Engelborghs, “The Correct Use of ‘Average’ Fluorescence Parameters,” *Photochem. Photobiol.*, vol. 67, no. 5, pp. 475–486, 1998.

[163] L. J. Charbonnière and N. Hildebrandt, “Lanthanide Complexes and Quantum Dots: A Bright Wedding for Resonance Energy Transfer,” *Eur. J. Inorg. Chem.*, vol. 21, pp. 3241–3251, 2008.

[164] Z. Chen, B. Nadal, B. Mahler, H. Aubin, and B. Dubertret, “Quasi-2D Colloidal Semiconductor Nanoplatelets for Narrow Electroluminescence,” *Adv. Funct. Mater.*, vol. 24, pp. 295–302, 2014.

[165] J. Q. Grim, S. Christodoulou, F. Di Stasio, R. Krahne, R. Cingolani, L. Manna, and I. Moreels, “Continuous-wave biexciton lasing at room temperature using solution-processed quantum wells.,” *Nat. Nanotechnol.*, vol. 9, no. 11, pp. 891–895, Oct. 2014.

[166] X. Li and H. Zhu, “Two-dimensional MoS2: Properties, preparation, and applications,” *J. Mater.*, vol. 1, no. 1, pp. 33–44, 2015.

[167] G. Konstantatos and E. H. Sargent, *Colloidal quantum dot optoelectronics and photovoltaics*. Cambridge University Press, 2013.

[168] B. Hötzer, I. L. Medintz, and N. Hildebrandt, “Fluorescence in Nanobiotechnology: Sophisticated Fluorophores for Novel Applications,” *Small*, vol. 8, no. 15, pp. 2297–2326, 2012.

[169] R. M. Clegg, *Chapter 1 Förster resonance energy transfer—FRET what is it, why do it, and how it’s done*, 1st ed., vol. 33, no. 08. Elesvier B.V., 2009.

[170] V. Raicu, “Efficiency of Resonance Energy Transfer in Homo-Oligomeric Complexes of Proteins,” *J. Biol. Phys.*, vol. 33, no. 2, pp. 109–127, 2007.

[171] A. R. Clapp, I. L. Medintz, J. M. Mauro, B. R. Fisher, M. G. Bawendi, and H. Mattoussi, “Fluorescence Resonance Energy Transfer Between Quantum Dot Donors and Dye-Labeled Protein Acceptors,” *J. Am. Chem. Soc.*, vol. 126, no. 1, pp. 301–310, 2004.

[172] P. L. Hernandez-Martinez, A. O. Govorov, and H. V. Demir, “Generalized theory of Förster-type nonradiative energy transfer in nanostructures with mixed dimensionality,” *J. Phys. Chem. C*, vol. 117, no. 19, pp. 10203–10212, 2013.

[173] D. L. Dexter, “A Theory of Sensitized Luminescence in Solids,” *J. Chem. Phys.*, vol. 21, no. 5, pp. 836–850, 1953.

[174] N. J. Turro, V. Ramamurthy, and J. C. Scaiano., *Modern Molecular*

Photochemistry of Organic Molecules. University Science Books, Sausalito, Calif., 2010.

[175] R. A. Marcus, "On the Theory of Oxidation-Reduction Reactions Involving Electron Transfer," *J. Chem. Phys.*, vol. 24, no. 5, pp. 966–978, 1956.

[176] R. A. Marcus, "Chemical and Electrochemical Electron-Transfer Theory," *Annu. Rev. Phys. Chem.*, vol. 15, pp. 155–196, 1964.

[177] R. A. Marcus, "Electrostatic Free Energy and Other Properties of States Having Nonequilibrium Polarization," *J. Chem. Phys.*, vol. 24, no. 5, pp. 979–989, 1956.

[178] H. L. Tavernier and M. D. Fayer, "Distance Dependence of Electron Transfer in DNA: The Role of the Reorganization Energy and Free Energy," *J. Phys. Chem. B*, vol. 104, no. 48, pp. 11541–11550, 2000.

[179] D. M. Adams, L. Brus, C. E. D. Chidsey, S. Creager, C. Creutz, C. R. Kagan, P. V. Kamat, M. Lieberman, S. Lindsay, R. A. Marcus, R. M. Metzger, M. E. Michel-Beyerle, J. R. Miller, M. D. Newton, D. R. Rolison, O. Sankey, K. S. Schanze, J. Yardley, and and X. Zhu, "Charge Transfer on the Nanoscale: Current Status," *J. Phys. Chem. B*, vol. 107, no. 28, pp. 6668–6697, 2003.

[180] Z. R. Grabowski, and K. Rotkiewicz, and W. Rettig, "Structural Changes Accompanying Intramolecular Electron Transfer: Focus on Twisted Intramolecular Charge-Transfer States and Structures," *Chem. Rev.*, vol. 103, no. 10, pp. 3899–4032, 2003.

[181] R. A. Marcus, "Enzymatic catalysis and transfers in solution. I. Theory and computations, a unified view," *J. Chem. Phys.*, vol. 125, no. 19, p. 194504, 2006.

[182] A. Müller, M. Ghosh, R. Sonnenschein, and P. Woditsch, "Silicon for photovoltaic applications," *Mater. Sci. Eng. B*, vol. 134, no. 2–3, pp. 257–262, Oct. 2006.

[183] T. Stelzner, M. Pietsch, G. Andrä, F. Falk, E. Ose, and S. Christiansen, "Silicon nanowire-based solar cells," *Nanotechnology*, vol. 19, no. 29, p. 295203, 2008.

[184] E. C. Garnett and P. Yang, "Silicon nanowire radial p-n junction solar cells.," *J. Am. Chem. Soc.*, vol. 130, no. 29, pp. 9224–9225, Jul. 2008.

[185] Z. Yu, A. Raman, and S. Fan, "Fundamental limit of light trapping in grating

structures," *Opt. Express*, vol. 18, no. S3, pp. 366–380, 2010.

[186] B. Tian, X. Zheng, T. J. Kempa, Y. Fang, N. Yu, G. Yu, J. Huang, and C. M. Lieber, "Coaxial silicon nanowires as solar cells and nanoelectronic power sources," *Nature*, vol. 449, pp. 885–889, Oct. 2007.

[187] M. S. Jang and H. Atwater, "Plasmonic Rainbow Trapping Structures for Light Localization and Spectrum Splitting," *Phys. Rev. Lett.*, vol. 107, no. 20, p. 207401, Nov. 2011.

[188] T. Trupke, M. A. Green, and P. Würfel, "Improving solar cell efficiencies by down-conversion of high-energy photons," *J. Appl. Phys.*, vol. 92, no. 3, p. 1668, 2002.

[189] W. G. J. H. M. van Sark, "Enhancement of solar cell performance by employing planar spectral converters," *Appl. Phys. Lett.*, vol. 87, no. 15, p. 151117, 2005.

[190] T. Förster, "Zwischenmolekulare Energiewanderung und Fluoreszenz.," *Annu. Phys.*, vol. 437, pp. 55–75., 1948.

[191] M. Stavola, L. D. Dexter, and S. R. Knox, "Electron-hole pair excitation in semiconductors via energy transfer from an external sensitizer," *Phys. Rev. B*, vol. 31, no. 4, pp. 2277–2289, 1985.

[192] A. P. Alivisatos, M. F. Arndt, S. Efrima, D. H. Waldeck, and C. B. Harris, "Electronic energy transfer at semiconductor interfaces. I. Energy transfer from two- dimensional molecular films to Si(111)," *J. Chem. Phys.*, vol. 86, no. 11, p. 6540, 1987.

[193] S. Lu and A. Madhukar, "Nonradiative resonant excitation transfer from nanocrystal quantum dots to adjacent quantum channels.," *Nano Lett.*, vol. 7, no. 11, pp. 3443–51, Nov. 2007.

[194] S. Lu, Z. Lingley, T. Asano, D. Harris, T. Barwicz, S. Guha, and A. Madhukar, "Photocurrent Induced by Nonradiative Energy Transfer from Nanocrystal Quantum Dots to Adjacent Silicon Nanowire Conducting Channels: Toward a New Solar Cell Paradigm," *Nano Lett.*, vol. 9, no. 12, pp. 4548–4552, 2009.

[195] W. G. J. H. M. Van Sark, P. L. T. M. Frederix, D. J. Van den Heuvel, and H. C. Gerritsen, "Photooxidation and photobleaching of single CdSe/ZnS quantum dots probed by room-temperature time-resolved spectroscopy," *J. Phys. Chem. B*, vol. 105, no. 35, pp. 8281–8284, 2001.

[196] V. W. Manner, A. Y. Koposov, P. Szymanski, V. I. Klimov, and M. Sykora, “Role of solvent–oxygen ion pairs in photooxidation of CdSe nanocrystal quantum dots,” *ACS Nano*, vol. 6, no. 3, pp. 2371–2377, 2012.

[197] S. A. Crooker, J. A. Hollingsworth, S. Tretiak, and V. I. Klimov, “Spectrally Resolved Dynamics of Energy Transfer in Quantum-Dot Assemblies: Towards Engineered Energy Flows in Artificial Materials,” *Phys. Rev. Lett.*, vol. 89, no. 18, p. 186802, Oct. 2002.

[198] B. N. Pal, Y. Ghosh, S. Brovelli, R. Laocharoensuk, V. I. Klimov, J. A. Hollingsworth, and H. Htoon, “‘Giant’ CdSe/CdS Core/Shell Nanocrystal Quantum Dots As Efficient Electroluminescent Materials: Strong Influence of Shell Thickness on Light-Emitting Diode Performance,” *Nano Lett.*, vol. 12, no. 1, pp. 331–336, 2012.

[199] Olivier Labeau, P. Tamarat, and B. Lounis, “Temperature Dependence of the Luminescence Lifetime of Single CdSe/ZnS Quantum Dots,” *Phys. Rev. Lett.*, vol. 90, no. 25, p. 257404, 2003.

[200] L. Novotny and B. Hecht, *Principles of Nano-Optics*. Cambridge University Press, 2006.

[201] L. Novotny, “Allowed and forbidden light in near-field optics. I. A single dipolar light source,” *J. Opt. Soc. Am. A*, vol. 14, no. 1, pp. 91–104, Jan. 1997.

[202] R. Chance, R. R.; Prock, A.; Silbey, “Molecular Fluorescence and Energy Transfer Near Interfaces,” in *Advances in Chemical Physics*, S. A. Prigogine, I., Rice, Ed. New York: Wiley, 1978, pp. 1–65.

[203] K. Bücher, J. Bruns, and H. G. Wagemann, “Absorption coefficient of silicon: An assessment of measurements and the simulation of temperature variation,” *J. Appl. Phys.*, vol. 75, no. 2, pp. 1127–1132, 1994.

[204] P. M. Platzman and P. A. Wolf., *Waves and interactions in solid state plasmas*. New York: Academic Press, 1973.

[205] A. O. Govorov, J. Lee, and N. A. Kotov, “Theory of plasmon-enhanced Förster energy transfer in optically excited semiconductor and metal nanoparticles,” *Phys. Rev. B*, vol. 76, no. 12, p. 125308, Sep. 2007.

[206] P. L. Hernández-Martinez and A. O. Govorov, “Exciton energy transfer between nanoparticles and nanowires,” *Phys. Rev. B*, vol. 78, no. 3, p. 35314,

Jul. 2008.

[207] E. D. Palik, *Handbook of optical constants of solids*. Academic Press: New York, 1998.

[208] C. Kagan, C. Murray, and M. Bawendi, “Long-range resonance transfer of electronic excitations in close-packed CdSe quantum-dot solids.,” *Phys. Rev. B. Condens. Matter*, vol. 54, no. 12, pp. 8633–8643, Sep. 1996.

[209] M. Lunz, A. L. Bradley, W.-Y. Chen, and Y. K. Gun□ko, “Two-Dimensional Förster Resonant Energy Transfer in a Mixed Quantum Dot Monolayer: Experiment and Theory,” *J. Phys. Chem. C*, vol. 113, no. 8, pp. 3084–3088, 2009.

[210] P. Yu and M. Cardona, *Fundamentals of semiconductors: physics and materials properties*, 4th ed. Springer, 2010.

[211] J. Lee, A. O. Govorov, and N. A. Kotov, “Bioconjugated Superstructures of CdTe Nanowires and Nanoparticles: Multistep Cascade Förster Resonance Energy Transfer and Energy Channeling,” *Nano Lett.*, vol. 5, no. 10, pp. 2063–2069, 2005.

[212] P. M. Whitmore, A. P. Alivisatos, and C. B. Harris, “Distance Dependence of Electronic Energy Transfer to Semiconductor Surfaces: 3nπ* Pyrazine/GaAs(110),” *Phys. Rev. Lett.*, vol. 50, no. 14, pp. 1092–1094, 1983.

[213] A. Antipov, M. Bell, M. Yasar, V. Mitin, W. Scharmach, M. Swihart, A. Verevkin, and A. Sergeev, “Luminescence of colloidal CdSe/ZnS nanoparticles: high sensitivity to solvent phase transitions,” *Nanoscale Res. Lett.*, vol. 6, no. 142, pp. 1–7, 2011.

[214] T. Franzl, T. A. Klar, S. Schietinger, A. L. Rogach, and J. Feldmann, “Exciton Recycling in Graded Gap Nanocrystal Structures,” *Nano Lett.*, vol. 4, no. 9, pp. 1599–1603, Sep. 2004.

[215] T. A. Klar, T. Franzl, A. L. Rogach, and J. Feldmann, “Super-Efficient Exciton Funneling in Layer-by-Layer Semiconductor Nanocrystal Structures,” *Adv. Mater.*, vol. 17, no. 6, pp. 769–773, Mar. 2005.

[216] B. Guzelturk, P. L. H. Martinez, Q. Zhang, Q. Xiong, H. Sun, X. W. Sun, A. O. Govorov, and H. V. Demir, “Excitonics of semiconductor QDs and wires for lighting and displays,” *Laser Photon. Rev.*, vol. 8, no. 1, pp. 73–93, 2014.

[217] A. L. Rogach, T. Franzl, T. A. Klar, J. Feldmann, N. Gaponik, V. Lesnyak, A. Shavel, A. Eychmüller, Y. P. Rakovich, and J. F. Donegan, "Aqueous Synthesis of Thiol-Capped CdTe Nanocrystals: State-of-the-Art," *J. Phys. Chem. C*, vol. 111, no. 40, pp. 14628–37, 2007.

[218] M. Naruse, E. Runge, K. Kobayashi, and M. Ohtsu, "Efficient optical excitation transfer in layered quantum dot nanostructures networked via optical near-field interactions," *Phys. Rev. B*, vol. 82, no. 12, p. 125417, Sep. 2010.

[219] U. Bovensiepen, H. Petek, and M. Wolf, *Dynamics at Solid State Surfaces and Interfaces: Volume 2: Fundamentals*, vol. 2. WILEY-VCH, 2012.

[220] B. C. Daly, K. Kang, Y. Wang, and D. G. Cahill, "Picosecond ultrasonic measurements of attenuation of longitudinal acoustic phonons in silicon," *Phys. Rev. B*, vol. 80, no. 17, p. 174112, Nov. 2009.

[221] "See supplementary material at [URL will be inserted by AIP] for more details about the layer by layer deposition procedure and for more details about the theoretical analysis.," *See supplementary material at [URL will be inserted by AIP] for more details about the layer by layer deposition procedure and for more details about the theoretical analysis.* .

[222] K. F. Mak, M. Y. Sfeir, Y. Wu, C. H. Lui, J. a. Misewich, and T. F. Heinz, "Measurement of the Optical Conductivity of Graphene," *Phys. Rev. Lett.*, vol. 101, no. 19, p. 196405, Nov. 2008.

[223] R. R. Nair, P. Blake, A. N. Grigorenko, K. S. Novoselov, T. J. Booth, T. Stauber, N. M. R. Peres, and A. K. Geim, "Fine Structure Constant Defines," *Science (80-.).*, vol. 320, no. June, p. 1308, 2008.

[224] A. S. Mayorov, R. V Gorbachev, S. V Morozov, L. Britnell, R. Jalil, L. a Ponomarenko, P. Blake, K. S. Novoselov, K. Watanabe, T. Taniguchi, and a K. Geim, "Micrometer-scale ballistic transport in encapsulated graphene at room temperature.," *Nano Lett.*, vol. 11, no. 6, pp. 2396–9, Jun. 2011.

[225] C. X. Guo, H. Bin Yang, Z. M. Sheng, Z. S. Lu, Q. L. Song, and C. M. Li, "Layered graphene/quantum dots for photovoltaic devices.," *Angew. Chemie Int. Ed.*, vol. 49, no. 17, pp. 3014–7, Apr. 2010.

[226] R. Graphene, Y. Lin, K. Zhang, W. Chen, Y. Liu, Z. Geng, J. Zeng, N. Pan, L. Yan, X. Wang, and J. G. Hou, "Dramatically Enhanced Photoresponse of Free

Anchored CdSe Nanoparticles," vol. 4, no. 6, pp. 3033–3038, 2010.

[227] G. Konstantatos, M. Badioli, L. Gaudreau, J. Osmond, M. Bernechea, F. P. Garcia de Arquer, F. Gatti, and F. H. L. Koppens, "Hybrid graphene-quantum dot phototransistors with ultrahigh gain.," *Nat. Nanotechnol.*, vol. 7, no. 6, pp. 363–8, Jun. 2012.

[228] I. Calizo, S. Ghosh, W. Bao, F. Miao, C. Ning Lau, and A. A. Balandin, "Raman nanometrology of graphene: Temperature and substrate effects," *Solid State Commun.*, vol. 149, no. 27–28, pp. 1132–1135, Jul. 2009.

[229] K. N. Kudin, B. Ozbas, H. C. Schniepp, R. K. Prud'homme, I. a Aksay, and R. Car, "Raman spectra of graphite oxide and functionalized graphene sheets," *Nano Lett.*, vol. 8, no. 1, pp. 36–41, Jan. 2008.

[230] I. K. Moon, J. Lee, R. S. Ruoff, and H. Lee, "Reduced graphene oxide by chemical graphitization," *Nat. Commun.*, vol. 1, no. 6, p. 73, Jan. 2010.

[231] D. Yang, A. Velamakanni, G. Bozoklu, S. Park, M. Stoller, R. D. Piner, S. Stankovich, I. Jung, D. a. Field, C. a. Ventrice, and R. S. Ruoff, "Chemical analysis of graphene oxide films after heat and chemical treatments by X-ray photoelectron and Micro-Raman spectroscopy," *Carbon N. Y.*, vol. 47, no. 1, pp. 145–152, Jan. 2009.

[232] J. Shen, Y. Hu, M. Shi, X. Lu, C. Qin, C. Li, and M. Ye, "Fast and Facile Preparation of Graphene Oxide and Reduced Graphene Oxide Nanoplatelets," *Chem. Mater.*, vol. 21, no. 15, pp. 3514–3520, Aug. 2009.

[233] T. N. Lambert, C. C. Luhrs, C. A. Chavez, S. Wakeland, M. T. Brumbach, and T. M. Alam, "Graphite oxide as a precursor for the synthesis of disordered graphenes using the aerosol-through-plasma method," *Carbon N. Y.*, vol. 48, no. 14, pp. 4081–4089, Nov. 2010.

[234] D. S. Sutar, P. K. Narayanam, G. Singh, V. D. Botcha, S. S. Talwar, R. S. Srinivasa, and S. S. Major, "Spectroscopic studies of large sheets of graphene oxide and reduced graphene oxide monolayers prepared by Langmuir–Blodgett technique," *Thin Solid Films*, vol. 520, no. 18, pp. 5991–5996, Jul. 2012.

[235] M. A. Pimenta, G. Dresselhaus, M. S. Dresselhaus, L. G. Cançado, A. Jorio, and R. Saito, "Studying disorder in graphite-based systems by Raman spectroscopy," *Phys. Chem. Chem. Phys.*, vol. 9, no. 11, pp. 1276–91, Mar.

2007.

[236] Y. Zhou, Q. Bao, L. A. L. Tang, Y. Zhong, and K. P. Loh, “Hydrothermal Dehydration for the ‘Green’ Reduction of Exfoliated Graphene Oxide to Graphene and Demonstration of Tunable Optical Limiting Properties,” *Chem. Mater.*, vol. 21, no. 13, pp. 2950–2956, Jul. 2009.

[237] J. I. Paredes, S. Villar-Rodil, P. Solís-Fernández, A. Martínez-Alonso, and J. M. D. Tascón, “Atomic force and scanning tunneling microscopy imaging of graphene nanosheets derived from graphite oxide.,” *Langmuir*, vol. 25, no. 10, pp. 5957–68, May 2009.

[238] V. C. Tung, M. J. Allen, Y. Yang, and R. B. Kaner, “High-throughput solution processing of large-scale graphene,” *Nat. Nanotechnol.*, vol. 4, no. November 2008, pp. 25–29, 2009.

[239] Z. Fan, K. Wang, T. Wei, J. Yan, L. Song, and B. Shao, “An environmentally friendly and efficient route for the reduction of graphene oxide by aluminum powder,” *Carbon N. Y.*, vol. 48, no. 5, pp. 1686–1689, Apr. 2010.

[240] C. D. Zangmeister, “Preparation and Evaluation of Graphite Oxide Reduced at 220 °C,” *Chem. Mater.*, vol. 22, no. 19, pp. 5625–5629, Oct. 2010.

[241] O. Akhavan, “The effect of heat treatment on formation of graphene thin films from graphene oxide nanosheets,” *Carbon N. Y.*, vol. 48, no. 2, pp. 509–519, Feb. 2010.

[242] D. K. Singh, P. K. Iyer, and P. K. Giri, “Role of molecular interactions and structural defects in the efficient fluorescence quenching by carbon nanotubes,” *Carbon N. Y.*, vol. 50, no. 12, pp. 4495–4505, Oct. 2012.

[243] H. Dong, W. Gao, F. Yan, H. Ji, and H. Ju, “Fluorescence resonance energy transfer between quantum dots and graphene oxide for sensing biomolecules.,” *Anal. Chem.*, vol. 82, no. 13, pp. 5511–7, Jul. 2010.

[244] S. Ithurria and B. Dubertret, “Quasi 2D Colloidal CdSe Platelets with Thicknesses Controlled at the Atomic Level,” *J. Am. Chem. Soc.*, pp. 16504–16505, 2008.

[245] A. Yeltik, B. Guzelturk, P. L. Hernandez-Martinez, A. O. Govorov, and H. V. Demir, “Phonon-Assisted Exciton Transfer into Silicon Using Nanoemitters: The Role of Phonons and Temperature E ffects in Förster Resonance Energy

Transfer," *ACS Nano*, vol. 7, no. 12, pp. 10492–10501, 2013.

[246] L. V. Keldysh, "Coulomb interaction in thin semiconductor and semimetal films.," *J. Exp Theor. Phys. Lett.*, vol. 29, pp. 658–660, 1979.

[247] S. G. Tikhodeev, N. A. Gippius, A. L. Yablonskii, A. B. Dzyubenko, L. V. Kulik, V. D. Kulakovskii, and A. Forchel, "Excitons in near surface quantum wells: Local probe of semiconductor/vacuum surface.," *Phys. Status Solidi*, vol. 164, pp. 179–182, 1997.

[248] N. A. Gippius, A. L. Yablonskii, A. B. Dzyubenko, S. G. Tikhodeev, L. V Kulik, V. D. Kulakovskii, and A. Forchel, "Excitons in near-surface quantum wells in magnetic fields: Experiment and theory," *J. Appl. Phys.*, vol. 83, no. 10, pp. 5410–5417, 1998.

[249] L. V Kulik, V. D. Kulakovskii, M. Bayer, A. Forchel, N. A. Gippius, and S. G. Tikhodeev, "Dielectric enhancement of excitons in near-surface quantum wells.," *Phys. Rev. B*, vol. 54, no. 4, pp. 2335–2338, 1996.

[250] A. W. Achtstein, A. Schliwa, A. Prudnikau, M. Hardzei, M. V Artemyev, C. Thomsen, and U. Woggon, "Electronic Structure and Exciton − Phonon Interaction in Two- Dimensional Colloidal CdSe Nanosheets," *Nano Lett.*, vol. 12, pp. 3151–3157, 2012.

[251] G. Peter and E. O. Gobel, "Dependence of Radiative Exciton Lifetimes in Quantum," *Phys. Rev. Lett.*, vol. 59, no. 20, pp. 2337–2340, 1987.

[252] E. I. Rashba and G. E. Gurgenishvili, "Edge absorption theory in semiconductors.," *Sov. Phys. Solid State*, vol. 4, pp. 759–760, 1962.

[253] , R. D. Schaller, M. Pelton, and D. V. Talapin, "Low-Threshold Stimulated Emission Using Colloidal Quantum Wells.," *Nano Lett.*, vol. 14, pp. 2772–2777, 2014.

[254] W. W. Yu, L. Qu, W. Guo, and X. Peng, "Experimental Determination of the Extinction Coefficient of CdTe , CdSe , and CdS Nanocrystals," *Chem. Mater.*, vol. 15, no. 14, pp. 2854–2860, 2003.

[255] D. Ricard, M. Ghanassi, and M. C. Schanne-Klein, "Dielectric confinement and the linear and nonlinear optical properties of semiconductor-doped glasses," *Opt. Commun.*, vol. 108, pp. 311–318, 1994.

[256] Z. Li, H. Qin, D. Guzun, M. Benamara, G. Salamo, and X. Peng, "Uniform

thickness and colloidal-stable CdS quantum disks with tunable thickness: Synthesis and properties," *Nano Res.*, vol. 5, no. 5, pp. 337–351, May 2012.

[257] C. A. Leatherdale, W. K. Woo, F. V Mikulec, and M. G. Bawendi, "On the Absorption Cross Section of CdSe Nanocrystal Quantum Dots," *J. Phys. Chem. B*, vol. 106, pp. 7619–7622, 2002.

[258] M. Kuno, *Introductory Nanoscience*. Garland Science: New York, 2011.

[259] M. D. Tessier, C. Javaux, I. Maksimovic, V. Loriette, and B. Dubertret, "Spectroscopy of Single CdSe Nanoplatelets," *ACS Nano*, vol. 6, no. 8, pp. 6751–6758, 2012.

[260] W. Demtroder, *Laser Spectroscopy*, 3rd ed. Springer: New York, 2003.

[261] R. C. Hilborn, "Einstein coefficients, cross sections, f values, dipole moments, and all that," *Am. J. Phys.*, vol. 50, p. 982, 1982.

[262] Y. Kalisky, *The Physics and Engineering of Solid State Lasers*. SPIE, 2006.

[263] C. Cohen-Tannoudji, B. Diu, and F. Laloe, *Quantum Mechanics*. Wiley: New York, 1977.

[264] B. Guzelturk, O. Erdem, M. Olutas, Y. Kelestemur, and H. V. Demir, "Stacking in Colloidal Nanoplatelets: Excitonic Properties.," *ACS Nano*, no. DOI: 10.1021/nn5053734, p. DOI: 10.1021/nn5053734, Dec. 2014.

[265] B. Cecile, B. Mahler, B. Nadal, B. Abecassis, M. D. Tessier, S. Ithurria, X. Xu, and B. Dubertret, "Two-Dimensional Growth of CdSe Nanocrystals, from Nanoplatelets to Nanosheets," *Chem. Mater.*, vol. 25, p. 639, 2013.

[266] E. M. Hutter, E. Bladt, B. Goris, F. Pietra, J. C. Van Der Bok, M. P. Boneschanscher, C. D. M. Donega, S. Bals, and D. Vanmaekelbergh, "Conformal and Atomic Characterization of Ultrathin CdSe Platelets with a Helical Shape," *Nano Lett.*, vol. 14, p. 6257, 2014.

[267] C. E. Rowland, I. Fedin, H. Zhang, S. K. Gray, A. O. Govorov, D. V Talapin, and R. D. Schaller, "Picosecond energy transfer and multiexciton transfer outpaces Auger recombination in binary CdSe nanoplatelet solids," *Nat Mater*, vol. 14, no. 5, pp. 484–489, May 2015.

[268] L. R. Bradshaw, K. E. Knowles, S. McDowall, and D. R. Gamelin, "Nanocrystals for Luminescent Solar Concentrators," *Nano Lett.*, vol. 15, no. 2, pp. 1315–1323, 2015.

[269] C. S. Erickson, L. R. Bradshaw, S. McDowall, J. D. Gilbertson, D. R. Gamelin, and D. L. Patrick, “Zero-Reabsorption Doped-Nanocrystal Luminescent Solar Concentrators,” *ACS Nano*, vol. 8, no. 4, pp. 3461–3467, 2014.

[270] J. Huang, Y. Yang, S. Xue, B. Yang, S. Liu, and J. Shen, “Photoluminescence and electroluminescence of ZnS:Cu nanocrystals in polymeric networks,” *Appl. Phys. Lett.*, vol. 70, no. 18, p. 2335, 1997.

[271] Z. Tan, Y. Zhang, C. Xie, H. Su, J. Liu, C. Zhang, N. Dellas, S. E. Mohney, Y. Wang, J. Wang, and J. Xu, “Near-Band-Edge Electroluminescence from Heavy-Metal-Free Colloidal Quantum Dots,” *Adv. Mater.*, vol. 23, no. 31, pp. 3553–3558, 2011.

[272] W. Zhang, Q. Lou, W. Ji, J. Zhao, and X. Zhong, “Color-tunable highly bright photoluminescence of cadmium-free cu-doped Zn-In-S nanocrystals and electroluminescence,” *Chem. Mater.*, vol. 26, no. 2, pp. 1204–1212, 2014.

[273] S. Xu, C. Wang, Z. Wang, H. Zhang, J. Yang, Q. Xu, H. Shao, R. Li, W. Lei, and Y. Cui, “Aqueous synthesis of internally doped Cu:ZnSe/ZnS core–shell nanocrystals with good stability,” *Nanotechnology*, vol. 22, no. 27, p. 275605, 2011.

[274] S. Sarkar, N. S. Karan, and N. Pradhan, “Ultrasmall Color-Tunable Copper-Doped Ternary Semiconductor Nanocrystal Emitters,” *Angew. Chemie Int. Ed.*, vol. 50, no. 27, pp. 6065–6069, 2011.

[275] A. R. Maity, S. Palmal, S. K. Basiruddin, N. S. Karan, S. Sarkar, N. Pradhan, and N. R. Jana, “Doped semiconductor nanocrystal based fluorescent cellular imaging probes,” *Nanoscale*, vol. 5, no. 12, pp. 5506–5513, 2013.

[276] F. Meinardi, H. McDaniel, F. Carulli, A. Colombo, K. a. Velizhanin, N. S. Makarov, R. Simonutti, V. I. Klimov, and S. Brovelli, “Highly efficient large-area colourless luminescent solar concentrators using heavy-metal-free colloidal quantum dots,” *Nat. Nanotechnol.*, vol. 10, no. 10, pp. 878–885, 2015.

[277] K. E. Knowles, K. H. Hartstein, T. B. Kilburn, A. Marchioro, H. D. Nelson, P. J. Whitham, and D. R. Gamelin, “Luminescent Colloidal Semiconductor Nanocrystals Containing Copper: Synthesis, Photophysics, and Applications,” *Chem. Rev.*, 2016.

[278] A. Govorov, P. L. H. Martínez, and H. V. Demir, *Understanding and Modeling*

FRETFörster-type Resonance Energy Transfer: Introduction to Förster-type Resonance Energy Transfer (FRET) FRET Series. Springer, 2016.

[279] S. Sarkar, A. R. Maity, N. S. Karan, and N. Pradhan, "Fluorescence Energy Transfer from Doped to Undoped Quantum Dots," *J. Phys. Chem. C*, vol. 117, no. 42, pp. 21988–21994, 2013.

[280] A. Sahu, M. S. Kang, A. Kompch, C. Notthoff, A. W. Wills, D. Deng, M. Winterer, C. D. Frisbie, and D. J. Norris, "Electronic impurity doping in CdSe nanocrystals," *Nano Lett.*, vol. 12, no. 5, pp. 2587–2594, 2012.

[281] M. Sharma, K. Gungor, A. Yeltik, M. Olutas, B. Guzelturk, Y. Kelestemur, T. Erdem, and H. V. Demir, "Copper-Doped Colloidal Semiconductor Quantum Wells for Luminescent Solar Concentrators," *arXiv:1606.06523*, Jun. 2016.

[282] M. D. Tessier, C. Javaux, I. Maksimovic, V. Loriette, and B. Dubertret, "Spectroscopy of Single CdSe Nanoplatelets," *ACS Nano*, vol. 6, no. 8, pp. 6751–6758, 2012.

[283] N. Durisic, A. G. Godin, D. Walters, P. Grütter, P. W. Wiseman, and C. D. Heyes, "Probing the 'Dark' Fraction of Core–Shell Quantum Dots by Ensemble and Single Particle pH-Dependent Spectroscopy," *ACS Nano*, vol. 5, no. 11, pp. 9062–9073, 2011.

[284] T. Franzl, A. Shavel, A. L. Rogach, N. Gaponik, T. A. Klar, A. Eychmüller, and J. Feldmann, "High-Rate Unidirectional Energy Transfer in Directly Assembled CdTe Nanocrystal Bilayers," *Small*, vol. 1, no. 4, pp. 392–395, 2005.

[285] N. Cicek, S. Nizamoglu, T. Ozel, E. Mutlugun, D. U. Karatay, V. Lesnyak, T. Otto, N. Gaponik, A. Eychmüller, and H. V. Demir, "Structural tuning of color chromaticity through nonradiative energy transfer by interspacing CdTe nanocrystal monolayers," *Appl. Phys. Lett.*, vol. 94, no. 6, p. 061105, 2009.